Physical Regulation of Cell Behaviors: Multifrequency AFM Measurement of Mechanoelectric, Mechanochemical, and Hydration Shell Effects on ECM and Cell Substrate Viscoelasticity



Casey Adam

St John's College

University of Oxford

Supervisors: Professor Sonia Contera and Professor Sarah Waters

A thesis submitted for the degree of

Doctor of Philosophy

Hillary 2021

Abstract

The extracellular matrix (ECM) is a scaffold of molecules, constructed and maintained by cells, that determines tissue structure. Cell-ECM interactions are crucial for maintaining healthy tissues. Understanding these interactions could provide insight into regenerative medicine and help develop new disease treatments. The mechanical properties of cells and the ECM are crucial in this interaction. Biological systems are viscoelastic (viscous and elastic), meaning they respond to applied forces with characteristic time delays known as time responses. For models of viscoelasticity that describe biological structures, time responses are the ratio of viscosity to elasticity. Furthermore, viscoelastic, electrical, and chemical properties of biological systems are coupled.

In this thesis, I applied advanced dynamic atomic force microscopy (AFM) to quantify effects of electrical and chemical stimuli on ECM viscoelasticity at cellular length scales. Mechanoelectric coupling in the ECM was studied by measuring how ions altered collagen (the most prevalent component of the ECM) mechanics. Increased ion concentration increased collagen elasticity and viscosity, maintaining constant time responses. Ion flow decreased collagen time responses. Additionally, these experiments demonstrated that collagen hydration shells are viscoelastic, suggesting fluid within tissues contributes directly to tissue viscoelasticity. Next, mechanochemical coupling in the ECM was studied by measuring viscoelasticity of ECMs produced by cells in response to growth factors and mutation. Cells deposited more ECM in the presence of growth factors, increasing ECM viscosity and elasticity, yet maintaining constant time responses. Mutants exhibited reduced ability to produce ECM, modify viscoelasticity, and less control over time responses. The final set of experiments measured viscoelasticity of substrates known to alter cell behaviors, demonstrating a potential relationship between substrate time responses and cell behaviors. Together, my findings suggest that ECM time responses remain constant in many environmental conditions. Alteration of time responses may be a physiological mechanism of regulating cell activities and tissue health.

Acknowledgements

Throughout the course of my PhD, I have been lucky to meet and receive help from many wonderful people and scientists.

First, I would like to thank Professor Sonia Contera and Professor Sarah Waters for taking me on as their student and allowing me to propose and design this project together with them. I am grateful for all of their feedback, discussions, and that they allowed me freedom and independence in choosing the direction of my PhD. I hope we stay in touch in the future!

Many thanks to the people of the Contera lab. Thanks to: Dr. Andrea Bonilla-Bruner for her help troubleshooting while I was learning how to operate the AFM, Dr. Zeinab Al-Rekabi for teaching me AM-FM AFM, Dr. Jacob Seifert for his excellent explanations of viscoelasticity and physics, for our fun discussions, and for introducing me to Yoga with Tim. Additional thanks to Alex Zagajewski for the discussions and hikes, as well as Viraj Alimchandani, Ania Wald, Renat Karimov, Jenna Elliott, Dr. Priyadarshani (Priya) Choudhary, and other Masters students of the lab for the fun social events and discussions. Additional thanks to Giulia Celora of the Waters lab for the fun discussions about collagen, swelling, and mechanics.

Special thanks to Dr. Alba Piacenti for our trips to Durham and Rome, explanations about contact mechanics, help proofreading, and for teaching me the PANDA technique that she developed. She is a thorough scientist, and a great friend.

Special thanks to Dr. (in both senses of the word) Alex Gordon-Weeks for his enthusiasm, knowledge, and for preparing the samples in the pancreatic cancer work (chapter 5). I hope our collaboration continues! Additional thanks to Dr. Algela Diana, for her collaboration in our attempt to perform AFM on mouse tumors and spheroids.

Special thanks to Professor Kislon Voitchovsky for our discussions about hydration shells and polymer brushes, and for training me in how to apply electric fields in liquid environments in an AFM. I was unable to complete this experiment before the end of the PhD due to covid delays. However, I intend to put his training to use in the future!

Thanks to the people of Asylum Research, for their help troubleshooting and explaining features of atomic force microscopy. My understanding of AM-FM AFM was greatly enhanced thanks to the two month correspondence I had with Dr. Roger Proksch and Dr. Aleks Labuda. Also thanks to Dr. Ryan Wagner for answering questions about AM-FM AFM and to Dr. Chris Mulcahy for pushing for the repair of our Cypher. Very special

thanks to Dr. Jonathan Moffatt of Asylum Research for his perseverance in advocating for the repair of our Cypher AFM after it broke and for all of his help answering questions and providing AFM protocols, especially the liquid perfusion protocol used in chapter 4.

Thanks to the people of Oxford Physics. In particular, thanks to Alan Francis and Bill Thompson in the Physics stores for providing materials and tools (especially double-sided foam) for my experiments. Thanks to Kieran McCall for his tours of the Helium and Nitrogen liquifiers, helping with our Nitrogen cylinders and dewars, our discussion on applying electric fields in liquid, and our informal chats.

Thanks to Dr. Alexander Anderson, Dr. Mark Robertson-Tessi, and Kimberly Luddy from Moffitt Cancer Center for helping me foster an interdisciplinary approach to biology, and for all their support in helping me reach Oxford. Additional thanks to Dr. Alexander Anderson for the stipend that paid my living costs during the first year of my PhD.

Special thanks to George Edick for telling me about poly(HEMA), used in chapter 6. I may not have ended up at Oxford insisting on a project about the physics of biology were it not for his mentoring, and his vast biological knowledge is invaluable to my thinking about cells and their environment.

Thanks to my brother, Dr. Joe Adam, for our discussions and proofreading. His understanding of many fields pushes me to become a better scientist, and I always benefit from hearing his thoughts. Additional thanks to my mother and father for their support, help proofreading, and the time we spent discussing my work.

Thanks to the Systems Biology DTC. I enjoyed the broad range of taught subjects, and met many lifelong friends there. Additional thanks to St. John's college, Oxford, especially Nigel, Tony, and Dan in the Porters Lodge and the scouts, for supporting the non-academic elements of my PhD. Additional thanks to William Blythe for his help proofreading.

Last, but not least, thanks to my examiners, Professor Stephen Tucker and Professor Núria Gavara, for taking the time to read and help improve my thesis. I enjoyed our discussions during the defense as well as their feedback!

Statement of Originality

I declare that the work presented in this thesis is my own. Any contributions made by my collaborators are explicitly acknowledged in the text. The major contributions to this thesis are the following.

- Dr. Alba Rosa Piacenti trained me in the PANDA technique that she developed. She also provided the control DMA data (from her collaboration with Nicholas Hawkins) and analyzed PANDA data for the rubber experiments in chapter 3.
- Dr. Alex Gordon-Weeks created the collagen V and collagen XI mutants and prepared all the cell derived ECM samples for me to measure with the experiments presented in chapter 5.

No part of this thesis has been accepted or submitted for any other degree. The work in this thesis has been disseminated at conferences in the following presentations.

- Casey Adam, Alex Gordon-Weeks, Sarah Waters, Sonia Contera. AM-FM AFM nanomechanical mapping of the effects of ion concentration growth factors and collagen V knockdown on the extracellular matrix secreted by fibroblasts in vitro (oral presentation, Microscience Microscopy Congress, Manchester, 2019).
- Casey Adam, Sarah Waters, Sonia Contera. Mechanoelectrical coupling in collagen I. 7th Multifrequency AFM conference (poster presentation, Madrid, 2017) and the Warwick bioelectricity workshop (poster presentation, Warwick, 2018).

Several publications based on the work presented in this thesis are currently being drafted.

Contents

1 Introduction **1**

1.1 How cells interact with their environment 4

1.1.1 What is the ECM? 5

1.1.2 How the ECM influences cell behaviors 7

1.1.3 How cell behaviors influence the ECM 8

1.1.4 Summary and outlook: How cells interact with their environment 9

1.2 Physical properties of biological systems 9

1.2.1 Coupling of physical properties of biomolecules 10

1.2.1.1 Piezoelectricity and endogenous voltages 10

1.2.2 Effect of water and salt on biomolecule multiphysics 11

1.2.2.1 Charge of biomolecules 11

1.2.2.1.1 Effect of pH 12

1.2.2.1.2 Effect of spatial confinement 14

1.2.2.1.3 Effect of ions 15

1.2.3 Summary: Physical properties of biological systems 16

1.3 Introduction to mechanics 16

1.3.1 Elasticity and viscosity 17

1.3.2 Viscoelasticity 18

1.3.2.1 Physical origin of viscoelasticity 19

1.3.3 Experimental quantification of viscoelasticity 20

1.3.3.1 Relaxation experiments 21

1.3.3.2 Creep experiments 21

1.3.3.3 Dynamic experiments 22

1.3.4 The standard linear solid (SLS) 23

1.3.4.1 The SLS during a relaxation experiment 25

1.3.4.2 The SLS during a creep experiment 26

1.3.4.3 The SLS during a dynamic experiment 26

1.3.5 Limiting cases of the SLS 27

1.3.5.1 Kelvin-Voigt (KV) materials 27
1.3.5.2 Maxwell (MW) materials 28
1.3.6 General Maxwell materials (GMM) 29
1.3.7 Relating models of viscoelasticity to physical quantities 30
1.3.8 Summary: Introduction to mechanics 32
1.4 Overall summary and outlook 33

2 Experimental Techniques **35**
2.1 Atomic force microscopy (AFM) 36
2.1.1 Cantilever calibration 38
2.1.2 Contact models 39
2.1.2.1 The Hertz contact model 39
2.1.2.2 The Hertz contact model with adhesion 40
2.1.3 Quantifying a sample's mechanical properties with AFM . . . 42
2.1.3.1 Methods to excite the cantilever 43
2.1.3.2 AFM indentations: Creep and relaxation experiments 44
2.1.3.2.1 Limitations of indentation experiments . . . 44
2.1.3.3 Photothermal AFM nano-DMA (PANDA) 45
2.1.3.3.1 Limitations of PANDA 47
2.1.3.4 Amplitude modulation-frequency modulation (AM-FM) 47
2.1.3.4.1 Limitations of AM-FM AFM 51
2.1.3.4.2 AM-FM AFM measurement statistics 51
2.2 Chapter summary and outlook 54

3 Development and Validation of a New Method to Analyze AM-FM AFM Data **56**
3.1 Error caused by performing AM-FM AFM without tip radius calibration 59
3.2 Development of a novel method to analyze AM-FM AFM data 60
3.2.1 Determining the best model of viscoelasticity to describe a sample 61
3.2.1.1 Extension to a GMM 63
3.2.1.2 Modification of the model test for a GMM 64
3.2.1.3 Comparing model test slopes for the SLS and GMM 66
3.2.2 Solving for material constants from AM-FM AFM data 67
3.2.2.1 Parameter estimation for a GMM 68
3.2.3 Reconstructing frequency-dependent behavior 70
3.3 Testing AM-FM AFM analysis on a rubber (SBR) control sample . . 70
3.3.1 Materials and Methods 70

3.3.2 SBR Results . . . 72
3.3.2.1 Distributions and statistics of SBR AM-FM AFM data 72
3.3.2.2 Measurement error due to uncalibrated tip radius . . 73
3.3.2.3 Best model for SBR viscoelasticity . . . 78
3.3.2.4 SBR material constants and frequency dependent behavior . . . 79
3.4 Conclusions . . . 84

4 Mechanoelectric Coupling in the ECM: Effect of Electrostatics and Ion Flow on Collagen I Mechanical Properties 86
4.1 Introduction . . . 86
4.2 Effect of electrostatics (ion concentration) on collagen viscoelasticity . 89
4.2.1 Materials and methods . . . 89
4.2.2 AM-FM AFM of sparse collagen in different PBS concentrations 92
4.2.2.1 Topology, storage moduli, and loss tangents . . . 92
4.2.2.2 Viscoelastic material constants . . . 96
4.2.3 AM-FM of concentrated collagen in different PBS concentrations 100
4.2.3.1 Topology, storage modulus, and loss tangent . . . 100
4.2.3.2 Viscoelastic material constants . . . 103
4.2.4 Imaging collagen's hydration shell . . . 108
4.2.5 Electrostatics discussion . . . 114
4.3 Effect of ion flow on collagen viscoelasticity . . . 117
4.3.1 AM-FM AFM of collagen pre- and post-ion flow . . . 119
4.4 Chapter conclusions . . . 122
4.4.1 Preliminary equivalent circuit model of collagen piezoelectricity 124
4.4.1.1 Calculating collagen's surface charge density . . . 127

5 Mechanochemical Coupling in the ECM: The Role of Growth Factors and Cell Behaviors in Modulating ECM Mechanics, and Implications for Pancreatic Cancer 131
5.1 Introduction . . . 131
5.2 Materials and methods . . . 134
5.3 Results . . . 137
5.3.1 Distributions and statistics of ECM AM-FM AFM data . . . 137
5.3.2 Topology, storage modulus, and loss tangent of cell-derived ECMs 143
5.3.3 Best model of viscoelasticity to describe cell-derived ECMs . . 151
5.3.4 Viscoelastic material constants of cell-derived ECMs . . . 157

5.4 Conclusions and discussion 164
5.4.1 Implications for tumor biology 167
5.4.2 Future work 168

6 Viscoelasticity of Cell Culture Substrates: Potential Modulation of Cell Behaviors by Substrate Time Responses 171
6.1 Materials and methods 174
6.2 Results 179
6.2.1 Substrate AM-FM AFM distributions and statistics 180
6.2.2 Viscoelasticity of poly(HEMA) substrates 182
6.2.2.1 AM-FM AFM measurements of poly(HEMA) substrates 182
6.2.2.2 PANDA measurements of poly(HEMA) substrates . 188
6.2.3 Viscoelasticity of pureCol substrates 189
6.2.3.1 Optimizing the preparation of pureCol substrates . . 190
6.2.3.2 AM-FM AFM measurements of pureCol substrates . 194
6.2.3.3 PANDA measurements of pureCol substrates 201
6.2.4 Substrate comparisons 207
6.3 Conclusions, discussion, and future work 213

7 Conclusions and Future Work 218
7.1 Hydration shells 222
7.2 Biological time responses 224
7.3 Implications for disease renormalization 228
7.3.1 Future work 229

Appendices 233

A Chapter 1 Appendix 233
A.1 Deriving monomer pKa shifts using the Gibbs free energy 233
A.1.1 Gibbs free energy of dissociation independent of molecular charge 234
A.1.2 Gibbs free energy of dissociation accounting for molecular charge 235
A.2 Effect of ions on molecular charge 236

B Chapter 3 Appendix 238
B.1 Dynamic mechanical analysis (DMA) 238
B.2 Propagating tip radius uncertainty in AM-FM calculation of sample E' 239
B.3 AC160TSA reconstructions of the SBR's frequency dependent behavior 241

C Chapter 4 Appendix **243**
C.1 Distributions and statistics of collagen and hydration shell AM-FM AFM data 243

D Chapter 6 Appendix **248**
D.1 Testing for hydrodynamic drag in PANDA measurements 248
D.2 Testing the effect of the trigger point on PANDA measurements . . . 250
D.3 Effect of the cantilever on PANDA results 252

Bibliography **254**

List of Figures

1.1 Depiction of the extracellular matrix (ECM) 5
1.2 Equivalent circuit models of linear viscoelasticity 25

2.1 Diagram of an atomic force microscope (AFM) 37
2.2 Procedure for calculating statistics from AM-FM AFM data 53
2.3 AFM techniques to measure sample viscoelasticity 55

3.1 Representative distributions of SBR AM-FM AFM measurements . . 72
3.2 Effect of user-controlled parameters on AM-FM AFM measurements . 75
3.3 Representative AM-FM AFM images of the SBR 76
3.4 Quantification of SBR E' and $\tan\delta$ 77
3.5 Representative model test for a single AM-FM AFM image of the SBR 79
3.6 Frequency dependent behavior of the SBR (AC240TSA). 81

4.1 Representative AM-FM AFM images of sparse collagen samples, polymerized at 0.02 mg collagen per mL PBS in different PBS solutions . 93
4.2 Distinguishing between mica and collagen 94
4.3 Effect of PBS concentration on sparse sample height, E', and $\tan\delta$ . . 95
4.4 Example model tests for sparse collagen samples 97
4.5 Effect of PBS concentration on sparse collagen material constants . . 98

4.6 Representative AM-FM AFM images of concentrated collagen samples, polymerized at 0.20 mg collagen per mL PBS in different PBS solutions 101
4.7 Effect of PBS concentration on concentrated sample height, E', $\tan\delta$ 102
4.8 Materials within concentrated samples 104
4.9 Example model tests for concentrated collagen samples 106
4.10 Effect of PBS concentration on concentrated sample material constants 107
4.11 Representative images of collagen's hydration shell 109
4.12 Effect of PBS concentration on hydration shell height, E', and $\tan\delta$. 111
4.13 Example model tests for collagen's hydration shells 112
4.14 Variability in hydration shell model test outcome 113
4.15 Ion coat hypothesis for tropocollagen in different PBS concentrations 116
4.16 Liquid perfusion setup for PBS flow 119
4.17 Effect of PBS flow on collagen fibril height, E', and $\tan\delta$ 120
4.18 Effect of PBS flow on collagen material constants 121
4.19 Preliminary equivalent circuit model of collagen piezoelectricity . . . 125
4.20 Comparison of measured and calculated collagen surface charge density 129

5.1 Representative distributions from AM-FM AFM of WT ECMs 138
5.2 Representative distributions from AM-FM AFM of colVKD ECMs . . 139
5.3 Representative distributions from AM-FM AFM of colXIKD ECMs . 141
5.4 Representative distributions from AM-FM AFM of gelatin 142
5.5 Representative AM-FM AFM height images of cell-derived ECMs . . 144
5.6 Feature height of cell-derived ECMs 145
5.7 Representative AM-FM AFM images of ECM storage moduli (E') . . 147
5.8 Storage modulus (E') of cell-derived ECMs 148
5.9 Representative AM-FM AFM images of ECM loss tangents ($\tan\delta$) . . 149
5.10 Loss tangent ($\tan\delta$) of cell-derived ECMs 150
5.11 Example model tests for cell-derived ECMs 152
5.12 Example model tests for acellular gelatin controls 153
5.13 Material constants of cell-derived ECMs 158
5.14 Material constants of each biological replicate of cell-derived ECMs . 163

6.1 Custom chamber for preparation of pureCol substrates 176
6.2 Representative distributions from AM-FM AFM of cell culture substrates 181
6.3 Representative AM-FM AFM images of poly(HEMA) substrates . . . 183
6.4 Effect of poly(HEMA) concentration on substrate height, E', and $\tan\delta$ 184
6.5 Example model tests for poly(HEMA) substrates 186

6.6 PANDA measurements at different points on poly(HEMA) substrates 189
6.7 Example indentation curves of pureCol substrates 192
6.8 Representative AM-FM AFM images of pureCol substrates measured by RC800PSA cantilevers 195
6.9 Representative AM-FM AFM images of pureCol substrates measured by AC240TSA cantilevers 196
6.10 Effect of crosslinking on pureCol substrate height, E', and $\tan\delta$ . . . 197
6.11 Example model tests for pureCol substrates 199
6.12 PANDA measurements at different points on pureCol substrates crosslinked with glutaraldehyde for 30 minutes 203
6.13 PANDA measurements at different points on pureCol substrates crosslinked with glutaraldehyde for 2 hours 205
6.14 PANDA measurements at different points on pureCol substrates crosslinked with glutaraldehyde for 24 hours 206
6.15 Comparison of substrate viscoelasticity. 209
6.16 Substrate time responses. 212

7.1 Proposed relationship between substrate time responses, substrate mechanics, cell behaviors, and various external stimuli 227

B.1 Frequency dependent behavior of the SBR (AC160TSA). 242

C.1 Representative distributions of AM-FM AFM measurements of sparse collagen samples 245
C.2 Representative distributions of AM-FM AFM measurements of concentrated collagen samples 246
C.3 Representative distributions of AM-FM AFM measurements of collagen hydration shells 247

D.1 Testing for hydrodynamic drag effects in PANDA measurements of poly(HEMA) and pureCol substrates 249
D.2 Representative effects of trigger point on PANDA measurements . . . 251
D.3 Effect of cantilever on PANDA measurements of pureCol substrates . 253

List of Tables

3.1 Material constants of the SBR 80

4.1 Ion properties of different phosphate buffered saline (PBS) solutions . 90

5.1 Model test RMSE for cell-derived ECMs 154

Chapter 1

Introduction

The interaction between cells and their environment plays a crucial role in modulating cell behaviors, maintaining tissues and organs, and regulating the health of an entire organism [1, 2]. Abnormal environmental conditions result in abnormal cellular activities and often lead to disease [1, 3]. Better understanding of the interaction between cells and their environment can provide new means of controlling cells to heal wounds, treat disease, and construct artificial tissues.

Diffusible factors in the cell's environment, such as gas (especially O_2 and CO_2), pH, salts and ions, nutrients, signaling molecules, and other molecules are important in modulating cell activities [4]. Additionally, a growing body of work has demonstrated that the mechanical properties (properties that dictate how an object responds to an applied force or deformation) of the surface or tissue in which a cell is located are crucial to determining cell activities [1, 3, 5–8], and can even override other cues from the cell's environment [9]. The mechanical properties of a substrate or tissue play a key role in regulating proliferation and survival [10–14], differentiation and development [9, 11, 12, 15–26], migration [27–35], morphology [12, 36–39], cytoskeletal properties and adhesion [23, 40–46], plasma membrane structure [30, 47, 48], cell signaling and gene expression [14, 24, 30, 34, 35, 38, 49–56], and other cell activities

[8, 26, 34, 35, 57–59]. For example, transplanting malignant tumor cells into different environments can renormalize the cells and remove their tumorgenic potential [60–63]. Placing stem cells on substrates with different mechanical properties alters their differentiation [9]. Consequentially, tailoring the mechanical properties of a cell's environment shows promise in treating disease and is fundamental for designing artificial tissues [1].

The electrical [2, 64–76], magnetic [77–82], and chemical [4, 83] properties of substrates and tissues also affect cell behaviors in a similar manner to mechanical properties. For example, endogenous electric fields are essential for wound healing [2, 64, 84] and embryonic development [2, 64, 85, 86] to progress properly, and these processes can be modulated by applying exogenous electric fields [2, 64].

While the physical properties of biological systems are often studied independently, they are in fact coupled, and hence do not exist independently of one another [78, 79, 83, 87–92]. That is, one type of stimulus (for example, a mechanical force or an electric field) will alter the mechanical, electrical, chemical, and even magnetic properties of the biological system. Therefore, understanding how tissues and substrates regulate cell behaviors requires an understanding of the substrate's coupled physical properties.

The physical properties of a cell's environment play an important role in disease, and can potentially be exploited to treat disease [1–3, 62]. Alterations to the physical properties of tissues serve as natural physiological defense mechanisms against disease and infection [2, 62, 93–98]. Placing diseased cells in different environments (with different physical properties) can renormalize the cells (restore normal phenotypes and activities) [2, 60–63, 99–110]. Additionally, subsequent removal of diseased cells from a renormalizing environment can restore their ability to cause disease [2, 60, 62, 63, 99–108]. Similarly, morphogenesis and wound healing can be modulated simply by applying an external electric field, rather than making genetic modifications to the cells [2, 64]. Such experiments suggest that the physical properties of a cell's

environment are key in regulating how the cell behaves [1–3, 62], and can override genetics [62, 106, 108]. These observations suggest that diseases could potentially be treated by altering the physical properties of tissues. Such future treatments could alter and tailor the physical properties of tissues by exploiting the coupling of physical properties in the system to control and renormalize diseased cells.

Early attempts at therapies that exploit the coupling of physical properties in biological systems show promise in treating many different conditions. For example, mechanical (ultrasound), chemical, and magnetic stimuli are used to modulate the electrical activity of the brain in neuromodulation therapies to treat the symptoms of neurodegenerative disorders [87, 111, 112]. Electrical stimuli are used to alter the chemical activities of cells in order to heal wounds [113, 114], and can restore sensation and motor control in paralyzed patients [114, 115]. Furthermore, combining such an electrical stimulus with mechanical stimuli (physical therapy) enhances the treatment's efficacy, and can even restore a paralyzed patient's ability to walk [114, 115]. Additionally, electric fields can be used to treat cancer, and improve survival rates and patient quality of life compared to standard treatments [116, 117]. Chemo-photothermal therapies also show promise in cancer treatment [118]. While promising, these therapies are still in their infancy because there is still much to understand regarding the basic mechanisms underlying the coupled physical properties of a cell and its environment.

The aim of this thesis is to improve the understanding of physical properties of tissues, and how these properties may be exploited for tissue engineering and disease treatment. Experiments in this thesis use quantitative methods based on atomic force microscopy to investigate the effect various stimuli have on the mechanics of biological systems. The first set of experiments in this thesis (chapter 4) examine mechanoelectric coupling in collagen, a physiologically relevant cell substrate. The second set of experiments (chapter 5) examine the effects of cell activity and chemical

signaling (mechanochemical coupling) on the mechanical properties of the substrates they produce. The third set of experiments (chapter 6) measure the viscoelastic properties of common cell culture substrates and form a preliminary correlation between these properties and the behaviors of cells on the substrates. Finally, the discussion in chapter 7 considers the implications of the findings in this thesis for renormalization therapies and tissue engineering.

The current chapter introduces biological systems and their physical properties in three parts. The first section provides an overview of how cells interact with their environment (section 1.1). The second section describes physical properties in biological systems (section 1.2). The third section defines mechanical properties, including basic mathematical models for these properties (section 1.3).

1.1 How cells interact with their environment

Metazoan cells live in the extracellular matrix (ECM), a scaffold of proteins and other molecules that spans multiple length scales (from the nanoscale to macroscale) and conveys important mechanical [1, 3], electrical [2], chemical [119], and possibly magnetic [77, 92] cues to the cells. Via these cues, the ECM is one of the key factors regulating normal and diseased cell behaviors [1, 3]. The ECM is often abnormal in disease, for example, fibrosis in solid tumors or plaques in neurodegenerative disorders [3]. Therefore, understanding the interaction between cells and the ECM is crucial to designing better treatments for a variety of diseases [1, 3].

In general, cells constantly undergo a cycle of sensing cues from the ECM, which alters their behavior [8], often resulting in modifications to the ECM [58], which are in turn sensed by cells, etc... [7, 49]. This cycle of sensing and activity modulation is called dynamic reciprocity [49], and occurs across multiple length scales, from nanometers (such as a cell attaching to the ECM) [1, 2, 15, 59, 120–124], to meters

(during processes like wound healing) [1, 2, 125]. Particularly relevant to cells are the nanoscale and microscale [15, 59, 120–124]. It is also important to note that the sensitivity of cells to physical cues from the environment over multiple length scales, as well as dynamic reciprocity, are not solely limited to multicellular organisms, but occur in all forms of life [1, 126–128].

1.1.1 What is the ECM?

The ECM, diagrammed in figure 1.1, is a complex network of biomolecules which maintains the three-dimensional structure of tissues and organisms [3, 4, 129]. The ECM is different for each tissue and includes a diverse array of molecules. Fibrillar proteins (for example collagen, fibronectin, and laminin) make up the bulk of the ECM and maintain the network's structure [3, 4, 129]. Many different molecules are

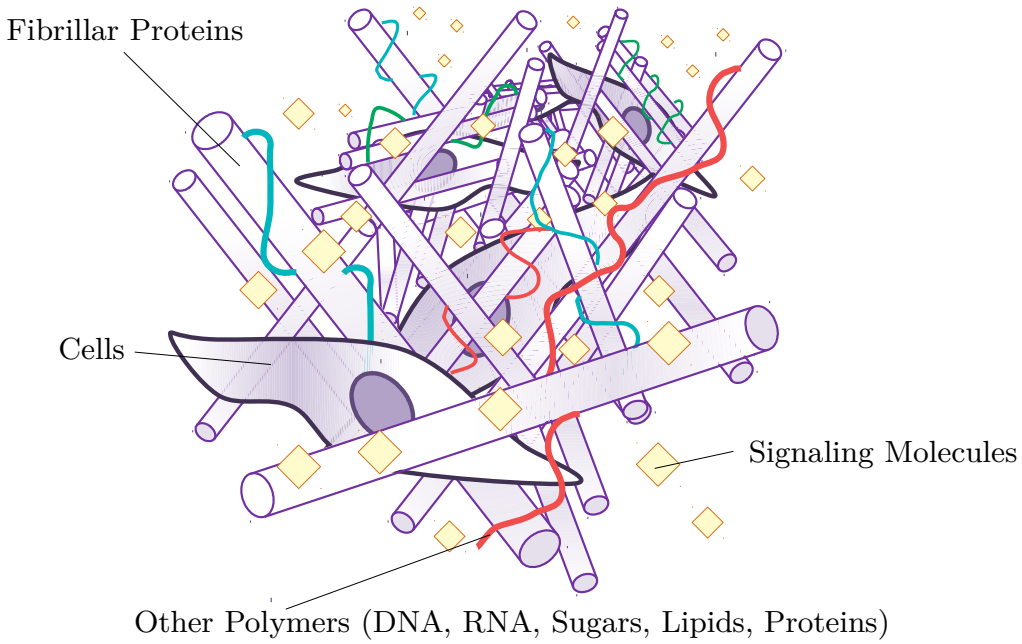


Figure 1.1: Depiction of the extracellular matrix (ECM). The ECM is a molecular scaffold in metazoans that maintains tissue architecture. The main structural component of the ECM consists of fibrillar proteins (purple cylinders) such as collagen. A diverse array of other molecules is incorporated among the fibrillar proteins. This array includes signaling molecules (yellow diamonds) and other polymers (squiggles) such as sugars, DNA, RNA, proteins, and other molecules.

incorporated among the fibrillar proteins [3, 4, 129]. First are signaling molecules such as growth factors, lipids, and other molecules [3, 129]. Second are molecules that alter the properties of the fibrillar proteins, such as crosslinkers like collagen XI and V or proteins that degrade the ECM such as MMPs or Trypsin [3, 129]. Additionally, other molecules incorporated in the ECM include: sugars, proteoglycans and glycoproteins (proteins modified to contain high levels of sugar), lipids, RNA, and DNA [3, 4, 129].

Of the diverse array of molecules in the ECM, collagen is one of the main components [3, 4, 129], comprising 30-40% of all protein in the human body [130]. Collagen plays a large role in dictating ECM architecture [131, 132]. In particular, collagen I is one of the key fibrillar proteins in the ECM, and is the most-common form of collagen [3, 129–132]. Collagen I is the major ECM component of skin, bones, and scar tissue (also called fibrosis in various diseases like cancer or heart disease) [3, 131, 132]. The mechanical properties of collagen I strongly affect the mechanical properties of the ECM, and the mechanical properties of collagen I alone can regulate cell behaviors [7, 9, 22, 27, 133–136].

Ions and water are also an important component of tissues, while not technically a part of the ECM [137, 138]. Biological molecules, including those of the ECM are surrounded by a shell of organized water molecules [137, 138]. This shell can modulate the properties of the encased biomolecule via mechanisms described in section 1.2.2 [137, 138]. Hydration shells are solid enough to probe experimentally at cellular length scales (nanoscale and microscale) [139–141], suggesting that shells can also be sensed by cells.

Cells sense the physical properties of the ECM through attachments to the ECM [31], and even cell-cell attachments [142]. Cells do not sit passively in the ECM, but instead constantly probe the ECM by applying their own forces to the network and nearby cells via contractions of their cytoskeleton (particularly via the cytoskeletal protein actin) [21, 31, 46, 143, 144].

1.1.2 How the ECM influences cell behaviors

Cells sense the surrounding ECM via attachments to the ECM [45, 145], such as focal adhesions [31, 145, 146], hemidesmosomes [145], and podosomes [143, 146]. While there is a large list of different cell-ECM attachments, they are constructed and function in a similar manner [4, 146]. The component of the attachment that anchors the cell to the ECM is a trans-membrane protein (a protein that spans the cell membrane) called a cell adhesion molecule (CAM) [4, 45, 145, 146]. Integrins are a highly-studied class of CAMs [4, 45, 145, 146]. One side of the CAM attaches to the ECM, while the other is attached to a complex of proteins inside the cytoplasm of the cell [145, 146]. This complex in turn connects to the cytoskeleton of the cell, which in turn connects to the cell nucleus [147].

Therefore, any time the ECM is deformed by an applied macroscopic or microscopic force, that movement can be relayed through the CAM, adhesion complex, and cytoskeleton, into the nucleus of the cell [38, 147–151]. When the nucleus deforms, different regions of DNA inside the nucleus are exposed or concealed, thereby changing what information the cell is able to access, and hence what activities the cell is able to perform at any given time [38, 147–150]. Similarly, molecules in the cell's cytoplasm or on the cell membrane can deform or redistribute themselves in response to the force [46, 47, 53, 54, 59, 148, 149], which can in turn change how these molecules interact to modulate cell activity [148, 149].

A second method by which the ECM modulates cell behavior is via the adhesion complex [51, 52, 151]. Many proteins in the complex on the cytoplasmic side of the CAM are mechanosensitive, meaning that they become active when they are deformed [151]. Similarly, many proteins on the plasma membrane, in the nucleus, and in the cytoplasm are also mechanosensitive [151]. When mechanosensitive proteins activate, they in turn activate signaling cascades that result in changes to the cell's activity [51, 52, 56, 151, 152].

A third method by which the ECM regulates cells is that cells in the ECM can gain access to growth factors and other signaling molecules, called ligands, that are attached to the fibrillar proteins of the matrix [4, 152, 153]. Such ligands bind receptors on the surface of the cell and initiate signaling cascades that ultimately change the cell's activities [4, 152, 153].

In summary, if the ECM deforms in response to an applied force, cell activity changes as a result of changes in the shape of the cell nucleus, as well as changes in the cell's internal signaling activity.

1.1.3 How cell behaviors influence the ECM

Modification of the ECM by cells is called tissue remodeling. Cells remodel the ECM and alter its physical properties via three main mechanisms. First, cells can directly reorganize the ECM by attaching to it and pushing or pulling [7, 58]. One main structure the cell uses to accomplish this task is called a fibropositor [7]. Such reorganization can change the topology of the ECM network, and alter its properties [7, 58]. Second, cells can degrade the ECM, often by secreting proteins like Trypsin or matrix metalloproteases (MMPs) [3]. Note that this degradation is often how cells access growth factors previously trapped in the ECM [3]. Third, cells can change the composition of the ECM by secreting ECM components or by secreting proteins that modulate the properties of the molecules in the ECM (such as crosslinkers) [3]. This remodeling can occur as a result of diffusible factors in the cell's environment [3] or of mechanical stimuli [55].

1.1.4 Summary and outlook: How cells interact with their environment

The interaction between cells and the ECM is crucial for maintaining healthy tissues, and is abnormal in disease. Much of this interaction occurs via physical forces, that can occur over multiple length scales, from nanoscale to macroscale. Forces are propagated both into and out of the cell. As described in the next section (1.2.1), these forces do not need to be mechanical in origin to cause the ECM or cytoskeleton to move. The mechanical, electrical, magnetic, and chemical properties of biological systems are coupled. Therefore, a mechanical, electrical, magnetic, or chemical force can cause movement (a mechanical displacement) of the cytoskeleton or ECM via this coupling. Regardless of their nature, the propagation and attenuation of forces, and their effect on determining cell behavior, is dictated by the physical properties of the cell and ECM. Therefore, quantifying these physical properties is crucial to understanding the cycle of how cells sense, respond to, and modify the ECM in normal and diseased tissues.

1.2 Physical properties of biological systems

The physical properties of cells, the ECM, and biomolecules dictate how they behave in response to a stimulus. In biological systems, any given stimulus (i.e. a mechanical, electrical, magnetic, and/or chemical stimulus) can alter the mechanical, electrical, chemical, and magnetic properties of the system [78, 79, 83, 87–92]. In other words, the physical properties of biomolecules are coupled. One type of stimulus gives rise to all others via mechanisms described in section 1.2.1. This coupling is sometimes referred to as "multiphysics." Additionally, properties of the solution in which the biomolecule is located are important in modulating this coupling, as described in section 1.2.2.

1.2.1 Coupling of physical properties of biomolecules

The physical properties of biomolecules are coupled due to their charged nature and small nanoscale size [88, 92]. For example, if a mechanical force is applied, and a molecule deforms, the charge density of the molecule will change [88]. Therefore, the electrical properties of the molecule change as a result of the applied force. Similarly, if a voltage is applied to a biomolecule, molecular charges will move in response to the voltage, causing a mechanical deformation in the molecule [88].

By Maxwell's equations, whenever a current (or varying voltage) is generated, a magnetic field is also generated and vice versa [78, 79]. Additionally, the ability of biomolecules to interact, bind receptors, and catalyze reactions requires the molecules to undergo a conformational change [83, 89–91]. Therefore, mechanical, electrical, and magnetic stimuli that cause conformational changes in a biomolecule alter the chemical properties: catalytic state, reactivity, and interactions of the biomolecule [119]. Thus, mechanical (and electrical or magnetic) stimuli that alter the chemical properties of a biomolecule can initiate cell signaling cascades [119]. Initialization of such a signaling cascade via a mechanical stimulus, relevant to chapter 5, is referred to as mechanochemical coupling [119].

1.2.1.1 Piezoelectricity and endogenous voltages

Mechanoelectric coupling is of particular focus in this thesis (chapter 4). A specific form of mechanoelectric coupling exhibited by biomolecules is piezoelectricity [88, 154–156]. A piezoelectric material generates an electric field in response to a deformation [157]. Similarly, a piezoelectric material deforms when a voltage is applied [157]. DNA, RNA, collagen, actin, lipids, and many other components of the ECM and cells are piezoelectric [88, 154–156].

Piezoelectricity of biomolecules plays an important role in processes like embryonic development, action potentials, wound healing, and many others [64, 88, 154–156].

Mechanical changes to the tissue (i.e. gastrulation, formation of a wound, etc...) during these physiological processes generate large voltages, which in turn alter cell activities necessary to perform the required tasks (i.e. form the correct structure, heal a wound, relay a nerve impulse, etc...) [2, 64].

Voltages that are natural to a tissue are called endogenous voltages [64]. Endogenous voltages can be generated by piezoelectric biomolecules in response to mechanical (or magnetic or chemical) changes of the system during processes such as gastrulation, formation of a wound, or the presence of a tumor [64, 84, 158, 159]. Additionally, endogenous voltages can be generated by ions flowing through a tissue [64]. The mechanism behind why ion flows generate endogenous voltages is still unclear. However the mechanism is likely related to the fact that the molecules in tissues have endogenous electric fields [2, 85, 86, 154–156, 158, 160, 161], and that (by Maxwell's laws) moving ions against this background field generates a voltage.

1.2.2 Effect of water and salt on biomolecule multiphysics

The charge, structure, and physical properties of a biomolecule are affected by the solution surrounding the molecule [162]. The surrounding solution can alter how molecules interact, and regulates the charge density of the molecule [162]. For example, the surrounding solution can: modulate hydrogen bonds, form electrostatic correlations, provide reagents to form covalent bonds, sterically block or free sites for covalent bonds, and shield molecular charges from neighboring charges. This section describes how the surrounding solution regulates the charge of a biomolecule, and thereby affects the coupling of the molecule's physical properties.

1.2.2.1 Charge of biomolecules

Most biomolecules (like DNA, RNA, polysaccharides, and proteins) are polymers [162, 163]. Polymers are molecular chains constructed by connecting several copies

of a repeating unit called a monomer [162]. Biological monomers include nucleotides, hydrocarbons, certain sugars, and amino acids [4, 162]. The charge of a polymer is dictated by the charges of the polymer's constituent monomers [162, 163].

Monomers can become charged if they have certain atoms (like, Oxygen, Nitrogen, and Phosphorous) that can gain or lose a proton (for example, a Lewis acid/base) [162, 163]. When the proton is attached to the monomer, it is "associated," and when the proton is not attached to the monomer, it is "dissociated" [162, 163]. Some monomers (typically containing Oxygen and Phosphorous) act as Lewis acids, and become charged in their dissociated state as in equation 1.1 [162, 163]. Others (typically containing Nitrogen) act as Lewis bases, and are charged in their associated state as in equation 1.2 [162, 163]. In other words, a given monomer M can exhibit one of the following dissociation/association reactions with its proton H [162, 163].

$$HM \overset{k_{HM}}{\rightleftharpoons} H^+ + M^- \tag{1.1}$$

$$HM^+ \overset{k_{HM}}{\rightleftharpoons} H^+ + M \tag{1.2}$$

The dissociation constant, k_{HM}, is a measure of whether the steady state of the reaction favors the dissociated or associated state, and is the ratio of molar concentrations (moles per unit volume, denoted by c) of the dissociated states over the molar concentration of the associated state at equilibrium as follows [162, 163].

$$k_{HM} = \frac{c_H c_M}{c_{HM}} \tag{1.3}$$

If $k_{HM} > 1$, the dissociated state is favored when the reaction reaches a steady state [162, 163]. The reverse is true if $k_{HM} < 1$ [162, 163].

1.2.2.1.1 Effect of pH

The monomer is not the only possible source of protons in equation 1.3. The solution

surrounding the monomer can supply protons, based on its pH [162, 163]. The pH of the solution ($\text{pH} = -\log_{10}(c_H)$) is related to k_{HM} by algebraically rearranging equation 1.3 to obtain the Henderson-Hasselbach equation [162, 163].

$$\text{pH} = -\log_{10}(k_{HM}) + \log_{10}\left(\frac{c_M}{c_{HM}}\right) \tag{1.4}$$

A constant specific to the monomer, called the pKa, can be defined from equation 1.4, where $\text{pKa} = -\log_{10}(k_{HM})$ [162, 163]. The pKa is the pH of the solution at which the monomer and its proton are associated 50% of the time [162, 163]. The pKa is specific to the given monomer and depends on the structure and constituent atoms of the monomer [162, 163].

For monomers free in solution, the fraction of monomers that are associated at any given time, α, is related to the pKa of the monomer by the Hendersson-Hasselbach equation 1.4 [162, 163].

$$\alpha = \frac{c_{HM}}{c_{HM} + c_M} = \frac{1}{10^{\text{pH}-\text{pKa}}} \tag{1.5}$$

The average charge, q, of the monomers in each state is the product of their valence (z, the charge number of an atom or molecule) and the elementary charge ($e_o = 1.602 \text{ x } 10^{-19}$ C), such that $q = ze_o$. Since protons have a valence of +1, $z_M = z_{HM} - 1$. The average charge of a monomer free in solution will depend on whether the monomer spends more time associated or dissociated.

$$\begin{aligned} q &= (\alpha)q_{HM} + (1-\alpha)\,q_M \\ &= \left(\frac{1}{10^{\text{pH}-\text{pKa}}}\right) q_{HM} + \left(1 - \frac{1}{10^{\text{pH}-\text{pKa}}}\right) q_M \end{aligned} \tag{1.6}$$

However, equation 1.6 becomes more complicated when the monomers are no longer free in solution, but confined in a polymer [162].

1.2.2.1.2 Effect of spatial confinement

Unlike when monomers are free in solution, the spatial confinement of the monomers within a polymer, as well as spatial confinement of polymers within a network like the ECM, subjects them to electrostatic interactions with neighboring monomers [162]. For example, suppose two monomers in close proximity have the ability to dissociate to H^+ and M^-. If one group dissociates, the second is less-likely to do so because two negative charges would then be in close proximity, which is less energetically favorable. Therefore, the pKa of the second group is shifted as a result of being confined near other charged groups [162].

In order to accurately model the charge of a polymer, shifts in monomer pKa values must be taken into account [162]. As derived in appendix section A.1, the shift in a monomer's pKa value due to electrostatic interactions with other charged monomers is obtained by: (i) assuming that the interaction energy of charged monomers obeys Coulomb's law, (ii) summing all Coulombic interactions monomer m has with each jth monomer in the system, (iii) substituting this interaction energy into the expression for the Gibbs free energy of the associated and dissociated states, and (iv) applying the equilibrium condition that the difference in the Gibbs free energy between the fully associated and fully dissociated states is zero [162].

$$\mathrm{pKa} = \mathrm{pKa}_0 - \log_{10}\left(\exp\left\{\frac{e_o^2}{4\pi\varepsilon k_B T}\left[z_m^*\left(\sum_{j\neq m}^{J}\frac{z_j^*}{\ell_{m,j}}\right) - z_m\left(\sum_{j\neq m}^{J}\frac{z_j}{\ell_{m,j}}\right)\right]\right\}\right) \quad (1.7)$$

Here, J is the total number of monomers in the polymer, $\ell_{m,j}$ is the distance between monomer m and j, pKa_0 is the pKa value when monomer m is free in solution, e_o is the elementary charge, k_B is Boltzmann's constant, T is the temperature of the system, ε is the dielectric constant of the solution in which the polymer is located, z^* denotes the valence of an associated monomer, and z denotes the valence of a dissociated monomer.

1.2.2.1.3 Effect of ions

The pKa value of a monomer can also be affected by the concentration of ions in the surrounding solution [162]. Ions typically come from dissociated salts in the solution [162, 164]. Ion screening blocks neighboring charges from one another, thereby decreasing the electrostatic interactions between monomers by hiding the monomers' charges from one another [162, 164]. The more ions in solution, the more screening occurs [162, 164]. The constant $e_o^2 \left(4\pi\varepsilon k_B T\right)^{-1}$ in equation 1.7 is related to the ion concentration in the solution near the monomer [162, 164], as derived in this section.

Surface charge screening by ions occurs because a thin layer of counterions (ions in the solution with an opposite charge to that of the monomer), will exist around any charge on the surface of the monomer [162, 164]. This layer of counterions is adsorbed to the surface of the monomer via electrostatic correlations [164]. The structural arrangement of the adsorbed counterions (intermixed in water molecules) is what gives rise to the hydration shells that surround biomolecules, mentioned in section 1.1.1 [138].

The simplest mathematical model of hydration shell/counterion distribution around a charged surface is known as the Debye-Hückel approximation, and arises from first order Taylor expansion of the Poisson-Boltzmann equation as detailed in appendix section A.2 [164]. Debye-Hückel theory provides a characteristic length scale, known as the Debye length (ℓ_D) [162, 164]. The Debye length is the distance over which the effect of a fixed charge (like that on a monomer) persists through the solution before being screened by counterions [162, 164].

$$\ell_D = \sqrt{\frac{\varepsilon k_B T}{e_o^2 N_A \sum_i z_i^2 c_i}} \tag{1.8}$$

Here, c_i is the concentration of ion i in the bulk solution, and is known for most experimental solutions as well as average physiological conditions. Avogadro's number

is represented as N_A. The more ions present in the solution (the larger the value of c_i), the smaller the value of ℓ_D. Therefore, more screening occurs when more ions are present in the solution.

A condensed expression of ion concentration in a solution is called the ionic strength I, and is defined as follows [164].

$$I = \frac{1}{2}\sum_i z_i^2 c_i \tag{1.9}$$

$$\ell_D = \sqrt{\frac{\varepsilon k_B T}{2e_o^2 N_A I}} \tag{1.10}$$

Applying equation 1.10, equation 1.7 becomes the following.

$$\mathrm{pKa} = \mathrm{pKa}_0 - \log_{10}\left(\exp\left\{\frac{N_A I}{2\pi\ell_D^2}\left[z_m^*\left(\sum_{j\neq m}^{J}\frac{z_j^*}{\ell_{m,j}}\right) - z_m\left(\sum_{j\neq m}^{J}\frac{z_j}{\ell_{m,j}}\right)\right]\right\}\right) \tag{1.11}$$

1.2.3 Summary: Physical properties of biological systems

The physical properties of biological systems are coupled due to the fact that biomolecules are small and charged. This coupling is important to the study of how forces in biology regulate cell behaviors. Factors that influence molecular charge influence the coupling of physical properties in biological systems. In particular, it is important to consider the pH and ionic strength of the solution surrounding a biomolecule, as well as the hydration shell of the biomolecule.

1.3 Introduction to mechanics

Forces are propagated from a cell to the ECM, and from the ECM to a cell via deformation of the biomolecules subjected to the forces (see section 1.1). As described in this section, the propagation and attenuation of forces in biology can be studied

with mechanics, the area of physics concerned with how objects respond to forces and deformations.

When a force (F) is applied, a sample will deform, and vice versa. Two quantities related to the force and deformation are stress and strain [162, 165]. Stress, σ, is defined as the force per unit area experienced by the material [162, 165]. Strain, ϵ, is the ratio of change in dimensions (Δx) of the object relative to the dimensions (x_0) of the object before deformation ($\epsilon = \Delta x/x_0$) [162, 165]. The relation between σ and ϵ depends on the material to which the mechanical stimulus is applied [162, 165]. Specifically, material viscosity and elasticity are key determinants in the propagation and attenuation of the applied force [162, 165].

1.3.1 Elasticity and viscosity

Elastic materials respond instantaneously to an applied stress/strain, and obey Hooke's law, where k is the stiffness (N m^{-1}) of the material [162, 165].

$$F = k\Delta x \tag{1.12}$$

Hooke's law can be written in terms of stress and strain by dividing equation 1.12 by the cross-sectional area. In this expression, E is defined as the Elastic modulus, also called the Young's modulus, of the sample in units of Pa [162, 165].

$$\sigma = E\epsilon \tag{1.13}$$

In contrast to elastic materials, viscous materials flow with the applied stimulus, and obey Newton's law, where η is the dynamic viscosity of the material (N s m^{-2} = Pa s) [162, 165].

$$\sigma = \eta\dot{\epsilon} \tag{1.14}$$

While η and E have units of Pa, they should be thought of as energy densities in the material, rather than pressures (Pa = J m^{-3}) [166]. E can be thought of as the potential energy density of the material that "resists" deformation [166]. Viscosity η is the kinetic energy density dissipated by the material per deformation rate [166]. More on the physical origin of elasticity and viscosity is discussed in section 1.3.2.1.

Note that these equations assume a linear stress/strain relationship (k, E, and η are constants, not functions) [162, 165]. These equations can be extended to nonlinear models [162, 165]. Often, large deformations of a material result in nonlinear stress/strain relationships [162, 165]. Small deformations typically result in linear stress/strain relationships [162, 165]. The range of (small) deformations where a material's response can be described with linear models is called the linear regime of the material [162, 165]. Deformations caused by a cell are typically small enough to render linear stress/strain relationships valid [162]. Therefore, nonlinear models will not be considered in this thesis.

Few materials in biology are purely elastic or purely viscous, and are instead viscoelastic [162]. In other words, biomaterials both store and dissipate energy when the material is deformed or changes shape [166]. The simultaneous storage and dissipation of energy means that biomolecules respond to a stimulus with characteristic time delays [162, 166]. As derived in the following sections, these time responses (τ) are the ratio of a material's dynamic viscosity to its elasticity, $\tau = \eta/E$.

1.3.2 Viscoelasticity

Viscoelastic materials exhibit characteristic time delays in their mechanical response [162, 165]. These time responses arise from the polymer chains within the material rearranging themselves when subjected to a mechanical stimulus [162, 165]. Examples of such a mechanical stimulus are stress relaxation, changing stress with constant strain (section 1.3.3.1) and/or creep, changing strain with constant stress (section

1.3.3.2) [162, 167].

1.3.2.1 Physical origin of viscoelasticity

Networks of polymers are typically viscoelastic [162, 165]. As described in section 1.1.1, the ECM is an example of such a polymeric network. Similarly, cells, DNA, and most other biomolecules are polymers [162]. When a polymeric network (a scaffold of polymers) is in a steady state, the polymers in the system exist in a statistically favored state, where polymer chains are coiled and entangled with one another [165, 168]. When a mechanical stimulus is applied to a polymeric network, the constituent polymers (and any water, ions, hydration shells, and other non-polymeric components) move, and the polymer chains slide relative to each other, thereby altering their coiling and entangling [165]. When the stimulus is removed, the network relaxes to the original state [165].

The sliding and tangling of polymers in a network requires time [165]. This time delay, between when a stress/strain is applied and when the network reaches a new steady state, is the hallmark of a viscoelastic material [162, 165]. A polymer network can exhibit multiple time responses, which arise from different conformations of the constituent polymers [162, 165]. Multiple time responses also exist if there are different types of polymers (and other molecules) in the network [162, 165].

In general, if polymers in the network have many covalent/strong interactions (such as crosslinks) with one another, the network will be more-elastic because such strong interactions hinder chain sliding and untangling [165]. Therefore, rather than sliding or twisting to accommodate the deformation, polymers in such a network are more likely to exhibit a large amount of potential energy "resisting" the deformation [168]. This potential energy that "wants" to return to the network's un-deformed state can be represented by the elastic modulus [166, 168]. Additionally, with less chain sliding in such an elastic network, less time will be required for the network to

reach a new steady state under the applied stress/strain. This is why purely elastic materials have an instantaneous time response [162, 166].

Polymers in a viscous network exhibit weak interactions with one another (such as hydrogen bonds and electrostatic interactions) [165]. Polymers in such a network slide relative to one another more easily than in a network with strong interactions [165, 168]. This sliding of polymer chains transfers kinetic energy to smaller molecules (like water and ions) near the polymer [168]. Energy is dissipated by the network via this transfer of kinetic energy as heat into the environment [168]. Additional energy dissipation occurs due to small thermodynamic perturbations of molecules in the network (since the temperature is greater than absolute zero) [168]. Energy dissipation is related to the viscosity of the material [166, 168]. Additionally, with greater ease of chain sliding in such a viscous network, more time will be required for the network to reach a new steady state under an applied stress/strain. For a purely viscous material (equation 1.14), polymers will never stop moving under the applied stimulus, never reaching a steady state [165]. Therefore, the time response of a purely viscous material is infinite [162, 166].

Since biological networks like cells and the ECM contain a mixture of strong and weak interactions, they can both store and dissipate energy, and therefore have finite time responses, making them viscoelastic [162, 165, 166, 168]. Typically, experiments do not directly measure interactions between polymers, but instead measure energy storage and dissipation by a material, or material time responses (details in section 1.3.3). These experimental measurements can then be used to infer information about interactions between polymers within a material (details in section 1.3.7).

1.3.3 Experimental quantification of viscoelasticity

Three main experiments are used to quantify a material's elastic modulus, E, viscosity, η, and time responses, $\tau = \eta/E$. First is a relaxation experiment, where a

constant strain ($\epsilon = \epsilon_0$, and $\dot{\epsilon} = 0$) is applied while the change in stress is measured [162, 165, 167]. Second is a creep experiment, where a constant stress ($\sigma = \sigma_0$, and $\dot{\sigma} = 0$) is applied and the change in strain is measured [162, 165, 167]. Third is a dynamic experiment, where an oscillatory stimulus at a given frequency, f, with angular frequency $\omega = 2\pi f$ is applied to the sample [162, 165, 167]. Dynamic experiments quantify a material's energy storage and dissipation [162, 165, 167]. In this thesis, oscillatory strains are applied so that $\epsilon(t) = \epsilon_0 \sin(\omega t)$.

1.3.3.1 Relaxation experiments

In a relaxation experiment, strain is held constant while the change in stress is measured [162, 165, 167].

$$\epsilon = \epsilon_0, \text{ and } \dot{\epsilon} = 0 \tag{1.15}$$

Therefore, a purely elastic material (equation 1.13) will experience a constant force ($\sigma = E\epsilon_0$) when the deformation is applied, while a viscous material (equation 1.14) will not experience any force ($\sigma = 0$). A viscoelastic material will respond with a time-dependent $\sigma(t)$. The details of $\sigma(t)$ depend on the type of viscoelasticity exhibited by the sample, and are discussed further in section 1.3.4.1.

1.3.3.2 Creep experiments

In a creep experiment, stress is held constant while the change in strain is measured [162, 167].

$$\sigma = \sigma_0, \text{ and } \dot{\sigma} = 0 \tag{1.16}$$

Therefore, a purely elastic material (equation 1.13) will strain instantaneously ($\sigma_0/E = \epsilon$) when the stress is applied, while a viscous material (equation 1.14) will continue to deform at a rate $\dot{\epsilon} = \sigma_0/\eta$. A viscoelastic material will respond with a time-dependent $\epsilon(t)$. The details of $\epsilon(t)$ depend on the type of viscoelasticity exhibited by the sample,

and are discussed further in section 1.3.4.2.

1.3.3.3 Dynamic experiments

In a dynamic strain experiment, $\epsilon(t) = \epsilon_0 \sin(\omega t)$ [162, 167]. Therefore, a purely elastic material (equation 1.13) will respond in-phase with the deformation ($\sigma(t) = \sigma_0 \sin(\omega t)$), while a purely viscous material (equation 1.14) will respond 90 degrees out-of-phase with the deformation ($\sigma(t) = \sigma_0 \omega \cos(\omega t)$). A viscoelastic material will experience a phase shift (δ) between zero and 90 degrees [162].

$$\begin{aligned} \sigma(t) &= \sigma_0 \sin(\omega t + \delta) \\ &= \sigma_0 \cos(\delta) \sin(\omega t) + \sigma_0 \sin(\delta) \cos(\omega t) \end{aligned} \tag{1.17}$$

Equation 1.17 can be re-written in terms of a quantity known as the complex modulus (E^*), the ratio of maximum stress to maximum strain ($E^* = \sigma_0/\epsilon_0$), as follows.

$$\sigma(t) = \epsilon_0 \left[E^* \cos(\delta) \sin(\omega t) + E^* \sin(\delta) \cos(\omega t)\right] \tag{1.18}$$

The component of equation 1.18 in-phase with the driving strain is called the storage modulus (E', in units of Pa, equation 1.19) [162, 165]. E' represents the elastic component of the material's dynamic response, the energy stored by the material that "resists" deformation [166].

$$E' = \frac{\sigma_0}{\epsilon_0} \cos(\delta) = E^* \cos(\delta) \tag{1.19}$$

The out-of-phase component of equation 1.18 is called the loss modulus (E'', in units of Pa, equation 1.20) [162, 165]. E'' represents the viscous component of the

material's response, the energy dissipated by the material [166].

$$E'' = \frac{\sigma_0}{\epsilon_0} \sin(\delta) = E^* \sin(\delta) \tag{1.20}$$

E' and E'' are energy densities (with units of Pa = J m^{-3}) [166], and are intrinsic material properties, properties that do not depend on geometry of the deformation [162, 165]. With E' and E'' defined, equation 1.18 can be rewritten as follows.

$$\sigma(t) = \epsilon_0 \left[E' \sin(\omega t) + E'' \cos(\omega t)\right] \tag{1.21}$$

Additionally, a dimensionless quantity known as the loss tangent ($\tan\delta$) can be defined from the phase shift (δ) as the ratio of E'' over E' [162, 165].

$$\tan\delta = \frac{\sin(\delta)}{\cos(\delta)} = \frac{E''}{E'} \tag{1.22}$$

The exact relationships between E', E'', and $\tan\delta$, and the sample's elasticity (E, from equation 1.13) and viscosity (η, from equation 1.14) depend on the nature of a material's viscoelasticity [165, 169]. Models of this nature, and the relationship between all these quantities, are discussed in the next sections (1.3.4, and 1.3.5).

1.3.4 The standard linear solid (SLS)

Mathematical models of viscoelasticity are often presented as equivalent circuit models, which represent the elastic components of a material's response with springs and viscous components with dampers [162, 165, 169]. For elements connected in parallel,

$$\sigma = \sum_{i=1}^{n} \sigma_i \tag{1.23}$$

where n is the number of arms in parallel, σ_i is the stress on the ith arm, and ϵ is constant across all arms. For elements connected in series,

$$\epsilon = \sum_{i=1}^{n} \epsilon_i \tag{1.24}$$

where ϵ_i is the strain on the ith arm and σ is constant across all n arms. Such equivalent circuit models are then used to obtain a differential equation for the stress/strain relationship of the material [162, 165, 169].

The standard linear solid (SLS) is the simplest model of linear viscoelasticity (where E and η are constants, not functions) that fully describes both creep and relaxation. The SLS consists of a spring and damper in series connected to a spring in parallel, as shown in figure 1.2 (A) [162, 165, 169]. Applying equations 1.23 and 1.24 to this configuration gives the following stress/strain relationship for the SLS [162, 165, 169].

$$\dot{\sigma}(t) + \frac{E_r}{\eta}\sigma(t) = (E_c + E_r)\,\dot{\epsilon}(t) + \frac{E_c E_r}{\eta}\epsilon(t) \tag{1.25}$$

Special cases of the SLS, where one of the elastic constants is much larger than the other, are known as the Maxwell (MW, where $E_c \to 0$) and Kelvin-Voigt (KV, where $E_r \to \infty$) models, and are discussed in 1.3.5.2 and 1.3.5.1, respectively [162, 165, 169]. Additionally, the SLS can be generalized by adding additional arms of springs and dampers in parallel to the equivalent circuit, as diagrammed in figure 1.2 (D) [162, 165, 169]. Note that E_c of the generalized model is actually a sum of E_c from individual SLSs. Therefore, the general model can be thought of as several SLSs connected in parallel. This generalized SLS is called the general Maxwell model (GMM) or the Wiechert model [162, 165, 169]. The GMM is useful for representing complicated systems like the ECM and cells, with multiple constituents and multiple time responses that dictate their mechanics [162, 165, 169–174].

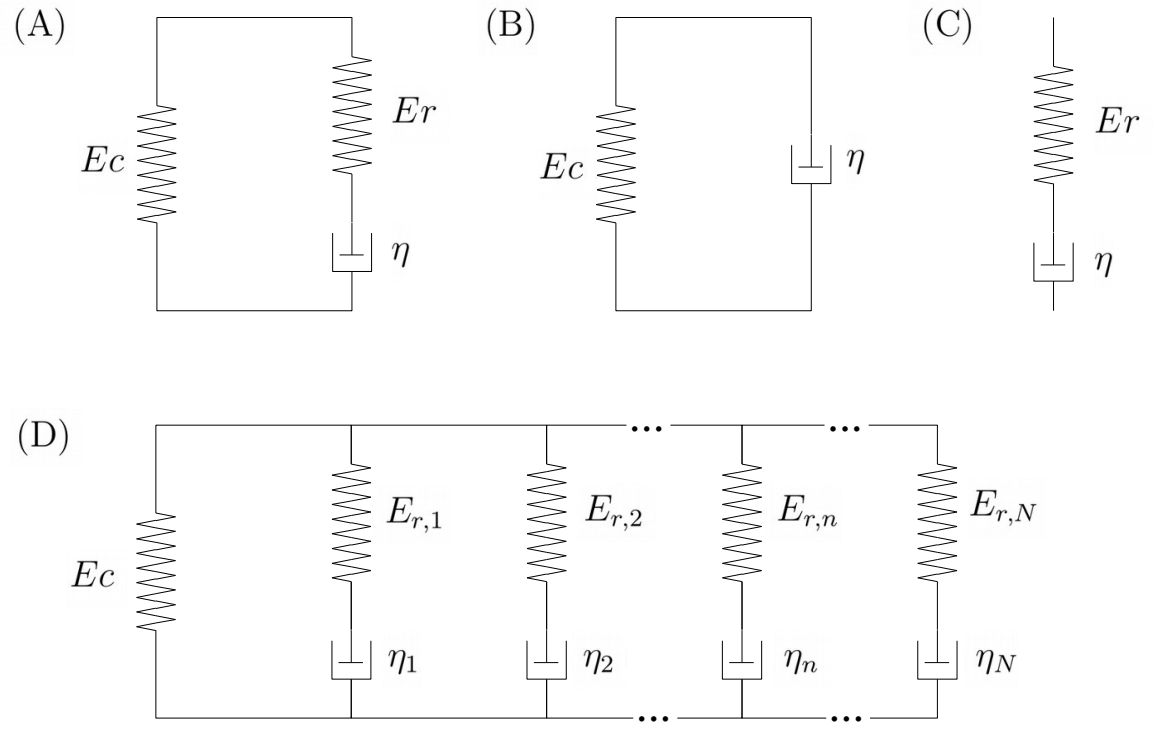


Figure 1.2: Equivalent circuit models of linear viscoelasticity. Elastic components of the material are represented as springs with elastic modulus E. Viscous components are represented as dampers with dynamic viscosity η. Panel (A) shows the standard linear solid (SLS), the simplest model of linear viscoelasticity that fully describes both creep and relaxation. Panel (B) shows the Kelvin-Voigt (KV) model, which is a special case of the SLS where $E_r \to \infty$. Panel (C) shows the Maxwell (MW) model, which is another special case of the SLS where $E_c \to 0$. Panel (D) shows the generalized SLS, known as the general Maxwell model (GMM), with a total of N arms, which often applies to biological systems.

1.3.4.1 The SLS during a relaxation experiment

Substituting the relaxation experiment (equation 1.15) into the differential equation for the stress/strain of the SLS (equation 1.25) gives the following result.

$$\dot{\sigma(t)} + \frac{E_r}{\eta}\sigma(t) = \frac{E_c E_r}{\eta}\epsilon_0$$

$$\sigma(t) = \sigma_0 e^{-\frac{E_r}{\eta}t} + E_c\epsilon_0 \tag{1.26}$$

The quantity $\tau_r = \eta/E_r$ has units of seconds and dictates the decay of the ex-

ponential in equation 1.26. Therefore, this characteristic timescale is the relaxation timescale of the SLS.

1.3.4.2 The SLS during a creep experiment

Substituting the creep experiment (equation 1.16) into the differential equation for the SLS (equation 1.25), and applying the initial condition $\epsilon(0) = \epsilon_0$ gives the following creep behavior for the SLS.

$$\begin{aligned} \frac{E_r}{\eta}\sigma_0 &= (E_c + E_r)\,\dot{\epsilon}(t) + \frac{E_c E_r}{\eta}\epsilon(t) \\ \epsilon(t) &= \frac{\sigma_0}{E_c}\left(1 - e^{-\frac{E_c E_r}{\eta(E_c+E_r)}t}\right) + \epsilon_0 e^{-\frac{E_c E_r}{\eta(E_c+E_r)}t} \end{aligned} \tag{1.27}$$

The exponentials in equation 1.27 contain another characteristic timescale of the SLS, called the creep timescale $\tau_c = \eta/E_c$.

1.3.4.3 The SLS during a dynamic experiment

In a dynamic strain experiment, a sinusoidal strain, $\epsilon(t) = \epsilon_0 \sin(\omega t)$, with frequency f and angular frequency $\omega = 2\pi f$ is applied to the sample. Substituting this expression into the stress/strain relationship for the SLS (equation 1.25) gives the following result.

$$\begin{aligned} \dot{\sigma}(t) + \frac{E_r}{\eta}\sigma(t) &= (E_c + E_r)\,\omega\epsilon_0 \cos(\omega t) + \frac{E_c E_r}{\eta}\epsilon_0 \sin(\omega t) \\ \sigma(t) &= \left[\frac{E_r^2 \eta\omega}{E_r^2 + \eta^2\omega^2}\right]\epsilon_0 \cos(\omega t) + \left[E_c + \frac{E_r \eta^2\omega^2}{E_r^2 + \eta^2\omega^2}\right]\epsilon_0 \sin(\omega t) \end{aligned} \tag{1.28}$$

Applying the definition of E' and E'' (from equation 1.21) produces the following relations between the sample's elastic and viscous constants E_r, E_c, η, and dynamic

constants E', E'', and $\tan\delta$.

$$E' = E_c + \frac{E_r \eta^2 \omega^2}{E_r^2 + \eta^2 \omega^2} \tag{1.29}$$

$$E'' = \frac{E_r^2 \eta \omega}{E_r^2 + \eta^2 \omega^2} \tag{1.30}$$

$$\tan\delta = \frac{E''}{E'} = \frac{E_r^2 \eta \omega}{(E_c + E_r)\,\eta^2 \omega^2 + E_r^2 E_c} \tag{1.31}$$

Equations 1.29 - 1.31 show that E', E'', and $\tan\delta$ are all dependent on the frequency of the applied strain. Therefore, in order to quantify a material's full viscoelastic response, it is necessary to either: (i) probe the material over a range of frequencies, or (ii) calculate the material constants and time responses (E_c, E_r, η, τ_r, and τ_c) from data at a single frequency, then use them to reconstruct the frequency-dependent behavior of the sample [162, 165, 169]. Both method (i) and (ii) are employed in this thesis, as described in chapter 2 and 3, respectively.

1.3.5 Limiting cases of the SLS

Limiting cases of the SLS are also widely used to represent linear viscoelastic materials [162, 165, 169]. The first case is a Kelvin-Voigt (KV) material, where $E_r \to \infty$. As diagrammed in figure 1.2 (B), a KV material is represented as a single spring and damper in parallel [162, 165, 169]. The second case is a Maxwell material (MW), where $E_c \to 0$. As diagrammed in figure 1.2 (C), a MW material is represented as a single spring and damper in series [162, 165, 169].

1.3.5.1 Kelvin-Voigt (KV) materials

Applying equations 1.23 and 1.24 to the equivalent circuit for a KV material (figure 1.2 (B)) gives the differential equation for the stress/strain relationship of a KV

material [162, 165, 169].

$$\sigma(t) = E_c\epsilon(t) + \eta\dot{\epsilon}(t) \tag{1.32}$$

Substituting the relaxation experiment (equation 1.15) into equation 1.32 shows that a KV material does not relax.

$$\sigma(t) = E_c\epsilon_0 \tag{1.33}$$

While KV materials do not relax, they exhibit creep with creep timescale $\tau_c = \eta/E_c$, as shown by applying equation 1.16 to equation 1.32 with the initial condition that $\epsilon(0) = \epsilon_0$.

$$\epsilon(t) = \frac{\sigma_0}{E_c}\left(1 - e^{-\frac{E_c}{\eta}t}\right) + \epsilon_0 e^{-\frac{E_c}{\eta}t} \tag{1.34}$$

Substituting a dynamic strain ($\epsilon(t) = \epsilon_0 \sin(\omega t)$), into equation 1.32 gives the following expressions for E', E'', and $\tan\delta$ of a KV material.

$$E' = E_c \tag{1.35}$$

$$E'' = \eta\omega \tag{1.36}$$

$$\tan\delta = \frac{E''}{E'} = \frac{\eta\omega}{E_c} \tag{1.37}$$

Therefore, for a KV material, E' is independent of the frequency of the applied oscillation.

1.3.5.2 Maxwell (MW) materials

Applying equations 1.23 and 1.24 to the equivalent circuit for a MW material (figure 1.2 (C)) gives the differential equation for the stress/strain relationship of a MW material [162, 165, 169].

$$\dot{\epsilon}(t) = \frac{\dot{\sigma}(t)}{E_r} + \frac{\sigma(t)}{\eta} \tag{1.38}$$

Substituting the relaxation experiment (equation 1.15) into equation 1.38 shows that a MW material relaxes with timescale $\tau_r = \eta/E_r$.

$$\sigma(t) = \sigma_0 e^{-\frac{E_r}{\eta}t} \tag{1.39}$$

MW materials also exhibit creep, as shown by applying equation 1.16 to equation 1.38 with the initial condition that $\epsilon(0) = 0$.

$$\epsilon(t) = \frac{\sigma_0}{\eta}t \tag{1.40}$$

Note that, as $t \to \infty$, so does $\epsilon(\infty)$. Therefore, MW materials creep indefinitely with a slope of σ_0/η.

Substituting a dynamic strain ($\epsilon(t) = \epsilon_0 \sin(\omega t)$), into equation 1.38 gives the following expressions for E', E'', and $\tan\delta$ of a MW material.

$$E' = \frac{E_r \eta^2 \omega^2}{\eta^2\omega^2 + E_r^2} \tag{1.41}$$

$$E'' = \frac{E_r^2 \eta \omega}{\eta^2\omega^2 + E_r^2} \tag{1.42}$$

$$\tan\delta = \frac{E''}{E'} = \frac{E_r}{\eta\omega} \tag{1.43}$$

Therefore, like the SLS (section 1.3.4.3), E', E'', and $\tan\delta$ of a MW material are frequency dependent.

1.3.6 General Maxwell materials (GMM)

The general Maxwell model is constructed by connecting several SLSs in parallel (figure 1.2 (D)) [169]. Therefore, the GMM exhibits one creep timescale and N relaxation timescales. Each of the N arms of the GMM have a single relaxation time τ_n. Since the SLSs are connected in parallel within a GMM, the total stress on

the system is the sum of the stresses on each SLS (equation 1.23) [169]. Therefore, equations derived in sections 1.3.4.1 thorough 1.3.4.3 can be summed in order to obtain the equations for a GMM with N arms in different conditions. As described in chapter 3, the only experiment that requires modeling with a GMM in this thesis is a dynamic experiment, where a sinusoidal $\epsilon(t) = \epsilon_o \sin(\omega t)$ is applied. The GMM equations in this case are as follows.

$$E' = E_c + \sum_{n=1}^{N} \frac{E_n \eta_n^2 \omega^2}{E_n^2 + \eta_n^2 \omega^2} \tag{1.44}$$

$$E'' = \sum_{n=1}^{N} \frac{E_n^2 \eta_n \omega}{E_n^2 + \eta_n^2 \omega^2} \tag{1.45}$$

$$\tan\delta = \frac{E''}{E'} = \frac{\sum_{n=1}^{N} \left(E_n^2 \eta_n \omega \prod_{j \neq n} \left(E_j^2 + \eta_j^2 \omega^2 \right) \right)}{E_c \prod_{n=1}^{N} \left(E_n^2 + \eta_n^2 \omega^2 \right) + \sum_{n=1}^{N} \left(E_n \eta_n^2 \omega^2 \prod_{j \neq n} \left(E_j^2 + \eta_j^2 \omega^2 \right) \right)} \tag{1.46}$$

1.3.7 Relating models of viscoelasticity to physical quantities

The SLS and related models can be informative about the physical properties of a material. In particular, E' vs. ω of each material (equation 1.29 for the SLS and equation 1.44 for the GMM) can be used to understand what polymer chains within the material are doing when a dynamic stimulus is applied [169]. For the SLS and the GMM, E' vs. ω has an S shape, with two plateaus and a transition between the plateaus [169]. This E' curve can be fit to plateaus, called the rubbery and glassy plateau, in a material's frequency dependent behavior as follows [175].

First, low frequency E' can be fit to a material's rubbery plateau [175]. When low frequency stimuli are applied, with $\omega \approx 0$, E' is constant with $E' = E_c$ for the SLS or GMM [169]. E_c can be fit to a material's rubbery plateau [175]. For low frequency stimuli that occur in the material's rubbery plateau, polymer chains in

the material have ample time to slide against one another and rearrange themselves (section 1.3.2.1) [162, 176–183]. This rearrangement is only limited by covalent bonds, such as crosslinks, within the material [162, 176–183]. Via free energy manipulations, the rubbery plateau (or E_c, if E_c has been fit to the rubbery plateau) can be related to the molecular weight between crosslinks of a material, M_x [162, 176–183]. The higher the value of M_x, the fewer crosslinks are in the material [162, 176–183].

$$M_x = \frac{\rho RT}{3E_c} \tag{1.47}$$

Here, ρ is the density of the material, R is the gas constant and T is the temperature. Note that, to derive equation 1.47, it must be assumed that the material is incompressible, that polymer chains within the material can assume any conformation, that the ends of the polymers are free, and that the formation of new crosslinks between polymer chains occurs independently of crosslinks that have already formed [176–183]. These assumptions are not necessarily valid for biological systems, where existing polymers (like those in the ECM) often nucleate and restrict the polymerization and conformation of other polymers in the material [4]. However, relaxing the assumptions behind equation 1.47 still finds that M_x is inversely proportional to E_c, with a similar expression to equation 1.47 [176–183]. Therefore, if E_c of a material (equivalent to the rubbery plateau's E' value) is known, M_x or M_x/ρ of a material can still be roughly estimated via equation 1.47, even if the assumptions used to derive equation 1.47 are not necessarily valid [176–183].

For high frequency stimuli, $\omega \to \infty$, $E' = E_c + E_r$ for the SLS, or $E' = E_c + \sum_{n=1}^{N} E_n$ for a GMM, and this higher plateau can be fit to a material's glassy plateau [169, 175]. When high-frequency stimuli that occur in a material's glassy plateau are applied, polymer chains within the material do not have time to rearrange themselves in response to the applied stimulus [169]. Therefore, only local chain movements can

occur, and the material behaves more like an elastic material due to the lack of time for polymer chains in the material to rearrange and dissipate energy [169].

The transition between the rubbery and glassy plateaus is called the glass transition [169]. Roughly speaking, more relaxation times in a material typically result in a broader glass transition (occurring over a larger frequency range) [169, 175]. This is so because the glass transition is dictated by a sum of contributions from each relaxation time within the material [169]. Consequentially, the glass transition is typically broad for GMM materials, and sharp for SLS materials [169].

If a MW material (equation 1.41) is fit to the glass transition, it only exhibits a glassy plateau, since $E_c \approx 0$ for a MW material [175]. Therefore, MW materials are more fluid, because they do not possess as many crosslinks or other types of covalent bonds [165]. KV materials do not exhibit a frequency-dependent E' because $E_r \approx \infty$ for a KV material, and therefore can only be fit to the rubbery plateau.

1.3.8 Summary: Introduction to mechanics

In summary, viscoelastic materials like cells and the ECM respond to mechanical stimuli with a time delay dictated by characteristic timescales, also known as time responses (τ). Creep, relaxation, and dynamic experiments can be performed to measure time responses, elasticity, and viscosity of a sample. The type of viscoelasticity a sample exhibits can be identified by the sample's behavior during these experiments, and modeled mathematically. The standard linear solid (SLS) is the simplest viscoelastic material that realistically models both creep and relaxation. The SLS has two time responses: a creep timescale $\tau_c = \eta/E_c$ and a relaxation timescale $\tau_r = \eta/E_r$. Special cases of the SLS are Kelvin-Voigt (KV) materials, where $\tau_r \to 0$, and Maxwell (MW) materials, where $\tau_c \to \infty$. The SLS can also be generalized to the general Maxwell model (GMM) for materials with multiple relaxation times.

1.4 Overall summary and outlook

The interaction between cells and the ECM is crucial for maintaining healthy tissues and organisms [1, 2, 62]. Understanding this interaction could provide insight into tissue engineering, and help develop new treatments for disease [1, 2, 62]. The mechanical properties of both cells and the ECM are important in this interaction [1, 62]. Biological systems are viscoelastic [162]. The majority of studies into the effects of mechanical properties on cells, including many of those presented in section 1.1, typically only consider the effects of ECM elasticity. Fewer studies consider viscosity, especially at the nanoscale. ECM viscosity is as important as elasticity in dictating cell behaviors over multiple length scales [15, 128, 170, 184–194]. For example, on matrices engineered to have the same elastic properties, but different time responses, cells behave differently based on the time responses they sense [15, 184]. Therefore, viscosity and time responses should not be ignored when measuring a cell's response to the ECM. Additionally, few studies address the coupling between mechanical properties, electrical properties, magnetic properties, and chemical properties of biomaterials and biological systems [78, 79, 83, 87–92]. The aim of this thesis is to gain insight into the interaction between cells and the ECM by quantifying ECM viscoelasticity (by modeling cells and the ECM with the SLS, GMM, and related models) at length scales relevant to cells, in physiological conditions, while acknowledging the coupling of this mechanical response to other non-mechanical stimuli. In general, this thesis operates under the hypothesis that applying different types of stimuli to biological systems alters their mechanical properties. The experiments in this thesis study the effect of various types of stimuli on ECM mechanics.

Specifically, the first set of experiments (chapter 4) examine mechanoelectric coupling in the ECM by studying how electrostatics and flowing ions alter collagen I mechanics. The second set of experiments (chapter 5) examines the effects of mechanochemical coupling (cell activity and chemical signaling) on ECM viscoelas-

ticity by measuring the mechanics of ECMs produced by cells in response to growth factors and mutation. The last set of experiments (chapter 6) examine the viscoelastic properties of common cell culture substrates known to alter cell behaviors and hypothesize a preliminary link between substrate viscoelasticity and cell behaviors.

In order to quantify viscoelasticity in these biological systems, relaxation, creep, and dynamic experiments were performed on ECM samples and cells. Chapter 2 describes how these experiments are performed at cellular length scales using atomic force microscopy (AFM), the main experimental tool of this thesis. Chapter 3 describes how a cutting edge AFM dynamic experiment can be expanded to estimate sample material constants and frequency-dependent behavior.

Chapter 2

Experimental Techniques

This chapter will describe the experimental techniques used in this thesis to measure the mechanical (viscoelastic) properties of biological materials. Materials and methods specific to each experiment are described in the relevant chapter.

Different experimental methods exist to measure the mechanical properties of a sample by performing stress relaxation (section 1.3.3.1), creep (section 1.3.3.2), and dynamic (section 1.3.3.3) experiments [167]. At the macroscale, two widely used techniques are rheometry and dynamic mechanical analysis (DMA) [167]. For nanoscale measurements, two widely used instruments are optical tweezers and atomic force microscopes (AFM) [167, 195]. Of the nanoscale techniques, AFM is a particularly useful tool because it can probe the nanoscale and microscale (relevant to cells), can be performed in biologically relevant conditions (on hydrated, unprocessed samples), and has higher resolution and more localized control than optical tweezers [196, 197]. This thesis uses AFM to quantify the viscoelastic properties of cells and the extracellular matrix (ECM). This chapter introduces AFM, and the three types of AFM experiments used in this thesis to measure the mechanical properties of a sample.

2.1 Atomic force microscopy (AFM)

AFM is the main experimental tool used for this thesis. AFM interacts with a sample via a probe known as a cantilever [196]. One end of the cantilever is fixed (indirectly) to a piezoelectric actuator (called the piezo), while the other end is free [196]. A tip, ranging from a few nanometers to a few micrometers in size, is attached to the side of the cantilever's free end that faces the sample [196]. A detection laser is reflected off the side of the cantilever's free end that faces away from the sample, to a photodiode (PD) [196]. This arrangement is diagrammed in figure 2.1 (A).

During an AFM experiment, the tip is brought into contact with a sample, then scanned across the sample's surface [196]. As the tip scans the surface, tip/sample interactions cause the cantilever to bend [196]. Cantilever bending alters the position of the detection laser on the PD (figure 2.1 (B)) [196]. These changes in laser spot position, converted to meters, are called the deflection z_c, and allow the AFM to record the cantilever's motion [196]. In order to accurately record sample properties (such as the height of surface features), a feedback loop is employed to regulate the cantilever's motion [196].

AFM feedback loops regulate the cantilever's proximity to the sample in order to maintain a constant z_c or a relevant parameter of z_c (such as the amplitude A or the phase ϕ of an oscillating cantilever), called the setpoint [196, 198–200]. The setpoint is a user determined parameter [196, 198–200]. Cantilever proximity to the sample is controlled by the voltage applied to the piezo, based on the setpoint and the recorded z_c (or A or ϕ) [196, 198–200]. Voltage driven expansion and contraction of the piezo causes vertical movement of the cantilever, and thereby alters the cantilever's (and the tip's) proximity to the sample until the recorded z_c (or A or ϕ) matches the setpoint [196].

AFM quantifies the mechanical properties of a sample by converting z_c, A, and/or ϕ to quantities that describe the tip/sample interaction (details in section 2.1.3) [196–

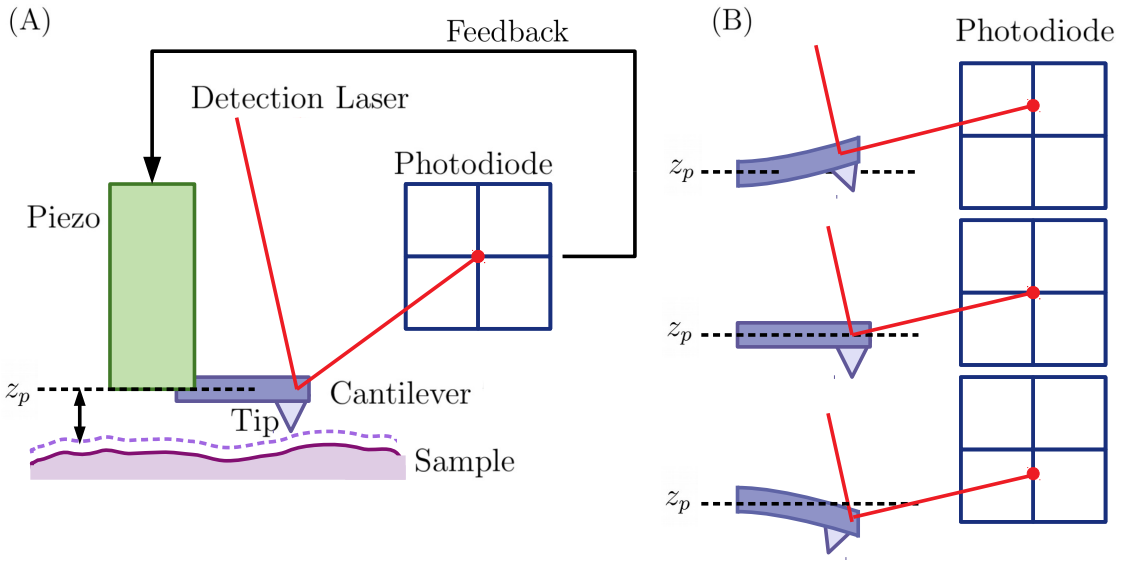


Figure 2.1: Diagram of an atomic force microscope (AFM). The basic components of the AFM are shown (A). A tip attached to the free end of a cantilever interacts with the sample (purple dotted line). A detection laser reflects from the back of the cantilever to a photodiode (PD). Cantilever deflection changes the laser spot position on the PD (B). Cantilever proximity to the sample is controlled by a piezo attached to the cantilever. Note that, in reality, the piezo is indirectly attached to the cantilever, but the hardware between the piezo and cantilever is not drawn here for ease of viewing. The z position of the piezo, z_p is indicated by a black dotted line. A feedback loop exists between voltage on the PD and voltage applied to the piezo, and alters z_p in order to maintain a constant deflection, amplitude, or phase, depending on the desired operation.

200]. Important tip/sample interaction quantities include: tip/sample interaction stiffness k_{eff}, force on the sample F, and indentation of the sample d [196–200]. The conversion of z_c, A, and/or ϕ to k_{eff}, F, and d depends on the AFM experiment being performed (details in section 2.1.3), and requires knowledge of cantilever properties obtained by calibrating the cantilever as described in section 2.1.1. Additionally, material properties like the elastic modulus (E, section 1.3.1), storage modulus (E', section 1.3.3.3), and loss modulus (E'', section 1.3.3.3) are calculated from k_{eff}, F, and d via application of contact models [196, 198–200]. Contact models describe the geometry of the tip/sample interaction, as described in section 2.1.2.

2.1.1 Cantilever calibration

Cantilever calibration is the first step in the process of quantifying sample properties from the measured cantilever motion on the PD [201, 202]. Specifically, the stiffness k_c, resonance frequency f_c, quality factor Q_c, and inverse optical lever sensitivity (InvOLS) of the cantilever must be calibrated [201, 202]. The InvOLS (with units of nm V^{-1}) allows conversion of V on the PD to nanometers of cantilever movement [201, 202]. Two methods of cantilever calibration are used in this thesis.

The first method of cantilever calibration involves pressing the cantilever against a hard surface [201]. In this case, only the cantilever will bend because the surface is much harder than the cantilever [201]. Therefore, the InvOLS can be calculated by dividing the distance (in nanometers) that the piezo extended downward, by the change in voltage on the PD [201]. Once the InvOLS is known, the cantilever is moved away from the sample and the cantilever's thermal spectrum is recorded [201–203]. From this thermal spectrum, f_c and Q_c can be calculated [201, 203]. The thermal noise method is then used to calculate k_c [201]. While this calibration method works for any cantilever, the hard surface can sometimes damage or blunt the tip during calibration, and thereby introduce experimental error [201].

The second method of cantilever calibration is the GetReal™ method. GetReal™ collects a thermal spectrum to obtain f_c and Q_c [201, 202, 204], then uses the Sader method to calculate k_c [201, 204–206], then the thermal noise method (with algebraic rearrangement) to calculate the InvOLS [201, 204, 207]. GetReal™ is performed far from the sample, and therefore avoids possible damage or blunting of the tip [201, 204]. However, GetReal™ requires measurement of expected cantilever properties [206] in advance of the calibration [201]. Therefore, GetReal™ calibration can only be performed for specific pre-measured cantilevers [201].

For both of these methods, the thermal spectrum of a cantilever is recorded over a range of frequencies [201, 203]. A fast Fourier transform (FFT) is then performed

to determine and fit the peaks in the spectrum which correspond to the resonance frequencies f_c of the cantilever [201, 203]. For each f_c, Q_c is calculated by dividing f_c by the bandwidth at half maximum (peak width, which is the change in frequency, at half the maximum amplitude) of the peak [201, 203].

2.1.2 Contact models

Contact models describe the interaction between the tip and sample [165]. The Hertz model is one of the fundamental models for the contact between an indenter, such as a cantilever tip, and a surface or sample [165, 208]. The Hertz model assumes that both the indenter and sample are spherical, homogeneous, elastic materials [165]. Additionally, the Hertz model assumes that no adhesion is present between the indenter and sample [165]. However, the Hertz model can be modified to account for adhesion (section 2.1.2.2) [165]. The Hertz contact model is applied in many AFM techniques (see sections 2.1.3.2, 2.1.3.3, and 2.1.3.4).

2.1.2.1 The Hertz contact model

The Hertz contact model relates the normal force F of the indenter/sample interaction to the indentation d of the sample and the effective elastic modulus E_{eff} of the contact (that is, of the combined indenter/sample) [165, 208].

$$F = gE_{\text{eff}}d^{\alpha} \tag{2.1}$$

Here, g and α are factors that depend on the geometry of the indenter. Throughout this thesis, tips with spherical geometry, called spherical indenters, were used. For such spherical indenters of radius R, $g = \left(4\sqrt{R}\right)/3$ and $\alpha = 3/2$ [165].

Hooke's law (equation 1.13) shows that the indenter/sample interaction stiffness (also called contact stiffness, k_{eff}) is the derivative of the interaction force in equation

2.1 with respect to the indentation of the surface [165]. Equation 2.2 is for a general indenter geometry, and equation 2.3 for spherical geometry [165].

$$\begin{aligned} k_{\text{eff}} &= \frac{dF}{dd} \\ &= \alpha g E_{\text{eff}} d^{\alpha-1} \qquad (2.2) \\ &= 2E_{\text{eff}}\sqrt{Rd} \qquad (2.3) \end{aligned}$$

Therefore, experiments can quantify E of a sample by applying some d to the sample's surface, measuring k_{eff}, then using equation 2.2 to calculate E_{eff} [165]. Once E_{eff} is known, E of the sample can be calculated via the following relation [165]. Here, the subscript I represents the indenter, subscript S represents the surface (sample), and ν represents the Poisson ratio of the indenter or surface [165].

$$\frac{1}{E_{\text{eff}}} = \frac{1-\nu_I}{E_I} + \frac{1-\nu_S}{E_S} \qquad (2.4)$$

If the indenter is more-rigid than the surface, $E_I >> E_S$, equation 2.4 simplifies to equation 2.5 [165].

$$E_S \approx E_{\text{eff}}\,(1-\nu_S) \qquad (2.5)$$

The equations derived in this section are for d applied in a direction normal to the surface of the sample [165]. Other sample deformations are not discussed here because such experiments were not applied in this thesis.

2.1.2.2 The Hertz contact model with adhesion

The Hertz contact model can be modified to account for adhesion between the tip and sample [165]. For this thesis, one common modification of the Hertz model that accounts for adhesion, called the Johnson-Kendall-Robertson (JKR) model, is

used. The JKR model applies to tip/sample interactions with short range (inside the contact area) adhesion forces [165]. The counterpart to the JKR model, for long range adhesive forces, is the Derjaguin-Muller-Toporov (DMT) model [165]. The DMT model does not apply to the samples in this thesis, and will therefore not be discussed further.

In general, for indenters of any shape, the expression for F and d in the non-adhesive (NA) and adhesive case can be related as follows.

$$d(a) = d_{\mathrm{NA}} - \sqrt{\frac{2\pi w a}{E_{\mathrm{eff}}}} \tag{2.6}$$

$$F(a) = F_{\mathrm{NA}} - \sqrt{8\pi w a E_{\mathrm{eff}}} \tag{2.7}$$

Here, w represents the adhesion energy per unit contact area, r represents the reduced radius, and a represents the contact area modified to account for adhesion. The contact area a for spherical indenters with adhesion forces (the JKR model) is as follows [165].

$$a^3 = \frac{r}{k_{\mathrm{eff}}}\left(F + 3\pi r w + \sqrt{6\pi r F + (3\pi w r)^2}\right) \tag{2.8}$$

Additionally, in an AFM experiment, typically $R <<$ sample dimensions, such that $r \approx R$ [92].

Many AFM tips have a sharpened pyramidal geometry with a small spherical end, and are often modeled as a spherical indenter [92]. However, other models can be used to describe solids with different geometries in the presence of adhesion. One such model, relevant to this thesis, is a hyperboloid indenter with adhesion, as follows [92, 209]. Here θ represents the tip semi-vertical angle.

$$d(a) = \frac{a\cot(\theta)}{2}\left[\frac{\pi}{2} + \arcsin\left(\frac{\left(\frac{a}{R\cot(\theta)}\right)^2 - 1}{\left(\frac{a}{R\cot(\theta)}\right)^2 + 1}\right)\right] - \sqrt{\frac{2\pi w a}{E_{\mathrm{eff}}}} \tag{2.9}$$

$$F(a) = E_{\text{eff}} a R^2 \cot^2(\theta) + E_{\text{eff}} \cot(\theta) \left[\frac{a^2 - R^2 \cot^2(\theta)}{2} \left(\frac{\pi}{2} + \arcsin \left(\frac{\left(\frac{a}{R\cot(\theta)}\right)^2 - 1}{\left(\frac{a}{R\cot(\theta)}\right)^2 + 1} \right) \right) \right] - \sqrt{8\pi w a E_{\text{eff}}} \quad (2.10)$$

For a large contact area (a deep indentation), $a \gg R\cot(\theta)$, and the arcsin terms simplify to $\arcsin(1) = \pi/2$ [92]. Therefore, equation 2.9 and 2.10 simplify to equation 2.11 and 2.12 respectively [92].

$$d(a) = \frac{\pi a \cot(\theta)}{2} - \sqrt{\frac{2\pi w a}{E_{\text{eff}}}} \quad (2.11)$$

$$F(a) = E_{\text{eff}} \cot(\theta) \left[aR\cot(\theta) + \frac{\pi}{2} \left(a^2 - R^2 \cot^2(\theta) \right) \right] - \sqrt{8\pi w a E_{\text{eff}}} \quad (2.12)$$

2.1.3 Quantifying a sample's mechanical properties with AFM

As discussed in the introduction (section 1.3.2), biological samples are viscoelastic, meaning that they respond to applied forces or deformations with characteristic time delays called time responses τ [162, 197]. Viscoelasticity is quantified by performing three main experiments (section 1.3.3): relaxation experiments (section 1.3.3.1) where the stress $\sigma(t)$ is measured in response to a constant strain ϵ_o, creep experiments (section 1.3.3.2) where the strain $\epsilon(t)$ is measured in response to a constant stress σ_o, or dynamic experiments (section 1.3.3.3), where an oscillatory stimulus, such as an oscillatory strain, is applied to the sample [162, 165, 167, 197].

In this thesis, creep and relaxation experiments were performed using AFM indentations [196, 197, 202]. Indentation experiments involve pressing the tip into the sample [196, 202]. Creep and relaxation experiments can be performed using dwells, where the tip continuously indents the sample [197, 202]. The type of experiment depends on the type of dwell: constant force for creep, and constant indentation for

relaxation [197, 202]. Details are provided in section 2.1.3.2.

Two types of dynamic experiments were applied in this thesis. One dynamic experiment (section 2.1.3.3) is a novel AFM indentation technique that sends an oscillatory stimulus to a sample during a dwell [92]. The second, described in section 2.1.3.4, is an imaging technique known as amplitude modulation-frequency modulation (AM-FM) AFM, where the tip is oscillated at two of its eigenmodes while scanning a sample [210]. For both dynamic experiments, the cantilever was not driven by indirect actuation via the piezo as in typical AFM (section 2.1). Instead, the cantilever was driven directly via photothermal actuation in order to remove spurious resonances from the system, as described in section 2.1.3.1.

2.1.3.1 Methods to excite the cantilever

In typical AFM, the cantilever is excited indirectly by the piezo [211, 212]. The piezo performing this indirect actuation has its own resonances [211, 212]. If a cantilever is driven by piezoelectric excitation, additional resonances from the piezo and the rest of the experimental system will be present in the cantilever's thermal spectrum, especially in liquid [211, 212]. These spurious resonances add noise to data from dynamic experiments (where the cantilever is oscillated) and thereby hinder accurate quantification of the tip/sample interaction [211, 212]. Fortunately, direct actuation of the cantilever can be performed to avoid these spurious resonances [213–218].

One direct actuation method relies on photothermal excitation (PTE) of the cantilever [213–219]. For PTE in this thesis, a blue laser (called the blueDrive$^{\text{TM}}$, Oxford Instruments Asylum Research, 405 nm wavelength) is focused at the base of the cantilever, near the cantilever's fixed end [213–219]. The power of the blue laser drives the cantilever's oscillation by changing the temperature at the base of the cantilever, causing the cantilever to bend [213–219]. The power of the blue laser is modulated to achieve the desired frequency and amplitude of the oscillation [213–219]. All dynamic

experiments in this thesis were performed using PTE.

2.1.3.2 AFM indentations: Creep and relaxation experiments

In indentation experiments, the tip is pushed into contact with the sample, causing a deflection z_c of the cantilever, and causing the sample to experience some force F and some indentation d (synonymous with deformation), until a target value is reached [196]. This target value is a specific value of F or z_c, and is referred to as the trigger point [196]. Once the trigger point is reached, the cantilever is then retracted from the sample. If the tip/sample interaction is adhesive, more force will be required to pull the cantilever away from the sample than to approach [196, 202].

Cantilever deflection z_c (in nanometers) is the difference in voltage between the top and bottom halves of the PD, multiplied by the cantilever InvOLS, $z_c = (V_{\text{top}} - V_{\text{bottom}}) \times \text{InvOLS}$ [196]. F is calculated using z_c and Hooke's law (equation 1.12), $F = k_c z_c$, where k_c is the cantilever's spring constant [196]. Sample indentation d is the difference between the z position of the piezo z_p and z_c, $d = z_p - z_c$ [196].

Relaxation (section 1.3.3.1) and creep (section 1.3.3.2) experiments are performed in indentation experiments by dwelling on the sample for a set amount of time after the trigger point is reached, but before the tip is retracted [196, 197, 202]. Dwell feedback is on z_p for relaxation experiments and z_c for creep experiments (note that, for creep, feedback should be on d, but this does not work well in practice) [92, 197, 202]. The relaxation (τ_r) and creep (τ_c) timescales can be calculated by fitting exponential functions to the force $F(t)$ or indentation $d(t)$ during the dwell, respectively [92, 197, 202]. These experiments are diagrammed in figure 2.3 (A).

2.1.3.2.1 Limitations of indentation experiments

A few factors can cause artifacts in the results of indentation experiments. First, if the sample is thin, only small indentations (of a few nanometers) should be used in

order to avoid probing the substrate through the sample [196]. Such small indentations can increase the difficulty of measuring relaxation or creep during a dwell [196]. Additionally, if the cantilever is softer than the sample, $k_c < k_{ts}$, the cantilever will bend during the indentation along with the sample [196]. In this case, force curves represent cantilever bending rather than sample deformation, which can lead to incorrect quantification of sample properties [196]. Therefore, it is easiest to perform indentations on samples that are at least a few hundred nanometers thick, with a cantilever that has greater stiffness than the sample [196].

2.1.3.3 Photothermal AFM nano-DMA (PANDA)

Photothermal AFM nano-dynamic mechanical analysis (PANDA) is a novel AFM technique developed in the Contera lab to perform dynamic experiments (section 1.3.3.3) [92]. This method quantifies a sample's storage modulus (E'), loss modulus (E''), and loss tangent ($\tan\delta = E''/E'$) over a wide range of frequencies [92]. PANDA is diagrammed in figure 2.3 (B). During PANDA, the tip indents the sample, then dwells on the sample (with feedback on z_p) for a time interval D, then retracts. During the dwell, the sample is allowed to fully relax [92]. After the sample relaxes, an oscillatory signal of varying frequency (starting at frequency f_0 and ending at frequency f_f) is applied to the sample [92]. This oscillation is called a chirp signal, and obeys the following expression [92]. A logarithmic chirp is used because a linear chirp causes artifacts at low frequencies [92].

$$f(t) = f_0 \sin\left(f_0 \left(\frac{f_f}{f_0}\right)^{1/D}\right) \tag{2.13}$$

The effective storage stiffness k' and loss stiffness k'' of the tip/sample interaction can be calculated for each frequency in the chirp by equating the sinusoidal force acting on the cantilever (with amplitude A_r and phase ϕ_r) when the tip is out of contact,

with the force needed to deform the sample (with amplitude A and phase ϕ) [92].

$$k' = k_c \left[\frac{A_r}{A} \cos\left(\phi_r - \phi\right) - 1 \right] \tag{2.14}$$

$$k'' = k_c \frac{A_r}{A} \sin\left(\phi_r - \phi\right) \tag{2.15}$$

$$\tan\delta = \frac{k''}{k'} \tag{2.16}$$

The geometric contributions to k' and k'' cancel when they are divided by one another [92]. Therefore, $\tan\delta$ measured by any technique is independent of the contact geometry (geometry of the tip/sample interaction) [92]. However, the same is not true for k' and k'' [92]. Therefore, storage and loss moduli of a sample (E' and E'') must be obtained by applying a contact model (section 2.1.2) to the expressions for k' and k'' [92]. Assuming that $E_{\text{tip}} \gg E_{\text{sample}}$, the equation for E' and E'' of the sample are shown below for the Hertz (equation 2.17 and 2.18) and JKR (equation 2.19 and 2.20) models, and are derived from equation 2.4 in section 2.1.2 [92].

$$E' = \left(\frac{1 - \nu_S^2}{2a_1} \right) k' \tag{2.17}$$

$$E'' = \left(\frac{1 - \nu_S^2}{2a_1} \right) k'' \tag{2.18}$$

$$E' = \left[\frac{1 - \frac{1}{6}\left(\frac{a_0}{a_1}\right)^{3/2}}{1 - \left(\frac{a_0}{a_1}\right)^{3/2}} \right] \left(\frac{1 - \nu_S^2}{2a_1} \right) k' \tag{2.19}$$

$$E'' = \left[\frac{1 - \frac{1}{6}\left(\frac{a_0}{a_1}\right)^{3/2}}{1 - \left(\frac{a_0}{a_1}\right)^{3/2}} \right] \left(\frac{1 - \nu_S^2}{2a_1} \right) k'' \tag{2.20}$$

Here, ν_S is the Poisson ratio of the sample, a_0 represents the contact radius of the cantilever at the point of zero load (when $F = 0$ during the cantilever's retraction), and a_1 represents the contact radius when the tip is still in the sample at the instant

retraction begins [92].

2.1.3.3.1 Limitations of PANDA

The limitations of PANDA are similar to those of indentation experiments. Specifically, sample properties can be incorrectly calculated if the cantilever is softer than the sample [92]. Additionally, the oscillations during the dwell must be smaller than the indentation (so the tip doesn't come off the sample during the chirp), but larger than the noise floor [92]. For both these reasons, as well as possibly probing the properties of the underlying substrate, PANDA is difficult to perform on thin samples (samples that are only a few nanometers thick) [92]. An additional limitation of PANDA is that cantilever resonance causes artifacts in the data. Therefore, only off resonance frequencies can be used to excite the cantilever [92].

2.1.3.4 Amplitude modulation-frequency modulation (AM-FM)

The main experimental technique used in this thesis is amplitude modulation-frequency modulation AFM (AM-FM AFM), and is diagrammed in figure 2.3 (C). AM-FM AFM is a form of tapping mode (TM) AFM. In TM, the tip is positioned just above the sample's surface, and driven by an AC voltage so that the tip intermittently "taps" the surface of the sample at a specific frequency [196, 198–200]. This frequency is usually the resonance frequency of the tip's first eigenmode [198–200]. An eigenmode is a natural resonance mode of the cantilever, and occurs at a specific frequency [198–200]. This eigenfrequency is called a resonance frequency when the applied frequency matches the eigenfrequency [198–200].

In standard TM, the amplitude (A) of the cantilever's oscillation is kept constant [198–200, 220]. This feedback on the amplitude is called amplitude modulation (AM) [198–200, 220]. Other forms of TM maintain a constant phase (ϕ) for phase modulation (PM), or a constant frequency (f) for frequency modulation (FM) [221].

Typically, TM is used to obtain high resolution images of nanoscale or atomic-scale features of a sample's surface [220]. Additional information beyond the topology of the sample is contained in ϕ and f [198–200]. During a TM experiment, tip/sample interaction forces shift ϕ and f by some $\Delta\phi = \phi - \phi_c$ and $\Delta f = f - f_c$, where ϕ_c and f_c are the reference phase and amplitude of the cantilever's oscillation when far from the sample [198–200]. In standard TM, $\phi_c = 90^o$ and f_c is the resonance frequency of the cantilever [198–200]. If the tip and sample have a repulsive interaction, $\Delta\phi < 0$ and $\Delta f > 0$ [198–200, 202]. The reverse is true for an attractive interaction, $\Delta\phi > 0$ and $\Delta f < 0$. Therefore, the mechanics of a sample can be quantified in a TM experiment by closely tracking $\Delta\phi$ or Δf [198–200, 222].

Bimodal TM allows close tracking of $\Delta\phi$ and Δf as well as sample topology [210, 220, 221]. In bimodal TM, the tip is driven at two eigenmodes instead of one (usually the lowest two), and two feedback loops are employed on the cantilever's vibration [210, 220, 221]. Like standard TM, bimodal imaging can provide high-resolution maps of a sample's surface [210, 220, 221]. Unlike standard TM, the additional observables of the second eigenmode (A_2, ϕ_2, and f_2 in addition to A_1, ϕ_1, and f_1) allow more of the sample's mechanical properties to be quantified [210, 220, 221].

In bimodal AFM, the first mode of the cantilever (the lower frequency eigenmode) is typically subject to AM, as in standard TM [210, 220, 221]. The second mode can be subject to AM (for AM-AM AFM), PM (for AM-PM AFM), or FM (for AM-FM AFM) [220, 221]. The equations relating bimodal observables in any of these configurations to the mechanical properties of a sample are interchangeable [221]. AM-FM AFM is slightly more accurate than AM-AM or AM-PM because AM-FM makes the second mode less likely to experience a drop in signal-to-noise-ratio [221]. Therefore, AM-FM AFM is typically used for quantifying sample viscoelasticity [221].

In AM-FM AFM, the AM feedback operating on the lower eigenmode, quantifies the height of features on the sample's surface [210, 220]. Additionally, the ratio of

power dissipated over power stored by the first mode's vibration provides the loss tangent ($\tan\delta$) of the sample [223, 224].

$$\tan\delta = \frac{\sin\left(\phi_1\right) - \frac{A_1}{A_{r,1}}}{\cos\left(\phi_1\right)} \tag{2.21}$$

Here, ϕ_1 is the phase of mode one, A_1 is the amplitude of mode one while interacting with the sample, and $A_{r,1}$ is the reference amplitude of mode one far from the sample (also called the free amplitude). Equation 2.21 is negative if $\phi_1 > 90^{\text{o}}$. Therefore, the tip and sample must exhibit a repulsive interaction for equation 2.21 to apply [202, 223, 224]. A repulsive interaction is typically achieved by pushing hard on the sample (the amplitude setpoint is less than 75% of the free amplitude) and by using a sharp tip [202, 210, 221].

The higher eigenmode is frequency-modulated (FM), and closely tracks the frequency shift of the cantilever due to tip/sample interactions, Δf_2 [210, 220, 221, 225]. Specifically, $\Delta f_2 = f_2 - f_{c,2}$, where f_2 is the frequency of mode two on the sample, and $f_{c,2}$ is the resonance frequency of the second eigenmode [210]. An additional feedback loop for the second mode, called a dissipation feedback loop, helps prevent the amplitude of the second mode from dropping below the detection limit if large frequency shifts occur [210, 220, 225]. The dissipation feedback loop alters the drive amplitude of the second mode in order to ensure that the mode has a high enough amplitude (above the noise floor), and is not used in AM-FM AFM calculations [210]. The FM loop, Δf_2, is used to solve for E' of the sample by relating Δf_2 to Δk_2 to E_{eff} by applying fractional calculus [225] or bimodal interaction theory and the Hertz contact model [221]. The latter derivation is presented here.

As the tip contacts a sample during AM-FM AFM, tip/sample interactions shift the stiffness of the cantilever at each eigenmode by some Δk [221]. Expressions for Δk of each eigenmode are obtained by modeling the cantilever's motion at each

eigenmode as a simple harmonic oscillator (SHO) [221]. Manipulating the equation for the SHO results in the expression for Δk of each eigenmode [221]. The approximation in equation 2.23 is obtained by applying a first-order Taylor expansion [221].

$$\Delta k_1 = \frac{A_{r,1}}{A_1}\frac{k_{c,1}}{Q_{c,1}}\cos\left(\phi_1\right) \tag{2.22}$$

$$\Delta k_2 = k_{c,2}\frac{\left(\omega_2^2 - \omega_{c,2}^2\right)}{\omega_{c,2}^2} \approx 2k_{c,2}\frac{\Delta f_2}{f_{c,2}} \tag{2.23}$$

Here, Q represents the quality factor of the cantilever and the subscript c indicates a parameter obtained via cantilever calibration. Once Δk of each mode is known, these values can be used to calculate E'_{eff} by applying the Hertz contact model (section 2.1.2.1) for spherical tip geometry (equation 2.3), and bimodal interaction theory (integrating Δk over the profile of the tip for each eigenmode) [221, 225].

$$E'_{\text{eff}} = \sqrt{\frac{2}{RA_1}}\frac{\Delta k_2^2}{\Delta k_1} = \sqrt{\frac{2A_1}{R}}\frac{4k_{c,2}^2\left(\Delta f_2\right)^2 Q_{c,1}}{k_{c,1}f_{c,2}^2 A_{r,1}\cos(\phi_1)} \tag{2.24}$$

Here, R denotes the tip radius. The value of R is typically calibrated before an AM-FM AFM experiment [220]. This calibration is described in further detail in chapter 3. The sample's E' can then be calculated from E'_{eff} via equation 2.4 or 2.5. In order to apply bimodal interaction theory to obtain equation 2.24, it is assumed that $A_2 \ll A_1$ [220, 221]. Therefore, it is recommended that $A_2 \leq 10\%$ of A_1 during AM-FM AFM experiments [210].

As previously mentioned, fractional calculus can be used to derive the same expression for E'_{eff} as equation 2.24 [225]. Additionally, the fractional calculus approach has also been used to derive expressions for E'_{eff} when the DMT model is applied instead of the Hertz model, or when the contact can be modeled with a Lennard-Jones force [225]. These contact models were not described in section 2.1.2, because they do not apply to the samples in this thesis.

2.1.3.4.1 Limitations of AM-FM AFM

AM-FM AFM must be performed with a repulsive tip/sample interaction with $A_2 \leq$ 10% of A_1 [224]. In addition to these conditions, there are several factors that can alter AM-FM AFM results. First, indentations in AM-FM AFM are typically only a few nanometers [220]. While these small indentations allow high-resolution maps of the sample, are less-likely to damage the sample, and allow AM-FM AFM to be performed on thin samples, they also increase the likelihood of incorrectly estimating E' and $\tan\delta$ due to moisture layers (only applicable to dry samples) or variations in sample topology [220, 224]. Second, the E' calculation for AM-FM AFM relies on the assumption that the Hertz contact model applies to the tip/sample interaction [220, 221]. This assumption is erroneous if a sample adheres to the tip. Therefore AM-FM AFM can give incorrect quantification of E' on adhesive samples [220, 221]. Third, certain types of dissipation (like adhesion, squeeze film dampening, or sample plasticity) can result in a calculated $\tan\delta$ higher than its actual value [224]. Fourth, due to the limits of the AFM, it is difficult for AM-FM AFM to accurately measure $\tan\delta$ less than 0.1 or higher than 10 [224]. In order to minimize the possibility that the measured E' or $\tan\delta$ are incorrect due to any of these issues, AM-FM AFM can be performed in conjunction with other techniques like PANDA, or with a reference mechanical spectrum.

2.1.3.4.2 AM-FM AFM measurement statistics

Biological samples consist of a complex mixture of molecules and structures [3, 4, 129]. Therefore, it is reasonable to hypothesize that distributions of the measured E' and $\tan\delta$ for a single AM-FM AFM image, and for multiple images across a sample, could be multimodal. In the case of multimodal distributions, calculating the mean, $|\overline{X}|$, and standard deviation, S, of the data in the usual manner could give uninformative results. For example, if the data distribution is bimodal, the mean will

fall between each peak, and therefore represent neither. To avoid this potential issue, $|\overline{X}|$ and S can be calculated from the coefficients of Gaussian fits to topology, E', and $\tan\delta$ distributions from AM-FM AFM measurements via the following procedure, diagrammed in figure 2.2.

Step one of the procedure in figure 2.2 is to fit single term and two term Gaussians to the data distributions. This fitting can be performed on the height, E', and $\tan\delta$ distributions from a single AM-FM AFM image, or distributions from all AM-FM AFM images of a given sample. The equation for the single term Gaussian, and the calculations to obtain $|\overline{X}|$ and S from this fit are shown in equations 2.25-2.27.

$$g_1(x) = a_1 e^{-\left(\frac{x-b_1}{c_1}\right)^2} \tag{2.25}$$

$$|\overline{X}| = b_1 \tag{2.26}$$

$$S = \sqrt{\frac{c_1^2}{2}} \tag{2.27}$$

Similarly, the equation for the two term Gaussian, and the calculations to obtain $|\overline{X}|$ and S from this fit are shown in equations 2.28-2.30

$$g_2(x) = a_1 e^{-\left(\frac{x-b_1}{c_1}\right)^2} + a_2 e^{-\left(\frac{x-b_2}{c_2}\right)^2} \tag{2.28}$$

$$|\overline{X}|_1 = b_1 \text{ and } |\overline{X}|_2 = b_2 \tag{2.29}$$

$$S_1 = \sqrt{\frac{c_1^2}{2}} \text{ and } S_2 = \sqrt{\frac{c_2^2}{2}} \tag{2.30}$$

Step two of the procedure shown in figure 2.2 is to determine whether $g_1(x)$ or $g_2(x)$ best describes the data. To this end, overlap of the sub Gaussians in $g_2(x)$ (subscript 1 or 2 in equation 2.28) can be compared. In this thesis, a threshold of 35% overlap was chosen to determine if the data was bimodal. That is, if less than 35% of each sub Gaussian overlaps with the other, $g_2(x)$ is used to represent the distribution, and equations 2.29 and 2.30 to calculate $|\overline{X}|_1$, S_1, $|\overline{X}|_2$, and S_2.

Otherwise, if more than 35% of each sub Gaussian overlaps with the other, $g_2(x)$ is fairly unimodal, and hence $g_1(x)$ better describes the data.

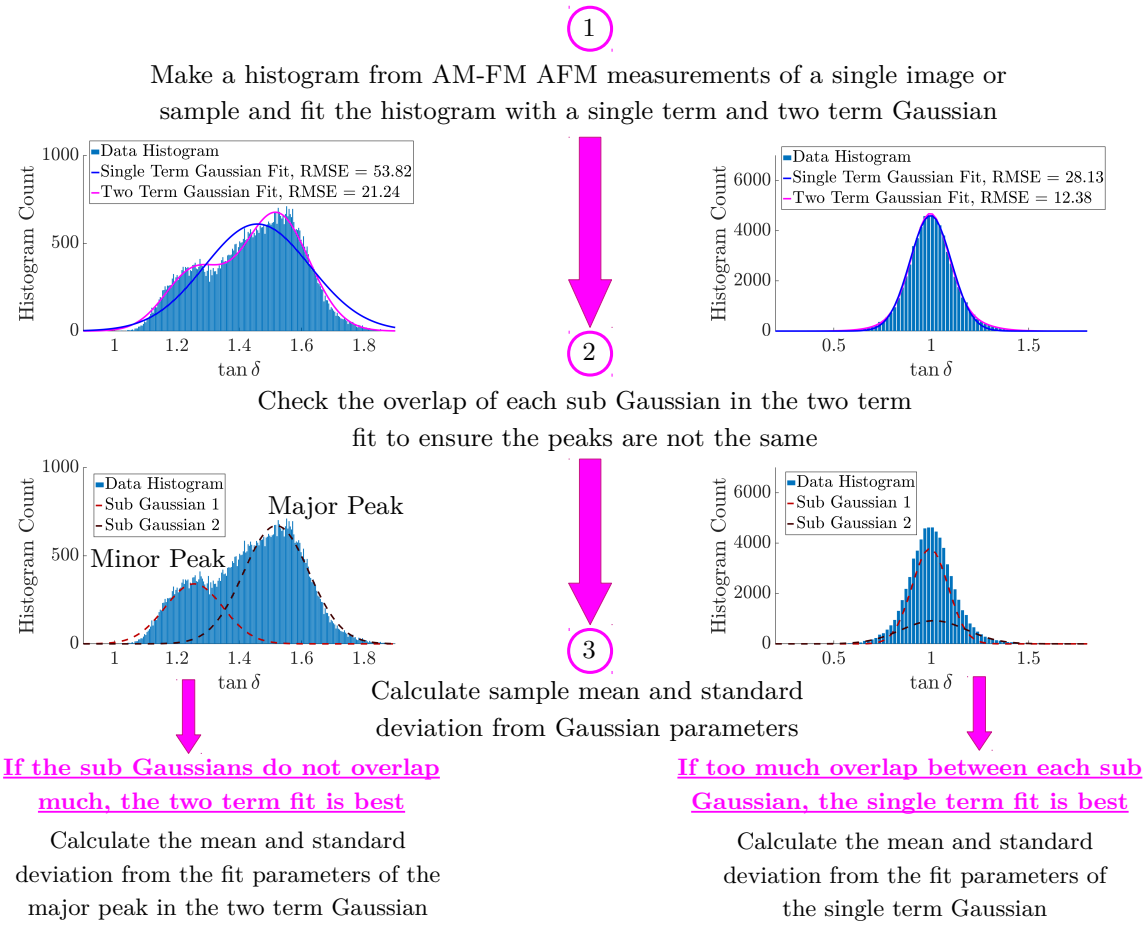


Figure 2.2: Procedure for calculating statistics from AM-FM AFM data. Applying the standard formulas to calculate the mean and standard deviation of data with a multimodal distribution can result in statistics that inaccurately represent the data. To avoid this issue, the mean and standard deviation can be calculated from Gaussians fit to histograms of the data. The first step of this calculation is to fit a histogram of AM-FM AFM data with a single term and two term Gaussian. Second, the procedure determines whether the single term or two term Gaussian better describes the data by calculating the overlap of each sub Gaussian in the two term model. If there is minimal overlap between the sub Gaussians, the two term model is used to calculate data statistics. Otherwise, the single term Gaussian is used. Finally, the mean and standard deviation of the data are calculated from the Gaussian that best fits the most prominent peak, the major peak, of the histogram. The histogram in the left column of the figure is best described by a two term Gaussian model. The histogram in the right column is best described by a single term Gaussian model. Root mean square error (RMSE) values of each fit are also shown.

Step three of the procedure shown in figure 2.2 is to calculate $|\overline{X}|$ and S of the data. If $g_1(x)$ better describes the data distribution, equations 2.26 and 2.27 are used to calculate $|\overline{X}|$ and S. If $g_2(x)$ better describes the distribution, $|\overline{X}|$ and S are calculated from either $|\overline{X}|_1$ and S_1 or $|\overline{X}|_2$ and S_2 by selecting the sub Gaussian (corresponding to $|\overline{X}|_1$ and S_1, or to $|\overline{X}|_2$ and S_2) that has a peak closest to the maximum value of the histogram. Therefore, $|\overline{X}|$ and S calculated from this procedure represent the most prominent peak, the "major peak," of the data histogram which corresponds to the most prevalent component of the distribution, and therefore of the sample. Analysis of the other "minor" peaks in distributions of samples in this thesis is left for future work.

2.2 Chapter summary and outlook

AFM is a powerful tool for quantification of a sample's viscoelasticity at the nanoscale or microscale (most-relevant to cells), in physiologically-relevant conditions (hydrated and unprocessed). This thesis employs three types of AFM experiments: (i) creep (τ_c) and relaxation (τ_r) experiments to measure the relevant timescales of a material, (ii) PANDA to measure E', E'', and $\tan\delta$ of a material over a broad range of frequencies, and (iii) AM-FM AFM to measure topology, E', and $\tan\delta$ of a sample at two discrete frequencies (two eigenfrequencies of the cantilever). Each technique is diagrammed in figure 2.3. The technique most-used in this thesis is AM-FM AFM. Time responses can be calculated from all three techniques. However, extracting time responses from AM-FM AFM data is more difficult because E' and $\tan\delta$ are measured at two different and discrete frequencies. Chapter 3 describes a new analysis method, developed in this thesis, for AM-FM AFM data to overcome this difficulty.

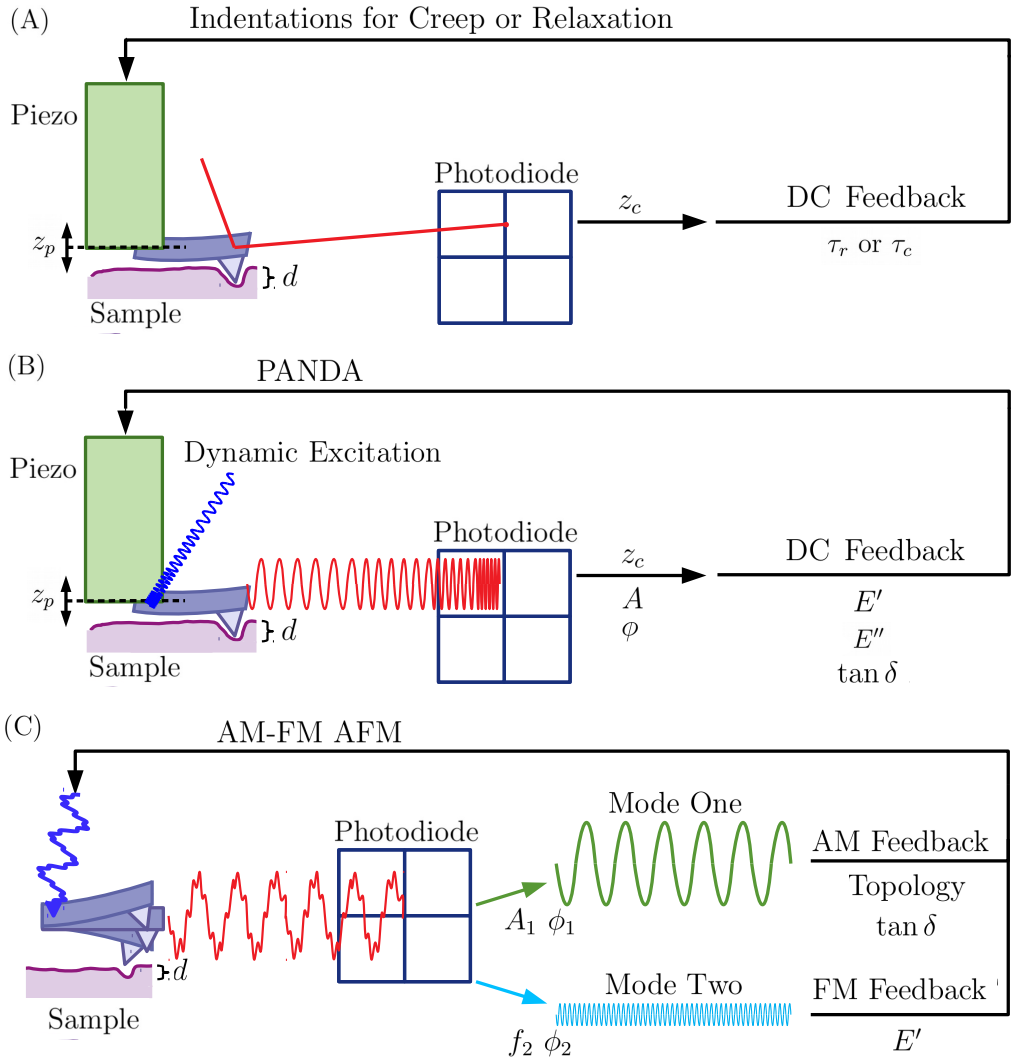


Figure 2.3: AFM techniques to measure sample viscoelasticity. (A) shows an indentation experiment (section 2.1.3.2), which can be used to perform creep or relaxation experiments. The sample is indented (d), and the tip dwells on the sample. Feedback during the dwell maintains a constant deflection (z_c) or z-sensor (z_p) for creep and relaxation experiments, respectively. Fitting an exponential curve to $d(t) = z_p(t) - z_c$ for creep experiments or $F(t) = z_c(t)k_c$ for relaxation experiments provides the creep (τ_c) and relaxation (τ_r) timescales. (B) shows a variation of an indentation experiment, PANDA (section 2.1.3.3). The sample is indented with a dwell. Dwell feedback is on z_p. During the dwell, a dynamic stimulus of varying frequency is applied via photothermal excitation (blue line, section 2.1.3.1). The resulting amplitude and phase are related to E', E'', and $\tan\delta$ of a sample over the range of excitation frequencies. (C) shows a second type of dynamic experiment, AM-FM AFM (section 2.1.3.4). In AM-FM AFM, the cantilever is excited at two frequencies using photothermal excitation. AM feedback operates on the first mode, and FM on the second. AM-FM AFM d is smaller than that of indentations or PANDA. AM-FM AFM observables at each mode are used to calculate $\tan\delta$ and E' of the sample.

Chapter 3

Development and Validation of a New Method to Analyze AM-FM AFM Data

Biological materials are viscoelastic, meaning they exhibit a time dependent mechanical response to stimuli, dictated by characteristic timescales τ of the material (section 1.3.2.1) [162]. Biological systems contain a complex mixture of molecules, and therefore exhibit many τs, which can often be modeled with the general Maxwell model (GMM, section 1.3.4) [169]. The GMM can be thought of as several standard linear solids (SLS) connected in parallel (section 1.3.4). The SLS is the simplest model of linear viscoelasticity that fully describes both creep and relaxation, with two elastic constants E_c, E_r, one viscous constant η, a creep timescale $\tau_c = \eta/E_c$, and a relaxation timescale $\tau_r = \eta/E_r$ [169]. The GMM has similar material constants to the SLS, but contains N different arms that dictate the material's relaxation [169]. The GMM therefore has N different E_r (written as E_n in this chapter), η_n, and τ_r (written in this chapter as τ_n) [169]. Special cases of the SLS are Maxwell (MW) and Kelvin-Voigt (KV) materials, where $E_c \to 0$ and $E_r \to \infty$, respectively (section 1.3.5) [169].

Several experimental techniques exist to quantify a sample's viscoelasticity [167, 195]. The main technique used in this thesis is amplitude modulation-frequency modulation atomic force microscopy (AM-FM AFM, section 2.1.3.4), which intermittently taps a sample via a tip connected to a cantilever that is oscillated at two of the cantilever's eigenmodes [210]. AM-FM AFM measures a sample's loss tangent ($\tan\delta$, section 1.3.3.3) and storage modulus (E', section 1.3.3.3). In AM-FM AFM, $\tan\delta$ is measured by the lower eigenmode of the cantilever ($\tan\delta_1$), with frequency f_1 and angular frequency $\omega_1 = 2\pi f_1$. E' is measured by a higher eigenmode of the cantilever (E'_2), with frequency f_2 and angular frequency $\omega_2 = 2\pi f_2$. AM-FM AFM does not directly quantify a sample's loss modulus E'', nor material constants (such as τ, E_c, E_r, and η). Quantification of E'' and material constants from AM-FM AFM's $\tan\delta_1$ and E'_2 is not straightforward because $\tan\delta$ and E' depend on the frequency of the applied stimulus (section 1.3.4.3). Therefore, $\tan\delta_1$ and E'_2 cannot be directly combined to calculate a sample's E'' and material constants.

Typically, in order to quantify E'' and material constants from $\tan\delta_1$ and E'_2, the frequency dependence of $\tan\delta$ and E' is ignored by assuming that the sample is a KV material for which E' is independent of frequency (section 1.3.5.1) [226]. Under this assumption, E'' and the material constants E_c, η, and τ_c can be calculated from the measured $\tan\delta_1$ and E'_2 as follows [226]. In the following equations, numbers in subscripts indicate the eigenmode to which the quantity corresponds.

$$E_c = E' \tag{3.1}$$

$$E''_1 = \tan\delta_1 E' \tag{3.2}$$

$$\eta = \frac{\tan\delta_1 E'}{\omega_1} \tag{3.3}$$

$$\tau_c = \frac{\eta}{E_c} \tag{3.4}$$

This standard analysis has two main issues. First, the assumption that the sample

is a KV material may be incorrect, since the standard analysis of AM-FM AFM data does not test which model of viscoelasticity best applies to a sample. Second, for samples that are MW materials, SLSs or GMMs, assuming that the sample is a KV material prevents quantification of the sample's relaxation time(s). This chapter describes the development (section 3.2) and validation (section 3.3) of a novel analysis method to address these issues. The new analysis first uses $\tan\delta_1$ and E_2' to determine the best model of linear viscoelasticity to describe a sample (section 3.2.1). Next, the new analysis calculates a sample's material constants from $\tan\delta_1$ and E_2' (section 3.2.2). Finally the new analysis reconstructs the frequency dependent $E'(f)$, $E''(f)$, and $\tan\delta(f)$ of the sample (section 3.2.3).

Additionally, this chapter addresses another potential issue in AM-FM AFM experiments. The calculation of E_2' in AM-FM AFM requires knowledge of the tip radius R (equation 2.24). Typically, R is determined via calibration on a sample of known E_2' [220]. For this calibration, the user manually enters R in the software so that the measured E_2' matches the expected E_2' of the calibration sample [220]. Calibration of R can also indicate whether the Hertz contact model (section 2.1.2.1) on which AM-FM AFM's calculation of E_2' (equation 2.24) is based, is a good model for the tip/sample interaction. When it is not possible to obtain the expected E_2' by calibrating R, it is a sign that the contact may be adhesive [220], and therefore that the Hertz model does not apply [220].

In spite of the benefits of calibrating R, it is sometimes difficult to determine the best calibration sample for a biological sample, due to the diversity of molecules in biological systems. Additionally, there is no guarantee that the calibration sample doesn't damage or blunt the tip (changing R) before AM-FM AFM is performed on the actual sample. Therefore, it would be convenient to skip calibration of R. The feasibility of doing so is assessed in this chapter (section 3.1).

3.1 Error caused by performing AM-FM AFM without tip radius calibration

In AM-FM AFM, the sample is intermittently tapped via a tip with radius R. The value of R must be known for AM-FM AFM's calculation of E_2' [220]. For spherical tip geometry, E_2' is proportional to $\sqrt{1/R}$ (equation 2.24). Typically, the tip radius is determined by performing AM-FM AFM on a calibration sample of known storage modulus (E_2'), and manually entering R to give good agreement with the known E_2' [220]. The calibration sample needs to have a similar E' to the sample used in the experiments [220]. However, obtaining such a calibration sample is difficult for a complex system made of many different components (including hydration shells and ions) like the ECM and cells.

It is possible to work around unknown R due to lack of a good calibration sample by using the manufacturer's specifications for the tip. Specifications for all tips include the mean tip radius $\overline{R}$ and range of possible radii. By definition of the standard deviation, the full range of R is larger than the standard deviation of R (S_R). However, S_R can be taken as the full range of possible radii to provide an upper bound for the error caused by lack of R calibration. Therefore, the values of $\overline{R}$ and S_R are known from the manufacturer.

The additional error in E_2' caused by uncalibrated R can be estimated from $\overline{R}$, S_R, the mean value of the measured E_2' ($\overline{E'_{2,\mathrm{m}}}$), and the standard deviation of the measured E_2' ($S_{E'_{2,\mathrm{m}}}$) via error propagation. The result is equation 3.5, as derived in appendix section B.2.

$$\frac{S_{E_2'}}{|\overline{E_2'}|} = \sqrt{\left(\frac{S_{E'_{2,\mathrm{m}}}}{|\overline{E'_{2,\mathrm{m}}}|}\right)^2 + \left(\frac{1}{2}\frac{S_R}{|\overline{R}|}\right)^2} \tag{3.5}$$

Therefore, the fraction of the error in E_2' due to uncertain R, written here as f_{ER}, is

calculated as follows.

$$f_{ER} = \sqrt{1 - \frac{S_{E'_{2,\mathrm{m}}}}{S_{E'_2}}} \tag{3.6}$$

It is possible that R changes during an experiment due to tip blunting [202]. However, blunting can be discounted for two reasons. First, significantly blunt tips often prevent the tip and sample from having a repulsive interaction [202]. As described in section 2.1.3.4, AM-FM AFM calculation of $\tan\delta_1$ (equation 2.21) does not work if the tip and sample do not have a repulsive interaction [202, 223, 224]. Therefore, it can be assumed that blunting is not significant enough to change $\overline{R}$ and S_R, as long as a repulsive tip/sample interaction is maintained and AM-FM AFM can still be performed. The second reason blunting can be discounted is that tip blunting can occur even when R is calibrated. Therefore, blunting does not add any additional error than what was already present with a calibrated R.

3.2 Development of a novel method to analyze AM-FM AFM data

It is not trivial to calculate the material constants of a sample (such as τs, E_c, E_r, and η) from AM-FM AFM observables (E'_2 and $\tan\delta_1$). Typically, this calculation is accomplished by assuming that the sample is a Kelvin-Voigt (KV, section 1.3.5.1) material [226]. However, this assumption is not necessarily accurate for biological samples. Therefore, a new AM-FM AFM analysis method was developed and employed for the work in this thesis to (i) determine which model of viscoelasticity a sample obeys (section 3.2.1), (ii) calculate the relevant material constants of the sample (section 3.2.2), and (iii) use these material constants to reconstruct E', E'', and $\tan\delta$ of the sample over a large frequency range (section 3.2.3).

3.2.1 Determining the best model of viscoelasticity to describe a sample

The first step in analyzing AM-FM AFM data should be to determine which model of viscoelasticity best applies to a sample. It is reasonable to assume that samples exhibit linear viscoelasticity during an AM-FM AFM experiment because sample deformations during AM-FM AFM are small (typically only a few nanometers) [220], and are therefore likely in the sample's linear viscoelastic regime (section 1.3.1) [165]. Therefore, only models of linear viscoelasticity (described in sections 1.3.4 - 1.3.6), are considered. Nonlinear viscoelasticity is left for future work.

As described in this section, a test to determine whether a sample is a MW, KV, or SLS material can be derived from the expressions for E' and $\tan\delta$ of the SLS. Since AM-FM AFM applies an oscillatory stimulus to the sample, this test is derived from algebraic manipulations of the equations describing the response of the SLS to dynamic stimulus (section 1.3.4.3). Specifically, $\tan\delta_1$ and $\tan\delta_2$, as well as E_2'' and E_2' can be related by algebraically manipulating equations 1.29 and 1.31 as follows.

First, consider the equation for $\tan\delta$ of the SLS (equation 1.31). To increase the ease of the algebraic manipulations, 1.31 can be rewritten in terms of τ_c and τ_r.

$$\frac{1}{\tan\delta} = \frac{\omega}{\tau_c}\left[\tau_r^2 + \tau_r\tau_c + \frac{1}{\omega^2}\right] \tag{3.7}$$

Therefore, $\tan\delta$ at a particular frequency can be related to $\tan\delta$ at another frequency by comparing the two frequencies. In the case of AM-FM AFM, the frequencies of interest are the first two eigenmodes. $\tan\delta_1$ measured by AM-FM AFM can be related to $\tan\delta_2$ as follows.

$$\frac{\tan\delta_2}{\tan\delta_1} = \frac{\omega_1}{\omega_2}\left[\frac{\tau_r^2 + \tau_r\tau_c + \frac{1}{\omega_1^2}}{\tau_r^2 + \tau_r\tau_c + \frac{1}{\omega_2^2}}\right] \tag{3.8}$$

The second step in this process is to relate E_2'' to E_2'. This step is accomplished

by grouping terms in the equation for E' of the SLS (equation 1.29) to obtain the following. Note that this step is only possible if the material is a SLS. This step is not possible if the material is a GMM, because E'' (equation 1.45) and E' (equation 1.44) of a GMM do not combine to $\tan\delta$ (equation 1.46) for a GMM.

$$E' = E_c + \tau_r \omega E'' \tag{3.9}$$

Equation 3.9 can be re-written in terms of $\tan\delta$ by dividing both sides of the equation by E' and rearranging terms.

$$\tan\delta = \frac{1}{\omega\tau_r}\left[1 - \frac{E_c}{E'}\right] \tag{3.10}$$

AM-FM AFM measures E' at the second eigenmode, so equation 3.10 can be used to solve for $\tan\delta_2$. This allows substitution of equation 3.8 into equation 3.10 to write $\tan\delta_2$ in terms of $\tan\delta_1$ via the following relation.

$$\begin{aligned} \frac{1}{\omega_2\tau_r}\left[1 - \frac{E_c}{E_2'}\right] &= \tan\delta_1 \frac{\omega_1}{\omega_2}\left[\frac{\tau_r^2 + \tau_r\tau_c + \frac{1}{\omega_1^2}}{\tau_r^2 + \tau_r\tau_c + \frac{1}{\omega_2^2}}\right] \\ \frac{1}{\tan\delta_1} &= \frac{E_c}{E_2'\tan\delta_1} + \omega_1\tau_r\left[\frac{\tau_r^2 + \tau_r\tau_c + \frac{1}{\omega_1^2}}{\tau_r^2 + \tau_r\tau_c + \frac{1}{\omega_2^2}}\right] \end{aligned} \tag{3.11}$$

Therefore, according to equation 3.11, a plot of $y = \tan\delta_1^{-1}$ vs. $x = (E_2'\tan\delta_1)^{-1}$ should be linear with a slope $m = E_c$ if the material is a SLS.

For a MW material, $E_c \approx 0$ and $\tau_c \to \infty$. Therefore, equation 3.11 simplifies to the following.

$$\frac{1}{\tan\delta_1} = \omega_1\tau_r \tag{3.12}$$

The line from equation 3.11 will be horizontal for a MW material.

For a KV material, $E_r \approx \infty$, $\tau_r \approx 0$, $E' = E_c$, and $E'' = \eta\omega$ (section 1.3.5.1). In this case, $y = E_c x$. The plot will still be linear, but will have a y-intercept of zero.

In summary, if a plot of AM-FM AFM observables $\tan\delta_1^{-1}$ vs. $(E_2' \tan\delta_1)^{-1}$ is linear, the sample can be modeled as a SLS, MW, or KV material. The R^2 value of a linear fit to this plot of AM-FM AFM observables can describe how well these simple models of linear viscoelasticity represent the sample. The sample is a SLS if it has a slope and y-intercept greater than zero. If the slope of the line is zero, the sample is a MW material. If the y-intercept is zero, the sample is a KV material.

3.2.1.1 Extension to a GMM

Under certain assumptions, the model test line (equation 3.11) could also work for a GMM. There are two possible explanations for why the model test equation may still be linear for a GMM. Both explanations are due to the fact that the GMM consists of several SLSs connected in parallel (section 1.3.6 and figure 1.2 (D)).

The first explanation for why AM-FM AFM data of a GMM sample fits the SLS is that the cantilever only excites one of the SLSs in the GMM, thereby making the material behave as a SLS for the particular excitation. This explanation is less likely, since AM-FM AFM is bimodal (section 2.1.3.4), and therefore excites the sample at two frequencies. The second, more likely, explanation is related to the distribution of relaxation times within a GMM.

For most GMM materials, the total number of arms in the GMM, N, is large. However, the distribution of the N τ_ns typically only has a few peaks, with values at different orders of magnitude (i.e. τ_n = ns, μs, ms, s, min, etc...) [170–174]. Depending on the excitation stimulus, some peaks (subgroups) in the distribution will contribute more to the resulting moduli than others. Typically, arms that contribute most to the material's response to a dynamic stimulus of frequency f have τ_n on the order of $1/f$ [227]. Arms with larger τ_n will respond too slow to contribute much to the material's response. Arms with faster τ_n will only contribute briefly to the material's initial response to the stimulus, leaving arms with $\tau_n \approx 1/f$ to dominate the majority

of the response. For example, a material's response to a dynamic stimulus with a frequency in the kHz range (like that applied by AM-FM AFM) is more likely to be dominated by GMM arms with τ_n on the order of μs-ms [227].

If AM-FM AFM only excites one subgroup of GMM arms that have similar τ_n, the subgroup could be approximated as a single SLS with a large standard deviation in its parameter values. However, the slope and y-intercept of the model test line (equation 3.11) would not be the same as that for a SLS. The values of these parameters for a GMM are derived in the following section.

3.2.1.2 Modification of the model test for a GMM

It is not possible to directly solve for the value of the GMM's slope, m_{GM}, and y-intercept, b_{GM}, because there are too few AM-FM AFM observables and too many unknowns, even if only a subgroup of GMM arms is excited. The unknowns include: E_1', $\tan\delta_2$, E_1'', E_2'', E_c, the number of arms N (for the material as a whole or for the subgroup of arms), and the N different E_n and η_n. However, it is possible to obtain an upper limit for the parameter values as follows. First, it is necessary to acknowledge the following four facts about the GMM.

i First, as described in section 1.3.6, the GMM equation for E_2' (equation 1.44) is as follows.

$$E_2' = E_c + \sum_{n=1}^{N} \frac{E_n \eta_n^2 \omega_2^2}{E_n^2 + \eta_n^2 \omega_2^2} = E_c + \chi_2 \tag{3.13}$$

ii For low frequencies, $\omega \sim 0$, and $E' = E_c$. For high frequencies, $\omega \to \infty$,

$$\chi \to \sum_{n=1}^{N} E_n \tag{3.14}$$

and $E' \to E_c + \sum_{n=1}^{N} E_n$. Therefore, there are two plateaus in E', one at low frequencies and one at high frequencies (section 1.3.7). The value of E' never

decreases with increasing frequency. Therefore, depending on the value of χ at a given frequency, the following is true.

$$\chi_1 \leq \chi_2 \leftrightarrow E'_1 \leq E'_2 \tag{3.15}$$

iii The value of E' at two different frequencies can be related as follows.

$$\frac{Ec}{E'_2} + \frac{\chi_2}{E'_2} = 1 = \frac{Ec}{E'_1} + \frac{\chi_1}{E'_1} \tag{3.16}$$

iv Finally, recall that the GMM equation for $\tan\delta_1$ (equation 1.46 of section 1.3.6) is as follows.

$$\tan\delta = \frac{E''}{E'} = \frac{E''}{E_c + \chi} \tag{3.17}$$

The first step in solving for m_{GM} and b_{GM} is to relate $\tan\delta_2$ and $\tan\delta_1$ using equation 3.17, the algebraically rearranging this relation to solve for E_c as follows.

$$\begin{aligned} \frac{\tan\delta_2}{\tan\delta_1} &= \frac{E''_2 E'_1}{E''_1 E'_2} = \frac{E''_2 E_c + E''_2 \chi_1}{E''_1 E_c + E''_1 \chi_2} \\ E_c &= \frac{\chi_1 - \frac{\tan\delta_2 E''_1}{\tan\delta_1 E''_2}\chi_2}{\frac{\tan\delta_2 E''_1}{\tan\delta_1 E''_2} - 1} \end{aligned} \tag{3.18}$$

Since $E'_1 \leq E'_2$ (equation 3.15) and since $E_c > 0$, both the numerator and denominator in equation 3.18 must be negative. The fact that the numerator must be negative results in the following inequality (note that the second step in the following manipulation employs equation 3.15).

$$\begin{aligned} \chi_1 &\leq \frac{E'_1}{E'_2}\chi_2 \\ \chi_1 + E_c &\leq \frac{E'_1}{E'_2}\chi_2 + E_c \end{aligned} \tag{3.19}$$

Substituting the expression for E' (equation 3.13) and $\tan\delta$ (equation 3.17) of the GMM into equation 3.19 results in the following inequality.

$$\begin{aligned} E_1' &\leq \frac{E_1'}{E_2'}\chi_2 + E_c \\ \frac{1}{\tan\delta_1} &\leq \frac{\chi_2}{\tan\delta_1 E_2'} + \frac{E_c}{E_1''} \end{aligned} \tag{3.20}$$

Bounds for m_{GM} and b_{GM} can now be calculated from the inequality in equation 3.20 as follows.

$$\frac{m_{\mathrm{GM}}}{\tan\delta_1 E_2'} + b_{\mathrm{GM}} = \frac{1}{\tan\delta_1} \leq \frac{\chi_2}{\tan\delta_1 E_2'} + \frac{E_c}{E_1''}$$

$$m_{\mathrm{GM}} \leq \chi_2 \tag{3.21}$$

$$b_{\mathrm{GM}} \leq \frac{E_c}{E_1''} \tag{3.22}$$

Equation 3.22 can be written in terms of AM-FM AFM observables by applying the expression for $\tan\delta$ of the GMM (equation 3.17) in the following form.

$$\frac{1}{\tan\delta_1} = \frac{E_c}{E_1''} + \frac{\chi_1}{E_1''} \tag{3.23}$$

Substituting equation 3.23 into equation 3.22 gives the following.

$$\begin{aligned} b_{\mathrm{GM}} + \frac{\chi_1}{E_1''} &\leq \frac{E_c}{E_1''} + \frac{\chi_1}{E_1''} \\ \frac{\chi_1}{E_1''} &\leq \frac{1}{\tan\delta_1} - b_{\mathrm{GM}} \\ \frac{\chi_1}{E_1'} &\leq 1 - \tan\delta_1 b_{\mathrm{GM}} \end{aligned} \tag{3.24}$$

3.2.1.3 Comparing model test slopes for the SLS and GMM

Note that, for the SLS, $m = E_c$ (equation 3.11). For the GMM $m_{GM} \neq E_c$. It is not possible to solve exactly for E_c of the GMM. However, it is possible to solve for

the upper and lower bounds of E_c from the expressions for the upper bound of m_{GM} (equation 3.21) and b_{GM} (equation 3.24) as follows.

Equation 3.16 relates the value of E' at two different frequencies for the GMM. The upper bounds for m_{GM} (equation 3.21), and b_{GM} (equation 3.24) can be substituted into equation 3.16 to obtain the following relation.

$$\begin{aligned} \frac{E_c}{E_2'} + \frac{\chi_2}{E_2'} &= \frac{E_c}{E_1'} + \frac{\chi_1}{E_1'} \\ \frac{E_c}{E_2'} + \frac{m_{\mathrm{GM}}}{E_2'} &\approx \frac{E_c}{E_1'} + 1 - \tan\delta_1 b_{\mathrm{GM}} \\ \frac{E_c}{E_2'} &= 1 - \tan\delta_1 b_{\mathrm{GM}} - \frac{m_{\mathrm{GM}}}{E_2'} + \frac{E_c}{E_1'} \end{aligned} \tag{3.25}$$

It is still not possible to solve for E_c in equation 3.25 because the value of E_c/E_1' is unknown, since E_1' is not measured by AM-FM AFM. However, E_c/E_1' cannot be less than zero because both E_c and $E_1' \geq 0$. Similarly, the upper bound of E_c/E_1' is one, which is only the case when $\chi_1 = 0$. These observations allow bounds to be placed on the value of E_c.

$$E_2'\left(1 - \tan\delta_1 b_{\mathrm{GM}}\right) - m_{\mathrm{GM}} \leq E_c \leq E_2'\left(2 - \tan\delta_1 b_{\mathrm{GM}}\right) - m_{\mathrm{GM}} \tag{3.26}$$

The applied frequencies ($\omega = 2\pi f$) in AM-FM AFM are high, typically in the kHz range. Therefore, the upper bound of E_c can likely be disregarded for AM-FM AFM because this upper bound occurs when $\chi_1 = 0$, which occurs only when ω is low. Therefore, for the rest of this analysis, it is assumed that E_c is close to its lower bound if the sample is a GMM.

3.2.2 Solving for material constants from AM-FM AFM data

As derived in the previous section (3.2.1), the slope and y-intercept of the model test line (equation 3.11) can be used to calculate the value of E_c for both the SLS

and GMM. However, the other material constants (E_r, η $\tau_r = \eta/E_r$ and $\tau_c = \eta/E_c$) remain unknown without additional manipulations. For a sample best modeled with the SLS, these additional manipulations require more algebraic rearrangements of the expression for E' (equation 1.29) and $\tan\delta$ (equation 1.31) of a SLS under dynamic stimulus. These manipulations result in the creation of another line that can be fit for the remaining material constants.

The first step in the process of creating the second line is to rearrange the equation for $\tan\delta$ of the SLS (equation 1.31) to solve for $E_c + E_r$ as follows.

$$E_c + E_r = \frac{\eta\omega - E_c \tan\delta}{\tau_r^2 \omega^2} \tag{3.27}$$

Similarly, the equation for E' of the SLS (equation 1.29) can also be rearranged to solve for $E_c + E_r$.

$$E_c + E_r = E' + \frac{E' - E_c}{\tau_r^2 \omega^2} \tag{3.28}$$

Equating equation 3.27 at the first cantilever eigenmode in AM-FM AFM with equation 3.28 at the second eigenmode provides the equation for the second line.

$$\begin{aligned} \frac{\eta\omega_1 - E_c \tan\delta_1}{\tau_r^2 \omega_1^2} &= E_2' + \frac{E_2' - E_c}{\tau_r^2 \omega_2^2} \\ \frac{\tan\delta_1}{\omega_2^2}\left[E_c + \frac{\omega_1^2}{\omega_2^2}\left(E_2' - E_c\right)\right] &= -E_2' \tan\delta_1 \omega_1^2 \tau_r^2 + \eta\omega_1 \end{aligned} \tag{3.29}$$

The slope of this second line provides $\tau_r = \sqrt{m_2}$. The y_2-intercept provides $\eta = b_2/\omega_1$. E_r can then be calculated as $E_r = \eta/\tau_r$ and $\tau_c = \eta/E_c$.

3.2.2.1 Parameter estimation for a GMM

As described in section 3.2.1.3, it is possible to calculate bounds in the value of E_c of a GMM from E_2', $\tan\delta_1$, and the parameters of the model test fit (equation 3.26). It can be assumed that E_c is equal to its lower bound (rationale for this assumption

can be found in section 3.2.1.3). However, even under this assumption, only three material values are known: E_c, $\tan\delta_1$, and E_2'. With this limited number of knowns, it is not possible to calculate the number of arms N in the material, nor all N values of E_n, η_n, and τ_n.

In order to estimate the relaxation behavior of the sample, it is necessary to apply additional assumptions about the subgroup of GMM arms that contributes most to the sample's response to AM-FM AFM stimulus. Specifically, it must be assumed that this subgroup can be approximated as a single SLS with a large standard deviation in its parameter values (see section 3.2.1.1). Under this assumption, rough values for E_r and η can be calculated from the expression for E' (equation 1.29) and $\tan\delta$ (equation 1.31) of a SLS under dynamic stimulus.

First, the value of χ_2 can be calculated by taking the difference between E_2' and E_c. Next, the expression for χ_2 can be combined with the expression for $\tan\delta_1$ of the SLS (equation 1.31) to create the following system of equations for τ_r and E_r of the GMM subgroup approximated by the SLS.

$$\tan\delta_1 = \frac{E_r\tau_r\omega_1}{E_c + (E_c + E_r)\tau_r^2\omega_1^2} \tag{3.30}$$

$$E_2' = \frac{E_c + (E_c + E_r)\tau_r^2\omega_2^2}{1 + \tau_r^2\omega_2^2} \tag{3.31}$$

This system gives the following expressions for τ_r and E_r.

$$\tau_r^3\left(\tan\delta_1 E_2'\omega_1^2\omega_2^2\right) - \tau_r^2\left(\omega_1\omega_2^2\right) + \tau_r\left(\tan\delta_1\left[E_c\omega_2^2 + \chi_2\omega_1^2\right]\right) - \chi_2\omega_1 = 0 \tag{3.32}$$

$$E_r = \chi_2\left(1 + \frac{1}{\tau_r^2\omega_2^2}\right) \tag{3.33}$$

Once τ_r and E_r are known, η can be calculated as $\eta = \tau_r E_r$, and τ_c can be calculated as $\tau_c = \eta/E_c$.

Since equation 3.32 is a cubic polynomial, there are three possible values for τ_r.

The root corresponding to the sample's τ_r can be determined by excluding negative and/or complex roots. If there is more than one real positive root, the root corresponding to the sample's τ_r can be selected by calculating $\tan\delta_1$ and E_2' from the material constants and choosing the value of τ_r which gives the closest calculated $\tan\delta_1$ and E_2' to the observed $\tan\delta_1$ and E_2'.

3.2.3 Reconstructing frequency-dependent behavior

Once a sample's material constants are known, it is possible to calculate E', E'', and $\tan\delta$ of the material for a dynamic stimulus at any frequency by substituting the constants into the relevant equation. These equations have already been derived in section 1.3, for a KV material (equations 1.35-1.37), a MW material (equations 1.41-1.43), and a SLS (equations 1.29-1.31). Since GMM samples must be approximated as a SLS in order to calculate sample material constants (section 3.2.2.1), SLS equations are used in the reconstruction for both SLS and GMM materials.

3.3 Testing AM-FM AFM analysis on a rubber (SBR) control sample

3.3.1 Materials and Methods

A sterine-butadiene rubber (SBR) was used as a calibration sample for the new AM-FM AFM analysis method due to the fact that SBRs are widely used, and therefore their properties are well known [228]. AFM experiments were performed on dry SBR samples with an Oxford Instruments Asylum Research Cypher ES AFM, using Oxford Instruments Asylum Research software version 16.9.220 in Igor Pro software version 6.38B01. AFM experiments were performed using AC240TSA cantilevers ($k_{c,1} \sim 2.5$ N/m, $k_{c,2} \sim 50$ N/m, $f_{c,1} \sim 60$ kHz in air, and $f_{c,2} \sim 390$ kHz in air, $R \sim 7 \pm 3$ nm)

and AC160TSA cantilevers ($k_{c,1} \sim 13$ N/m, $k_{c,2} \sim 364$ N/m, $f_{c,1} \sim 290$ kHz in air, and $f_{c,2} \sim 1.5$ MHz in air, $R \sim 7 \pm 3$ nm). The cantilever was driven via photothermal actuation (section 2.1.3.1) with full blueDrive$^{\text{TM}}$ power, and calibrated via Asylum Research's GetReal$^{\text{TM}}$ calibration method (section 2.1.1) in order to avoid blunting the tip. During AFM experiments, AM-FM AFM was performed on the SBR, then photothermal actuation AFM nano-dynamic mechanical analysis (PANDA, section 2.1.3.3) was performed at select points on the same spot of the rubber as the final AM-FM AFM image. Two AM-FM AFM experiments were performed. First, a single spot on the SBR was scanned multiple times with a variety of drive amplitudes and setpoints, to test if AM-FM AFM could provide stable quantification of E_2' and $\tan\delta_1$ without calibrating R. Second, multiple spots on the SBR were scanned, to quantify the SBR's E_2' and $\tan\delta_1$.

After the experiment, AM-FM AFM height images of SBR topology were flattened using Asylum Research software version 16.10.208 in Igor Pro software version 6.38B01, in order to remove any variations in sample topology that were not due to SBR features. This flattening was done by hand, in order to avoid introducing flattening artifacts. The processed files were then analyzed by a custom script in MATLAB R2019b 9.7.0.1261785 that calculated $\tan\delta_1$ and E_2' of the sample (equations 2.21 and 2.24, section 2.1.3.4), then performed the new AM-FM AFM analysis method (developed in section 3.2).

PANDA data analysis (calculating E' and E'' from the measured k' and k'', section 2.1.3.3) was performed by Dr. Alba Rosa Piacenti. Additionally, dynamic mechanical analysis (DMA) of the SBR was performed by Dr. Alba Rosa Piacenti and Nicholas Hawkins, and provided by Dr. Alba Rosa Piacenti as a macroscale control for the nanoscale PANDA and AM-FM AFM measurements. DMA details are provided in appendix section B.1.

The new AM-FM AFM analysis method was applied to the SBR, and the results

were compared to both PANDA and DMA measurements. The new AM-FM AFM analysis method is valid if it can reproduce values similar to PANDA and DMA measurements of the SBR.

3.3.2 SBR Results

3.3.2.1 Distributions and statistics of SBR AM-FM AFM data

As shown in figure 3.1, individual AM-FM AFM images of the SBR had varying distributions of E_2' and $\tan\delta_1$. Such variation likely arose from variation in the features, curvature, or topology, of the sample surface at any given area. Images exhibited uni-

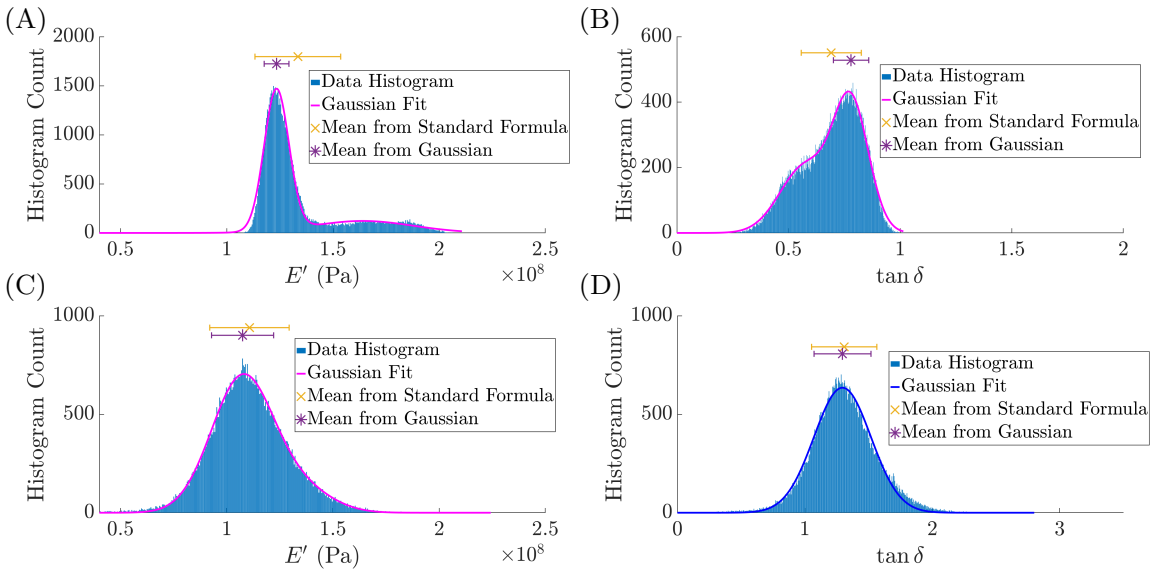


Figure 3.1: Example distributions of SBR AM-FM AFM measurements. All distributions were obtained from the values of individual pixels from a single AM-FM AFM image of the SBR. Two different AM-FM AFM images, collected on different areas of the SBR surface, are shown. Storage modulus, E', and loss tangent, $\tan\delta$, distributions from the first image are shown in (A) and (B), respectively. Similarly, E' and $\tan\delta$ distributions from the second image are shown in (C) and (D), respectively. A Gaussian fit to the distribution is shown as a magenta line if a two term Gaussian was used or as a dark blue line if a single term Gaussian was used. Selection of the single or two term Gaussian is described in section 2.1.3.4.2. The mean (points) and standard deviation (error bars) calculated via the standard formulas and via the Gaussian fit constants (as described in section 2.1.3.4.2) are shown as an orange x or a purple asterisks, respectively. These measurements were obtained with an AC240TSA cantilever, but are representative of those taken with an AC160TSA as well.

modal or bimodal distributions. As shown in figure 3.1 (A), the presence of bimodal distributions in the data influenced calculation of the mean and standard deviation of AM-FM AFM measurements, and thereby resulted in sample statistics that did not accurately represent the data. To overcome this issue, as described in section 2.1.3.4.2, the mean and standard deviation of AM-FM AFM measurements of the SBR were calculated by fitting Gaussians to the data distributions, rather than via the standard formulas. Figure 3.1 (A) shows that calculating the mean from Gaussians results in statistics that represent the most prominent peak of the distribution. Figure 3.1 (B) shows that this Gaussian fit method of calculating sample statistics matches the values from the standard formulas if the data distribution is unimodal. Therefore, the mean and standard deviation of all AM-FM AFM data presented in this chapter were calculated by fitting Gaussians to the data distributions as described in section 2.1.3.4.2. For individual image statistics, the distribution used for the fit comprised of pixel values from a single AM-FM AFM image. For overall statistics, the distribution comprised of pixel values from all AM-FM AFM images of the SBR.

3.3.2.2 Measurement error due to uncalibrated tip radius

It was first necessary to ensure that lack of tip radius (R) calibration does not interfere with correct quantification of E_2' and $\tan\delta_1$. To this end, the effect of user controlled parameters during an AM-FM AFM experiment was studied by scanning a single spot on the SBR multiple times, with a variety of drive amplitudes and setpoints, in order to ensure that, regardless of how the user handled the AFM, the measured E_2' and $\tan\delta_1$ were consistent.

During an AM-FM AFM experiment (section 2.1.3.4), the user controls the amplitude feedback loops for both modes (AM for the first mode, and dissipation feedback for the second mode) by changing the setpoint (A_s) and drive amplitude of each mode [202, 210, 220]. Note that the user does not directly control FM of the second mode

because the cantilever's resonance frequency is what regulates the FM feedback loop [202, 210, 220]. The drive amplitude determines the free amplitude A_r of the cantilever's oscillation [202]. Combinations of user-controlled parameters (A_s and A_r) can be summarized by a single metric for each eigenmode, the ratio of $A_{s,1}/A_{r,1}$ and $A_{s,2}/A_{r,2}$. The lower the ratio, the harder the user is tapping on the sample [202].

To examine the feasibility of performing AM-FM AFM without first calibrating R, AM-FM AFM was performed on the SBR with a variety of A_s and A_r combinations for each mode. This test was performed to ensure that: (i) AM-FM AFM could still correctly quantify a sample's E_2' even without first calibrating R, (ii) that uncertain R did not result in too large an error in E_2', and (iii) test how $\tan\delta_1$ and E_2' depended on user-determined parameters. The test in (iii) is necessary to ensure that the values of $\tan\delta_1$ and E_2' are stable regardless of how the user handles the AFM during the experiment. If the value of $\tan\delta_1$ and E_2' vary with A_s/A_r, it would be difficult to determine the actual value of the sample without calibration of R.

Figure 3.2 shows the effect of A_s/A_r on E_2' and $\tan\delta_1$. The data in figure 3.2 were collected with an AC160TSA cantilever, but similar results were obtained with an AC240TSA cantilever (not shown). The dissipation feedback parameters ($A_{s,2}/A_{r,2}$) did not affect $\tan\delta_1$ and E_2'. This result is expected, because the dissipation feedback of mode 2 only prevents the mode's amplitude from falling below the detection floor, and is not used in AM-FM AFM calculations (section 2.1.3.4) [210, 220, 225].

AM feedback parameters affected E_2' and $\tan\delta_1$. In general, if $A_{s,1}/A_{r,1}$ was too high, the value of $\tan\delta_1$ and E_2' varied more in response to changes in $A_{s,1}/A_{r,1}$. If $A_{s,1}/A_{r,1}$ was too low, the topology image became distorted (not shown) or the dissipation feedback could no longer operate. In the later case, the dissipation feedback was likely lost because the tip was tapping the sample too hard, and the resulting slamming of the cantilever against the sample interfered with the AFM's ability to drive the second mode. Regardless, loss of the dissipation image or distortion in the

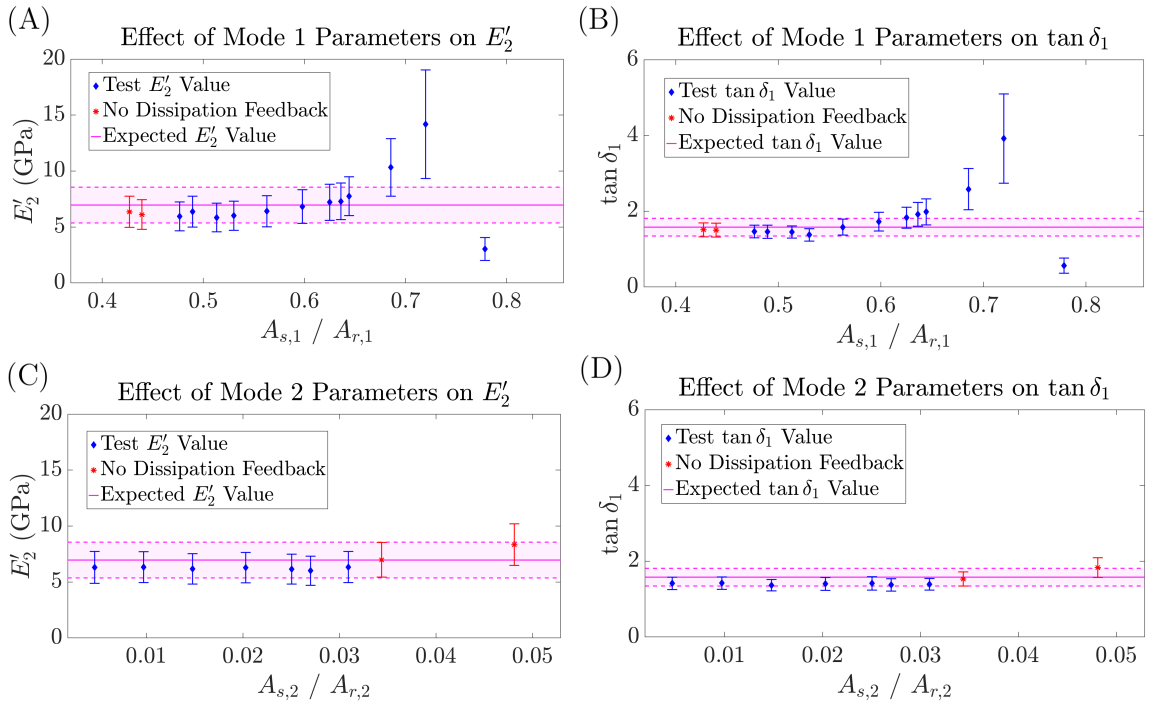


Figure 3.2: Effect of user-controlled parameters on AM-FM AFM measurements. The ratio of setpoint A_s over free amplitude A_r of each AM-FM AFM eigenmode is controlled by the user. The effect of mode 1 $A_{s,1}/A_{r,1}$ on E_2' and $\tan\delta_1$ is shown in (A) and (B), respectively (blue diamonds). The same for mode 2 is shown in (C) and (D), respectively (blue diamonds). Red asterisks indicate images where the AFM could not adequately track the dissipation of the second mode (due to the specific A_s and A_r), and thus could not adequately perform dissipation feedback. Magenta lines indicate the mean value of E_2' and $\tan\delta_1$ from AM-FM AFM data not part of the imaging parameter test. Error bars and shading represent the standard deviation.

sample's features during the scan, are signs that the user's $A_{s,1}/A_{r,1}$ is too high or too low to accurately quantify the sample. Still, AM-FM AFM quantification of $\tan\delta_1$ and E_2' was stable for several values of $A_{s,1}/A_{r,1}$. These results suggest that reliable and consistent quantification of $\tan\delta_1$ and E_2' can be obtained as long as the user decreases $A_{s,1}/A_{r,1}$ just enough to ensure a repulsive tip/sample interaction ($\phi_1 < 90^o$), then does not decrease $A_{s,1}/A_{r,1}$ any further. Representative AM-FM AFM images of the SBR obtained using this procedure are shown in figure 3.3

After performing AM-FM AFM at multiple spots on the SBR surface (resulting in 25 AM-FM AFM images from AC240TSA scans and 13 images from AC160TSA

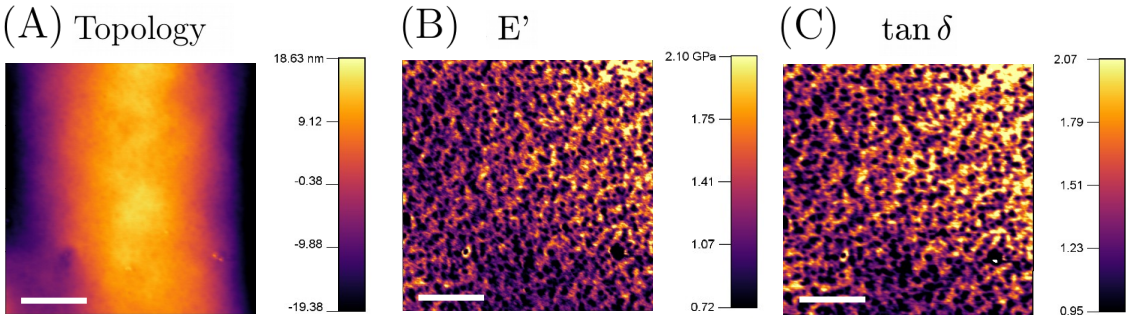


Figure 3.3: Representative AM-FM AFM images of the SBR. SBR topology (A), storage modulus E' (B), and loss tangent $\tan\delta$ (C) are shown. Scale bars are 1 μm.

scans), the mean E_2' and $\tan\delta_1$ were calculated by fitting a gaussian to the resulting distributions for each quantity. The mean ± standard deviation of the SBR's $\tan\delta_1$ was 1.9 ± 0.5 for the AC240TSA and 1.6 ± 0.4 for the AC160TSA. The mean ± standard deviation of the SBR's E_2' was 570 MPa ± 89 MPa for the AC240TSA and 7.0 GPa ± 0.6 GPa for the AC160TSA. Applying equation 3.6, the uncertainty in R contributed to 79% of $S_{E_2'}$ from AC240TSA measurements and 65% of $S_{E_2'}$ from AC160TSA measurements. These results suggests that, if R is not calibrated, the uncertainty in R is not negligible, and should be propagated through the measured E_2'. However, E_2' can still be reliably measured, even without calibrating R. The only downside to lack of R calibration is that there is no longer an indication of tip/sample pairings where the Hertz contact model does not apply (e.g. adhesive contacts) [220] without the use of additional experiments like indentations, PANDA, or DMA.

In order to ensure that AM-FM AFM measurements correctly quantified E_2' and $\tan\delta_1$, both quantities were compared with the PANDA and DMA controls (figure 3.4). The measured $\tan\delta_1$ agreed well with the DMA control. However, AM-FM AFM's E_2' was 10-100x larger than E' measured by DMA.

Comparison of DMA and AM-FM AFM data with PANDA measurements shows that the discrepancy between E_2' and the DMA control is not due to uncertain R or the use of an incorrect $A_{s,1}/A_{r,1}$. Instead, the observed overestimation of E_2' by

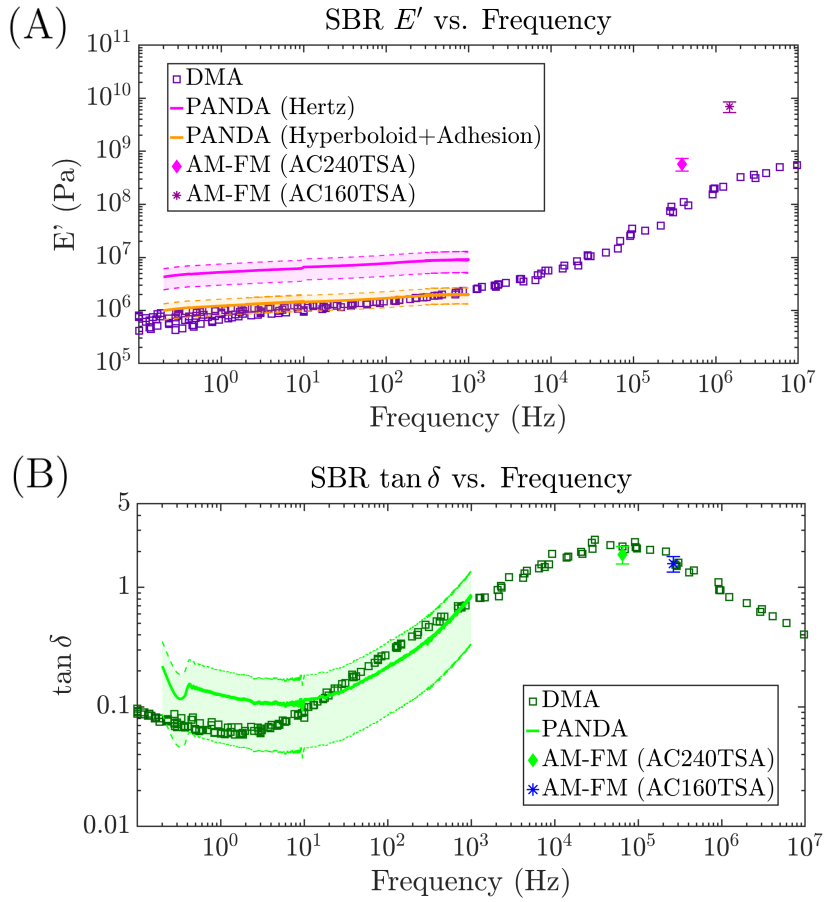


Figure 3.4: Quantification of SBR E' and $\tan\delta$. SBR storage modulus, E', and loss tangent, $\tan\delta$, are shown in (A) and (B), respectively. Both quantities were measured with DMA (squares), PANDA (lines), and AM-FM AFM (points with error bars). PANDA E' was calculated by applying the Hertz contact model (pink) or the hyperboloid with adhesion (orange). AM-FM AFM was performed using AC240TSA (diamonds) and AC160TSA (asterisks) cantilevers. PANDA data was obtained with an AC240TSA, and matches data obtained with an AC160TSA (not shown). Error bars and shading represent the standard deviation.

AM-FM AFM is due to the fact that AM-FM AFM employs the Hertz contact model (section 2.1.2.1) to calculate E'_2. PANDA E' calculated with the Hertz contact model shows similar disagreement with the DMA. PANDA E' calculated by modeling the contact geometry as a hyperboloid indenter with adhesion (section 2.1.2.2) agrees well with the DMA, suggesting that this model is the best contact model for the tip/SBR interaction. In other words, adhesion is present between the tip and SBR. The Hertz contact model upon which AM-FM AFM relies assumes that no adhesion is

present between the tip and sample, and therefore inadequately describes the tip/SBR interaction. While reliance on the Hertz model results in an incorrect estimation of E_2' for AM-FM AFM, the value of $\tan\delta_1$ is correct because $\tan\delta$ is independent of contact geometry [92].

In summary, quantification of $\tan\delta_1$ and E_2' in AM-FM AFM is still possible, even with an uncertain tip radius R. It is not necessary to use a sample of known modulus to calibrate R. However, incorrect quantification of E_2' will occur if the Hertz contact model is not suitable to describe the tip/sample interaction.

3.3.2.3 Best model for SBR viscoelasticity

Figure 3.5 shows a plot of $y = \tan\delta_1^{-1}$ vs. $x = (E_2'\tan\delta_1)^{-1}$ (equation 3.11) for AM-FM AFM data at a single spot on the SBR (that is, for a single AM-FM AFM image). Each image was fit with the model test line. The mean $\pm$ standard deviation R^2 value of the fits is 0.99 ± 0.02 for data taken with an AC240TSA, and 0.95 ± 0.04 for data taken with an AC160TSA. For both cantilevers, the slope and y-intercept of the fit are greater than zero.

For the reasons described in section 3.2.1.1, the good fit of the SBR data to the plot of $y = \tan\delta_1^{-1}$ vs. $x = (E_2'\tan\delta_1)^{-1}$ (equation 3.11) suggests that a subgroup of GMM arms within the SBR, all with similar τ_n, contributed most to E_2' and $\tan\delta_1$. Specifically, the AM-FM AFM excitation frequencies in these experiments are more likely to excite GMM arms with τ_n on the order of 0.1-10 μs. The good fit of the SBR data to the SLS suggests that this subgroup of arms can be approximated as a single SLS, likely with a large standard deviation in its parameter values (E_c, E_n, and η_n).

It is interesting to note that the model test plot in figure 3.5 seems to have a hyperbolic or logarithmic shape, rather than a linear shape. Cursory investigation into the reason for this observation was not forthcoming. Therefore, understanding of why the model test for a GMM results in a curve, rather than a line, is left for

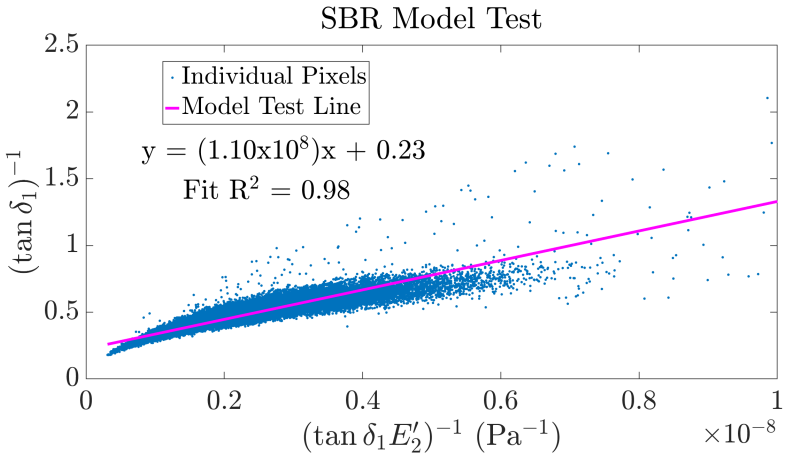


Figure 3.5: Representative model test for a single AM-FM AFM image of the SBR. All pixels from a single AM-FM AFM image of the SBR are shown (points) along with the linear fit to the data (magenta line, equation 3.11), used to determine the best description of the SBR's viscoelastic response. The fit equation and R^2 value are also shown. The data in this figure are taken from a single AM-FM AFM image, but are representative of the fits to other images.

future work. Future investigation of this observation may improve the calculation of GMM material constants from AM-FM AFM data. However, the large R^2 values of the linear fits suggest that, even though the model test appears to have a hyperbolic shape, a line still approximates the trend in the data well. Again, this observation supports the notion that AM-FM AFM excites a subset of GMM arms, all with similar τ_n, and that this subset can be approximated as a single SLS.

3.3.2.4 SBR material constants and frequency dependent behavior

Material constants of the SBR were calculated as described in section 3.2.2, and are shown in table 3.1. As expected for a subgroup of GMM arms being approximated as a single SLS, the calculated material constants have large standard deviations. However, calculated material constants agree well with literature values [228]. Most of the parameter values agree between the SLS and the GMM. However, E_c is two orders of magnitude lower for the GMM than the SLS. Comparison with SBR DMA at low frequencies (figure 3.6 (A)) shows that the GMM's estimation of E_c is more

accurate than the SLS's estimation.

Table 3.1: Material constants of the SBR. Material constants were calculated for all AM-FM AFM images taken at different spots on the sample surface (a total of 25 for the AC240TSA and 13 for the AC160TSA). Table values represent the mean ± standard deviation of these calculations.

Parameter	Cantilever	GMM	SLS
E_c (Pa)	AC240TSA	$2.65\times10^{6} \pm 2.27\times10^{6}$	$1.97\times10^{8} \pm 1.26\times10^{8}$
	AC160TSA	$4.42 \times10^{7} \pm 1.07 \times10^{8}$	$5.23 \times10^{9} \pm 1.00\times10^{9}$
E_r (Pa)	AC240TSA	$4.23\times10^{8} \pm 2.86\times10^{8}$	$3.32\times10^{8} \pm 2.61\times10^{8}$
	AC160TSA	$8.22 \times10^{9} \pm 1.50 \times10^{9}$	$3.81 \times10^{9} \pm 1.70 \times10^{9}$
η (Pa s)	AC240TSA	533.91 ± 257.52	406.57 ± 304.47
	AC160TSA	$2.82 \times10^{3} \pm 534.20$	$1.61 \times10^{3} \pm 636.79$
τ_r (s)	AC240TSA	$1.73\times10^{-6} \pm 0.97\times10^{-6}$	$1.34\times10^{-6} \pm 0.18\times10^{-6}$
	AC160TSA	$4.48 \times10^{-5} \pm 8.08 \times10^{-5}$	$2.34 \times10^{-5} \pm 4.80 \times10^{-5}$
τ_c (s)	AC240TSA	$3.45\times10^{-4} \pm 5.37\times10^{-4}$	$2.10\times10^{-4} \pm 1.85\times10^{-4}$
	AC160TSA	$3.44 \times10^{-7} \pm 0.40 \times10^{-7}$	$4.29 \times10^{-7} \pm 0.32 \times10^{-7}$

The values of E', E'', and $\tan\delta$ for the SBR over a range of frequencies ($E'(f)$, $E''(f)$, and $\tan\delta(f)$) were calculated by substituting the GMM material constants in table 3.1, into equations 1.29, 1.30 and 1.31, respectively. This reconstruction of the SBR's frequency-dependent behavior is shown in figure 3.6 for AC240TSA cantilevers, and in appendix figure B.1 for AC160TSA cantilevers. Reconstructions using SLS material constants are not shown since the SBR is a GMM material.

The accuracy of reconstructed $E'(f)$, $E''(f)$, and $\tan\delta(f)$ can be assessed via comparison to PANDA and DMA control data (also shown in figure 3.6). Even though a hyperboloid indenter with adhesion is a better model of the tip/SBR interaction (figure 3.4), AM-FM AFM only uses the Hertz contact model to calculate E_2'. Therefore, AM-FM AFM reconstructions were compared to PANDA data calculated with the Hertz contact model, not the adhesive hyperboloid model. Therefore, AM-FM AFM reconstructions of $E'(f)$ and $E''(f)$ should match PANDA curves (Hertz model) at low frequencies, but should be 10-100x larger (section 3.3.2.2) than the DMA. The reconstructed $\tan\delta(f)$ should match both PANDA and DMA data.

The estimated value of E_c agrees with PANDA well. However, as previously

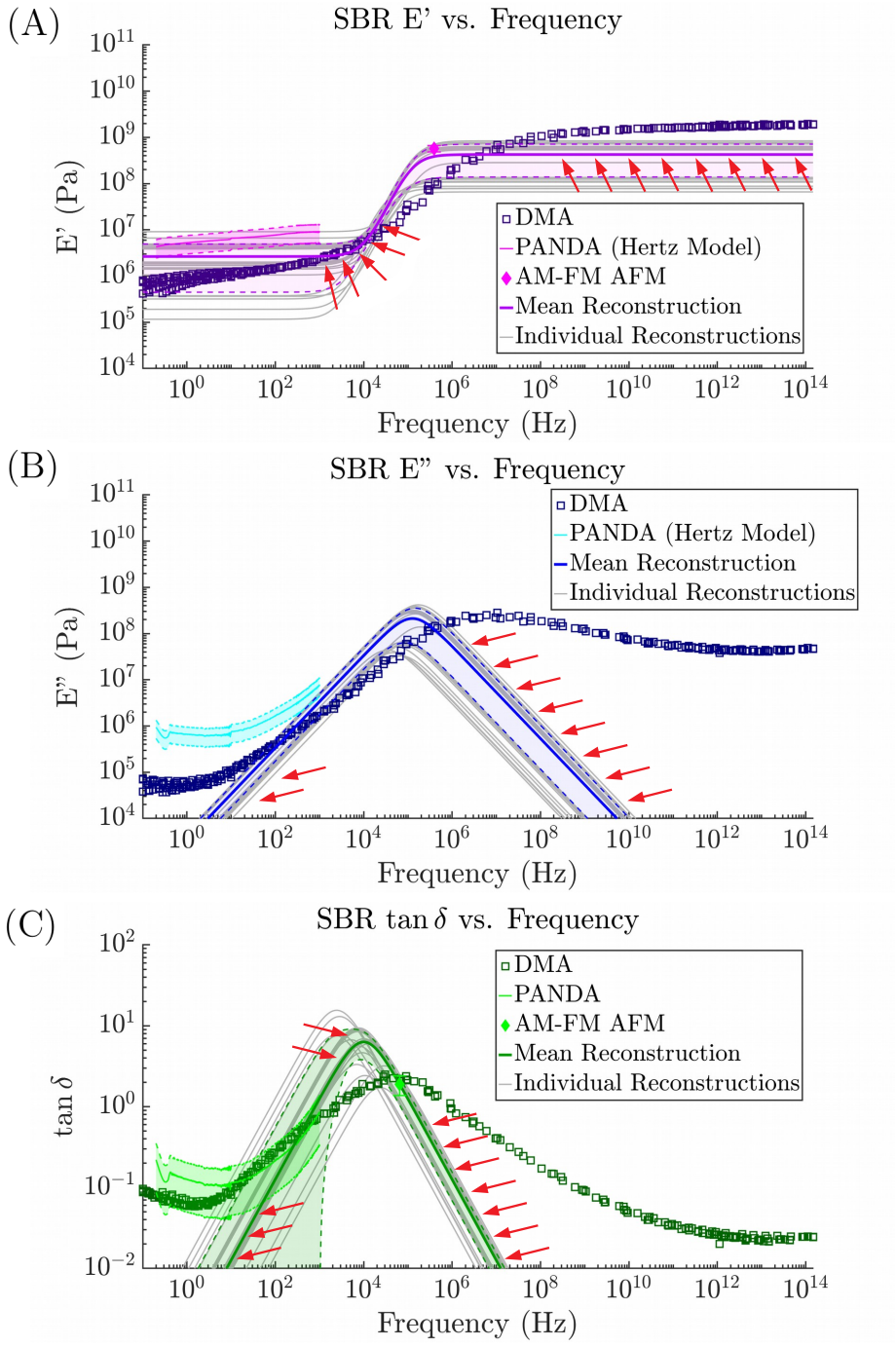


Figure 3.6: Frequency dependent behavior of the SBR (AC240TSA). Storage moduli (E'), loss moduli (E''), and loss tangents ($\tan\delta$) over a range of frequencies are shown in (A), (B), and (C), respectively. Mean AM-FM AFM reconstructions are compared to control DMA (squares) and PANDA measurements. AM-FM AFM reconstructions from each of the 25 individual AM-FM AFM images are also shown in gray. Red arrows indicate regions where the reconstruction deviates from the controls by failing to account for all arms in the GMM. PANDA E' and E'' were calculated using the Hertz contact model. PANDA and AM-FM AFM were performed using an AC240TSA cantilever. Error bars and shading represent the standard deviation.

described (section 3.3.2.2), both the estimated E_c and PANDA results are higher than the DMA values because both PANDA and AM-FM AFM employ the Hertz contact model.

Red arrows in figure 3.6 (A) indicate frequencies where the reconstruction of $E'(f)$ deviates from the control. There are two main regions where the reconstruction does not accurately predict E'. First (i) is the transition between the low frequency and high frequency plateaus of E' (the glass transition of the SBR [175], section 1.3.7), which occurs between 10^2 - 10^8 Hz in the DMA. Second (ii) is the glassy plateau (section 1.3.7) [175] of E' ($> 10^9$ Hz in the DMA).

(i) For the glass transition [175], DMA shows that SBR E' transitions gradually (between 10^2 - 10^8 Hz) from the low frequency to the high frequency plateau. The transition in the reconstruction is sharper (ranges only between 10^4 - 10^6 Hz) and underestimates E' between 10^2-10^4 Hz. These observations suggest that the glass transition of the SBR results from a sum of the various contributions of multiple different τ_n of different orders of magnitude (i.e. ns, μs, ms, etc...). This sum results in a broad glass transition, as expected for a GMM [169]. Since the AM-FM AFM reconstruction only uses a single τ_n, the transition is much sharper than the reality. Therefore, these results suggest that GMM arms in the subgroup that contribute to the SBR's response to AM-FM AFM are only part of the subgroup of arms that contributes to the SBR's glass transition.

(ii) For the glassy plateau [175] of the SBR, the reconstruction underestimates $E'(f)$. Again, this observation suggests that GMM arms that contribute most to this plateau are not part of the subgroup that dictates the SBR's response to AM-FM AFM stimulus. This observation is not surprising, since the microsecond τ_n that dictate the SBR's response to AM-FM AFM stimulus would respond too slowly to affect the SBR's response to higher frequency stimuli ($f > 10^7$ Hz).

As shown in figure 3.6 (B), the reconstructed $E''(f)$ aligns well with PANDA results between 10^3 - 10^6 Hz. As expected, the value of E'' calculated by PANDA and the reconstruction is higher than that of the DMA due to the use of the Hertz contact model (as already discussed section 3.3.2.2). For frequencies outside of this 10^3 - 10^6 Hz range, E'' is underestimated by the reconstruction (indicated by red arrows in figure 3.6 (B)). This observation is a byproduct of using the SLS to approximate the GMM for the reconstruction. For the SLS, $N = 1$, and E'' simply increases to a peak (for frequencies near the glass transition of the sample), then decreases again (equation 1.30). For a GMM, E'' can have a broader peak due to contributions from the additional τ_n [169]. Therefore, it is not surprising that $E''(f)$ is not adequately reconstructed for frequencies too slow or too fast for the subgroup of GMM arms that respond to AM-FM AFM stimulus.

In general, the reconstructed $\tan\delta(f)$ overlaps with the PANDA and DMA controls, and deviates from PANDA and DMA results when the reconstructed E' and E'' do so as well (figure 3.6 (C)). Specifically, reconstructed $\tan\delta$ matches the controls well between 10^2 - 10^3 Hz, and again between 10^4 - 10^6 Hz. The lack of agreement between the reconstructed $\tan\delta$ and controls at 10^3 - 10^4 Hz is due to the reconstruction's inability to capture the glass transition between the low and high frequency plateaus in E'. The discrepancies between reconstruction $\tan\delta(f)$ and the controls at frequencies larger than 10^6 Hz, or smaller than 10^2 Hz are due to the reconstruction's inability to accurately model $E''(f)$.

Reconstructions performed with an AC160TSA (figure B.1) showed similar results. However, estimation of the transition in E' was more accurate, and therefore the reconstructed $\tan\delta$ was more accurate (although not perfect) between 10^5 and 10^6 Hz. Additionally, the reconstructed E_c was higher than that of the AC240TSA. This observation suggests that the accuracy of the reconstruction may vary, depending on where f_1 and f_2 occur relative to the glass transition. Based on the DMA, the SBR's

glass transition was between 10^4 and 10^6 Hz. For the AC240TSA, f_1 and f_2 were in this transition. For the AC160TSA, f_1 and f_2 occurred toward the end of the transition. These results suggest that the reconstruction may be better at predicting lower frequency behaviors of a sample when f_1 and f_2 are lower than or inside the glass transition. If f_1 and f_2 are higher than the glass transition, the reconstruction may be better at predicting glass transition and high frequency behavior. In the future, it would be interesting to test this hypothesis with additional cantilevers that have f_1 and f_2 at different frequencies relative to the glass transition of the sample.

Together, these results suggest that AM-FM AFM data can be used to perform limited reconstructions of a GMM sample's frequency dependent $E'(f)$, $E''(f)$, and $\tan\delta(f)$. For the most-accurate measurement of a sample's frequency dependent behavior, it is best to combine AM-FM AFM data with other techniques like PANDA, rather than rely only on the reconstruction of $E'(f)$ and $E''(f)$ from AM-FM AFM data. However, these results suggest that AM-FM AFM reconstructions can capture important quantities of a sample's frequency dependent behavior, especially for frequencies near f_1 and f_2. At the bare minimum, the reconstruction allows for fairly-accurate estimation of E', E'', and $\tan\delta$ at the two frequencies used in AM-FM AFM and can be used to predict E_c, and hence the crosslink density of a sample (equation 1.47, section 1.3.7). In the future, it would be interesting to derive a method of estimating N from AM-FM AFM data, possibly by comparing observations made with several cantilevers with different resonance frequencies.

3.4 Conclusions

In summary, AM-FM AFM can be performed on samples to accurately quantify $\tan\delta_1$ and E_2' of the sample (within the limits of AM-FM AFM discussed section 2.1.3.4.1), even without first calibrating the tip on a sample of known modulus (sections 3.1 and

3.3.2.2). If the tip radius is not calibrated, the additional uncertainty in E_2' should be taken into account. Additionally, there may be no indicator if the Hertz contact model does not apply unless AM-FM AFM is performed together with other types of experiments such as PANDA or DMA. Regardless of tip calibration or lack thereof, the measured E_2' can be incorrect if the Hertz contact model, on which AM-FM AFM calculation of E_2' relies, is not a good model for the tip/sample interaction. Still, this error will occur regardless of whether or not the user knows the Hertz model is not a good model for the tip/sample contact, because AM-FM AFM calculation of E_2' relies on the Hertz contact model [221, 225]. In the future, it would be prudent to expand (as already done for the DMT model and the Lennard-Jones potential via fractional calculus [225]) the calculation of E_2' in AM-FM AFM to include other contact models like the JKR model and the adhesive hyperboloid.

Additionally, the new analysis developed in this chapter can be used on AM-FM AFM data to extract information about the sample's viscoelastic response. First, $\tan\delta_1$ and E_2' can be used to test whether the sample obeys any of the standard models of linear viscoelasticity (MW, KV, SLS, and GMM), and distinguish between each model (section 3.2.1 and 3.3.2.3). Once the best model for a sample's viscoelastic response is known, model parameters can then be calculated, and the frequency dependent behavior of a sample's $E'(f)$, $E''(f)$, and $\tan\delta(f)$ can be reconstructed.

Accuracy of the reconstruction is limited if the sample is a GMM, but can, at the bare minimum, predict E_1', $\tan\delta_2$, and E_c of the sample from the measured $\tan\delta_1$ and E_2'. For the most accurate measurement of $E'(f)$, $E''(f)$, and $\tan\delta(f)$, it is best to combine AM-FM AFM with other techniques like PANDA, rather than rely solely on the reconstruction. Still, future AM-FM AFM experiments can use the analysis developed in this chapter to gain additional insight into a sample's viscoelastic behavior from AM-FM AFM data. This new analytical method is employed in chapters 4, 5, and 6 to study the viscoelastic properties of *in vitro* ECMs and substrates.

Chapter 4

Mechanoelectric Coupling in the ECM: Effect of Electrostatics and Ion Flow on Collagen I Mechanical Properties

4.1 Introduction

The extracellular matrix (ECM) is a complex polymeric scaffold, constructed from a diverse array of molecules, that maintains the structure of tissues (section 1.1). The mechanical properties of the ECM are important in determining cell behaviors [1, 3, 5–8]. Additionally, the mechanical properties of the ECM are coupled to its electrical (and other) properties [78, 79, 83, 87–92]. A common form of this mechano-electric coupling in the molecules of the ECM is piezoelectricity (section 1.2.1.1), where applied voltages generate a strain, and applied strains generate a voltage [157].

Collagen is one of the most-prevalent components of the ECM, is piezoelectric [88, 154–156], and accounts for 30% - 40% of all protein in the human body [130].

Collagen I is one of the key fibrillar proteins in the ECM, is the most-common form of collagen, and plays a prominent role in dictating ECM architecture [131, 132, 135, 229]. The complexity of the ECM is often simplified *in vitro* by using matrices constructed only of collagen I [7, 9, 22, 27, 133–136, 229]. Collagen and collagen matrices are viscoelastic, and behave as a standard linear solid (SLS, section 1.3.4) or, more commonly, a general Maxwell material (GMM, section 1.3.6) [170, 188–193].

In tissues, collagen I structures are hierarchical, and span length scales from nanometers (a single collagen monomer) to meters (i.e. skin) [131, 132, 135]. The collagen monomer is known as tropocollagen [131, 132, 135]. Tropocollagen consists of three polypeptide chains that twist around each other, and is a few nanometers in diameter and several hundred nanometers in length [131, 132, 135]. Tropocollagen molecules assemble spontaneously with regularly-staggered ends to form fibrils (a few nanometers in diameter and a few micrometers long) [131, 132, 135, 230]. The staggering of molecules within the fibril gives rise to a repeating structure 67 nanometers in size, called a D-band [131, 132, 135]. These D-banded fibrils assemble into fibers (microns to millimeters in diameter and millimeters long) that dictate many elements of tissue architecture [21–23] and mechanics [24]. This spontaneous formation of hierarchical structures is called self-assembly [230].

The mechanism of collagen self-assembly is still not fully understood because the self-assembly process is dictated by complex interactions between tropocollagen molecules. These interactions include crosslinks and electrostatic correlations between tropocollagen molecules, both of which are influenced by extracellular ion concentration [132, 231, 232] and tropocollagen's hydration shell [170, 233, 234]. Of these factors, the hydration shell of tropocollagen is particularly important in tropocollagen self-assembly [170, 233, 234]. Additionally, collagen and collagen I are piezoelectric (section 1.2.1.1). Therefore collagen I's mechanical properties pre- or post-polymerization, and self-assembly are likely affected by applied voltages.

Since collagen is piezoelectric, and since its polymerization and self-assembly depend on electrostatic correlations, it is reasonable to hypothesize that electrostatics and applied voltages alter the mechanical properties of collagen structures. In this case "electrostatics" refers to the interactions between collagen and surrounding ions from salts. In particular, the ionic strength, I, a measure of ion concentration in the solution surrounding the collagen (section 1.2.2.1.3, equation 1.9), likely affects tropocollagen self-assembly and the mechanical properties of the resulting fibrils. Increasing I is hypothesized to weaken intermolecular interactions between tropocollagen molecules [231, 235–237], and has been shown to increase the storage modulus, E', of collagen at the nanoscale [131, 238–240] and macroscale [237, 241], and increase the loss modulus, E'', of collagen at the macroscale [235]. Details on E' and E'' can be found in section 1.3.3.3. It remains unclear how time responses of collagen fibrils vary with ionic strength at the nanoscale.

The purpose of the experiments presented in this chapter is to study mechanoelectric coupling in collagen I at the nanoscale. Experiments presented in this chapter used amplitude modulation-frequency modulation atomic force microscopy (AM-FM AFM, section 2.1.3.4, figure 2.3 (C)) to quantify the role of electrostatics and applied voltages in modulating the nanoscale mechanical properties of collagen I. Specifically, the storage modulus (E') and loss tangent ($\tan\delta$) of collagen I in various conditions were measured via AM-FM AFM. Collagen I was then modeled as a GMM in order to calculate collagen's elastic constants (E_c and E_r), viscosity (η), and time responses ($\tau_r = \eta/E_r$ and $\tau_c = \eta/E_c$) by applying the analysis method described in section 3.2. Two main experiments are presented in this chapter. The first investigates the role of I in modulating collagen I polymerization and nanoscale mechanics (section 4.2). The second investigates how flowing ions (applying a voltage via physiologically-relevant mechanism [64]) alters the nanoscale mechanics of collagen I (section 4.3).

4.2 Effect of electrostatics (ion concentration) on collagen viscoelasticity

4.2.1 Materials and methods

The effect of electrostatics on the mechanical properties of collagen I was studied by varying I of the solution in which the collagen was polymerized and imaged. The solution used in these experiments was phosphate buffered saline (PBS), in order to mimic the ionic environment of the human body. PBS concentration was altered in order to change I of the solution. In this chapter, PBS solutions are written as factors of physiological ion concentrations. For example 4x PBS has four times the physiological ion concentrations, and 0x PBS refers to ultraPure milliQ water.

A solution of 1x PBS matches physiological ion concentrations, and consists of: 137 mM NaCl (Thermo Fisher 10428420), 2.7 mM KCl (Sigma-Aldrich P3911), 10 mM Na_2HPO_4 (Sigma-Aldrich 71640), and 1.8 mM KH_2PO_4 (Sigma-Aldrich P0662) [242]. An additional buffer called 4-(2-hydroxyethyl)-1-piperazineethanesulfonic acid (HEPES, Sigma-Aldrich H3375) was also added to the PBS at a concentration of 16 mM in 1x PBS in order to ensure that the pH remained at 7.4 (physiological) even for low PBS concentrations. HEPES is a standard buffer in cell culture, and has a formal charge of zero at pH 7.4 [243]. The formal charge of zero means that HEPES does not contribute to I of the PBS [243].

A single stock solution of 10x PBS was prepared, then diluted in milliQ water to the desired concentration (0.05x, 0.5x, 1x, 2x, or 4x) for each experiment. With the additional control of 0x PBS, six different I were tested in total. The ion concentrations in these six solutions are shown in table 4.1.

Collagen samples were prepared on ice by diluting a collagen stock solution with various amounts of 10x PBS and milliQ water, resulting in a 20 μL solution of

Table 4.1: Ion properties of different phosphate buffered saline (PBS) solutions

	0x PBS (Water)	0.05x PBS	0.5x PBS	1x PBS (Physiological)	2x PBS	4x PBS
Na^+ (mM)	0	2.1	2.05	41.1	82.1	164.2
K^+ (mM)	0	0.10	1.0	1.9	3.9	7.7
Cl^- (mM)	0	5.0	4.97	99.5	199.0	397.9
$H_2PO_4^-$ (mM)	0	0.10	0.6	1.3	2.6	5.1
HPO_4^{2-} (mM)	0	0.4	3.9	7.7	15.5	31.0
HEPES (mM)	0	0.8	8.0	16.0	32.0	64.0
H^+ (mM) (from water)	1×10^{-7}	4×10^{-5}	4×10^{-5}	4×10^{-5}	4×10^{-5}	4×10^{-5}
OH^- (mM) (from water)	1×10^{-7}	2.5×10^{-4}	2.5×10^{-4}	2.5×10^{-4}	2.5×10^{-4}	2.5×10^{-4}
Ionic Strength (mM) (equation 1.9)	1×10^{-7}	4.4	43.7	87.4	174.7	349.4
Debye Length (nm) (equation 1.10)	31 μm	4.6	1.5	1.0	0.73	0.52

tropocollagen in the desired PBS concentration (0x, 0.05x, 0.5x, 1x, 2x, or 4x PBS) at pH 7.4. Both "sparse" tropocollagen solutions, with 0.02 mg collagen per mL (section 4.2.2), and "concentrated" solutions, with 0.20 mg collagen per mL (section 4.2.3), were studied. The collagen stock solution was prepared by diluting 3 mg human collagen I (Sigma-Aldrich C5483) in 10% acetic acid (Thermo Fisher 10384970) to a final concentration of 4 mM, and stored at 4 ^{o}C.

Sparse or concentrated mixtures (20 μL drops) of tropocollagen in PBS were deposited onto a freshly cleaved mica disk. The sample was placed in a humid chamber to prevent drying out, then left to polymerize at 37 ^{o}C for one hour. After polymerizing, the sample was moved to an Oxford Instruments Asylum Research Cypher ES AFM, and 200 μL of additional PBS, the same solution used for sample polymerization, were added to prevent the sample from drying. AM-FM AFM imaging was performed using the short, thin tip of an RC800PSA cantilever ($k_{c,1} \sim 0.2$ N/m, $k_{c,2} \sim 18$ N/m, $f_{c,1} \sim 25$ kHz in liquid, $f_{c,2} \sim 170$ kHz in liquid, $R \sim 15$ nm $\pm$ 5 nm) driven by photothermal excitation (section 2.1.3.1) at 0.3x blueDrive^{TM} power. The cantilever was calibrated via the Oxford Instruments Asylum Research GetReal^{TM} calibration method (section 2.1.1) to avoid blunting the tip. Experiments were performed in Ox-

ford Instruments Asylum Research software version 16.9.220 and 15.09.112 with Igor Pro software version 6.38B01 and 6.37, respectively. AM-FM AFM imaging (section 2.1.3.4) was performed on multiple spots in at least three different positions on each sample. At least two biological replicates of each sample were measured. It was not possible to perform indentations (section 2.1.3.2) or PANDA (section 2.1.3.3) on the sample because the collagen layer was too thin.

After the experiment, height images of the resulting AM-FM AFM data were flattened using Oxford Instruments Asylum Research software version 16.10.208 in Igor Pro software version 6.38B01, in order to remove any variations in sample topology that weren't due to collagen. This flattening was done by hand, to avoid introducing flattening artifacts. The processed files were then analyzed by a custom script written in MATLAB R2019b 9.7.0.1261785. This custom script calculated $\tan\delta$ and E' of the sample (equations 2.21 and 2.24, section 2.1.3.4), then calculated E_c, E_r, η, $\tau_r = \eta/E_r$, and $\tau_c = \eta/E_c$ of the sample, by applying the analysis described in chapter 3, section 3.2. The custom script calculated the mean and standard deviation of fibril height, E', and $\tan\delta$ by fitting a Gaussian to the distribution of values within a particular biological replicate or within the sample as a whole, as described in section 2.1.3.4.2. This method of calculating the mean and standard deviation was used in order to minimize the effects of bimodal or multimodal distributions of the data. Example measurement distributions that demonstrate the necessity of calculating the mean and standard deviation in this manner are shown in appendix section C.1. The mean and standard deviation of the remaining quantities were calculated in the usual manner (not a Gaussian fit). For comparisons, p values were calculated by paired t-tests if only two samples were compared, or by linear regression if more than two samples were compared.

4.2.2 AM-FM AFM of sparse collagen in different PBS concentrations

Collagen I was polymerized and imaged via AM-FM AFM in six different PBS concentrations that had 0x, 0.05x, 0.5x, 1x, 2x, and 4x the average physiological extracellular ionic strength (I), at a sparse concentration of 0.02 mg collagen I per mL PBS.

4.2.2.1 Topology, storage moduli, and loss tangents

Representative AM-FM AFM images of sparse collagen I samples in the six different PBS solutions are shown in figure 4.1. Aligned collagen fibrils formed in 0.5x - 4x PBS solutions. D-bands were visible on fibrils in 1x and 2x PBS. Collagen fibrils formed in 0.05x PBS, but tangled onto themselves rather than aligning. In water (0x PBS), collagen did not polymerize into fibrils. It is already known that aligned fibrils of any polymer are more likely to form in solutions of higher I [162]. Higher I renders interactions between monomers (such as tropocollagen) and ions or water molecules more energetically favorable than monomer-monomer interactions [162]. Therefore, the resulting polymers in solutions of higher I are less likely to tangle on themselves or clump together [162].

Also shown in figure 4.1, it was possible to observe the underlying mica (section 4.2.1) underneath the collagen. Since mica is much stiffer than the tip, any AM-FM AFM measurements corresponding to mica pixels quantify tip motion rather than sample properties. Therefore, it was necessary to threshold out the mica, in order to ensure that the measured height, E', and $\tan\delta$ belonged only to collagen. This thresholding was accomplished as follows. For each image, the mean and standard deviation of the height of all pixels was calculated (in the usual manner, not via a Gaussian). Only pixels with heights above the calculated mean + standard deviation were considered to be collagen. Representative images of this threshold are shown in figure 4.2. Occasionally this thresholding method erroneously identified mica or

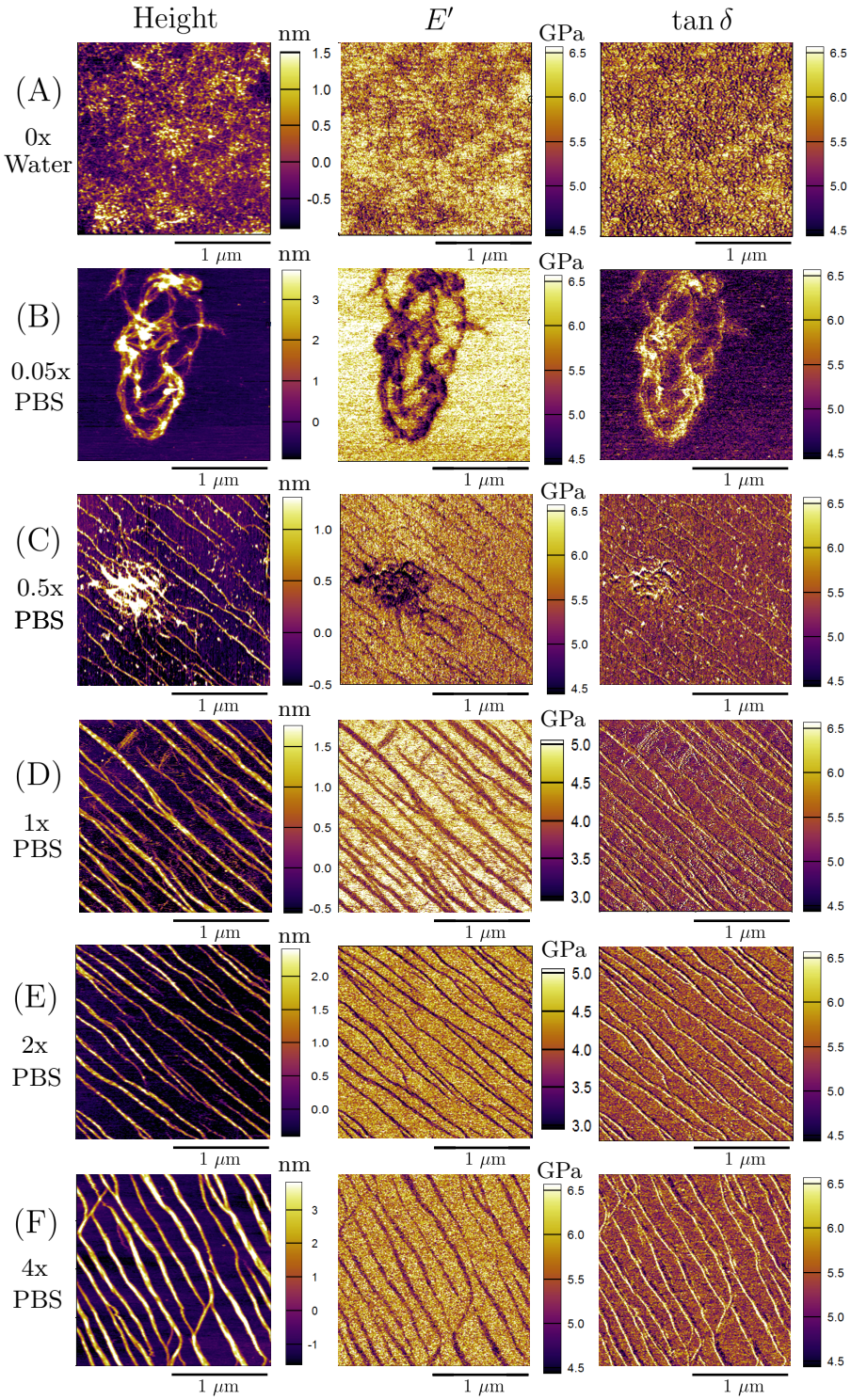


Figure 4.1: Representative AM-FM AFM images of sparse collagen samples, polymerized at 0.02 mg collagen per mL PBS in different PBS solutions. Sample height is shown in the left column, storage modulus, E', in the middle column, and loss tangent, $\tan\delta$, in the right column. Each row represents a different PBS concentration. Collagen in PBS solutions with 0x (water), 0.05x, 0.5x, 1x, 2x, or 4x physiological extracellular ion concentrations are shown in (A)-(F), respectively.

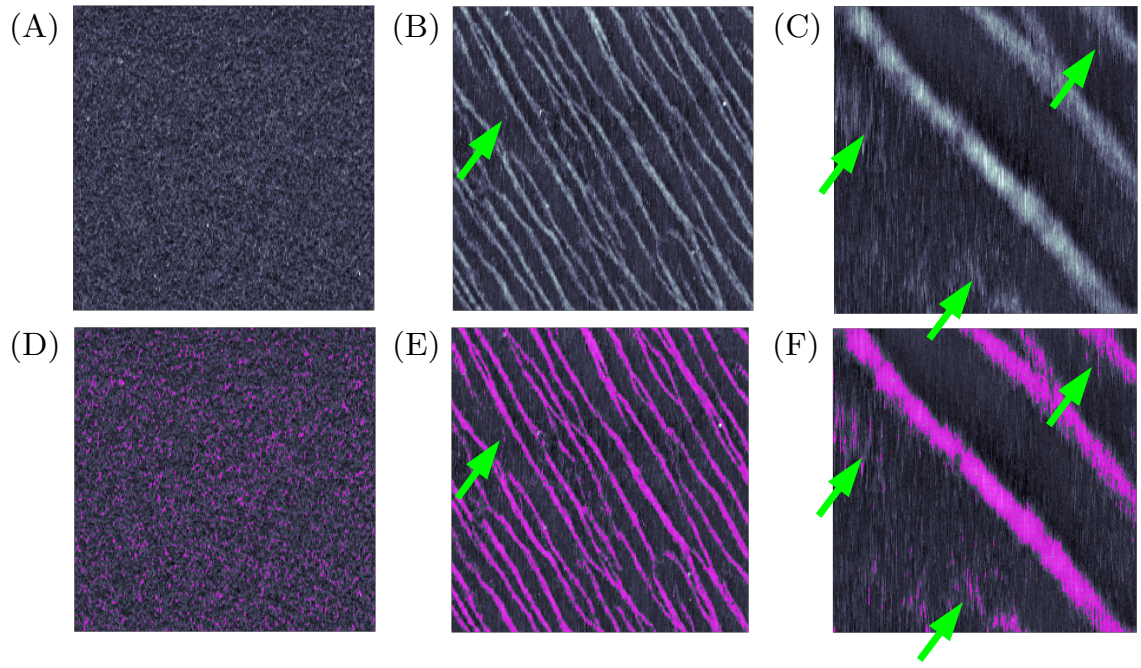


Figure 4.2: Distinguishing between mica and collagen. It was necessary to threshold out the mica underneath collagen samples in order to ensure that only pixels belonging to collagen were analyzed. Thresholds were based on the height value of each pixel. Example height images from a 2 μm x 2 μm scan are shown of collagen in water (A), and in 1x PBS (B). A zoomed image (500 nm x 500 nm) of collagen in 1x PBS is shown in (C). Pixels identified as collagen via the height threshold are colored magenta in (D)-(E). Green arrows indicate areas where the threshold mistakenly identified mica, or debris on the mica, as collagen.

debris on the mica as collagen (green arrows of figure 4.2). However, this height-based threshold still eliminates most of the mica from consideration. While the height-based threshold works to identify collagen, it would be useful to improve the thresholding algorithm in the future.

The mean feature height $\pm$ standard deviation calculated from all samples was 2.60 $\pm$ 0.65 nm. Since the diameter of a single collagen fibril is 1.5 nm [131, 132, 135], these results suggest that sparse samples were a single fibril deep. Figure 4.3 (A) shows the mean heights of collagen samples in each PBS solution. The height of collagen fibrils increased in 0.05x PBS to 4x PBS ($p = 0.05$). Biological replicates had more variability in water and 0.05x PBS due to different sizes of the collagen

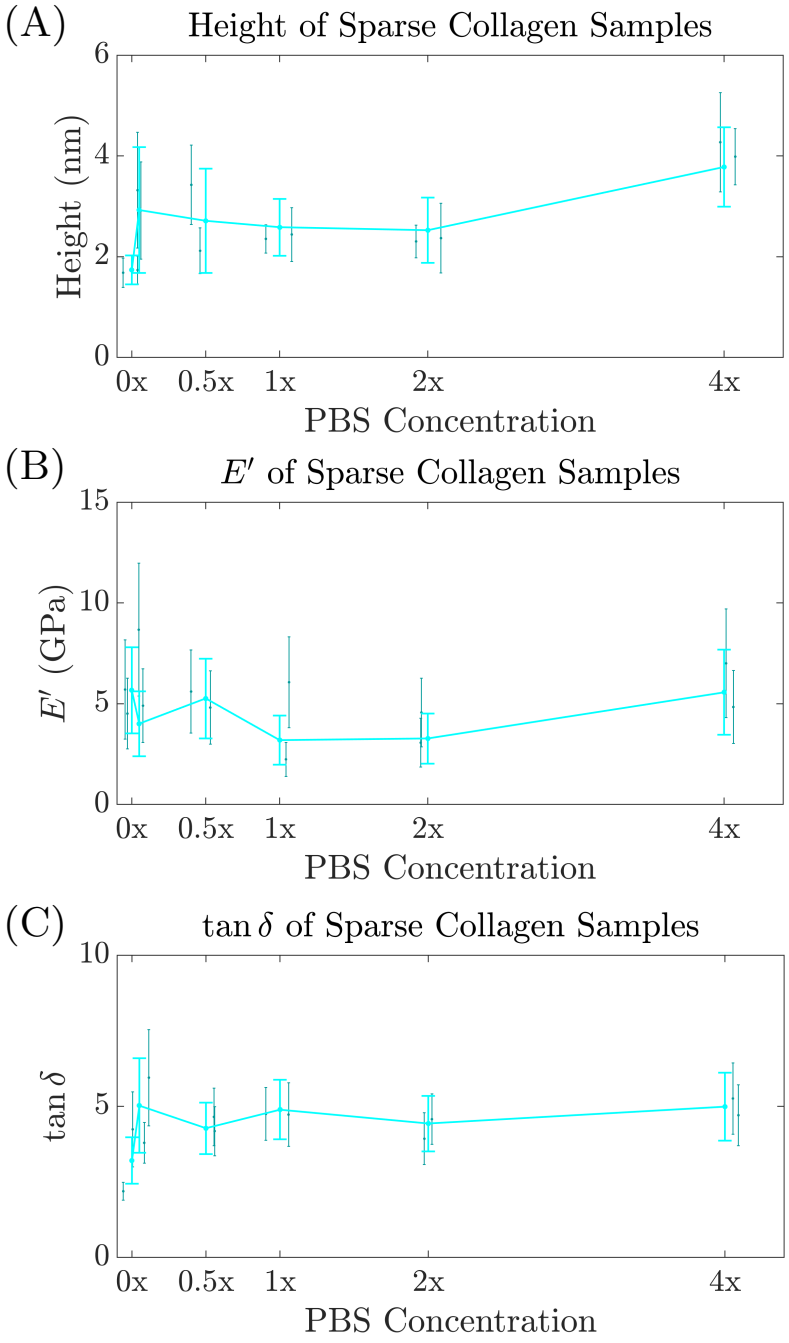


Figure 4.3: Effect of PBS concentration on sparse sample height, E', and $\tan\delta$. The effects of PBS concentration on collagen height (A), storage modulus, E' (B), and loss tangent, $\tan\delta$ (C) are shown. Larger points connected by lines represent overall mean values, calculated from all measured pixels. Smaller points represent mean values of individual biological replicates, calculated from all measured pixels within a particular replicate. Error bars represent the standard deviation.

tangles and clumps present in these samples (figure 4.1).

Figure 4.3 (B) shows the mean storage modulus, E', of collagen in each PBS concentration. In general E' was constant for collagen in water, 0.05x PBS, and 0.5x PBS ($p = 0.89$). E' decreased from 0.5x PBS to 1x PBS ($p = 0.03$), then increased in 1x PBS to 4x PBS ($p = 0.05$). Figure 4.3 (C) shows the mean loss tangent, $\tan\delta$, of collagen in each PBS concentration. The value of $\tan\delta$ remained constant at a mean $\pm$ standard deviation of 3.40 $\pm$ 0.74 for all sparse samples ($p = 0.38$). Since $\tan\delta = E''/E'$, these results together suggest that collagen fibrils increase both energy storage and dissipation as PBS concentration increases.

4.2.2.2 Viscoelastic material constants

Material constants of each sample were calculated in order to further study the effects of I on the mechanical properties of collagen. To this end, the analysis developed in section 3.2 was applied. First, the model test line (equation 3.11, section 3.2.1) was fit to AM-FM AFM E' and $\tan\delta$ in order to determine if sparse collagen samples were MW, KV, SLS, or GMM materials. Example model tests are shown in figure 4.4. The mean $\pm$ standard deviation R^2 value of the model test fit was calculated from the fits on each individual AM-FM AFM image, and was 0.50 $\pm$ 0.17 for samples in water, 0.31 $\pm$ 0.35 for samples in 0.05x PBS, 0.65 $\pm$ 0.15 for samples in 0.5x PBS, 0.59 $\pm$ 0.20 for samples in 1x PBS, 0.61 $\pm$ 0.15 for samples in 2x PBS, and 0.46 $\pm$ 0.17 for samples in 4x PBS. The R^2 values of the fits are low, but not unreasonably so for biological samples. Additionally, based on the thresholding results in figure 4.2, it is possible that the imperfect removal of mica pixels could be adding noise to the data and thereby interfering with the fit. Bearing this in mind, the fits suggest that sparse collagen samples can be modeled as linear viscoelastic materials.

Both the slope and y-intercept of model test lines for each sample were greater than zero (not shown). Therefore, sparse samples can be modeled with the GMM or

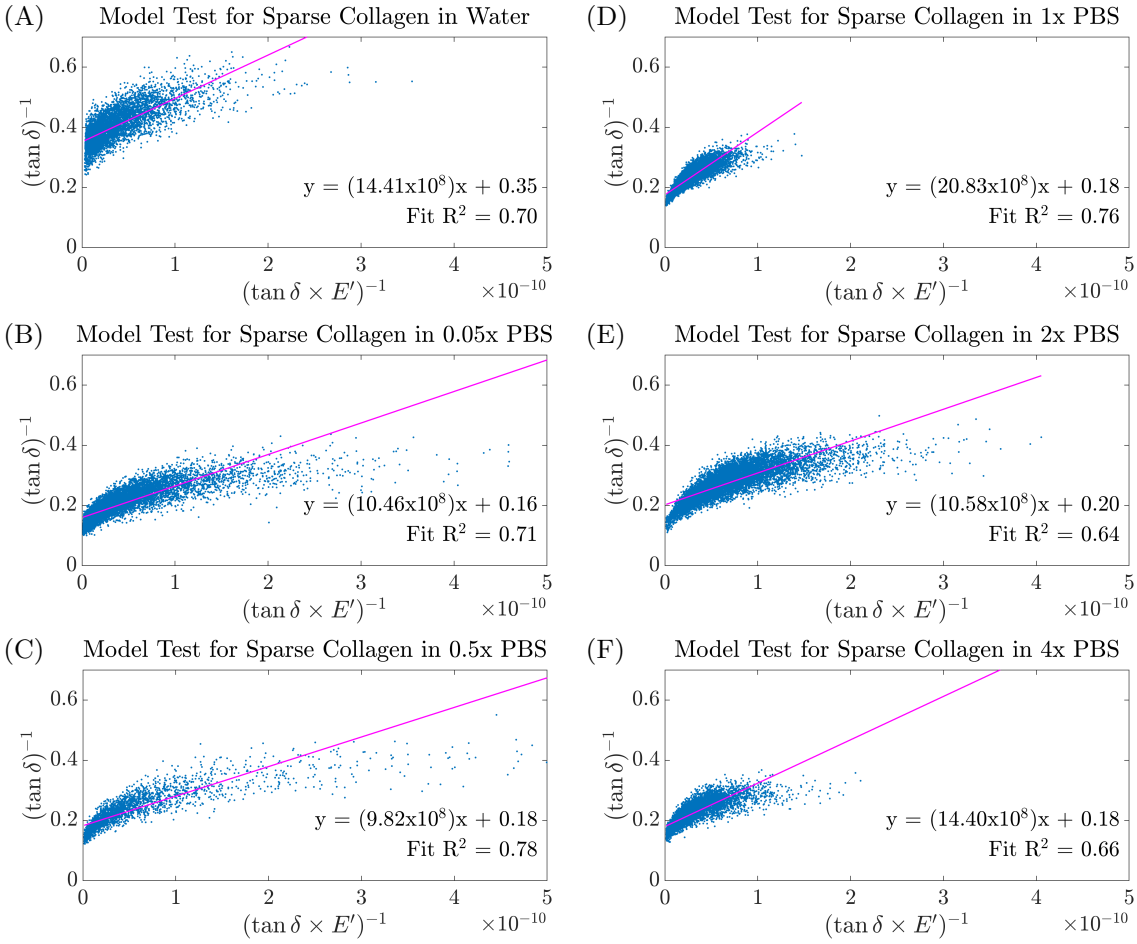


Figure 4.4: Example model tests for sparse collagen samples. Model test plots (equation 3.11) for sparse collagen samples in water (0x PBS), 0.05x PBS, 0.5x PBS, 1x PBS (physiological), 2x PBS, and 4x PBS are shown in (A)-(F), respectively. Each test was performed on a single AM-FM AFM image of the sample. Blue dots represent the value of a single pixel. The model test is shown as a magenta line. Fit equations and R^2 values are also shown.

SLS, as expected from the literature [170, 188–193]. It is interesting to note that, as in chapter 3 (section 3.3.2.3), the model test has a hyperbolic shape. This observation suggests that sparse collagen samples are GMMs. As discussed in section 3.3.2.3, the model test of a GMM can be approximated by a line, but has a hyperbolic shape.

Next, E_c of the collagen samples was calculated as described in section 3.2.1. Collagen E_c should be on the order of hundreds of MPa in liquid [238, 240]. Calculating E_c for the SLS (via the calculations in section 3.2.1) resulted in a predicted E_c on

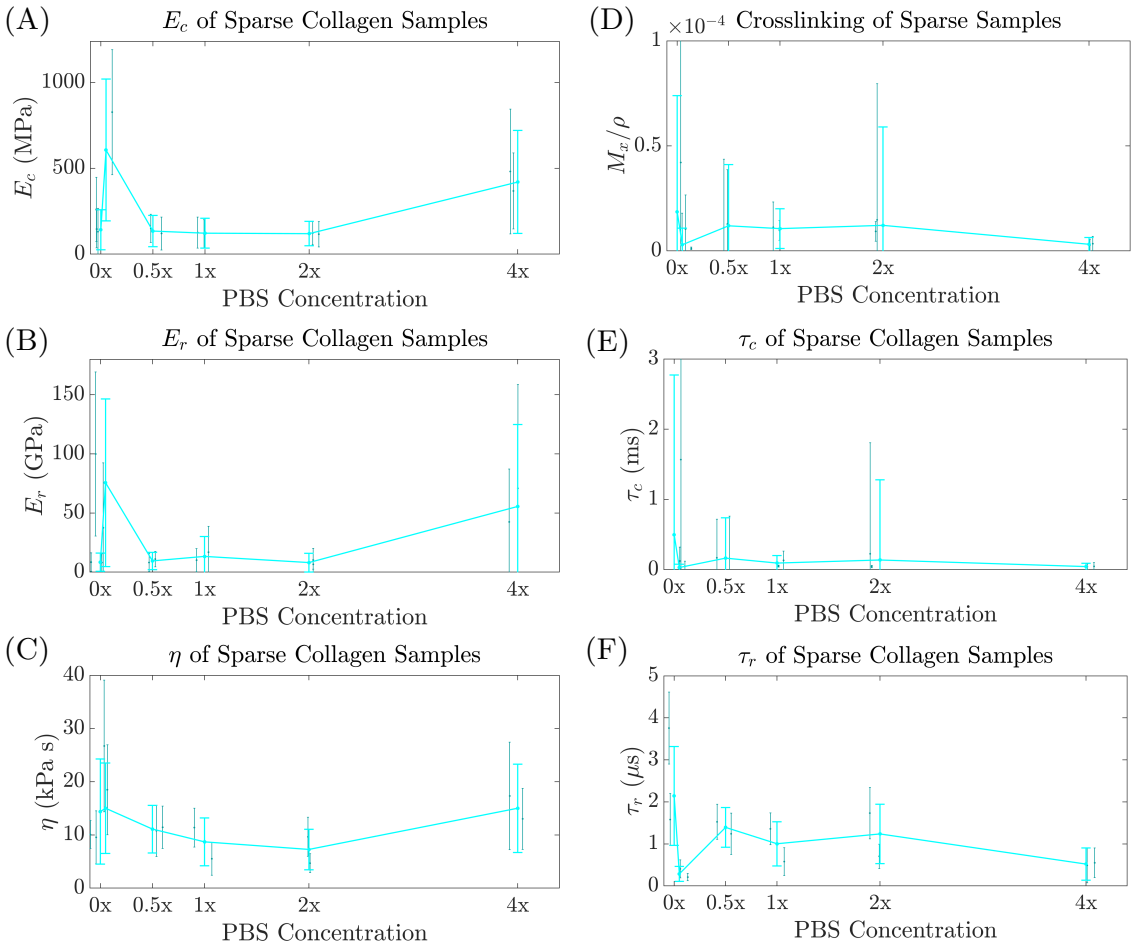


Figure 4.5: Effect of PBS concentration on sparse collagen material constants. Sparse collagen samples were modeled as general Maxwell materials, with material constants calculated as described in section 3.2.1.3 and 3.2.2.1. The effect of PBS concentration on E_c (A), E_r (B), η (C), crosslinking (D), τ_c (E), and τ_r (F) are shown. The molecular weight between crosslinks divided by the density of collagen (M_x/ρ) is the crosslink metric used in (D). Larger points connected by lines represent overall mean values of the samples, calculated from all model test lines. Smaller dots with error bars represent mean values of individual biological replicates, calculated from all model test lines within a particular replicate. Error bars represent the standard deviation.

the order of a few GPa (not shown). Estimated E_c for a GMM (via the calculations in section 3.2.1.3) agreed with the literature values, and is shown in figure 4.5 (A). This observation confirms the hypothesis that sparse samples are GMM materials. Therefore, E_r and η were calculated as described in section 3.2.2.1, and are shown in figure 4.5 (B) and (C), respectively. E_c, E_r, and η remain roughly constant for

collagen in water, 0.05x PBS, and 0.5x PBS (p = 0.72, 0.73, and 0.15, for E_c, E_r, and η, respectively). All three material constants increase between 1x PBS and 4x PBS (p = 0.04, 0.03, and 0.02 for E_c, E_r, and η, respectively). These observations confirm the hypothesis in section 4.2.2.1, that energy storage and dissipation, relating to elasticity and viscosity of collagen fibrils, by collagen fibrils change together as a result of I.

As described in section 1.3.7, insight into crosslinking within collagen molecules (that is, between tropocollagen molecules) in the various PBS solutions can be gained by applying equation 1.47 to the estimated value of E_c. Since the density ρ of collagen fibrils for these samples is unknown, applying equation 1.47 can only provide the ratio of the molecular weight of collagen between crosslinks M_x over the density of tropocollagen molecules within the sample, M_x/ρ. Figure 4.5 (D) shows the effect of PBS concentration on M_x/ρ. For samples in water, 0.05x PBS, and 0.5x PBS, M_x/ρ was constant ($p = 0.999$). The value of M_x/ρ decreased between 1x PBS and 4x PBS ($p = 0.03$). This decrease in M_x/ρ could occur as a result of (i) decreasing M_x, (ii) increasing ρ, or (iii) both. If (i) or (iii) is the case, these results suggest that the number of crosslinks between tropocollagen molecules increases with increasing PBS concentration. If (ii) or (iii) is the case, these results suggest that I modulates the packing of tropocollagen into fibrils. Further discussion of these results is saved for section 4.2.5, where mechanisms for (i)-(iii) are proposed.

The time responses, $\tau_r = \eta/E_r$ and $\tau_c = \eta/E_c$, of sparse samples were also calculated, since τs play an important role in how a cell would sense collagen I in the various PBS concentrations [15]. The effect of PBS concentration on τ_r and τ_c is shown in figure 4.5 (E) and (F). PBS concentration did not alter τ_r or τ_c (p = 0.38 and 0.44, respectively). This observation is related to the constant $\tan\delta$ of these samples. Since collagen simultaneously alters energy storage and dissipation (related to E and η) in different PBS concentrations, the resulting $\tan\delta$ and τs remain constant.

4.2.3 AM-FM of concentrated collagen in different PBS concentrations

Next, concentrated collagen I was polymerized and imaged via AM-FM AFM in six different PBS concentrations that had 0x, 0.05x, 0.5x, 1x, 2x, and 4x the average physiological extracellular ionic strength (I), at a concentration of 0.20 mg collagen I per mL PBS. Similar to sparse collagen samples (section 4.2.2), it was not possible to perform indentations or PANDA because concentrated samples were too thin (see section 2.1.3.2.1 and 2.1.3.3.1).

4.2.3.1 Topology, storage modulus, and loss tangent

Representative AM-FM AFM images of concentrated collagen I samples in the six different PBS solutions are shown in figure 4.6. Aligned collagen fibrils formed in 2x - 4x PBS. Collagen fibrils also formed in 0.05x, 0.5x, and 1x PBS, but tangled on themselves and did not align. As in the sparse samples, collagen clumped on itself in water. As with sparse samples, it is not surprising that collagen did not form fibrils in solutions of lower ionic strength. It is already known that polymers in solutions of higher I are less likely to tangle on themselves or clump together [162]. Interestingly, aligned fibrils only appeared in 2x and 4x PBS for concentrated samples, compared to 0.5x, 1x, 2x, and 4x PBS for sparse samples (figure 4.1). This observation suggests that, as the concentration of collagen increases, higher I may be required to make interactions between tropocollagen and water more favorable than tropocollagen-tropocollagen interactions.

The mica background of each image was thresholded out of analysis based on the height value of each pixel within an image, as with sparse collagen samples (figure 4.2). After this threshold was imposed, the resulting height, E', and $\tan\delta$ of pixels belonging to collagen were analyzed. The mean height $\pm$ standard deviation of concentrated samples in all six PBS solutions was 3.47 ± 0.65 nm. Since the diameter of a

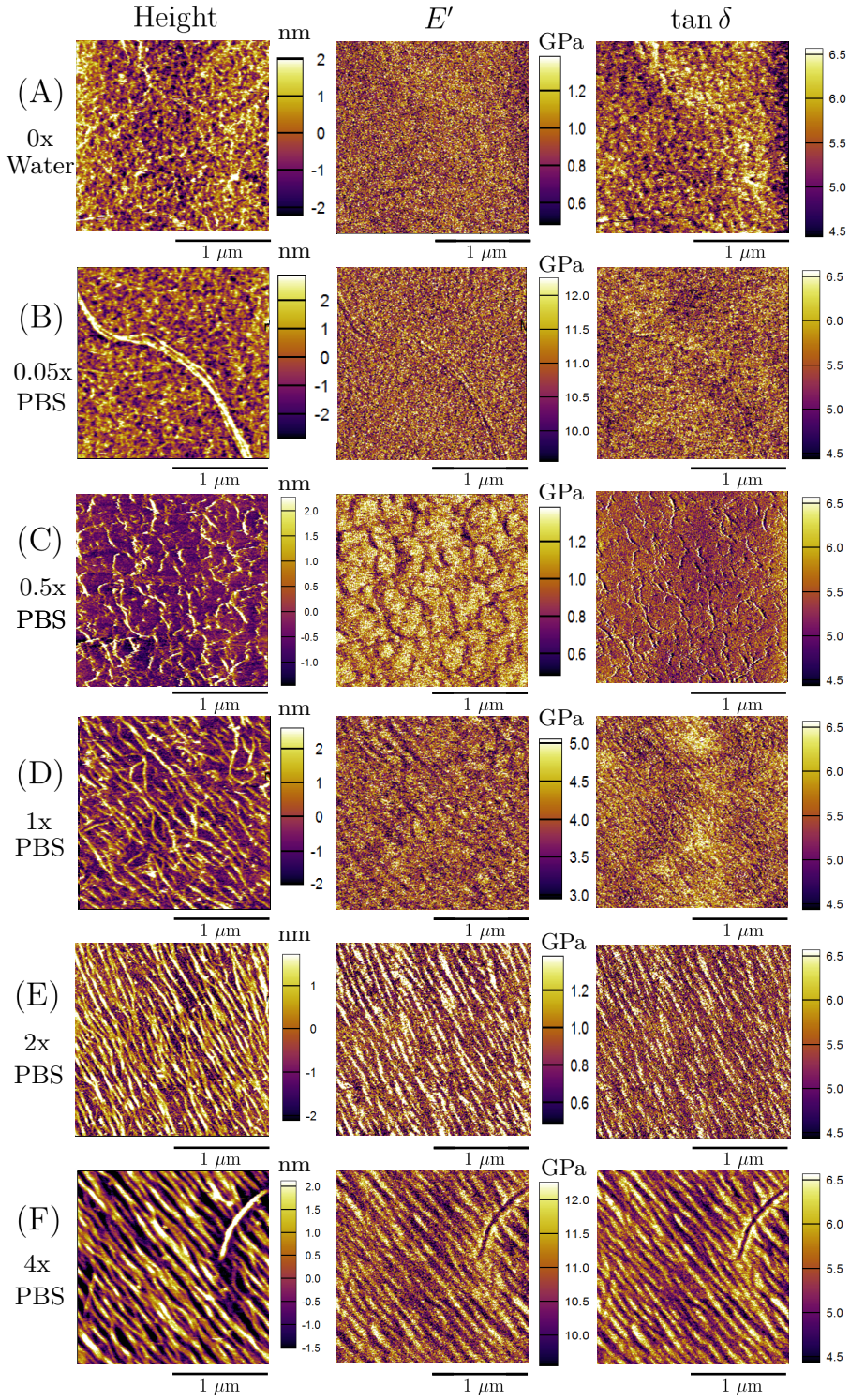


Figure 4.6: Representative AM-FM AFM images of sparse collagen samples, polymerized at 0.20 mg collagen per mL PBS in different PBS solutions. Sample height is shown in the left column, storage modulus, E', in the middle column, and loss tangent, $\tan\delta$, in the right column. Each row represents a different PBS concentration. Collagen in PBS solutions with 0x (water), 0.05x, 0.5x, 1x, 2x, or 4x physiological extracellular ion concentrations are shown in (A)-(F), respectively.

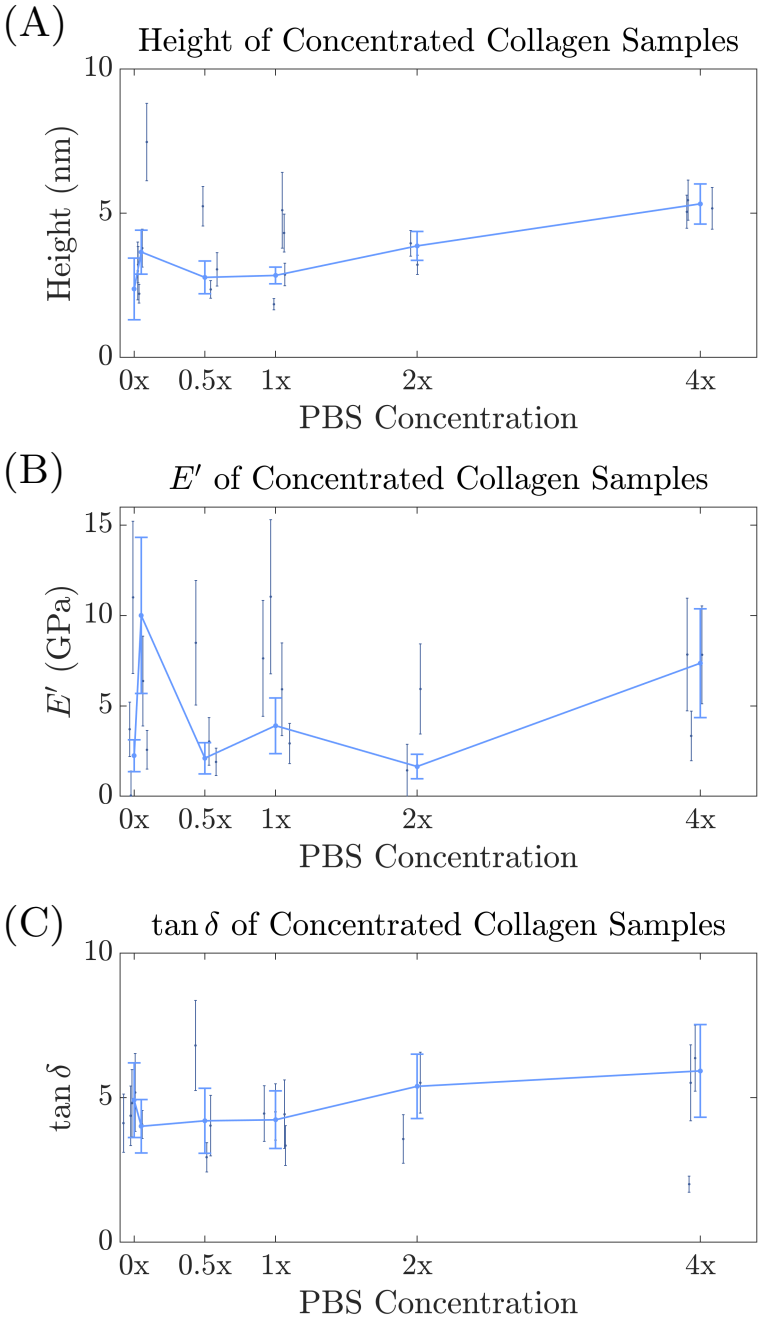


Figure 4.7: Effect of PBS concentration on concentrated sample height, E', and $\tan\delta$. The effect of PBS concentration on collagen height (A), storage modulus, E' (B), and loss tangent, $\tan\delta$ (C) are shown. Larger points connected by lines represent overall mean values, calculated from all measured pixels. Smaller dots represent mean values of individual biological replicates, calculated from all measured pixels within a particular replicate. Error bars represent the standard deviation.

single collagen fibril is 1.5 nm [131, 132, 135], these results suggest that concentrated samples were two fibrils deep.

Figure 4.7 (A) shows the mean heights of concentrated samples in each PBS solution. The height of collagen fibrils increased from 0.05x PBS to 4x PBS ($p = 0.01$), similar to sparse samples. Biological replicates had more variability in water, 0.05x, 0.5x, and 1x PBS due to the fact that collagen tangles and clumps in these samples had varying heights, as shown in figure 4.6. Again, this observation is similar to that of sparse samples (figure 4.3 (A)).

Figure 4.7 (B) shows the mean storage modulus, E', of collagen in each PBS concentration. In general E' varied more, but was not significantly different between samples in water, 0.05x PBS, 0.5x PBS, and 1x PBS ($p = 0.69$). This observation is due to the large variability between biological replicates, which depended on sample clumping and tangling, as already described. E' increased in 2x PBS to 4x PBS ($p = 0.02$). This observation is similar to sparse samples (figure 4.3 (B)), where E' did not vary in samples with clumps and tangles, but increased once aligned collagen fibrils formed in the sample. Figure 4.7 (C) shows the mean loss tangent, $\tan\delta$, of collagen in each PBS concentration. The measured $\tan\delta$ of concentrated samples was slightly higher than sparse samples ($\tan\delta$ of sparse samples was 3.40 $\pm$ 0.74, $p = 0.20$). Concentrated sample $\tan\delta$ remained constant at a mean $\pm$ standard deviation of 4.78 $\pm$ 1.17 ($p = 0.78$), similar to sparse samples (figure 4.3 (C)). As with sparse samples, these results together suggest that concentrated collagen fibrils increase both energy storage and dissipation as PBS concentration increases.

4.2.3.2 Viscoelastic material constants

Material constants of each sample were calculated in order to further study the effects of I on the mechanical properties of concentrated collagen samples. To this end, the analysis developed in section 3.2 was applied. First, the model test line (equation

3.11, section 3.2.1) was fit to AM-FM AFM E' and $\tan\delta$ in order to determine if concentrated collagen samples were MW, KV, SLS, or GMM materials. The mean $\pm$ standard deviation R^2 value of the model test fit was calculated from the fits on each individual AM-FM AFM image, and was 0.18 $\pm$ 0.22 for samples in water, 0.42 $\pm$ 0.27 for samples in 0.05x PBS, 0.15 $\pm$ 0.17 for samples in 0.5x PBS , 0.36 $\pm$ 0.29 for samples in 1x PBS, 0.04 $\pm$ 0.13 for samples in 2x PBS, and 0.14 $\pm$ 0.11 for samples in 4x PBS. The R^2 values of the fits are low. An example model test with one such low R^2 value is shown in figure 4.8 (A). The model test in figure 4.8 (A) was taken from a single AM-FM AFM image, but is representative of all images with a low R^2 value in the model test. The plot in figure 4.8 (A) suggests that, rather than concentrated collagen samples behaving as something other than a linear viscoelastic material, the bad fit of the model test line for these samples is the result of two materials being present within the sample. The linear fit breaks down because the algorithm does not recognize the different materials. In the future, it would be interesting to apply clustering algorithms to the model test plot in order to identify different materials

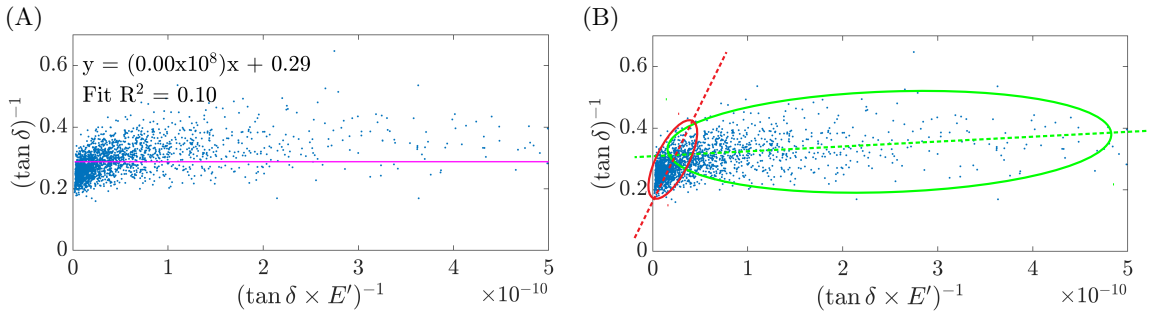


Figure 4.8: Materials within concentrated samples. An example of a model test plot (equation 3.11) with a low R^2 value is shown in (A). Blue dots represent values from individual pixels of a single AM-FM AFM image. The fit is shown as a magenta line, with the resulting equation and R^2 value displayed. The image was taken in 2x PBS but is representative of all concentrated samples with low R^2 values of the model test fit. While the R^2 value of the fit is low, this appears to be due to two types of materials being present in the sample, highlighted by the circles and lines in (B). The red circle and line indicate a SLS or GMM in the sample, because the line has a slope and y-intercept greater than zero (see section 3.2.1). The green circle and line indicate a MW material, because the slope is roughly zero (see section 3.2.1).

within a sample. Additionally, it would be helpful to expand the algorithm in order to trace back model test pixels to the original image, in order to identify exactly which features belong to each material. However, such improvement of the fitting algorithm is left to future work.

The two materials in the sample are highlighted in figure 4.8 (B). One material appears to be obey the SLS or GMM while the other appears to be a MW material. In order to investigate further into the nature of these materials, model tests with higher R^2 values than the average were studied, and plotted in figure 4.9. From these selected tests, it is likely that the SLS or GMM material is collagen, as expected from the literature [170, 188–193] and from the results with sparse samples (section 4.5).

Two possible explanations for the MW material within concentrated samples are as follows. First, the MW material may be a result of noise caused by mica, and imperfect removal of mica pixels by the height threshold. Second, the MW material could be related to collagen's hydration shell, or to ions trapped between collagen fibrils, since samples are multi layered, and roughly two fibrils deep as already discussed in section 4.2.3.1. The second possibility is addressed further in section 4.2.4 and 4.2.5.

Based on figure 4.9, collagen in concentrated samples can be modeled as a GMM or SLS, since both the slope and y-intercept of model test lines for each sample were greater than zero (not shown). Next, E_c of concentrated samples was calculated as described in section 3.2.1 for the SLS and GMM. Collagen E_c should be on the order of hundreds of MPa in liquid [238, 240]. As with sparse samples, E_c for the SLS (via the calculations in section 3.2.1) was on the order of a few GPa (not shown). Estimated E_c for a GMM (via the calculations in section 3.2.1.3) agreed with the literature values, and is shown in figure 4.10 (A). Therefore, concentrated samples are GMM materials. Concentrated sample E_c, E_r and η were calculated as described in section 3.2.2.1, and are shown in figure 4.5 (A), (B), and (C), respectively. All

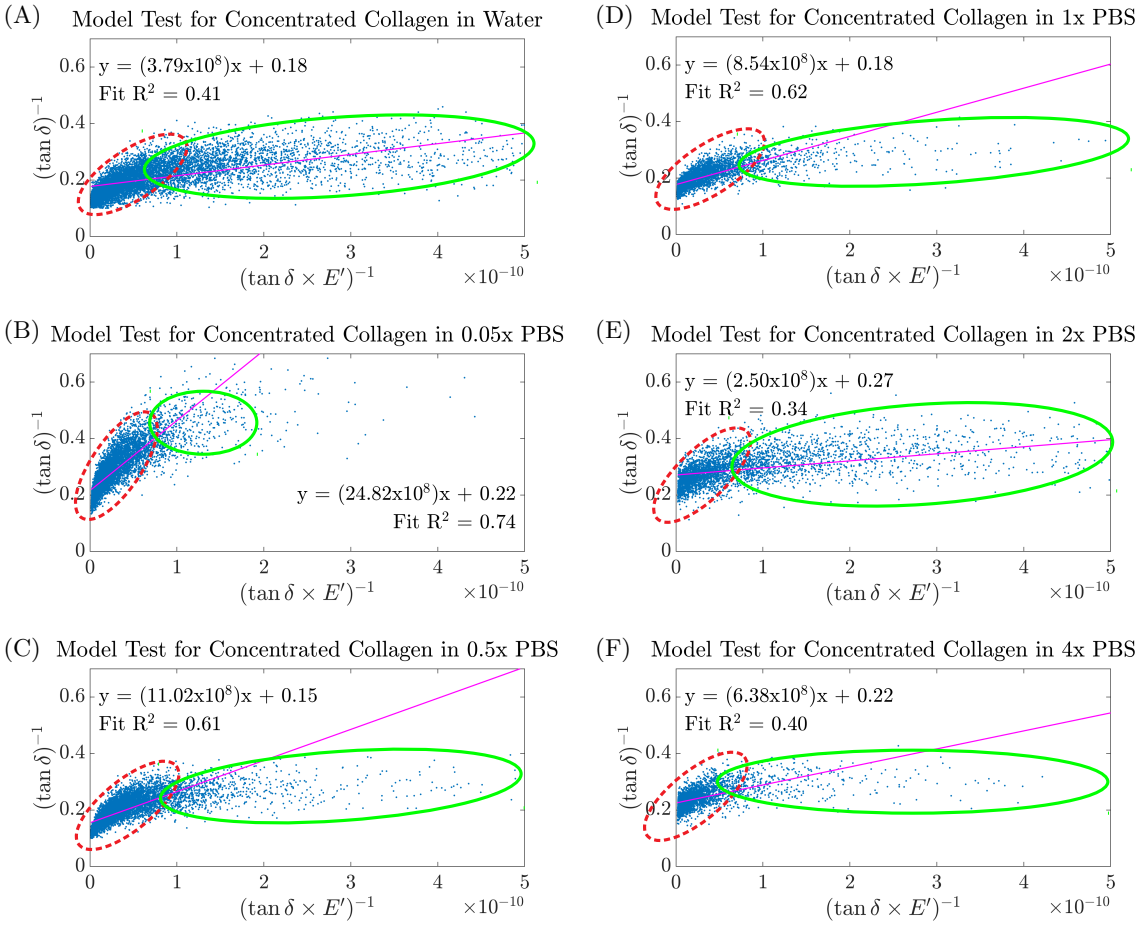


Figure 4.9: Example model tests for concentrated collagen samples. Example model test plots (equation 3.11) of concentrated collagen samples in water (0x PBS), 0.05x PBS, 0.5x PBS, 1x PBS (physiological), 2x PBS, and 4x PBS are shown in (A)-(F), respectively. Each test was performed on a single AM-FM AFM image, chosen specifically for having a higher R^2 value than the overall average of the sample. Blue dots represent the value of a single pixel. The model test is shown as a magenta line. Fit equations and R^2 values are also shown. Two materials are present in the sample, indicated by red (with a dashed line) and green (with a solid line) circles. The green circles indicate a Maxwell (MW) material within the sample. The R^2 value of the model test fit improves when fewer pixels in the image belong to the MW material.

three quantities are constant (p = 0.62, 0.71, 0.91, respectively) until aligned fibrils form in 2x PBS, after which they increase (p = 0.04, 0.02, 0.02, respectively). The trends in these quantities are similar to those of sparse samples (figure 4.5). These observations confirm that energy storage and dissipation, relating to elasticity and viscosity of collagen fibrils, by concentrated samples change together as a result of I.

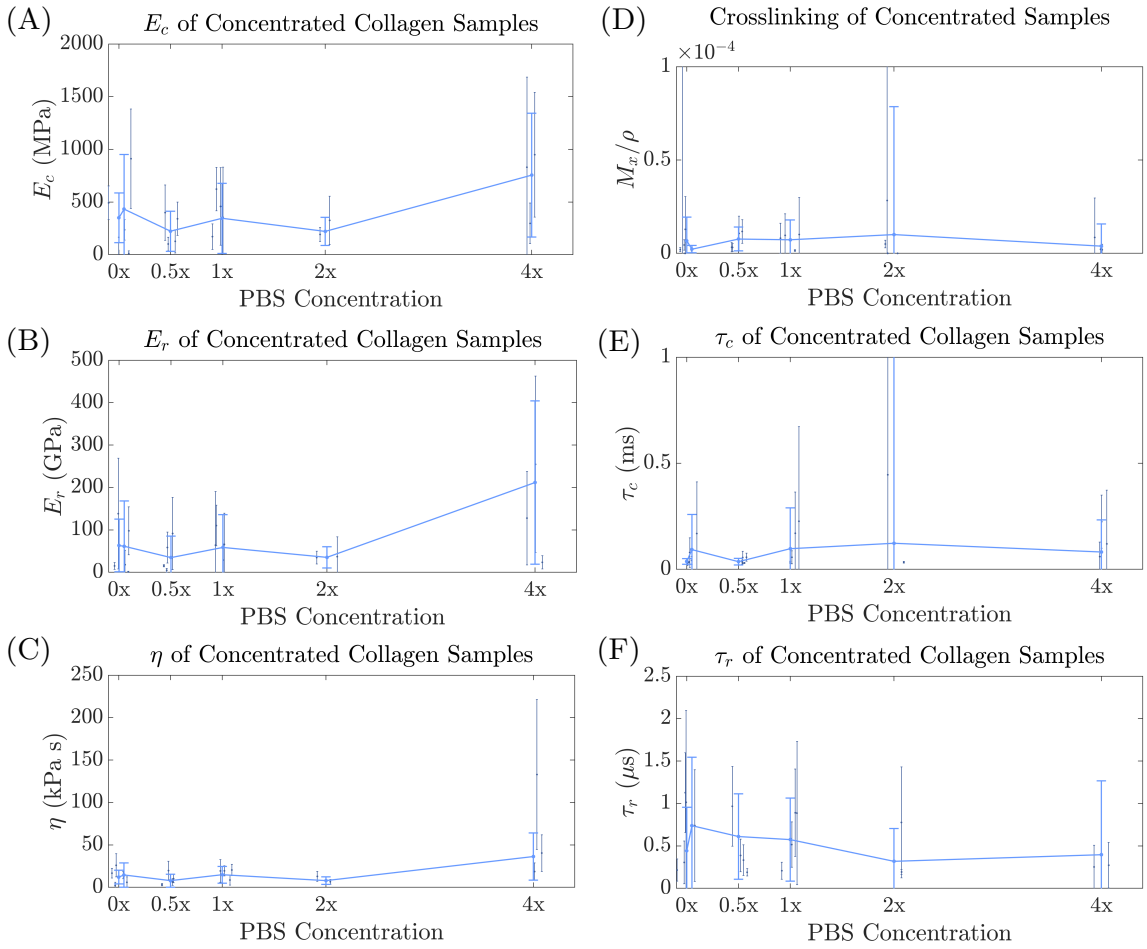


Figure 4.10: Effect of PBS concentration on concentrated sample material constants. Concentrated collagen samples were modeled as general Maxwell materials, with material constants calculated as described in section 3.2.1.3 and 3.2.2.1. The effect of PBS concentration on E_c (A), E_r (B), η (C), crosslinking (D), τ_c (E), and τ_r (F) are shown. The crosslink metric used in (D) is the molecular weight between crosslinks divided by the density of collagen (M_x/ρ). Larger points connected by lines represent overall mean values of the samples (calculated from all model test lines). Smaller dots represent mean values of individual biological replicates (calculated from all model test lines within a particular replicate). Error bars represent the standard deviation.

Also in a similar manner to sparse collagen samples, M_x/ρ of concentrated samples (figure 4.10 (D)) remained constant ($p = 0.45$) until aligned fibrils formed in 2x PBS, after which M_x/ρ decreased ($p = 0.05$). Explanations for this trend were already proposed in section 4.2.2.2, and further discussion will be saved for section 4.2.5.

The effect of PBS concentration on τ_c and τ_r of concentrated samples is shown

in figure 4.5 (E) and (F), respectively. In a similar manner to sparse samples, PBS concentration did not alter τ_r or τ_c of concentrated samples ($p = 0.45$ and 0.19, respectively). Since collagen simultaneously altered energy storage and dissipation (related to E and η) in different PBS concentrations, the resulting $\tan\delta$ and τs remained constant.

4.2.4 Imaging collagen's hydration shell

For concentrated samples in water, 0.05x PBS, 0.5x PBS, 1x PBS, and 2x PBS, higher setpoint to free amplitude ratios of the first mode ($A_{s,1}/A_{r,1}$) resulted in images of a surface with different features than the underlying collagen, shown in figure 4.11. Scanning these features multiple times resulted in the same image each time (figure 4.11 (D)-(H)), suggesting that the features are stable, and are not artifacts. Additionally, in some spots on the samples, it was possible to image collagen and the surface simultaneously (figure 4.11 (A)-(C)), again revealing a difference in the mechanical properties of each layer.

It was difficult to quantify E' or $\tan\delta$ for over 90% of the pixels in AM-FM AFM images of the features because the imaging conditions necessary to apply AM-FM AFM calculations (section 2.1.3.4) were not satisfied. Specifically, the phase of mode one was often greater than 90^o whenever the tip interacted with the features. This attractive interaction resulted in negative values for both E' and $\tan\delta$ (section 2.1.3.4). For the remaining (less than) 10% of the measured pixels, a repulsive tip/sample interaction was obtained and it was possible to quantify E' and $\tan\delta$.

The difficulty in obtaining a repulsive tip/sample interaction with the features suggests that the features were more fluid than the underlying collagen, and suggests hydration effects such as squeeze film damping [224]. Taken together, these results suggest that an organized fluid layer exists around collagen fibrils, and is stable enough to image. In other words, it is possible to image collagen's hydration shell (section

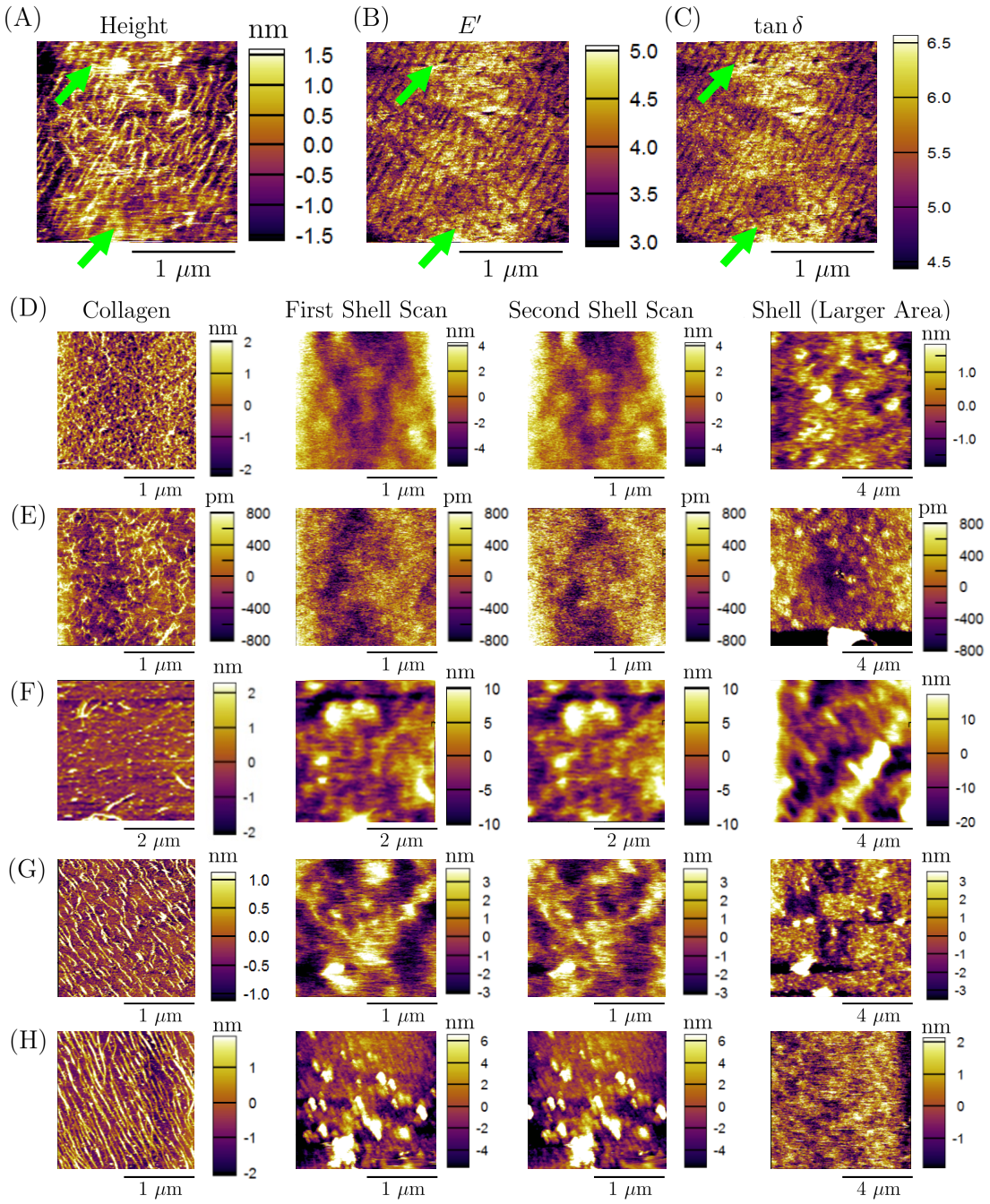


Figure 4.11: Representative images of collagen's hydration shell. First, the height (A), storage modulus, E' (B), and loss tangent, $\tan\delta$ (C), of a spot where both collagen and its hydration shell (green arrows) were visible are shown. This image was taken in 1x PBS. It was possible to observe hydration shells around collagen fibrils in water (D), 0.05x PBS (E), 0.5x PBS (F), 1x PBS (G), and 2x PBS (H). Hydration shells were not observed in 4x PBS. In (D)-(H), height images of collagen fibrils (left column), and their corresponding hydration shell (middle two columns) are shown. Shell images were taken in the same spot as the fibril image. Two scans of the shell (same spot) are shown to demonstrate that the shell is stable. The right column shows height images of collagen's hydration shell in a larger field of view.

1.1.1) in these samples. It is already known that collagen possesses a hydration shell, and that the structure and properties of this shell play an important role in how collagen polymerizes [170, 233, 234]. Additionally, this is not the first instance of hydration layers around biological samples being imaged with AFM [139–141].

As figure 4.11 shows, mica was not typically visible through the hydration shell. Therefore, the height threshold used to distinguish sample from mica was not employed to analyze E' and $\tan\delta$ of hydration shell images. Quantification of hydration shell height, E', and $\tan\delta$ from only the pixels where a repulsive tip/sample interaction was obtained is shown in figure 4.12.

Hydration shell heights were a few nm for all conditions, and did not correlate with the Debye length of the PBS solution (table 4.1). This observation suggests that Debye-Hückel theory, typically used to model the distribution of ions around charged surfaces (section 1.2.2.1.3, appendix A.2) [162, 164], may be insufficient to describe the hydration shells of biomolecules. The fact that it was possible to measure $\tan\delta$ and E' of collagen's hydration shells also suggests that the shell is a non-fluid (non-Newtonian) material, beyond the ion layer described by Debye-Hückel theory.

It is important to note that, while it was possible to quantify E' and $\tan\delta$ for some pixels of the shell image, it is possible that these pixels corresponded to regions where the tip was able to break through and interact with the underlying collagen instead of the shell. However, comparing shell measurements with collagen measurements (figure 4.7) shows that shell E' and $\tan\delta$ are different from collagen E' and $\tan\delta$. More variation in shell E' and $\tan\delta$ with PBS concentration occurs than that of collagen measurements. These results suggest that the tip is not simply measuring collagen alone. However, it may be possible that the measured shell E' and $\tan\delta$ actually represent a combined collagen/shell measurement, where the tip partially probes the collagen through the shell. With the hope of distinguishing between these possibilities, the model test line (equation 3.11, section 3.2.1) was fit to shell E' and

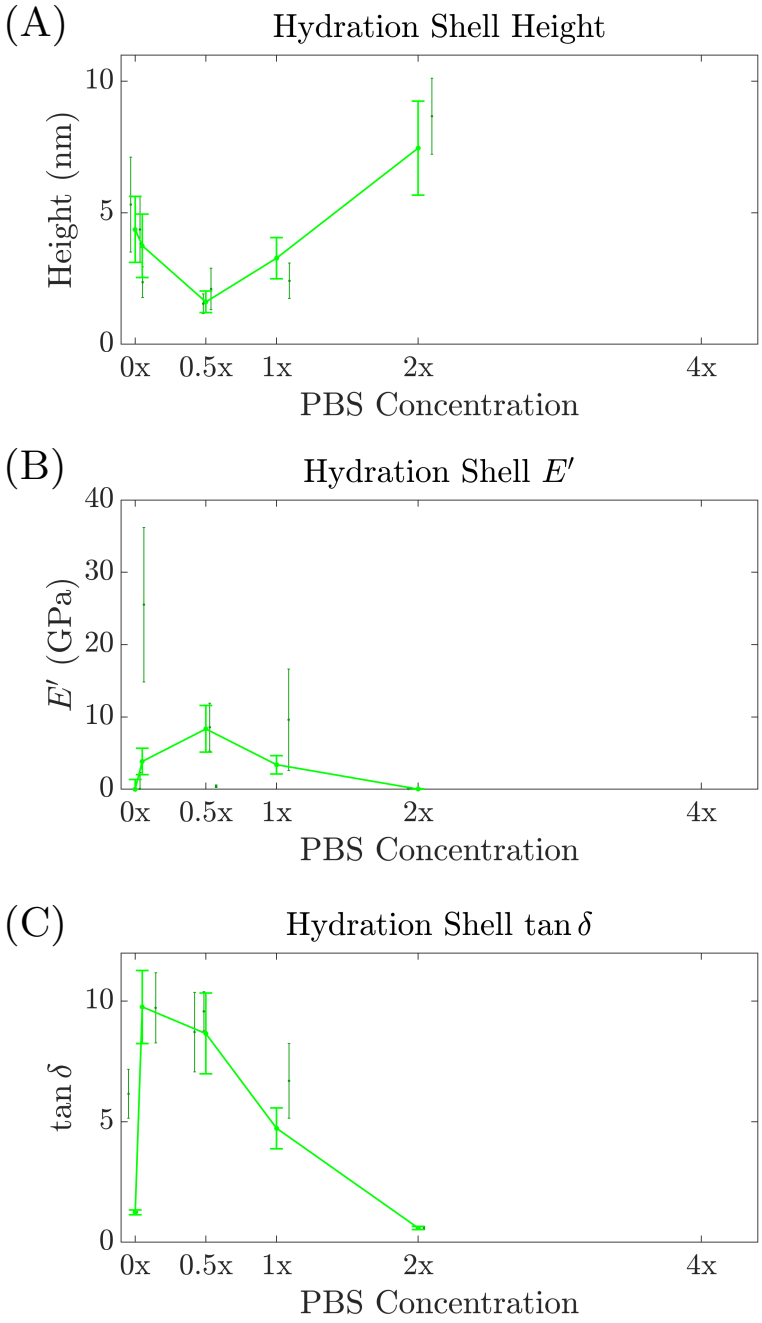


Figure 4.12: Effect of PBS concentration on hydration shell height, E', and $\tan\delta$. The effect of PBS concentration on the height (A), storage modulus, E' (B), and loss tangent, $\tan\delta$ (C), of collagen's hydration shell are shown. It was not possible to image hydration shells in 4x PBS. Larger points connected by lines represent overall mean values, calculated from all measured pixels. Smaller dots represent mean values of individual biological replicates, calculated from all measured pixels within a particular replicate. Error bars represent the standard deviation.

$\tan\delta$ measurements.

Example model tests are shown in figure 4.13. The mean $\pm$ standard deviation R^2 value of the model test fit for shell data was calculated from the fits on each individual AM-FM AFM image, and were 0.70 $\pm$ 0.23 in water, 0.53 $\pm$ 0.26 in 0.05x PBS, 0.61 $\pm$ 0.24 in 0.5x PBS, 0.69 $\pm$ 0.18 in 1x PBS, and 0.61 $\pm$ 0.43 in 2x PBS. Surprisingly, these R^2 values were higher than those of the collagen (section 4.2.3.2) underlying the shell. Additionally, both the slope and y-intercept of the fit were greater than zero (not shown), suggesting that the shell or the collagen/shell is a GMM or SLS.

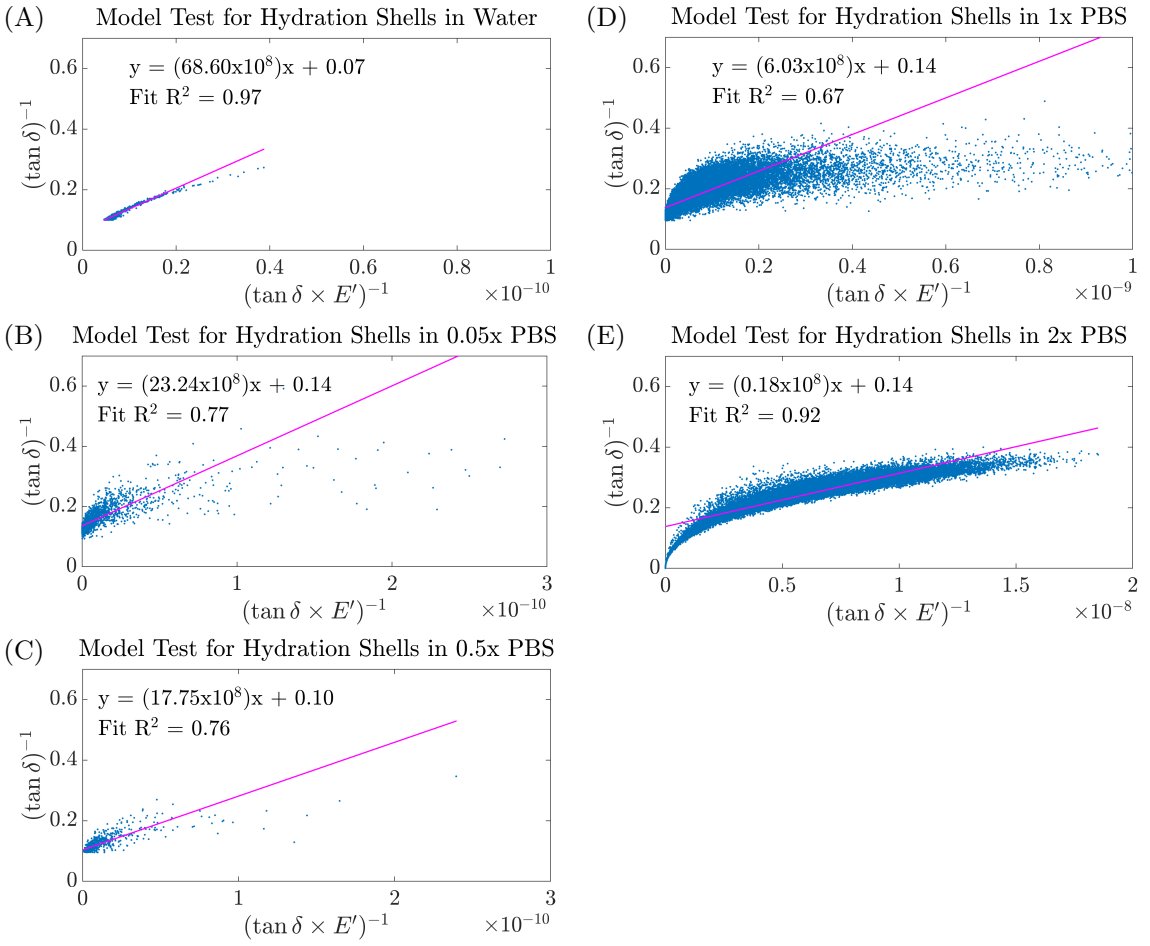


Figure 4.13: Example model tests for collagen's hydration shells. Model test plots (equation 3.11) for hydration shells in water (0x PBS), 0.05x PBS, 0.5x PBS, 1x PBS (physiological), and 2x PBS are shown in (A)-(E), respectively. Hydration shells were not observed in 4x PBS. Individual pixel values are shown as blue dots. The model test is shown as a magenta line. Fit equations and R^2 values are also shown.

Closer comparison of hydration shell model tests, shown in figure 4.14, demonstrates that shell model test outcomes varied between images. In some cases, shells behaved as SLS or GMM materials (figure 4.14 (A)), while in others, shells behaved as MW materials (figure 4.14 (B)). This observation can help distinguish whether the measured E' and $\tan\delta$ belonged to hydration shells alone or to convoluted shell/collagen measurements. Based on the results in section 4.2.3.2, collagen obeys the GMM, and a second material in the sample behaves as a MW material. Therefore, it is possible that model tests that behaved as SLS or GMM materials (figure 4.14 (A)) could represent a convoluted shell/collagen measurement. Similarly, model tests that behaved as MW materials (figure 4.14 (B)) could represent a hydration shell measurement.

Regardless of whether the shell alone or the convoluted shell/collagen was probed by AM-FM AFM, these results still have biological implications. Since cells probe their surroundings at the same length scales (nm) as those in this AM-FM AFM experiment [15, 59, 120–124], these results suggest that cells may be able to feel the hydration shell of the ECM or the combined shell/ECM just as the AFM tip did

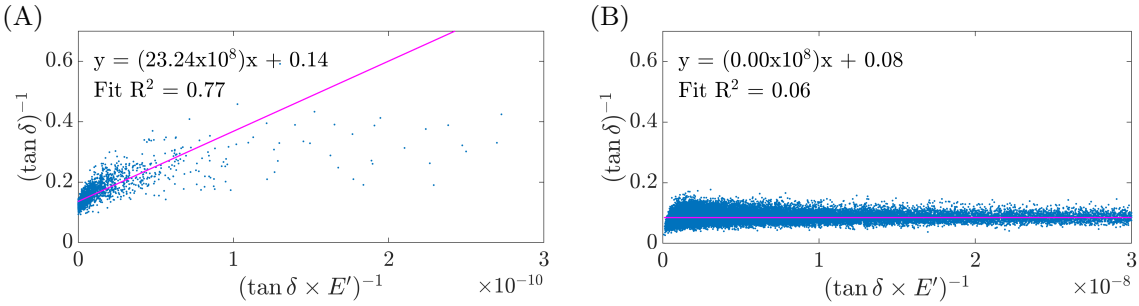


Figure 4.14: Variability in hydration shell model test outcome. Model test plots (equation 3.11) for hydration shells in 0.05x PBS samples are shown, and are representative of the variability in test results of other samples. A model test for a single AM-FM AFM image where the shell behaved as a standard linear solid or general Maxwell material is shown in (A). A model test for a second AM-FM AFM image on the same sample where the shell obeyed the Maxwell model is shown in (B). Individual pixel values are shown as blue dots. The model test is shown as a magenta line. Fit equations and R^2 values are also shown.

in these experiments. Therefore, the ability of AM-FM AFM to quantify collagen's hydration shell, even if only for less than 10% of the measured pixels, raises the possibility that the fluid environment of tissues acts as an additional solid within the tissue that contributes directly to tissue mechanics.

Regardless of whether hydration shells, or shells/collagen, behave as SLS, GMM, or MW materials, these results suggest that, for the applied AM-FM AFM stimulus, hydration shells in some locations on the sample behaved as linear viscoelastic solids. This observation means that hydration layers in biological systems could potentially contribute to E, η, and the time responses within the system, and could even function as additional arms in the GMM for materials like the ECM. Additionally, the results of this section, combined with section 4.2.3.2 (figure 4.8 and 4.9) suggest that shells are measured simultaneously with collagen, thereby supporting the notion that hydration shells can act as additional materials in the system. Further quantification of shell material constants and time responses is left for future work, when it can be established whether the measured E' and $\tan\delta$ belong only to the shell or to a convoluted collagen/shell measurement. However, the possibility that the fluid environment of the ECM directly (as opposed to indirectly via contributions like modulating molecular charge, section 1.2.2.1.3) contributes to tissue mechanics is an intriguing avenue for future research.

4.2.5 Electrostatics discussion

AM-FM AFM nanoscale measurements of collagen E' and $\tan\delta$ (section 4.2.2 and 4.2.3) suggest that collagen simultaneously alters energy storage and dissipation in solutions of different ionic strength (I). These nanoscale observations agree with macroscale observations [188]. Such simultaneous alteration of energy storage and dissipation results in constant timescales within the collagen, regardless of I. Macroscopic collagen matrices also exhibit constant time responses with respect to temper-

ature, hydration, and mechanical pre-loading [189, 190]. Additionally, plant cell walls (the ECM of the plant) also exhibit constant time responses across growth zones [166]. Together, these observations suggest a multiscale and potentially universal biological feedback within the ECM and its equivalents that maintains constant time responses across spatial scales in certain environmental conditions.

The mechanism behind these constant time responses is likely related to the ions within the solution surrounding the collagen. The results of section 4.2.4 suggest that collagen's hydration shell, a structure of organized molecules surrounding the collagen, is solid enough to contribute to collagen's mechanics. Additionally, the mechanical properties of hydration shells (figure 4.12) varied more than those of collagen (figure 4.3 and 4.7) with respect to I. Together, these results suggest that hydration shell and ion dynamics with tropocollagen molecules are responsible for alterations to energy storage and dissipation by the collagen.

It is already known that intermolecular interactions between tropocollagen molecules weaken as I increases [70, 237]. It is hypothesized that this weakening is due to increasing ion adsorbtion to tropocollagen molecules as I increases [231, 236, 237]. Such ion adsorption could weaken interactions between tropocollagen molecules by sterically blocking carboxyl and other amino acid groups on tropocollagen that play an important role in aggregating and crosslinking tropocollagen molecules [231, 236, 237]. Therefore, as ion concentration increases, collagen likely trades the formation of covalent bonds (crosslinks) directly between tropocollagen molecules for ionic bonds (electrostatic correlations) between ion coatings. This ion coat hypothesis is diagrammed in figure 4.15.

The results in figure 4.5 (D) and 4.10 (D) suggest that, as I increases, (i) the molecular weight between crosslinks decreases, meaning the number of crosslinks increases, (ii) that the density of tropocollagen within collagen molecules increases, or (iii) both occur. As PBS concentration increases, the height of the resulting fibrils

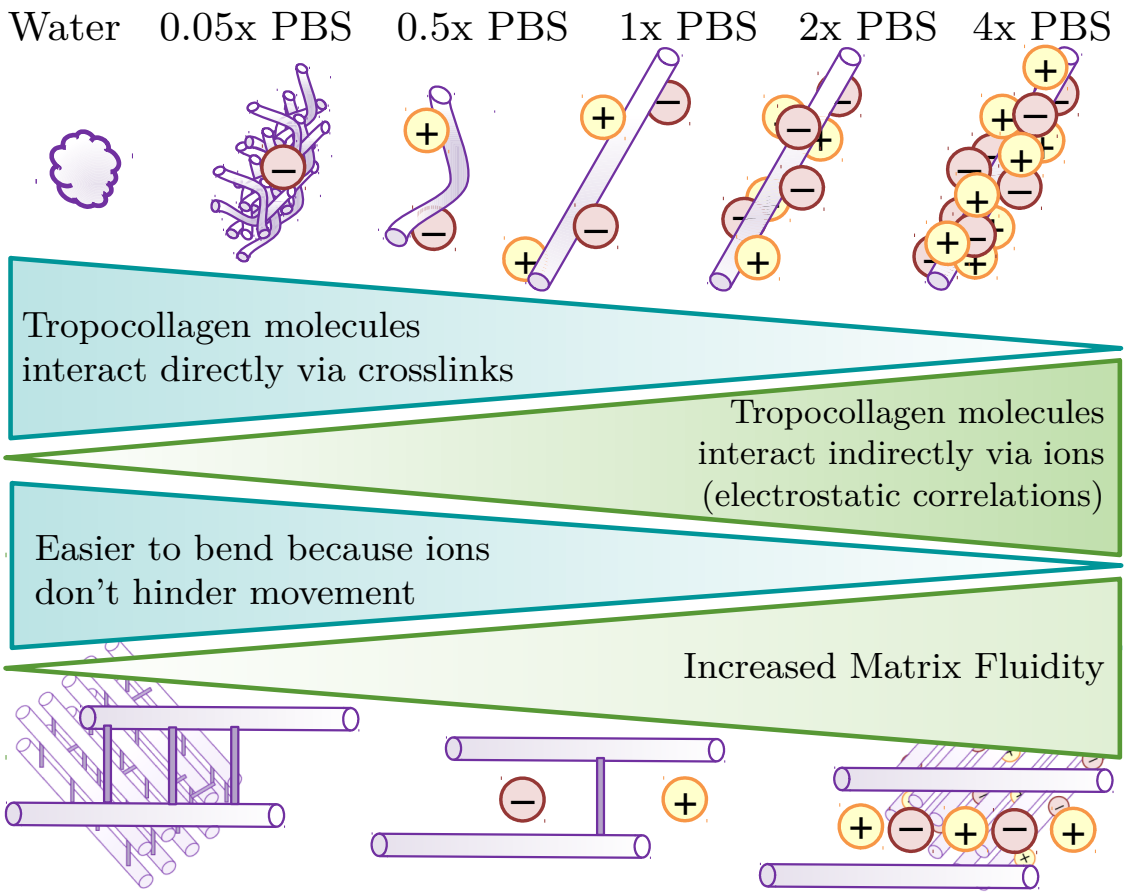


Figure 4.15: Ion coat hypothesis for tropocollagen in different PBS concentrations. As PBS concentration increases, so does the ionic strength I of the solution. With increasing I, the number of ions (circles with "+" or "-") adsorbed to the surface of tropocollagen molecules (purple cylinders or squiggles) increases as well. This ion coating causes tropocollagen molecules to interact indirectly via electrostatic correlations. In solutions of low I, tropocollagen molecules interact directly by forming crosslinks (purple rectangles).

also increases (figure 4.3 (A) and 4.7 (A)). This observation suggests that the packing of tropocollagen into fibrils changes with I, and therefore that (ii) or (iii) occurred. Since previous studies found that crosslinking between tropocollagen decreases with I [231, 236, 237], (ii) is the most likely case. It makes sense that a decrease in crosslinking, and thus a shift to electrostatic correlations, would also increase the density of tropocollagen packing within collagen fibrils, since the range of electrostatic correlations is short, only a few nm, based on the Debye length of the solution (table 4.1).

Therefore, these results support the ion coat hypothesis.

In solutions of higher I, mechanical stimuli to the sample would allow collagen chains to slide along each other by exchanging electrostatic correlations. This sliding could serve as the mechanism for collagen to increase energy dissipation with increasing I. Increasing ion adsorption to collagen in solutions of higher I could also increase the difficulty of deforming collagen fibrils, due to electrostatic interactions between adsorbed ions on the collagen and in collagen's hydration shell. This mechanism could account for increase in energy storage with I.

Regardless of the mechanism, the constant time responses observed in these electrostatic experiments and in the literature [188–190, 227] suggest that the time responses of collagen are constant over multiple length scales in a variety of conditions. In order to understand the implications of these constant time responses for cell behaviors, it is interesting to note when the time responses of collagen are altered by external stimuli. It is known that macroscale time responses of collagen change with pH [188] and in disease states [187]. Therefore, alterations to tissue time responses could serve as a physiological mechanism to alter cell activities. One example of such a case could be embryonic development, where ion flows over the embryo play a crucial role in dictating how cells behave to form tissues [2, 64]. It is possible that the voltage generated by ion currents within the embryo alter the developing tissue time responses. This hypothesis is tested in the following section.

4.3 Effect of ion flow on collagen viscoelasticity

Ion flows play a crucial role in generating voltages *in vivo* (section 1.2.1.1) [64]. Therefore, for this experiment, 1x PBS was flowed over collagen fibrils in order to examine the effect of applied voltage, via ion flow, on the mechanical properties of collagen I. Only the sparse collagen concentration of 0.02 mg collagen per mL PBS

was tested in order to ensure that hydration shells did not interfere with quantification of the collagen (section 4.2.4). Sample preparation, imaging, and data analysis were carried out as in the electrostatic case (section 4.2.1).

PBS was flowed over the collagen sample via the Oxford Instruments Asylum Research Cypher ES liquid perfusion setup [202]. Briefly, liquid perfusion, the flow of 1x PBS over the sample, was achieved by (i) attaching inlet and outlet tubing to the cantilever holder, (ii) pressurizing the cell containing the sample and cantilever to prevent liquid from spilling and to ensure that the PBS flow would exit the chamber via the outlet, then (iii) push/pulling PBS over the sample via two syringes [202].

The Cypher's liquid perfusion holder, containing an inlet port and outlet port was used, as shown in figure 4.16 (A). A syringe full of 1x PBS was connected to the inlet via tubing, and an empty syringe was attached to the outlet [202]. The holder and syringes were then moved to the Cypher ES and the cantilever was calibrated as in section 4.2.1 [202]. Before the sample or any liquid was added, the cell was tested for leaks by increasing the pressure of the cell to 250 mbar and waiting at least 10 minutes to ensure that the pressure did not decrease [202]. The cell was then depressurized, and the sample was added to the cell [202]. A small amount of 1x PBS was then pushed onto the sample from the inlet syringe, and a second leak test, with pressure at 80 mbar, was performed [202]. The pre-flow E' and $\tan\delta$ of the collagen were then measured at a single spot on the sample using AM-FM AFM (section 2.1.3.4). Next, a PBS flow was created by manually pushing 1x PBS from the inlet syringe and pulling 1x PBS to the outlet syringe [202]. The rate of the push/pull was determined in order to maintain a constant pressure of $\sim$50 mbar [202]. This push/pull lasted for roughly two minutes. Immediately after the flow stopped, AM-FM AFM was performed on the same spot of the sample to quantify post-flow E' and $\tan\delta$ of the collagen. The resulting pre- and post-flow AM-FM AFM data was processed and analyzed as in the electrostatics case (section 4.2.1).

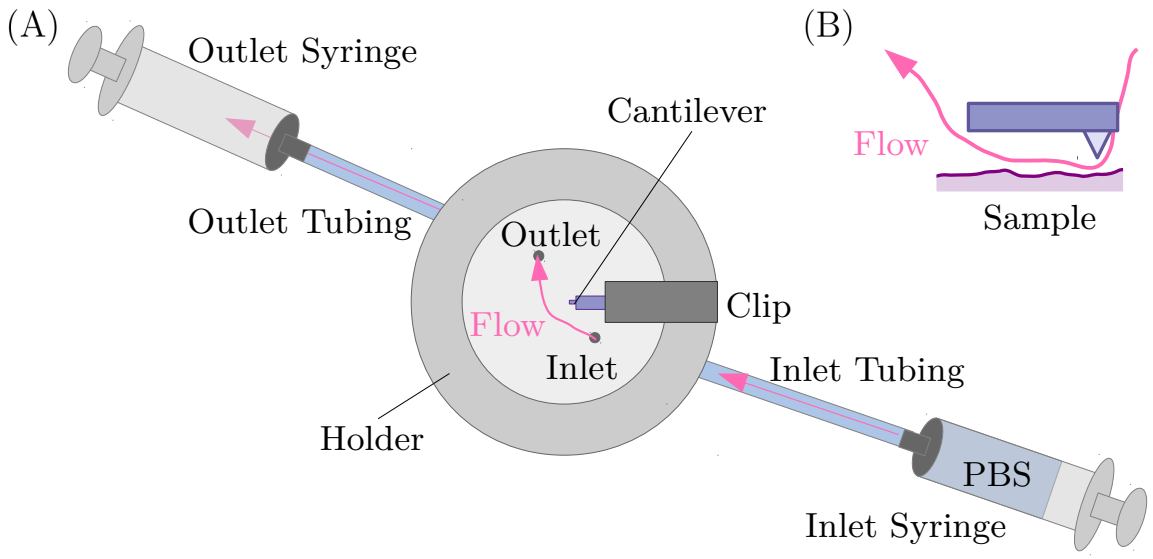


Figure 4.16: Liquid perfusion setup for PBS flow. (A) Shows how PBS flow was established over the sample, from the perspective of the sample. The Cypher's liquid perfusion holder, which contains an inlet and outlet, was used. PBS flow over the sample surface (magenta arrows) was established by connecting a syringe full of 1x PBS to the inlet and an empty syringe to the outlet and push/pulling PBS over the sample. (B) Shows a side view of the PBS flow over the sample.

4.3.1 AM-FM AFM of collagen pre- and post-ion flow

Collagen fibrils in 1x PBS were imaged with AM-FM AFM before and after flowing 1x PBS over the sample. The same spot of the sample was measured each time in order to directly compare measurements before and after the flow. This resulted in a total of six images, two before the flow, and four after the flow. As in the electrostatics case, pixels belonging to mica were discarded by applying a height threshold to the data (figure 4.2). Once pixels belonging to collagen fibrils were identified, the corresponding height, E', and $\tan\delta$ were analyzed. Figure 4.17 shows the mean and standard deviation of these values before and after PBS flow. The flow significantly changed E' and $\tan\delta$ of the sample (p values are shown in figure 4.17).

The analysis developed in section 3.2 was applied to AM-FM AFM images of the sample collected before and after the PBS flow, in order to gain insight into the mechanism behind alterations to E' and $\tan\delta$ by the flow. First, the model test

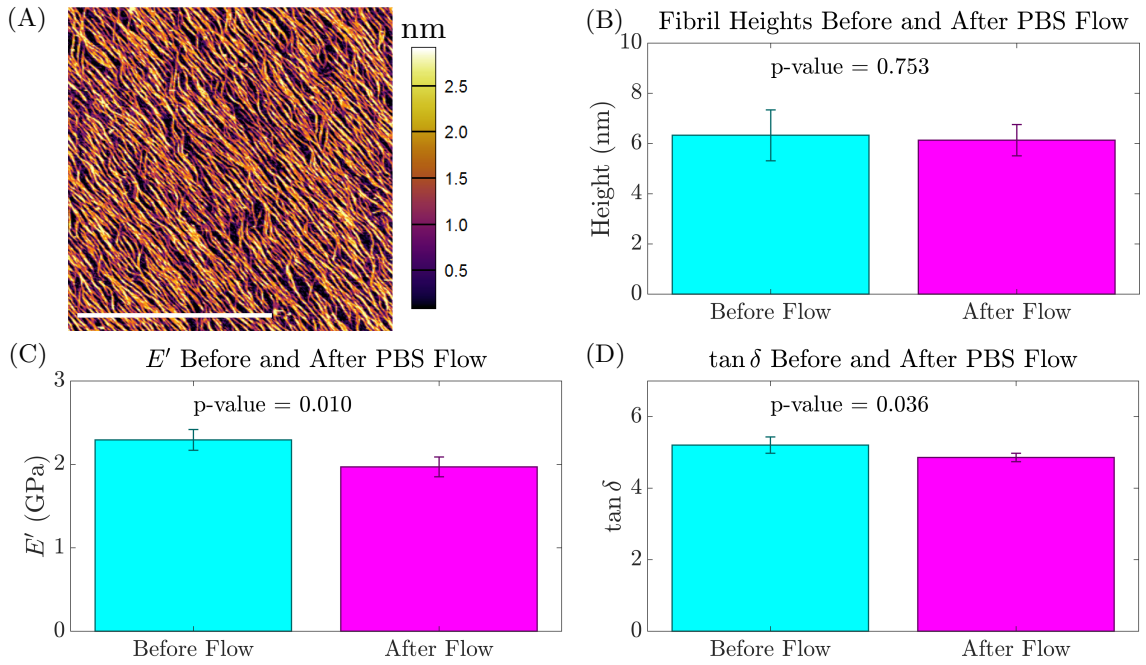


Figure 4.17: Effect of PBS flow on collagen fibril height, E', and $\tan\delta$. An image of collagen fibrils after PBS was flowed over the sample is shown in (A) to demonstrate that any observed changes in sample mechanics were not due to destruction of the sample by the flow. The white scale bar is 3 μm. Comparisons of the mean height (B), storage modulus, E' (C), and loss tangent, $\tan\delta$ (D), of collagen fibrils before and after flow are also shown. Error bars represent the standard deviation of the measurements. Comparison p values were calculated from a two-tailed t-test.

line (equation 3.11, section 3.2.1) was fit to AM-FM AFM E' and $\tan\delta$ in order to determine if concentrated collagen samples were MW, KV, SLS, or GMM materials. The mean $\pm$ standard deviation R^2 value of the model test fit was 0.89 $\pm$ 0.06 for images taken before collagen flow, and 0.75 $\pm$ 0.02. These values are slightly better than sparse samples in 1x PBS from electrostatics experiments (0.59 $\pm$ 0.20, section 4.2.2.2). Thus, collagen fibrils before and after PBS flow can still be modeled with the GMM. The material constants of collagen fibrils before and after PBS flow were calculated as described in section 3.2.2.1 and are shown in figure 4.18.

The results in figure 4.18 suggest that PBS flow alters the elastic constants of collagen fibrils. The only significant change ($p = 0.026$) was that flow increased the value of E_c. Note that the value of E_c for these samples was between 50-100 MPa.

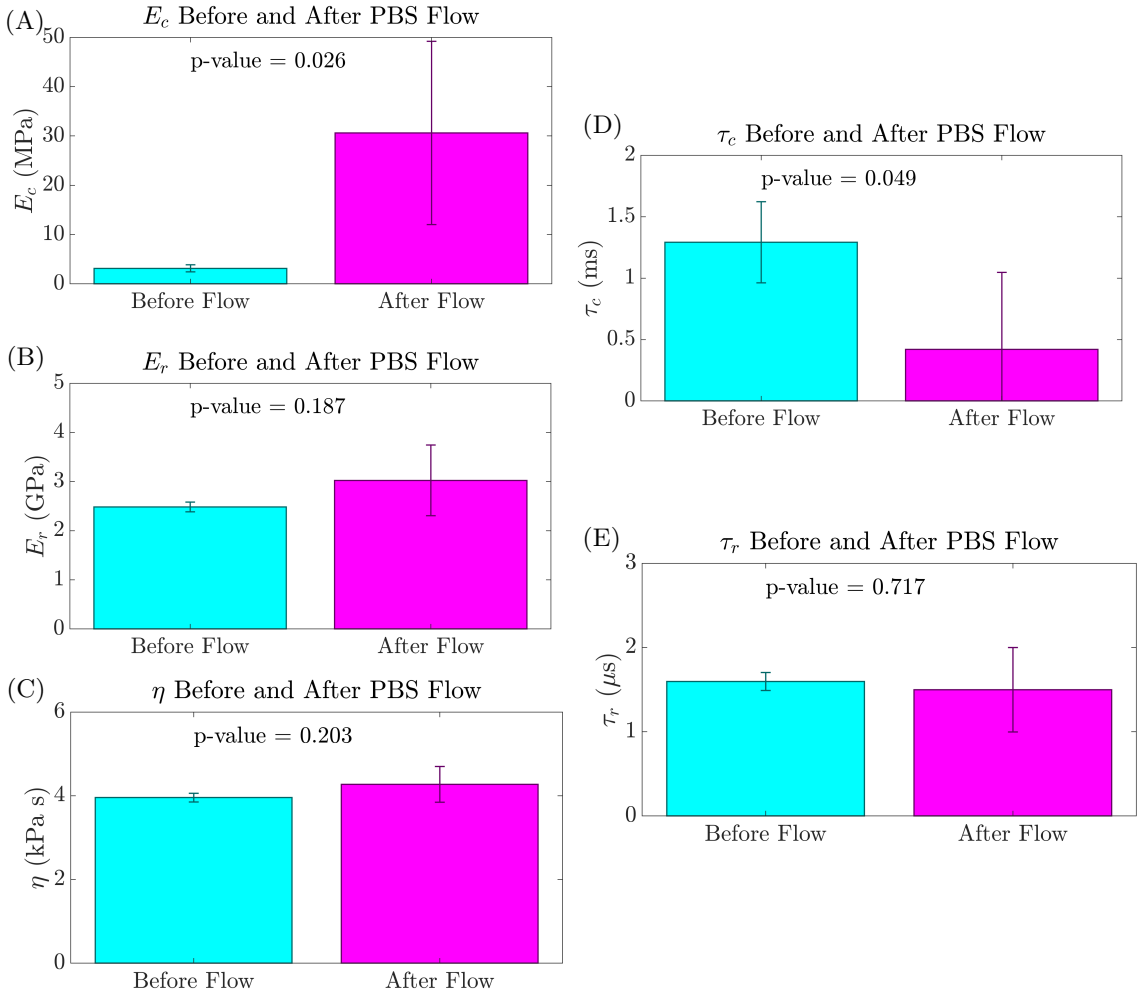


Figure 4.18: Effect of PBS flow on collagen material constants. The effect of PBS flow on E_c, E_r, η, τ_c, and τ_r of collagen fibrils is shown in (A)-(E), respectively. Error bars represent the standard deviation of the measurements. The p value displayed on each plot was calculated from a two-tailed t-test.

While this value seems lower than previous results on sparse collagen fibrils in 1x PBS (where E_c had a mean $\pm$ standard deviation of 122 MPa $\pm$ 70 MPa, section 4.2.2.2), these values are still within one standard deviation of those in section 4.2.2.2.

The value of E_r potentially increased. The p value, calculated from a two tailed t-test, for the increase in E_r was not significant ($p = 0.187$). However, a p value of 0.187 indicates an 81% chance that the observed increase was real. A similar finding occurred for η ($p = 0.203$). In the future, it would be interesting to perform more biological replicates to test whether the lack of significant change in E_r and η is simply

due to the small number of images (six) for this experiment.

The value of τ_c decreased ($p = 0.049$), while τ_r remained constant ($p = 0.717$) in response to PBS flow. Therefore, these results suggest that flowing ions increases the elasticity, and thereby decreases the time responses of collagen fibrils. Interestingly, a similar phenomenon occurs in liver disease, where the time responses of diseased livers change as a result of increasing E', but constant E'' [187]. The fact that PBS flow altered the creep time response of collagen fibrils suggests that physiological processes where ion flows and voltages are generated, such as during wound healing and embryonic development [2, 64], alter tissue time responses via the flow. Since time responses play an important role in determining cell behavior [15, 184], these results suggest that the voltages generated by ion flows within tissues could alter cell behavior by altering tissue time responses. Such control of cell behaviors via altered tissue time responses could explain why ion flows within tissues are essential for processes like wound healing and morphogenesis to proceed correctly.

4.4 Chapter conclusions

In this chapter, the effect of electrostatics and ion flow on collagen I, the most prevalent component of the ECM [3, 4, 129], mechanics was investigated via AM-FM AFM. For collagen fibrils, E' and E'' both increased with increasing ionic strength, I, of the surrounding solution. The mechanism behind this increase is likely related to ion dynamics between tropocollagen molecules. Since E' and E'' were altered simultaneously, $\tan\delta$ and the time responses of the fibrils remained constant. Only by flowing ions over collagen fibrils did fibril time responses change. This observation suggests that there is a feedback which maintains constant time responses in tissues, unless an additional stimulus is applied. A physiological mechanism of altering cell activities could be to tailor tissue time responses via stimuli such as ion flows during processes

where cell behaviors must dramatically change, for example to form tissue during embryonic development or to heal a wound [2, 64].

It would be interesting to investigate which environmental conditions, besides ion flows, have the ability to alter tissue time responses. Possible candidates that could alter collagen time responses are the pH of the solution, or the presence of divalent ions like Ca^{2+} or Mg^{2+} [231, 244]. These factors affect collagen self-assembly [231, 244], so could play a role in modulating collagen's time responses. Electrostatic experiments in PBS solutions at different pH, or containing divalent ions, could be performed in order to see if either of these factors affect E', $\tan\delta$, or τ of collagen fibrils.

Additionally, it would be interesting to further explore the effects of applied voltages on collagen mechanics. Several steps can be taken to improve the experimental setup to generate PBS flow in future experiments. First, AM-FM AFM could be performed at several time points after the PBS flow, to determine whether the effects of ion flow are permanent or temporary. Second, a more controlled flow rate could be established by using a syringe pump instead of manually push/pulling the syringes to cause PBS flow. Third, it may be possible, though difficult, to measure the voltage generated by the PBS flow by inserting an electrode in the cell, just above the sample [245]. Keeping the electrode just above the sample would be challenging, but could potentially be accomplished by taping the electrode to the side of the cell, or by snaking the electrode through the inlet tubing, if the electrode is thin enough [245]. Fourth, in order to directly test the effects of applied voltage on collagen viscoelasticity, instead of indirectly via ion flow, a voltage could be applied to the sample in liquid via a potentiostat [245].

The experiments in this chapter also demonstrate that it is possible to image collagen's hydration shell, as well as measure the mechanical properties of the shell or a convolution of the shell and underlying collagen. These results suggest that the hydration shell around collagen is stable, and can even behave as a linear viscoelastic

solid. Therefore, hydration shells could also contribute directly to tissue mechanics, rather than indirectly by modulating the charge of molecules in the tissue. It would be interesting to develop better methods to measure hydration shell mechanics in the future, in order to study their role in tissue mechanics and potentially exploit the fluid environment of tissues to treat disease.

Hydration shell dynamics could be further studied by performing liquid perfusion on concentrated samples while imaging collagen's hydration shell pre- and post-flow in order to study how flowing ions affect hydration shells. Additionally, the experiments in this chapter could be repeated on collagen hydrogels, in order to see if the trends observed in collagen fibrils and shells are the same when they are incorporated into a gel, and so that indentations (section 2.1.3.2) and PANDA (section 2.1.3.3) could also be used on the sample.

Finally, collagen mechanics, hydration shell mechanics, and their interaction could be investigated theoretically, in order to better understand the physics of biological systems. A preliminary approach to such a theoretical model could be to expand equivalent circuit models of linear viscoelasticity (section 1.3.4) to include an equivalent circuit for piezoelectricity. Solutions to such a model could then be validated against AFM experiments with an applied voltage, in order to gain insight into the piezoelectric behavior of collagen at the nanoscale. Preliminary construction of such a model is presented in section 4.4.1.

4.4.1 Preliminary equivalent circuit model of collagen piezoelectricity

Collagen is piezoelectric, meaning a voltage, V_{pie}, is generated by collagen when a strain is applied, ϵ_{app}, and that collagen experiences a strain, ϵ_{pie}, when a voltage, V_{app}, is applied [157]. For simplicity, it can be assumed that collagen exhibits a linear piezoelectric response as follows [246–248]. The constants μ_v and μ_ϵ dictate

the coupling between ϵ_{app} and V_{pie}, and V_{app} and ϵ_{pie}, respectively.

$$V(t) = V_{\text{app}}(t) + V_{\text{pie}}(t) = V_{\text{app}}(t) + \mu_v \epsilon_{\text{app}}(t) \tag{4.1}$$

$$\epsilon(t) = \epsilon_{\text{app}}(t) + \epsilon_{\text{pie}}(t) = \epsilon_{\text{app}}(t) + \mu_\epsilon V_{\text{app}}(t) \tag{4.2}$$

While the exact mechanism is unknown, collagen's piezoelectricity is likely related to the electrical double layer, the layer of counterions and organized water molecules around biomolecules (section 1.2.2.1.3) [246–248]. When collagen is deformed, its surface charge density, q_{col}, will change, which will in turn affect the arrangement of ions in the double layer around the molecule. Since tissues and collagen matrices have their own charge [246–248], the movement of ions in the double layer against this background charge could generate the voltage responsible for the piezoelectric effect [246–248]. With this mechanism in mind, the following equivalent circuit model, diagrammed in figure 4.19, can be constructed to model collagen's piezoelectric response by coupling an RC circuit for the double layer (electrical effects) with standard linear viscoelastic models for collagen (mechanical effects) [246–248].

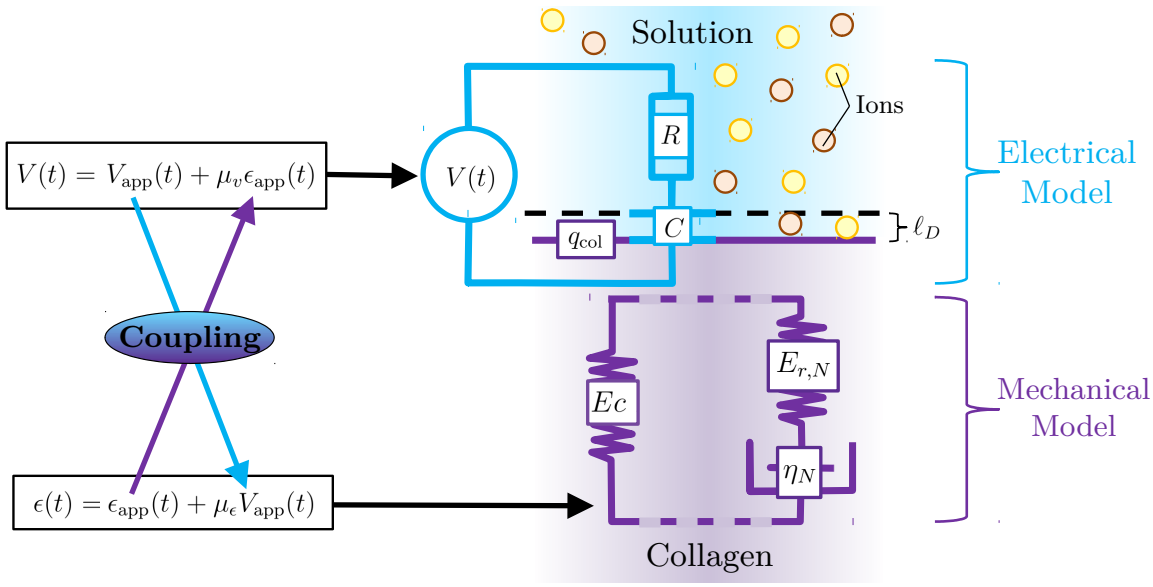


Figure 4.19: Preliminary equivalent circuit model of collagen piezoelectricity. The model schematic and relevant material constants are shown.

The double layer is often modeled as a resistor of resistance R that dissipates electrical energy and a parallel plate capacitor of capacitance C that stores electrical energy connected in series [246–248]. One plate of the capacitor is the surface of the collagen, and the other is the boundary between the bulk solution and the layer of counterions surrounding the collagen [246–248]. This boundary occurs at the Debye length, ℓ_D (section 1.2.2.1.3, equation 1.10). Energy dissipation by the double layer occurs because ions are not static within the double layer, and because charges in the layer will resist applied voltages [246–248]. This model of the double layer results in the following equations.

$$V = R\dot{q}_{\text{col}}(t) + \frac{q_{\text{col}}(t)}{C} \tag{4.3}$$

Substituting equation 4.1 into equation 4.3 gives the differential equation for the electrical activity of the double layer. This equation represents the effect that an applied strain has on the system, the mechanical $\rightarrow$ electrical component of piezoelectricity.

$$\begin{aligned} V_{\text{tot}}(t) &= R\dot{q}_{\text{col}}(t) + \frac{q_{\text{col}}(t)}{C} \\ V_{\text{app}}(t) + \mu_v \epsilon_{\text{app}}(t) &= R\dot{q}_{\text{col}}(t) + \frac{q_{\text{col}}(t)}{C} \\ \dot{q}_{\text{col}}(t) + \frac{q_{\text{col}}(t)}{RC} &= \frac{V_{\text{app}}(t) + \mu_v \epsilon_{\text{app}}(t)}{R} \end{aligned} \tag{4.4}$$

The effect that V_{app} has on the system, the electrical $\rightarrow$ mechanical component of piezoelectricity, can be obtained by substituting equation 4.2 into the relevant differential equation for the sample (modeling the sample as a MW (equation 1.38), KV material (equation 1.32), SLS (equation 1.25), or GMM). Since collagen is a SLS or GMM [170, 188–193], the differential equation for the SLS (equation 1.25) is used here. The GMM is left for future work.

$$\dot{\sigma}(t) + \frac{E_r}{\eta}\sigma(t) = (E_c + E_r)\,\dot{\epsilon}_{\text{tot}}(t) + \frac{E_c E_r}{\eta}\epsilon_{\text{tot}}(t)$$
$$= (E_c + E_r)\,\dot{\epsilon}_{\text{app}}(t) + \frac{E_c E_r}{\eta}\epsilon_{\text{app}}(t)$$
$$+ \mu_\epsilon\,(E_c + E_r)\,\dot{V}_{\text{app}}(t) + \frac{\mu_\epsilon E_c E_r}{\eta}V_{\text{app}}(t) \qquad (4.5)$$

Substituting various functions for $V_{\text{app}}(t)$ and $\epsilon_{\text{app}}(t)$ into the system of equations given by equation 4.4 and 4.5 allows analytical solutions of how collagen behaves during various experiments to be obtained. For a DC voltage $V_{\text{app}}(t) = V_o$, for an AC voltage, $V_{\text{app}}(t) = V_o \sin(\omega_V t)$. The various forms of $\epsilon_{\text{app}}(t)$ can be obtained from the expressions for relaxation (equation 1.15), creep (equation 1.16), and dynamic stimuli ($\epsilon_{\text{app}}(t) = \epsilon_o \sin(\omega t)$). The resulting analytical solutions can then be compared to experimental data.

As described in section 1.2.2, the surface charge density of collagen, q_{col}, depends on the salt concentration and pH of the surrounding solution. Therefore, in order to analytically solve the proposed system of equations for collagen's piezoelectric response (equations 4.4 and 4.5), it is necessary to first know the initial value of $q_{\text{col}}(0)$ before any stimulus is applied. The value of $q_{\text{col}}(0)$ can be calculated as described in the following section.

4.4.1.1 Calculating collagen's surface charge density

The charge of a single tropocollagen molecule, and thereby that of the resulting collagen fibrils, is the sum of all charges on the individual amino acids, a, within tropocollagen (section 1.2.2). The surface charge density of the collagen, $q_{\text{col}}(0)$, is then this value divided by the surface area of a tropocollagen molecule. Approximating a tropocollagen molecule as a cylinder of radius $r_{\text{tcol}} = 0.75$ nm and height

$h_{\text{tcol}} = 300$ nm [131, 132] gives the following expression for $q_{\text{col}}(0)$.

$$q_{\text{col}}(0) = \frac{\sum_{a=1}^{A} q_a}{2\pi \left(r_{\text{tcol}}^2 + r_{\text{tcol}} h_{\text{tcol}}\right)} \tag{4.6}$$

The charge of a single amino acid, q_a, can be calculated via equation 1.6. The geometrical constraint of the amino acids within tropocollagen can be modeled as shifts in the amino acid's pKa value, per equation 1.11 (derived from Debye-Hückel theory, section 1.2.2.1.3). The distance between the ath amino acid and neighboring amino acids, needed to use equation 1.11, can be calculated based on the structure of tropocollagen.

Tropocollagen I consists of three polypeptide chains wrapped around each other in a triple helix. This triple helix consists of two $\alpha 1$ chains and one $\alpha 2$ chain [131, 132, 135]. The triple helix can be approximated using pyrimidal geometry with 1.8 nm between neighboring amino acids within a single chain, and 0.7 nm between neighboring amino acids in different chains. These values were calculated from r_{tcol} and h_{tcol} [131, 132], and the number of amino acids in the $\alpha 1$ and $\alpha 2$ chains. The amino acids and their position in the $\alpha 1$ and $\alpha 2$ chains can be obtained from the uniProt database at `https://www.uniprot.org/uniprot/P02452` and `http://www.uniprot.org/uniprot/P08123`.

Figure 4.20 compares $q_{\text{col}}(0)$ calculated as described in this section to literature values [232]. In the literature, $q_{\text{col}}(0)$ was measured indirectly by studying the streaming current [232]. Streaming current, dI_s/dp, can be related to the charge at the Debye length (ℓ_D, equation 1.8) from the surface [232], and related back to surface charge via the Poisson-Boltzmann equation (equation A.2) [232]. While the literature study did not directly calculate $q_{\text{col}}(0)$ from dI_s/dp, the shape of dI_s/dp and $q_{\text{col}}(0)$ vs. pH, as well as the isoelectric point (point where $dI_s/dp = q_{\text{col}}(0) = 0$) are comparable between the calculations and experimental values [232].

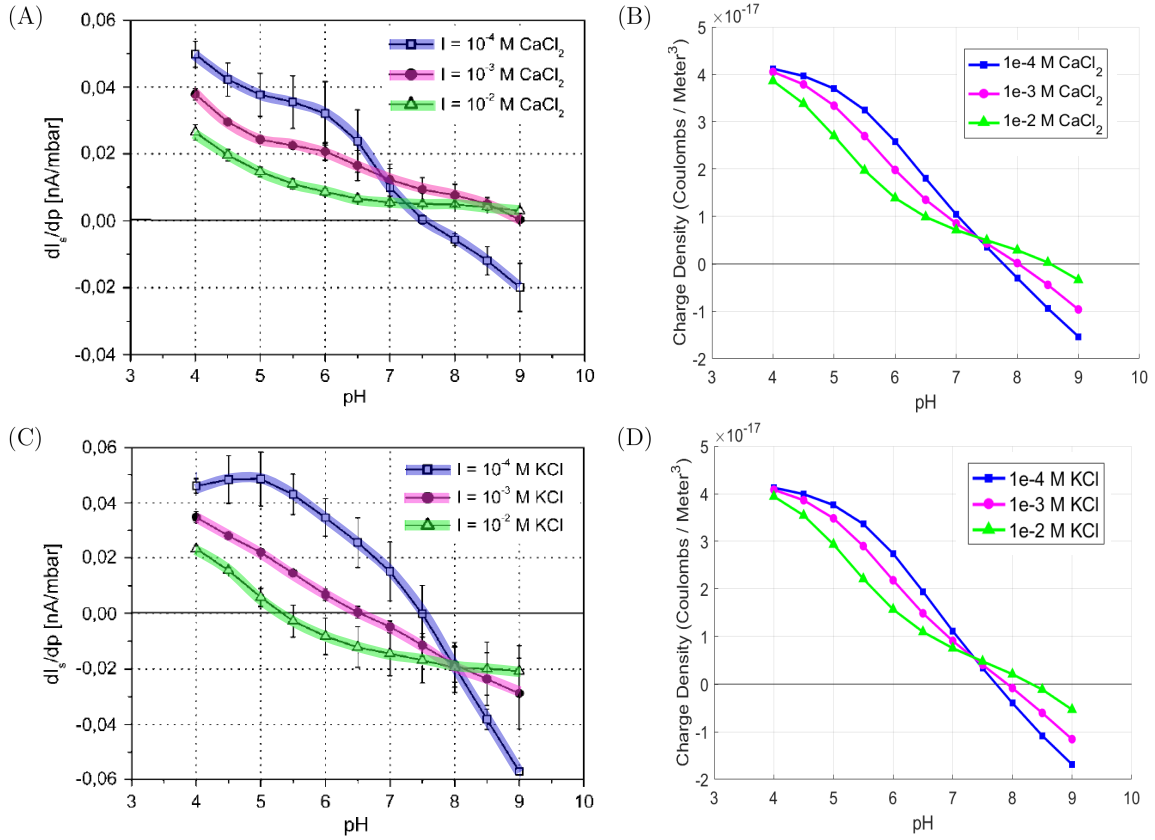


Figure 4.20: Comparison of measured and calculated collagen surface charge density. Experimental measurements of collagen's surface charge [232] are shown for collagen I in $CaCl_2$ (A) and KCl (C). Calculated values of the surface charge density are also shown for collagen I in $CaCl_2$ (B) and KCl (D). Experiments indirectly measured surface charge by instead quantifying the streaming current dI_s/dp rather than the actual surface charge density. However, the shape of the charge vs. pH curves and the isoelectric point, where $dI_s/dp = 0$ and where the charge density = 0, should still match between the experimental and calculated values.

The shape of the calculated $q_{\text{col}}(0)$ vs. pH agrees well with the measured streaming current vs. pH. However, the calculated $q_{\text{col}}(0)$ overestimates the isoelectric point of collagen. There are several possible explanations for this discrepancy. First, it is possible that electrostatics between neighboring tropocollagen molecules should be taken into account by the calculation. Second, a different model may be necessary to accurately represent collagen's hydration shell, since this shell is solid enough to image with the AFM (section 4.2.4). Such a shell is not the liquid layer of ions modeled by Debye Hückel theory. This fact likely means that additional corrections

are needed to calculate accurate amino acid pKa shifts instead of, or in addition to, equation 1.11, derived from Debye-Hückel theory.

Additional corrections to calculate accurate amino acid pKa shifts due to collagen's thick, almost solid hydration shell could potentially be derived by altering the steps in Debye Hückel theory's derivation. Debye-Hückel theory is derived from the Nernst equation and a Taylor expansion of the Poisson Boltzmann equation (section 1.2.2, details in appendix A.2) [164]. Therefore, to model collagen's shell, it may be necessary to use a different function than the Boltzmann distribution and the Nernst equation (equation A.13) to model the distribution of ions around the charged collagen surface. Exploring this option is left to future work. Alternatively, it may be necessary to use a different approximation of the Poisson-Boltzmann equation (section A.14) than the Taylor expansion used in Debye-Hückel theory. However, preliminary investigation into (ii) found that applying other approximations such as the Stern layer or other standard models of the electrical double layer [164] did not correct the model's overestimation of collagen's isoelectric point (not shown).

Alternatively, it may be possible that Debye-Hückel theory still represents collagen's hydration shell, since the calculation of $q_{\text{col}}(0)$ using Debye-Hückel theory has the correct shape of $q_{\text{col}}(0)$ vs. pH compared to the literature (figure 4.20). It may be possible to still use Debye-Hückel theory, but derive a correction factor (for example, a constant that can be subtracted from the resulting charge calculation) to account for the calculation's overestimation of the isoelectric point. The possible approaches to deriving such a correction factor are left for future work.

Regardless, this section's preliminary calculation of $q_{\text{col}}(0)$ confirms that there is still much to be done in understanding and modeling the physics of hydration shells in biology. Further theoretical exploration of the charge calculation described in this section could shed light on the physics of hydration shells, and thereby enhance understanding of the role that such shells play in biological systems.

Chapter 5

Mechanochemical Coupling in the ECM: The Role of Growth Factors and Cell Behaviors in Modulating ECM Mechanics, and Implications for Pancreatic Cancer

5.1 Introduction

The mechanical properties of the ECM play an important role in dictating cell behaviors [1, 3, 5–8]. As briefly mentioned in the preamble of chapter 1 (before section 1.1), the ECM is dramatically restructured during disease [1, 3, 93]. One example of this restructuring is a condition known as fibrosis, the dense deposition of aligned collagen I fibers [3, 93]. While the main component of fibrosis is collagen I, other ECM components can also be incorporated into fibrotic tissue [3, 93]. Fibrosis occurs in scars, heart disease, and solid tumors, and changes the mechanical properties of

the tissue [3, 93]. Since the mechanical properties of tissue regulate cell behaviors, cells in fibrotic tissues likely have altered activities compared to those in nominal, non-fibrotic, tissues [187].

Typically, fibrotic collagen I is not produced by diseased cells, but is instead secreted by surrounding normal cells [3, 93]. For example, in cancer, the remodeling of tumor ECM and deposition of fibrosis is typically performed by fibroblasts, the main cell type responsible for building and maintaining the ECM, or other stromal cells, which become "activated" by nearby tumor or immune cells [3, 93]. Fibroblasts and other stromal cells are activated by signaling molecules involved in wound healing, that are secreted by diseased cells or immune cells in the diseased tissue [249]. While thousands of molecules can activate fibroblasts, certain cell signaling proteins called growth factors (GFs, section 1.1.1) often play a key role [249]. Transforming growth factor β (TGFβ) and platelet derived growth factor (PDGF) are two important GFs that have the ability to activate fibroblasts [3, 249].

The role of fibrosis in disease progression is contradictory [62]. For example, in solid tumors, fibrosis sometimes helps the tumor progress (metastasize, grow at a faster rate, avoid immune cells and drugs, etc...) [3, 62, 93], but other times contains the tumor and hinders cancer progression [62, 93]. Pancreatic tumors are good model systems to demonstrate the dual nature of fibrosis, because such tumors are typically highly fibrotic [93]. Cells in pancreatic tumors are surrounded by fibrosis to the point where the fibrotic ECM acts as a barrier to drugs and immune cells which could eliminate tumor cells [93]. Depending on the orientation of the fibrotic tissue relative to the pancreatic tumor, fibrosis can help tumor progression (if the fibers are normal to the tumor surface, roughly) or hinder tumor progression (if the fibers are tangent to the tumor surface, roughly) [62, 93]. Additionally, the mechanical properties of fibrotic tissue are thought to play a role in determining whether the fibrosis helps or hinders tumor progression [3, 62].

Several factors could modulate the mechanical properties of fibrosis. In particular, small nonfibrillar collagens are often incorporated into fibrotic collagen I deposits [93, 250–253]. In pancreatic tumors, two of these nonfibrillar collagens, called collagen V (colV) [93, 250, 251] and collagen XI (colXI) [252, 253], are thought to play a role in crosslinking fibrotic tissue. Knocking down either colV or colXI hinders tumor progression, and reduces the amount of fibrosis around pancreatic tumors [93, 250–253]. Additionally, the presence of TGFβ [55, 254–257] and PDGF [258–263] in pancreatic tumors affects the structure of the fibrotic tissue and plays a role in tumor progression [249]. Typically, more fibrosis occurs around areas with more TGFβ and knocking down TGFβ can reduce fibrosis [55, 249, 254–257, 260]. Similarly, tumor regions with more PDGF often have more ECM, and knocking down PDGF can reduce fibrosis [249, 258–262]. However, PDGF can also hinder tumor progression [263]. Pancreatic tumors likely have a heterogenous distribution of these GFs within the tumor, with regions of the tumor that contain no TGFβ or PDGF, one or the other GF, and both GFs [249].

It is reasonable to hypothesize that, because colV, colXI, TGFβ, and PDGF all affect the structure of pancreatic tumor fibrosis, these molecules also affect the mechanical properties of the fibrosis. In other words, the mechanical properties of collagen I in fibrotic tissue are likely modulated by these factors, and could help explain why fibrosis helps tumor progression in one case, but hinders tumor progression in another. The purpose of the experiments in this chapter is to quantify the nanoscale mechanical properties of *in vitro* ECMs deposited by fibroblasts in response to these various molecules. AFM creep and relaxation experiments (section 2.1.3.2) and amplitude modulation-frequency modulation atomic force microscopy (AM-FM AFM, section 2.1.3.4) were employed to fulfill this aim. The aims of the experiments in this chapter are: (i) to investigate the role of cell signaling (GFs) in modulating ECM mechanics, and (ii) to investigate whether colV and colXI are actually used in ECM

crosslinking, and why they may have an effect on ECM mechanics. Experiments in this chapter simulate pancreatic tumor environments by exposing fibroblasts to various combinations of TGFβ and PDGF, and allowing the fibroblasts to build their own *in vitro* ECM in response to these GFs. ECMs produced by mutant fibroblasts unable to secrete colV or colXI were studied in addition to ECMs produced by unmutated, wild type (WT) fibroblasts.

5.2 Materials and methods

Cell-derived ECM samples were prepared and provided by Dr. Alex Gordon-Weeks, per the standard protocol [264]. Briefly, cell culture wells (ibidi 80426) were coated with gelatin (Sigma-Aldrich G1393) crosslinked with 1% glutaraldehyde (Sigma-Aldrich 340855) in Dulbecco's PBS (DPBS, Sigma-Aldrich D5796). Mouse embryonic fibroblast (NIH3T3) cells were then seeded onto the crosslinked gelatin mats, and allowed to grow and deposit ECM for 5-8 days until the deposited ECM was clearly visible using second harmonic generation (SHG). The cells generating the ECMs were: wild type (WT) NIH3T3 mouse embryonic fibroblasts, collagen V knockdown (colVKD) mutant NIH3T3s, collagen XI knockdown (colXIKD) mutant NIH3T3s, or no cells as a control. The mutant cells were created by Dr. Alex Gordon-Weeks, who mutated the α1 chain of the colV and XI tropocollagen molecules. The α1 chain is one of the three polypeptide chains that make up the tropocollagen V and XI triple helix [250].

To prepare the ECMs, cells were cultured in high glucose Dulbecco's Modified Eagle's Medium (DMEM, Sigma-Aldrich D5796) supplemented with 10% fetal calf serum (FCS, Sigma-Aldrich C8056). Four wells of each cell type were prepared. Each well was then exposed to growth factors (GFs), added to the medium each day during the 5-8 day growth period. The first well was left untreated, the second well was treated with PDGF (bioLegend 558802), the third treated with TGFβ (bioLegend

763102), and the fourth treated with both PDGF and TGFβ. The resulting ECMs consisted mostly of collagen I, as determined by Dr. Alex Gordon-Weeks.

At the end of the 5-8 day growth period, ECMs were de-cellularized using Triton-X-100 (Fisher BioReagents BP151-500). Samples were then washed three times with DPBS, then delivered to me. Samples were stored at 4 ^{o}C until they were imaged using an Oxford Instruments Asylum Research Cypher ES AFM. All imaging was performed as fast as possible, within 14 days, to prevent degradation of the ECMs, which are stable at 4 ^{o}C for two weeks [264]. At least two biological replicates were performed for all ECMs except those produced by colXIKD cells.

ECMs were prepared for AFM as follows. First, PBS was removed from each well. Second, the bottom of one well was cut out of the dish using a scalpel. Quickly, to prevent the sample from drying out, the well bottom was secured to a magnetic disk (which secures the sample to the AFM during an experiment) using double-sided foam (RS Components 554-844), and moved to the Cypher ES AFM.

In order to simulate physiological conditions, and to keep the sample hydrated, 200 - 400 μL of live cell imaging solution (1x PBS with HEPES, where 1x denotes the fact that the PBS reflects physiological ion concentrations, Sigma-Aldrich A14291DJ) were deposited onto the sample. Live cell imaging solution was also added to any remaining wells in the dish to keep the remaining wells hydrated for future experiments. Any unused wells were kept on ice or returned to 4 ^{o}C.

After adding the live cell imaging solution to the sample, three AFM experiments were performed on the sample. The first two experiments were (i) microscale and (ii) nanoscale creep (section 1.3.3.2) and relaxation (section 1.3.3.1) experiments (section 2.1.3.2). Indirect cantilever actuation was used for creep and relaxation experiments (section 2.1.3.1). The third experiment was AM-FM AFM (section 2.1.3.4). AM-FM AFM is this chapter's main experimental technique. For AM-FM AFM, the cantilever was driven by photothermal actuation (section 2.1.3.1) at full blueDrive$^{\text{TM}}$

power. All experiments were performed using Oxford Instruments Asylum Research software version 16.9.220 in Igor Pro software version 6.38B01.

Microscale creep and relaxation experiments were performed using a modified AC240TSA cantilever ($k_c \sim 2.6$ nN/nm, $R = 49.21\ \mu\text{m} \pm 0.72\ \mu\text{m}$) with a glass bead (Whitehouse Scientific Ltd. NIST Traceable monodisperse particle standard MS0049) glued (flex+bond weicon 13351085) to the tip. Nanoscale experiments were performed on the sample using an unmodified AC240TSA cantilever ($k_1 \sim 1.6$ nN/nm, $k_2 \sim 58.8$ nN/nm, $f_1 \sim 21$ kHz in liquid, $f_2 \sim 150$ kHz in liquid, $R = 7 \pm 3$ nm). At least three positions on each sample were measured. Both cantilevers were calibrated via glass indentation and the thermal noise method, detailed in section 2.1.1. While this calibration method increases the risk of blunting the tip, GetReal$^{\text{TM}}$ calibration could not be used on the modified AC240TSA because the modified AC240TSA is not in the cantilever database required for GetReal$^{\text{TM}}$ calibration (section 2.1.1). Therefore, the glass indentation method was used to keep calibration of both cantilevers consistent.

After the experiment, AM-FM AFM height images of ECM topology were flattened using Oxford Instruments Asylum Research software version 16.10.208 in Igor-Pro software version 6.38B01, in order to remove any variations in sample topology that were not due to ECM features. This flattening was done by hand, in order to avoid introducing flattening artifacts. The processed files were then analyzed by a custom script in MATLAB R2019b 9.7.0.1261785 that calculated the loss tangent, $\tan\delta$, and storage modulus, E', of the sample (equations 2.21 and 2.24, section 2.1.3.4), then tested the best model to describe the ECM's viscoelasticity and calculated the relevant material constants (as described in section 3.2). Data from relaxation and creep experiments were also analyzed in MATLAB R2019b 9.7.0.1261785 by fitting exponential curves to dwell data in order to calculate relaxation τ_r and creep τ_c time responses (section 2.1.3.2). Sample comparison p values were calculated from paired t tests between samples.

5.3 Results

5.3.1 Distributions and statistics of ECM AM-FM AFM data

E' and $\tan\delta$ distributions varied depending on the type of cell-derived ECM being measured. Figure 5.1 shows that E' and $\tan\delta$ distributions of ECMs produced by WT cells were multimodal. Such multimodal distributions indicate that multiple materials and different ECM configurations were likely present in any given area of the sample. Since the ECM is composed of a complex mixture of molecules and structures [3, 4, 129], it is likely that the peaks in the multimodal E' and $\tan\delta$ distributions correspond to various different ECM constituents.

As shown in figure 5.1, the multimodal E' and $\tan\delta$ distributions of WT cell-derived ECMs prevented accurate calculation of sample means and standard deviations when the standard formulas were used. To overcome this issue, as described in section 2.1.3.4.2, the mean and standard deviation of AM-FM AFM data were calculated by fitting Gaussians to the data distributions, rather than via the standard formulas. In this case, the mean and standard deviation represent the most prominent peak of the distribution, corresponding to the most prevalent component of the ECM. As shown by figure 5.1, this Gaussian fit method of calculating sample statistics matches the values from the standard formulas in many cases, and especially if the distribution is unimodal. Therefore, as described in section 2.1.3.4.2, the mean and standard deviation of all AM-FM AFM measurements of cell-derived ECMs were calculated by fitting Gaussians to the data distributions.

Figure 5.2 shows that E' and $\tan\delta$ distributions for ECMs produced by colVKD cells appeared unimodal, but were often best described with a two term Gaussian model (equation 2.28). The fact that the distributions were nearly unimodal suggests that colVKD ECMs contain fewer distinct components than WT ECMs. Rather than arising from different constituent components of colVKD ECMs, the observed

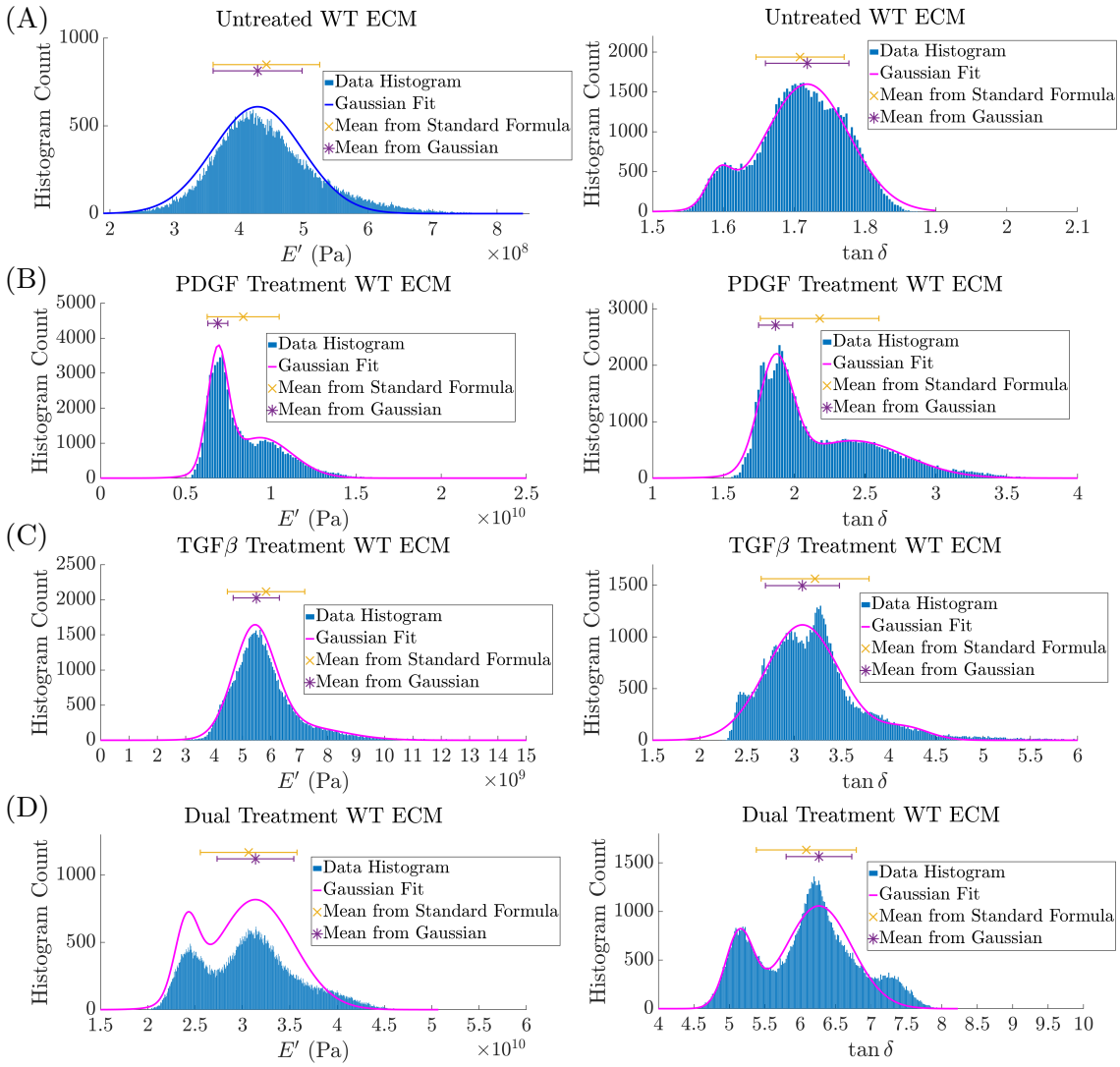


Figure 5.1: Representative distributions from AM-FM AFM of WT ECMs. All distributions were obtained from the values of individual pixels of a single AM-FM AFM image. Storage modulus, E', and loss tangent, $\tan\delta$, distributions are shown in the left and right column, respectively, for ECMs produced by wild type (WT) cells without exposure to growth factors (A), treated with PDGF (B), treated with TGFβ (C), or exposed to a dual treatment of both PDGF and TGFβ (D). A Gaussian fit to the distribution is shown as a magenta line if a two term Gaussian was used or as a dark blue line if a single term Gaussian was used. Selection of the single or two term Gaussian is described in section 2.1.3.4.2. The mean (points) and standard deviation (error bars) calculated via the standard formulas and calculated from the Gaussian fit constants (as described in section 2.1.3.4.2) are shown as an orange x or a purple asterisks, respectively. While some fits, shown in (A) and (D), overestimate the height of the histogram peak, the mean and standard deviation extracted from these fits still match those calculated from the standard formulas.

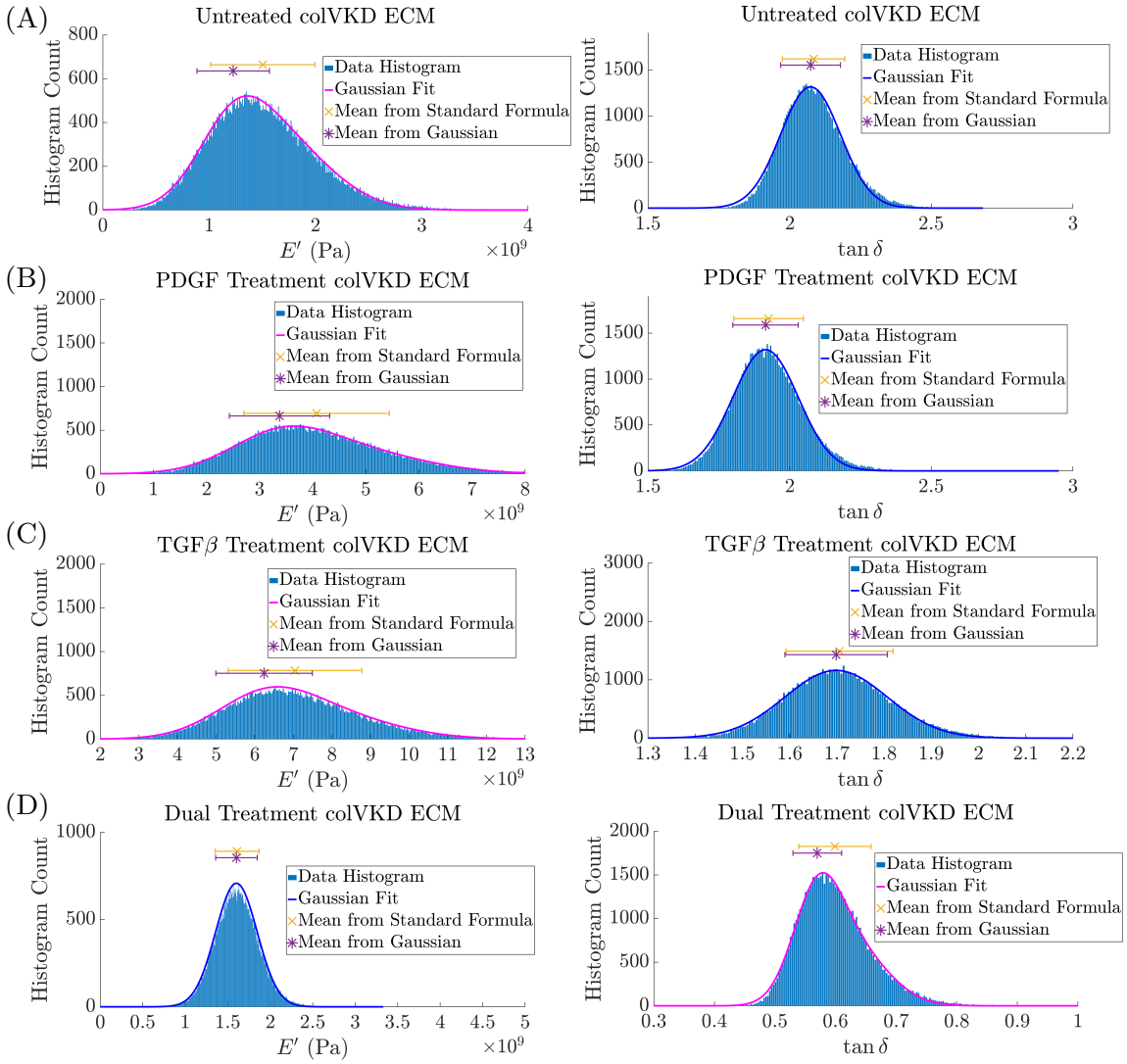


Figure 5.2: Representative distributions from AM-FM AFM of colVKD ECMs. All distributions were obtained from the values of individual pixels of a single AM-FM AFM image. Storage modulus, E', and loss tangent, $\tan\delta$, distributions are shown in the left and right column, respectively, for ECMs produced by collagen V knockdown (colVKD) mutants without exposure to growth factors (A), treated with PDGF (B), treated with TGFβ (C), or exposed to a dual treatment of both PDGF and TGFβ (D). A Gaussian fit to the distribution is shown as a magenta line if a two term Gaussian was used or as a dark blue line if a single term Gaussian was used. Selection of the single or two term Gaussian is described in section 2.1.3.4.2. The mean (points) and standard deviation (error bars) calculated via the standard formulas and calculated from the Gaussian fit constants (as described in section 2.1.3.4.2) are shown as an orange x or a purple asterisks, respectively. While some fits, shown in (D), overestimate the height of the histogram peak, the mean and standard deviation extracted from these fits still match those calculated from the standard formulas.

bimodal distributions of colVKD ECMs likely arise from different ECM structures, such as different orientations, clumping, or varying intermolecular interactions of the constituent polymers. Also shown in figure 5.2, calculating the mean and standard deviation of colVKD ECM E' and $\tan\delta$ using the standard formulas or via a Gaussian fit to the distribution both result in similar values.

Similar distributions to those of AM-FM AFM measurements of ECMs produced by colVKD cells were also observed for ECMs produced by colXIKD cells, figure 5.3, and acellular gelatin controls, figure 5.4. Again, these distributions appeared unimodal, but were often best described with a two term Gaussian model. As with colVKD ECMs, this observation suggests that colXIKD ECMs and gelatin controls contained fewer components, and that the observed bimodal distributions likely arose from different ECM structures rather than different ECM constituents. Regardless, calculating the mean and standard deviation of colXIKD ECM or gelatin E' and $\tan\delta$ using the standard formulas or via a Gaussian fit to the distribution both resulted in similar values for the mean and standard deviation.

The multimodal distributions from measurements of ECMs produced by WT cells required the use of Gaussian fits to calculate means and standard deviations that represented the data well. For acellular controls and mutant ECMs, the mean and standard deviation could be accurately calculated via either method. Therefore, in order to ensure that means and standard deviations accurately represented the data in this chapter, these quantities were calculated from Gaussian fits (section 2.1.3.4.2) to distributions of the height, E', and $\tan\delta$ measurements. For biological replicate statistics, the distribution used for the fit comprised of pixel values from all AM-FM AFM images from a particular biological replicate. For overall statistics, the distribution comprised of pixel values from all AM-FM AFM images of a sample. The means and standard deviations of other quantities, such as the viscoelastic material constants of a sample, were calculated via the standard formulas.

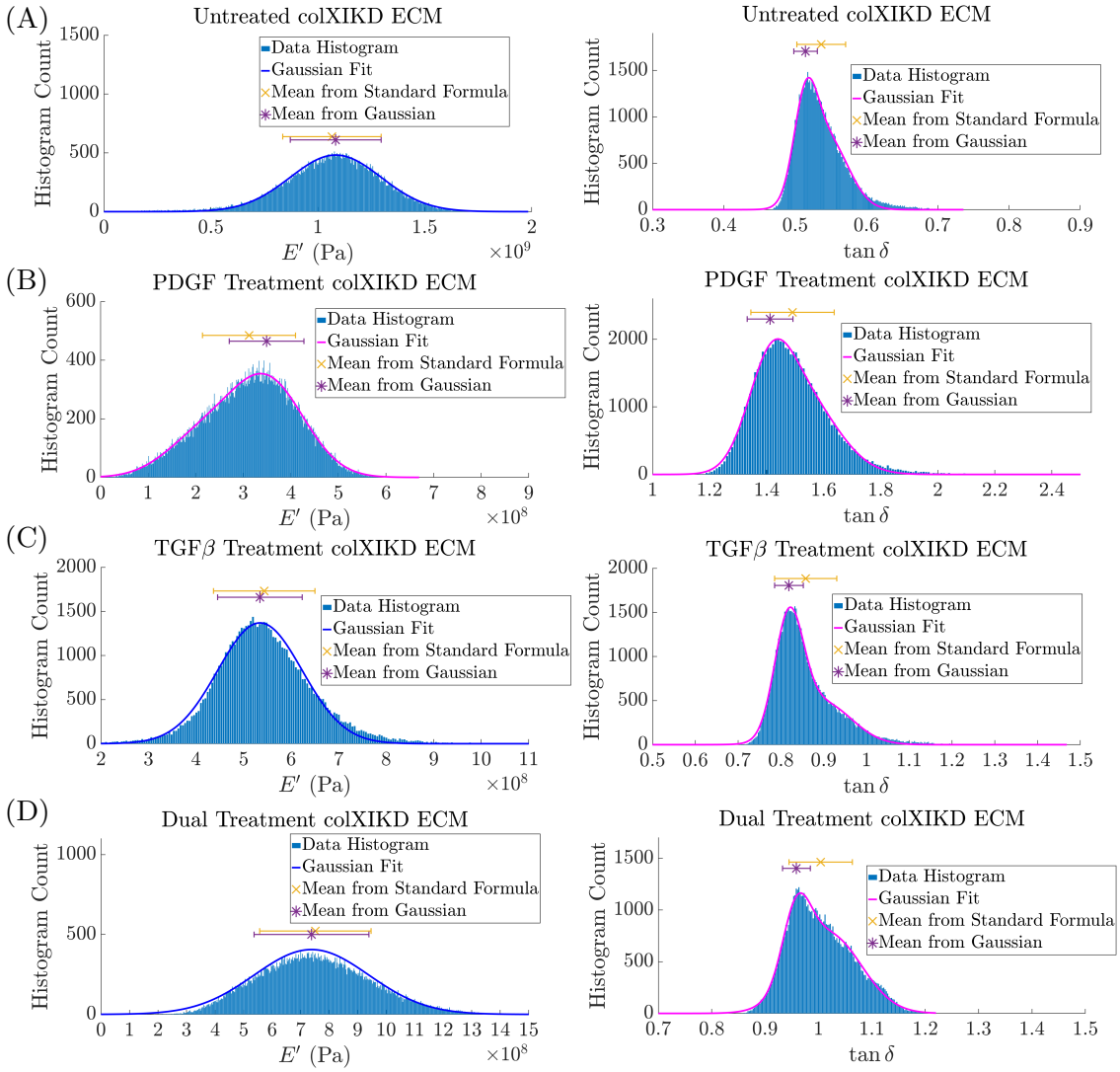


Figure 5.3: Representative distributions from AM-FM AFM of colXIKD ECMs. All distributions were obtained from the values of individual pixels of a single AM-FM AFM image. Storage modulus, E', and loss tangent, $\tan\delta$, distributions are shown in the left and right column, respectively, for ECMs produced by collagen XI knockdown (colXIKD) cells without exposure to growth factors (A), treated with PDGF (B), treated with TGFβ (C), or exposed to a dual treatment of both PDGF and TGFβ (D). A Gaussian fit to the distribution is shown as a magenta line if a two term Gaussian was used or as a dark blue line if a single term Gaussian was used. Selection of the single or two term Gaussian is described in section 2.1.3.4.2. The mean (points) and standard deviation (error bars) calculated via the standard formulas and calculated from the Gaussian fit constants (as described in section 2.1.3.4.2) are shown as an orange x or a purple asterisks, respectively. While some fits, shown in (D), overestimate the height of the histogram peak, the mean and standard deviation extracted from these fits still match those calculated from the standard formulas.

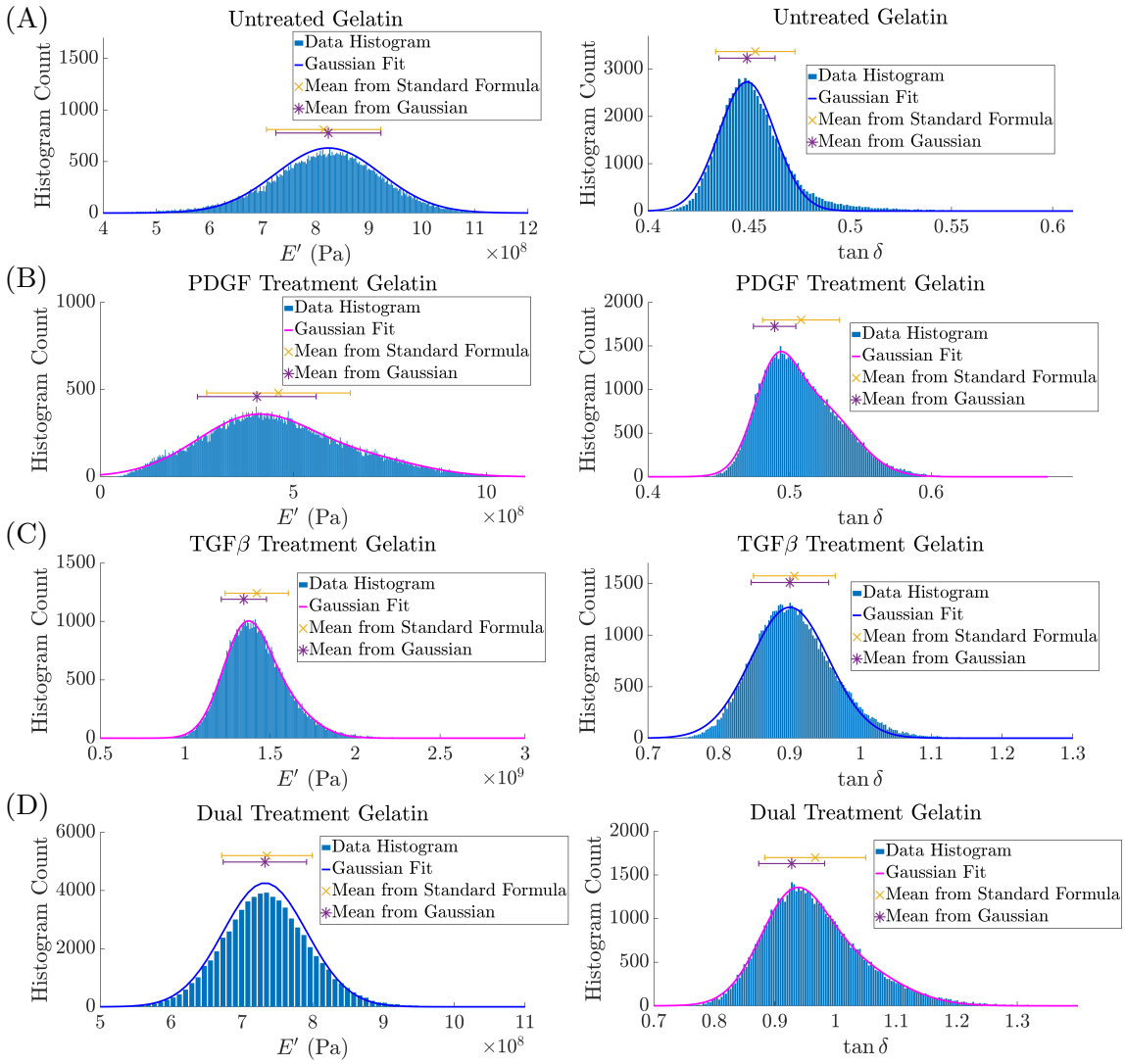


Figure 5.4: Representative distributions from AM-FM AFM of gelatin. All distributions were obtained from the values of individual pixels of a single AM-FM AFM image. Storage modulus, E', and loss tangent, $\tan\delta$, distributions are shown in the left and right column, respectively, for acellular matrices composed of gelatin without exposure to growth factors (A), treated with PDGF (B), treated with TGFβ (C), or exposed to a dual treatment of both PDGF and TGFβ (D). A Gaussian fit to the distribution is shown as a magenta line if a two term Gaussian was used or as a dark blue line if a single term Gaussian was used. Selection of the single or two term Gaussian is described in section 2.1.3.4.2. The mean (points) and standard deviation (error bars) calculated via the standard formulas and calculated from the Gaussian fit constants (as described in section 2.1.3.4.2) are shown as an orange x or a purple asterisks, respectively. While some fits, shown in (A) and (D), overestimate the height of the histogram peak, the mean and standard deviation extracted from these fits still match those calculated from the standard formulas.

5.3.2 Topology, storage modulus, and loss tangent of cell-derived ECMs

AM-FM AFM was performed on de-cellularized ECMs produced on gelatin mats by WT (not mutated), colVKD, and colXIKD fibroblasts in response to growth factors (GFs). Gelatin mats, without any cells, treated with each GF served as aceullular controls. The four GF treatments were: untreated, PDGF only, TGFβ only, or both PDGF and TGFβ (dual). Representative AM-FM AFM images of sample topologies are shown in figure 5.5.

As shown in figure 5.5, cells deposited ECM in all conditions. ECM topology varied, depending on the cells producing the matrix and GF treatment. WT ECMs showed the largest change in ECM topology between different GF treatments. Untreated WT cells deposited a few small fibers. PDGF treated WT cultures had some small and some large fibers. TGFβ and dual treated WT ECMs had many large fibers. Mutant ECMs in untreated cultures were similar to WT cultures. However, unlike WT cultures, mutant fibroblasts did not produce fibers in response to GFs. Instead of large fibers, mutants deposited a few sparse ECM clumps and small fibrils. These observations are confirmed by the mean heights of each sample, shown in figure 5.6 (A). Additionally, these observations are representative of the entire sample, as confirmed by Dr. Alex Gordon Weeks via second harmonic generation (SHG, not shown). The height of gelatin samples (acellular controls) did not vary with GF treatment. This observation confirms that ECM deposited in WT, colVKD, and colXIKD samples was the result of cell activities. Additionally, these results show that mutation impairs cell abilities to secrete and organize ECM into large fibers.

Observations from figure 5.5 and 5.6 (A) are general for all samples. However, variation in sample topology was observed between certain biological replicates, as shown in figure 5.6 (B). WT cultures showed the most variation between biological replicates. In particular, the second and fourth biological replicate of TGFβ and

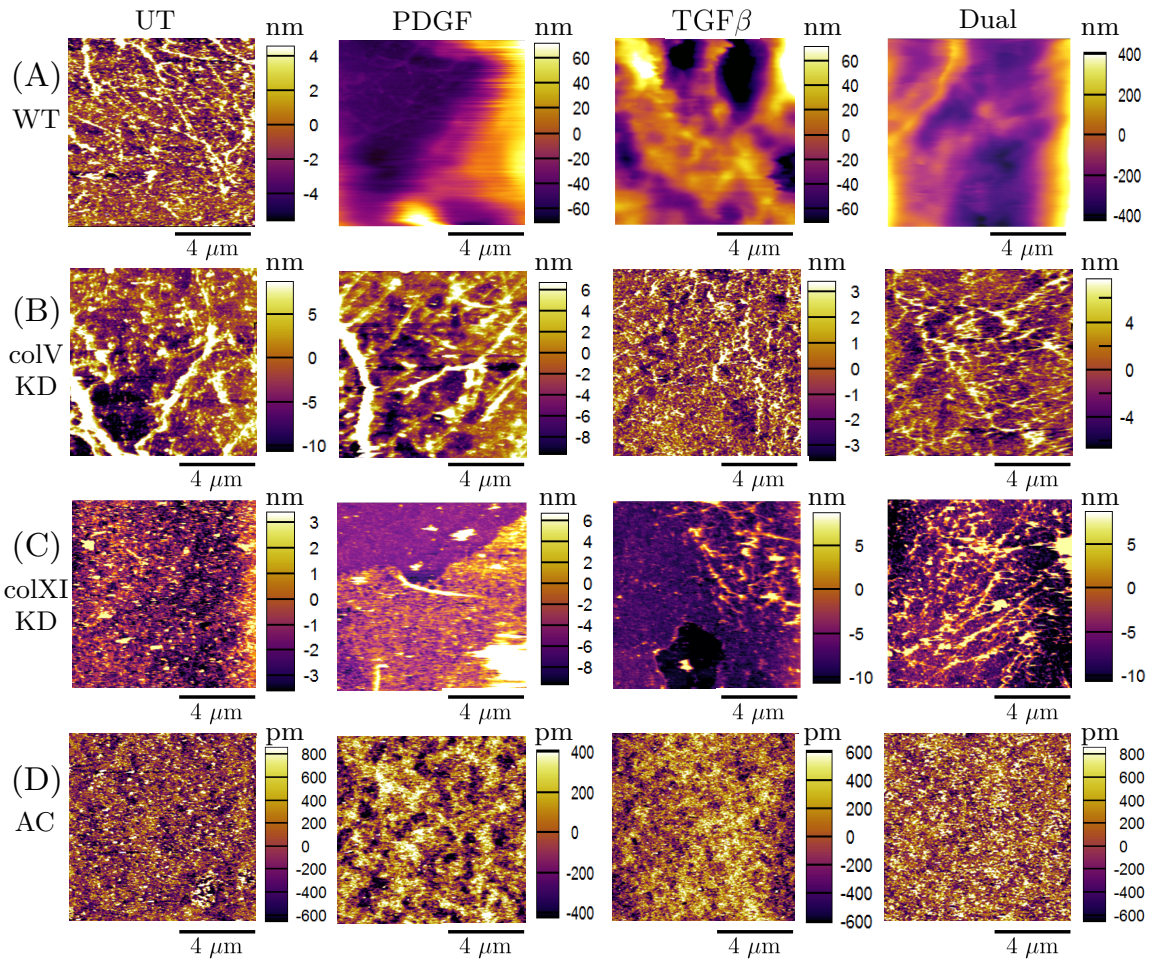


Figure 5.5: Representative AM-FM AFM height images of cell-derived ECMs. ECMs were produced on gelatin mats by different fibroblast cell types in cultures exposed to various growth factors (GFs). GF treatments, shown left to right, were: untreated (UT), PDGF only, TGFβ only, or both PDGF and TGFβ (dual). ECMs produced by wild type (WT) cells, collagen V knockdown (colVKD) mutant cells, and collagen XI knockdown (colXIKD) mutant cells are shown in (A)-(C), respectively. Additionally, acellular control (AC) matrices, gelatin mats without any cells but treated with the various GFs, are shown in (D).

dual treated WT samples formed larger fibers, while the other two replicates did not. Example images from each of these cases are shown in figure 5.6 (C) and (D), respectively. Variation between colVKD replicates depended on the size of the clumped ECM in these samples, rather than an overall change in ECM topology. Gelatin samples did not vary in height between biological replicates. Together, these results suggest that WT cells produce ECM in response to GFs in a cell dependent manner.

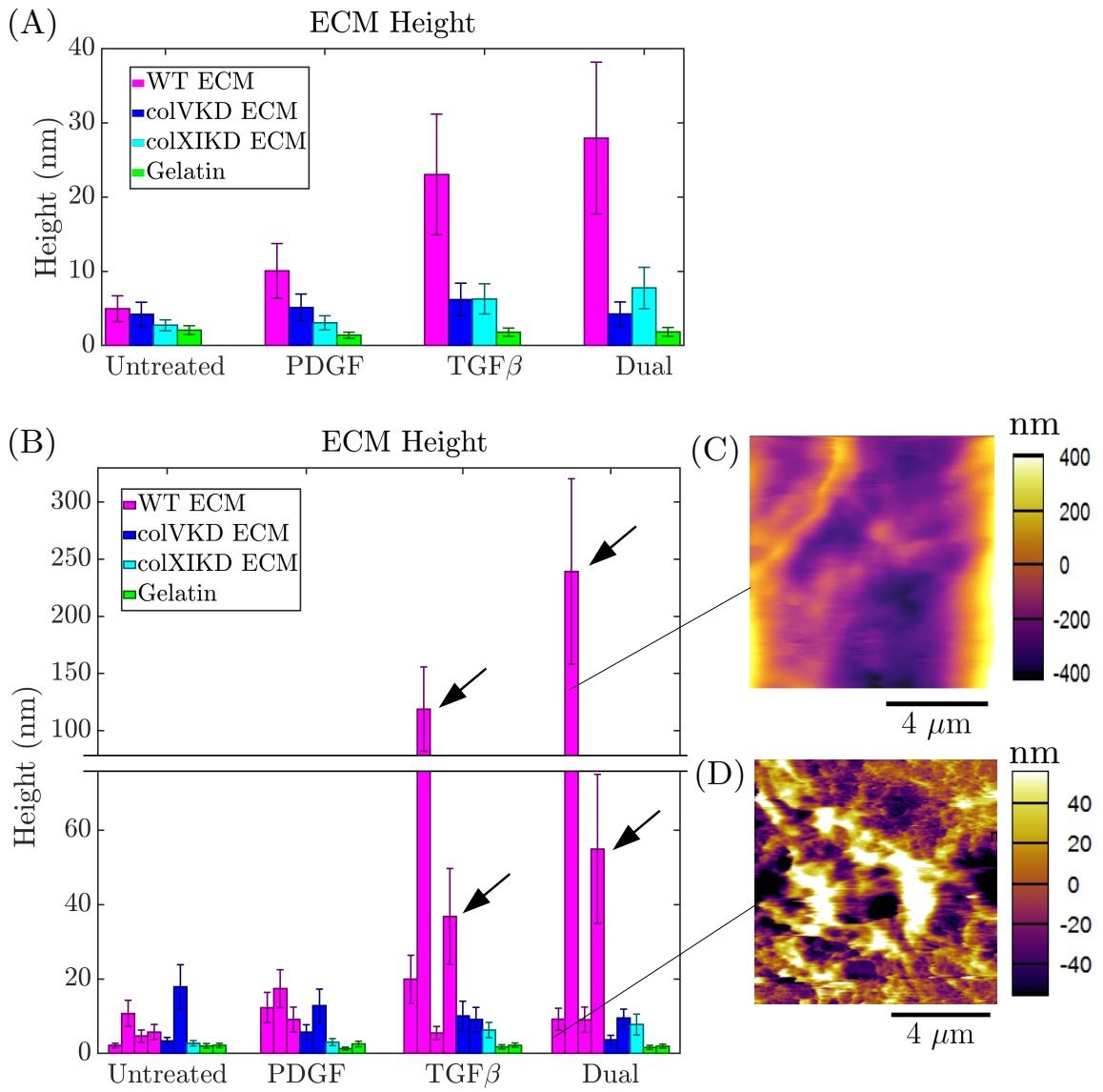


Figure 5.6: Feature height of cell-derived ECMs. Cell-derived ECMs were produced by wild type (WT, magenta) fibroblasts, collagen V knockdown (colVKD, dark blue) mutants, and collagen XI knockdown (colXIKD, light blue) mutants in untreated cultures, PDGF treated cultures, TGFβ treated cultures, cultures treated with both PDGF and TGFβ (dual). Gelatin (green) served as an acellular control. Mean heights of features calculated from all AM-FM AFM images of a sample are shown in (A). Mean heights of features calculated from each biological replicate are shown in (B). All error bars represent standard deviations. Black arrows indicate biological replicates where cells deposited more ECM fibers. A representative image of large fibers from a biological replicate of dual WT cultures is shown in (C). A different biological replicate of dual WT cultures, with smaller fibers, is shown in (D) to highlight the variation in sample topology between biological replicates. While both images were of dual treated WT ECMs, they are representative of the variation between biological replicates of all WT samples.

Therefore, resulting ECM topology is spatially heterogeneous, depending on the cells in any given area. Mutation limits the heterogeneity in topology of the secreted ECM, likely by limiting cell abilities to secrete and organize ECM fibers.

Next, AM-FM AFM measurements of E' and $\tan\delta$ in each sample were compared, to see if differences in sample topology between the various conditions correlated with differences in these mechanical properties. Representative AM-FM AFM images of sample E' are shown in figure 5.7. The E' images in figure 5.7 correspond to the topology images in figure 5.5 for each sample. Figure 5.8 (A) shows how ECM storage moduli, E', varied between samples. The value of E' varied more in WT samples than mutant samples in response to GF treatment. WT samples with more fibers (TGFβ and dual treated samples) had higher E' as well ($p < 0.01$ for both samples). For mutant samples and gelatin, E' did not vary much with GF treatment ($p > 0.5$ for all comparisons). For colVKD samples, PDGF treatment slightly increased E' ($p = 0.01$, compared to untreated). Other treatments did not alter colVKD ECM E' significantly from the untreated samples, or the gelatin control ($p = 0.30$, 0.55, and 0.12 for untreated, TGFβ, and dual, respectively, vs. galatin in the same treatment). For colXIKD samples, E' did not vary significantly with GF treatment ($p = 0.65$, 0.12, and 0.68 for PDGF, TGFβ, and dual vs. untreated, respectively), and was not significantly different from the gelatin control ($p = 0.95$, 0.45, 0.23, and 0.96 for untreated, PDGF, TGFβ, and dual, respectively vs. gelatin in the same condition). For gelatin controls, E' did not vary with GF treatment ($p = 0.25$, 0.23, and 0.61 for PDGF, TGFβ, and dual, respectively, vs. untreated), suggesting that any observed changes in E' are the result of cell activities, rather than the GFs incorporating into the gelatin. Together, these results suggest that the changes in WT sample topology are accompanied by changes in E'. Mutation impairs cellular abilities to deposit ECM, as well as modulate E' of the resulting matrix.

Figure 5.8 (B) shows how ECM E' varied between biological replicates. As with

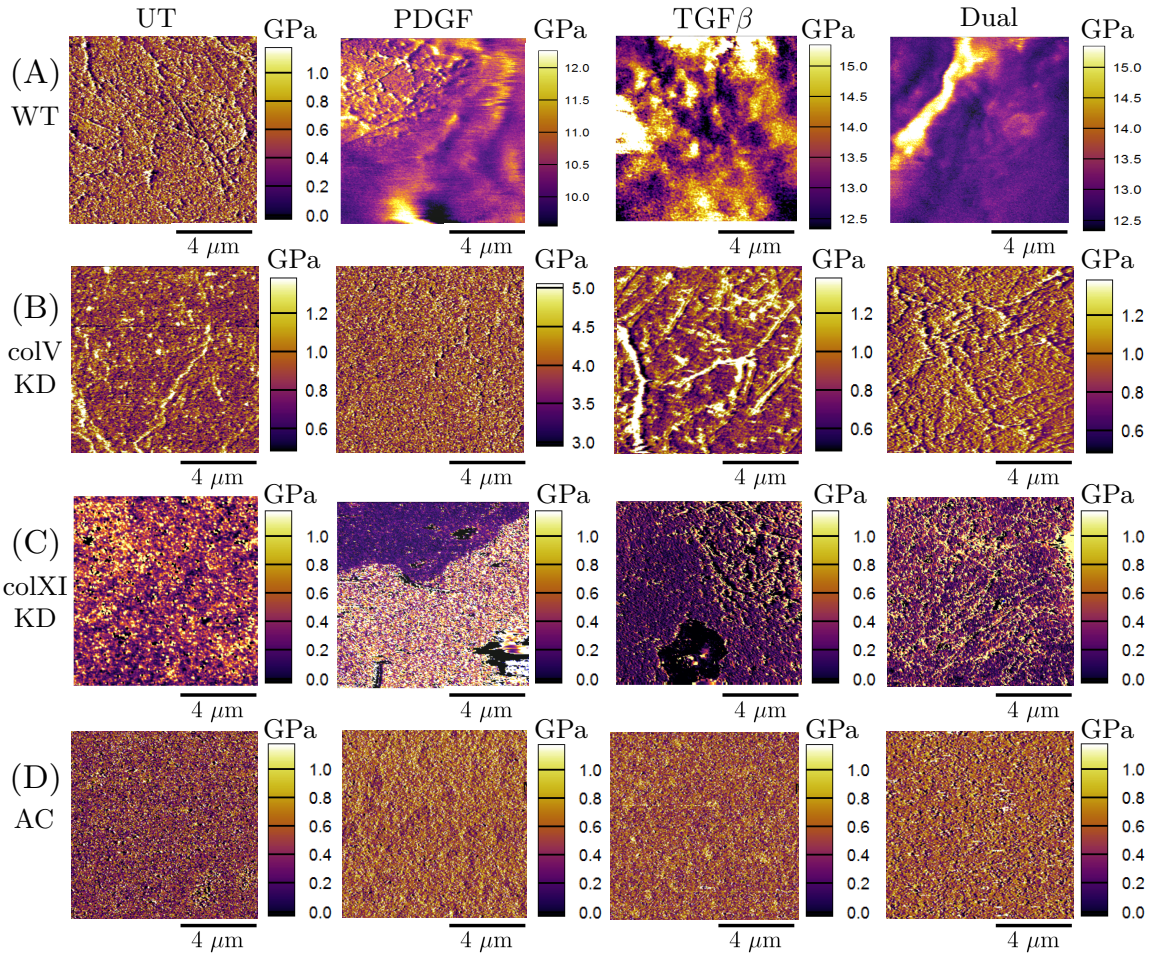


Figure 5.7: Representative AM-FM AFM images of ECM storage moduli (E'). ECMs were produced on gelatin mats by different fibroblast cell types in cultures exposed to various growth factors (GFs). GF treatments, shown left to right, were: untreated (UT), PDGF only, TGFβ only, or both PDGF and TGFβ (dual). Matrices produced by wild type (WT) cells, collagen V knockdown (colVKD) mutants, and collagen XI knockdown (colXIKD) mutants are shown in (A)-(C), respectively. Additionally, acellular control (AC) matrices, gelatin mats without any cells but treated with the various GFs, are shown in (D). All E' images in this figure correspond to the height images in figure 5.5.

ECM topology (figure 5.6), biological replicates showed more variation for WT samples than for mutant or gelatin samples. For WT samples, the increase in E' of samples that had larger fibers was not universal for all biological replicates. For example, not all biological replicates in TGFβ and dual treated WT cultures increased E'compared to untreated WT cultures. Less variation was observed between biological replicates

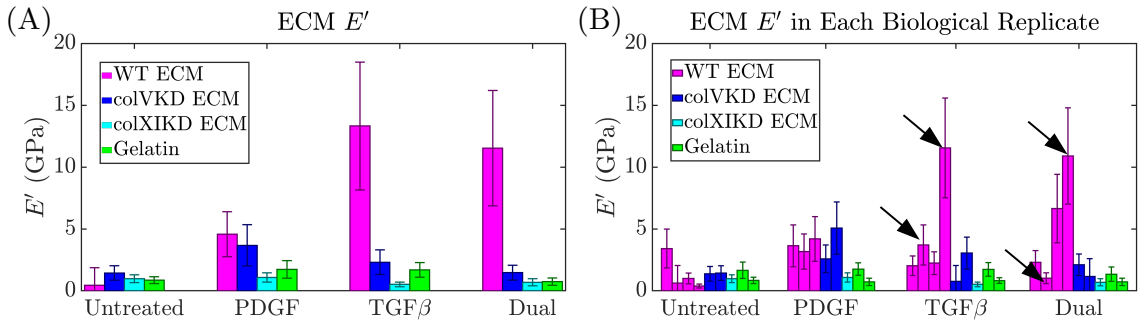


Figure 5.8: Storage modulus (E') of cell-derived ECMs. Cell-derived ECMs were produced by wild type (WT, magenta) fibroblasts, collagen V knockdown (colVKD, dark blue) mutants, and collagen XI knockdown (colXIKD, light blue) mutants in untreated cultures, PDGF treated cultures, TGFβ treated cultures, or dual treated cultures. Gelatin (green) served as an acellular control. The mean E' calculated from all AM-FM AFM images of a sample is shown in (A). The mean E' calculated for each biological replicate is shown in (B). All error bars represent the standard deviation. Black arrows indicate biological replicates where cells deposited more ECM fibers.

of colVKD ECMs and gelatin controls. Additionally, E' of all biological replicates for mutant matrices was much closer to that of gelatin. Together, these results suggest that the elastic properties of WT ECMs are the result of cell activities and are heterogeneous, depending on the cells depositing and remodeling the matrix. Therefore, ECM E' is likely spatially heterogeneous across the sample. Mutation (both colVKD and colXIKD) impairs cell abilities to modify their surroundings, thereby resulting in a more homogeneous E' throughout the ECM.

Representative AM-FM AFM images of sample loss tangents, $\tan\delta$, are shown in figure 5.9. The $\tan\delta$ images in figure 5.9 correspond to the topology images in figure 5.5 and E' images in figure 5.7. Figure 5.10 (A) shows how the mean $\tan\delta$ varied between samples. As with sample height and E', WT ECMs showed more variation in $\tan\delta$ with GF treatment than mutant or gelatin samples. In particular, samples with larger fibers (TGFβ and dual treated WT samples) had higher $\tan\delta$ than samples with fewer fibers ($p = 0.02$ for both treatments compared to untreated). The value of $\tan\delta$ for all WT matrices was significantly higher than the gelatin control ($p < 0.01$ for all comparisons). The value of $\tan\delta$ for mutant ECMs did not vary with GF

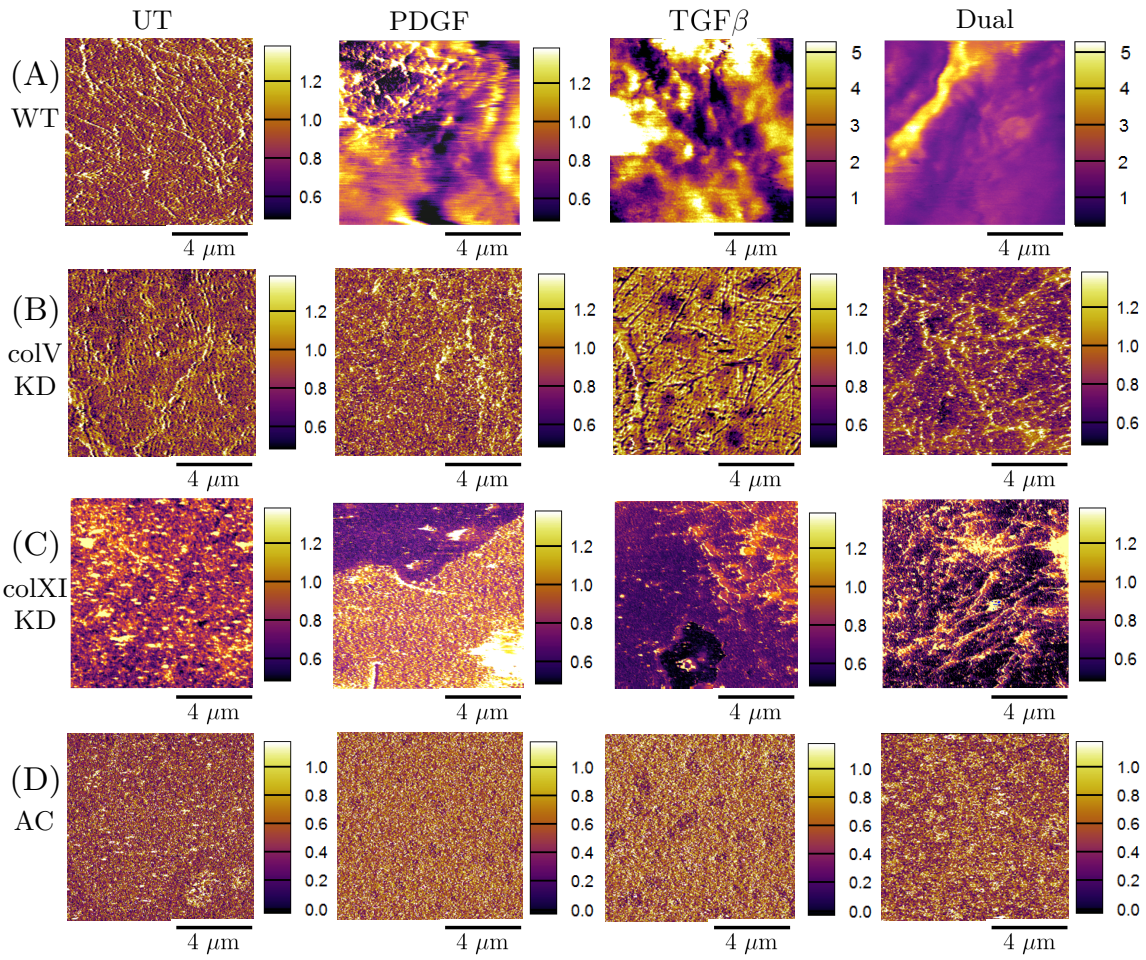


Figure 5.9: Representative AM-FM AFM images of ECM loss tangents ($\tan\delta$). ECMs were produced on gelatin mats by different fibroblast cell types in cultures exposed to various growth factors (GFs). GF treatments, shown left to right, were: untreated (UT), PDGF only, TGFβ only, or both PDGF and TGFβ (dual). Matrices produced by wild type (WT) cells, collagen V knockdown (colVKD) mutants, and collagen XI knockdown (colXIKD) mutants are shown in (A)-(C), respectively. Additionally, acellular control (AC) matrices, gelatin mats without any cells but treated with the various GFs, are shown in (D). All $\tan\delta$ images in this figure correspond to the height images in figure 5.5 and storage modulus images in figure 5.7.

treatment. Specifically, for colVKD samples, $\tan\delta$ was only slightly higher than the gelatin control in some of the samples ($p = 0.03$, 0.33, 0.07, and 0.71 for untreated, PDGF, TGFβ, and dual vs. gelatin in the same treatment). For colXIKD samples, only dual treatment resulted in $\tan\delta$ higher than the gelatin control ($p = 0.06$).

Figure 5.10 (B) shows how ECM $\tan\delta$ varied between biological replicates. The

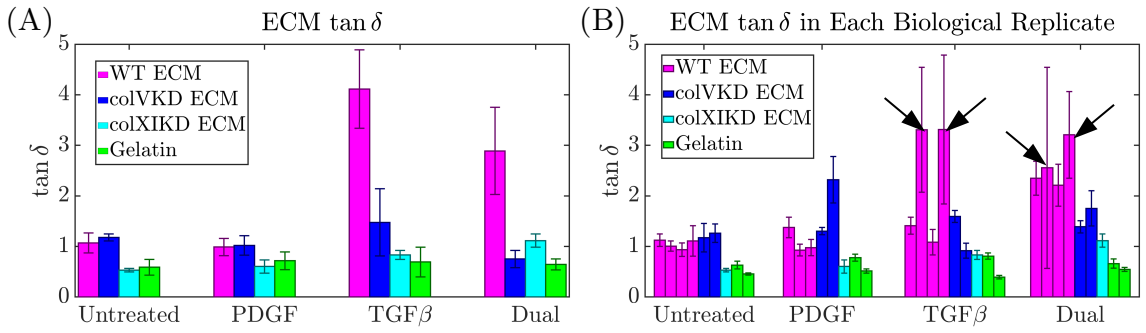


Figure 5.10: Loss tangent ($\tan\delta$) of cell-derived ECMs. Cell-derived ECMs were produced by wild type (WT, magenta) fibroblasts, collagen V knockdown (colVKD, dark blue) mutants, and collagen XI knockdown (colXIKD, light blue) mutants in untreated cultures, PDGF treated cultures, TGFβ treated cultures, or dual treated cultures. Gelatin (green) served as an acellular control. The mean $\tan\delta$ calculated from all AM-FM AFM images of a sample is shown in (A). The mean $\tan\delta$ from each biological replicate is shown in (B). All error bars represent the standard deviation. Black arrows indicate biological replicates where cells deposited more ECM fibers.

value of $\tan\delta$ was more consistent between biological replicates than sample height or E'. However, as with topology and E', $\tan\delta$ varied more between biological replicates of WT samples than mutant or gelatin samples. WT samples that had more fibers (black arrows in figure 5.10 (B)) had higher $\tan\delta$, and/or higher variation in $\tan\delta$. The value of $\tan\delta$ did not vary much with GF treatment between biological replicates of mutant samples. For colVKD samples, $\tan\delta$ only varied significantly between biological replicates in PDGF treated samples. For gelatin controls, $\tan\delta$ did not vary between biological replicates. These observations suggest that $\tan\delta$ of WT ECMs depends on cell activities, and is likely spatially heterogeneous across the sample, depending on the cells in any given area. Mutation impairs cell abilities to modify their surroundings, thereby resulting in a more homogeneous $\tan\delta$ throughout the ECM, regardless of GFs.

Together, the results in this section suggest that cell activities alter topology, energy storage, and energy dissipation of the ECM they produce. GF treatment causes cells to alter the amount of ECM they deposit, as well as the mechanical properties of the resulting matrices, in a heterogeneous manner. Knocking down

collagen V or collagen XI impairs cell abilities to deposit and modify ECM. However, some alterations to E' and $\tan\delta$ still occurred in mutant ECMs. This observation suggests that ECM mechanics are not solely dependent on ECM topology, but are also related to cell modifications to the ECM. Comparing colVKD ECMs to colXIKD ECMs suggests that lack of collagen XI impairs cell alterations to the ECM more than lack of collagen V. However, lack of collagen V or collagen XI both hinder cell modifications to matrix topology and mechanics in response to GFs.

5.3.3 Best model of viscoelasticity to describe cell-derived ECMs

The analysis method developed in chapter 3 was applied to AM-FM AFM data for each ECM in order to better understand how cells modify ECM mechanics in response to GFs and mutation. First, the the model test (equation 3.11, section 3.2.1) was applied to AM-FM AFM data to determine whether cell-derived ECMs could be modeled as linear viscoelastic materials that obeyed the general Maxwell model (GMM, section 1.3.6), standard linear solid (SLS, section 1.3.4), Maxwell (MW) model (section 1.3.5.2), or Kelvin-Voigt (KV) model (section 1.3.5.1). Representative model tests are shown in figure 5.11 and 5.12.

For all samples, model test plots exhibited different behavior, depending on the AM-FM AFM image to which the test was applied. Panel (A)-(F) of figure 5.11 show representative model tests for ECMs produced by cells. Some tests fit well to the SLS (figure 5.11 (A)). Others have a hyperbolic shape, and likely fit well to the GMM (figure 5.11 (B) and (C)). Others potentially behave more like MW materials (figure 5.11 (D)). At least two different materials are present in some of the model tests (green arrows in figure 5.11). Similar observations were made for gelatin control samples (figure 5.12 (A)-(F)). Therefore, these results suggest that a number of materials are present within each sample.

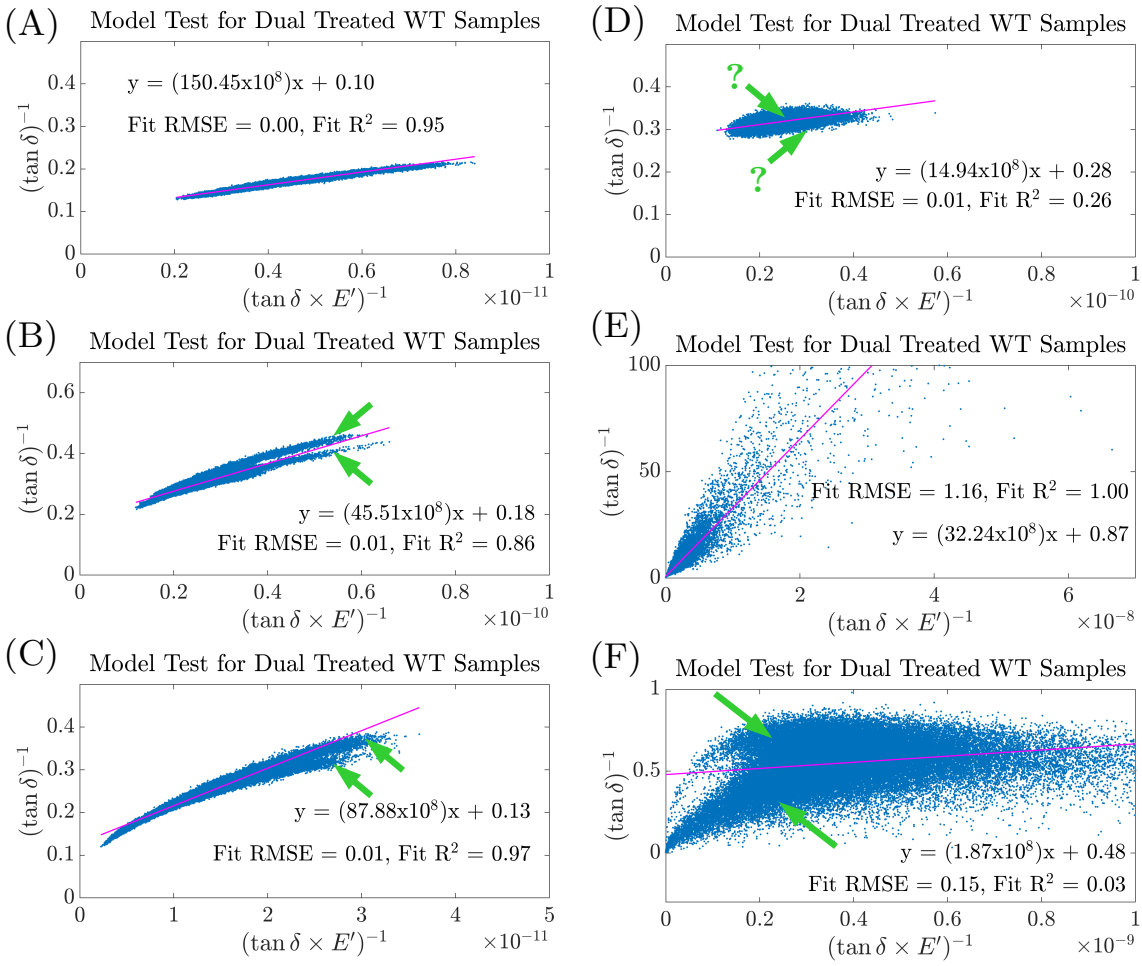


Figure 5.11: Example model tests for cell-derived ECMs. Each plot corresponds to a single AM-FM AFM image. Blue dots represent individual pixels. The model test line (equation 3.11) is shown in magenta. The fit equation, R^2 value, and root mean square error (RMSE) are also shown. Green arrows indicate samples where two materials are present. Green question marks indicate samples where two materials may or may not be present. All tests in this figure correspond to dual treated WT samples, but represent the results for all WT and mutant ECMs.

It is also interesting to note that, unlike the collagen data in chapter 4, the R^2 value is not a good metric to describe how well the model test line (equation 3.11) fits ECM data. For example, the model tests in figure 5.12 (E) and (F) have R^2 values of 1.00, even when the model test line only roughly describes the trends in the data. This incorrectly high R^2 value occurs because the standard deviation of the AM-FM AFM data is larger than the residuals of the fit, making $R^2 \to 1$. This large

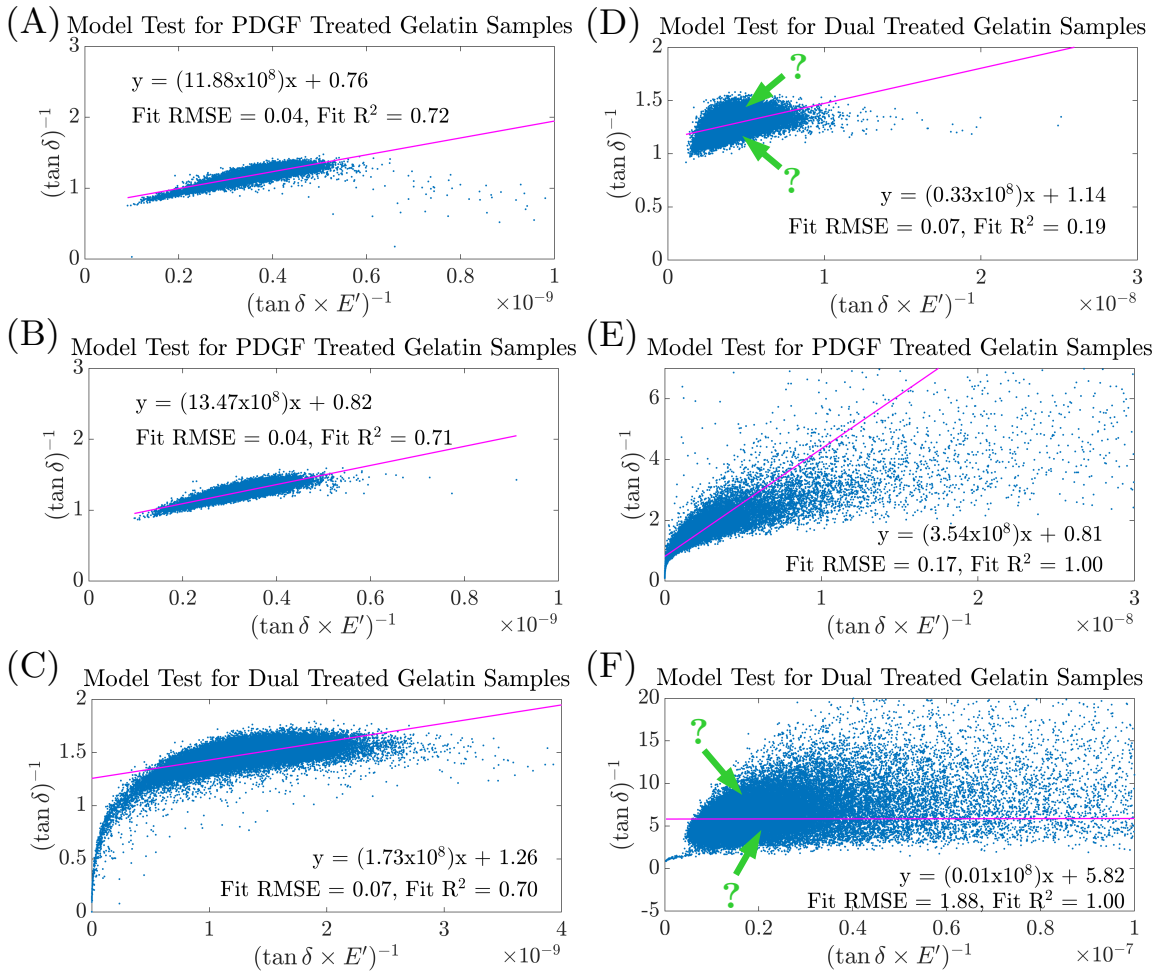


Figure 5.12: Example model tests for acellular gelatin controls. Each plot corresponds to a single AM-FM AFM image. Blue dots represent individual pixels. The model test line (equation 3.11) is shown in magenta. The fit equation, R^2 value, and root mean square error (RMSE) are also shown. Green arrows indicate samples where two materials are present. Green question marks indicate samples where two materials may or may not be present. Model tests displayed in this figure are representative of the results for all gelatin samples.

variation in the data could be the result of multiple materials, with slightly different mechanical properties, being present within a single image. Regardless, due to the large variation in the data, the R^2 value is not a good metric to describe how well the model test fits AM-FM AFM data for the ECM samples. Since the root mean square error (RMSE) does not use the standard deviation in the data for its calculation of goodness of fit, RMSE is the better metric to use for these samples. RMSE values

closer to zero represent better fits.

As shown in figure 5.11, model test RMSEs slightly increase if there are multiple materials in the image (figure 5.11 (B), (C), (F)). RMSE values substantially increase if there is large variation in E' and $\tan\delta$ within the image (figure 5.12 (D), (F)). The mean $\pm$ standard deviation RMSE for all samples was 0.012 ± 0.72. Table 5.1 shows the mean $\pm$ standard deviation in RMSE values of each sample, calculated from fits to each individual AM-FM AFM image of the sample. All RMSE values are reasonably low, suggesting that all samples can be described as linear viscoelastic materials. Additionally, only $2\% \pm 2.5\%$ (mean $\pm$ standard deviation) of the images in all samples had fit RMSEs > 0.2. The highest percentage of images with RMSE > 0.2 was 10%. This observation further supports the notion that cell-derived ECMs are linear viscoelastic materials.

It is interesting to note that the highest standard deviations in RMSE values occur for WT samples (table 5.1). This observation could be related to the fact that WT cells have the greatest ability to deposit and remodel ECM, and thereby that WT ECMs exhibit the greatest heterogeneity in topology, E', and $\tan\delta$ (as described in section 5.3.2). This observation supports the notion that samples with higher RMSE are still linear viscoelastic materials, but that the model test fit is low because multiple materials are present within a given AM-FM AFM image/model test. The presence

Table 5.1: Model test RMSE for cell-derived ECMs. The mean $\pm$ standard deviation of the root mean square error (RMSE) for model test (equation 3.11) fits to AM-FM AFM data are shown for each sample. ECMs were produced by normal (WT) fibroblasts, collagen V knockdown fibroblasts (colVKD), collagen XI knockdown fibroblasts (colXIKD), or were acellular gelatin controls. ECMs were treated with: no treatment (UT), PDGF, TGFβ, or both growth factors (dual).

Treatment	WT	colVKD	colXIKD	Gelatin
UT	0.1891 ± 1.0969	0.0518 ± 0.0354	0.1188 ± 0.0432	0.1041 ± 0.0439
PDGF	0.0745 ± 0.0569	0.0900 ± 0.1262	0.1304 ± 0.0599	0.0715 ± 0.0388
TGFβ	0.3722 ± 2.4528	0.0598 ± 0.0390	0.1040 ± 0.0342	0.0878 ± 0.0657
Dual	0.0993 ± 0.5258	0.1261 ± 0.3156	0.0671 ± 0.0366	0.1047 ± 0.1675

of multiple materials in the sample hides the trends in the model fit test. Since the ECM is a complex mixture of molecules [4], it is not surprising that multiple materials are present within the samples. Such materials could be: ECM components secreted by cells (such as fibronectin, laminin, glycoproteins, proteoglycans, and others, see section 1.1.1), PDGF or TGFβ that incorporated into the ECM, hydration shell effects (shells were not thick or stable enough to image in these samples, but could potentially alter ECM mechanics, as discussed in chapter 4), different collagen I topologies and factors affecting how collagen is organized within different fibrils and fibers, or other factors. Regardless, cell-derived ECMs are linear viscoelastic materials.

As discussed in section 3.3.2.3 and 4.2.2, the observation that most of the model tests had a hyperbolic shape (examples of this hyperbolic shape occur in figure 5.11 (B)-(D), (F), and figure 5.12 (C), and (D)-(F)) suggests that the general Maxwell model (GMM, section 1.3.6) is the best model to describe sample viscoelasticity. In order to further confirm that the GMM was a good model for ECM viscoelasticity, creep and relaxation experiments (section 2.1.3.2) were performed at the nanoscale (using the same AC240TSA cantilever used in AM-FM AFM) and microscale (using a modified AC240TSA cantilever with an attached bead) with approach velocities of 1.0 micron per second and 10.0 microns per second. Creep and relaxation experiments occurred in three steps. First, the tip was pressed into the sample until a trigger point of 100 nN was reached, which resulted in a specific indentation depth (details to follow) of the sample. Second, the tip dwelled on the sample for 60 seconds. Third, the tip was retracted from the sample. More details on performing AFM creep and relaxation experiments are provided in section 2.1.3.2.

It was difficult to engage the samples with the tip to perform creep or relaxation experiments. Typically, the deflection would fluctuate before the trigger point was reached, suggesting the tip needed to be partially inside the sample to "feel" that the sample was there. This fact made it difficult to obtain a complete withdraw of the

cantilever from the sample at the end of each dwell, and the tip had to be manually moved to 50 μm or higher away from the sample, then manually re-engaged between each indentation with a dwell. It was not possible to avoid this scenario, regardless of: the trigger point (even decreasing the trigger point to 1 nN did not solve this issue), approach velocity, or use of the modified cantilever (not shown).

Measured indentation depths were all less than 1 μm (not shown). However, the fact that the tip started each experiment inside the ECM could potentially mean that indentation depths were much deeper and potentially outside the ECM's linear viscoelastic regime. Regardless of this caveat, it was still possible to fit exponentials to the creep and relaxation dwells. Microscale and nanoscale creep and relaxation timescales ranged between 10 and 400 seconds for all samples (not shown). These finite timescales suggest that the samples obeyed the SLS, GMM, or other models of viscoelasticity that accurately model both creep and relaxation. If the ECMs were KV or MW materials, relaxation timescales would be zero or creep timescales would be infinite, respectively (see section 1.3.5.1 and 1.3.5.2). It is difficult to conclude much else from these creep and relaxation experiments, due to the fact that the exact indentation depths during each dwell are unknown. In the future, it would be prudent to repeat indentation and creep experiments after optimizing the choice of cantilever, and being more selective in spots on the sample to indent.

In summary, cell-derived ECMs are linear viscoelastic materials. The finite creep and relaxation times measured in creep and relaxation experiments suggest that the samples exhibit both creep and relaxation at the nanoscale and microscale. This observation supports conclusions drawn from AM-FM AFM data. The slope and y-intercept of the model test (equation 3.11) fits to AM-FM AFM data were greater than zero for all samples, suggesting that the samples obey the SLS or GMM. The observation of multiple lines within AM-FM AFM model tests suggest that multiple materials are present in each sample, and therefore that the GMM is a better model

to represent cell-derived ECMs, compared to the SLS which only represents a single material. Additionally, as described in chapter 3, the hyperbolic shape of many of the AM-FM AFM model test plots supports the notion that the GMM is the best model to describe ECM viscoelasticity in these experiments.

5.3.4 Viscoelastic material constants of cell-derived ECMs

The GMM (section 1.3.6) is the best model of linear viscoelasticity to describe the samples in this chapter, as determined in the previous section. Therefore, material constants of each sample were calculated as described in section 3.2.1.3 and 3.2.2.1. Mean values (calculated from all images of a given sample) of each material parameter and are shown in figure 5.13. Error bars in figure 5.13 represent the range of the data, rather than the standard deviation as in previous figures. This is so because the data typically ranged several orders of magnitude. This large range resulted in large standard deviations, which often hid the fact that very few data points were less than the mean. Error bars in figure 5.13 are displayed as the range to illustrate this fact.

Figure 5.13 (A) and (B) show the effects of GF treatment on the elastic constants (E_c and E_r) of the various ECMs. For both WT and colVKD samples, E_c and E_r changed several orders of magnitude with GF treatment. WT and colVKD samples treated with TGFβ had the highest E_c and E_r ($p = 0.04$ and 0.05, respectively compared to untreated samples). WT E_c and E_r was significantly different between each GF treatment ($p < 0.01$ for all comparisons). Only TGFβ treatment caused a significant increase in E_c and E_r of colVKD ECMs from untreated colVKD ECMs ($p < 0.01$ for E_c and E_r comparisons in TGFβ vs. untreated, $p > 0.2$ for all other comparisons). E_c and E_r of ECMs produced by colXIKD cells were constant for all GF treatments ($p > 0.4$ for all comparisons). ECMs produced by colXIKD cells had similar E_c and E_r to gelatin controls, with the exception of dual treated samples,

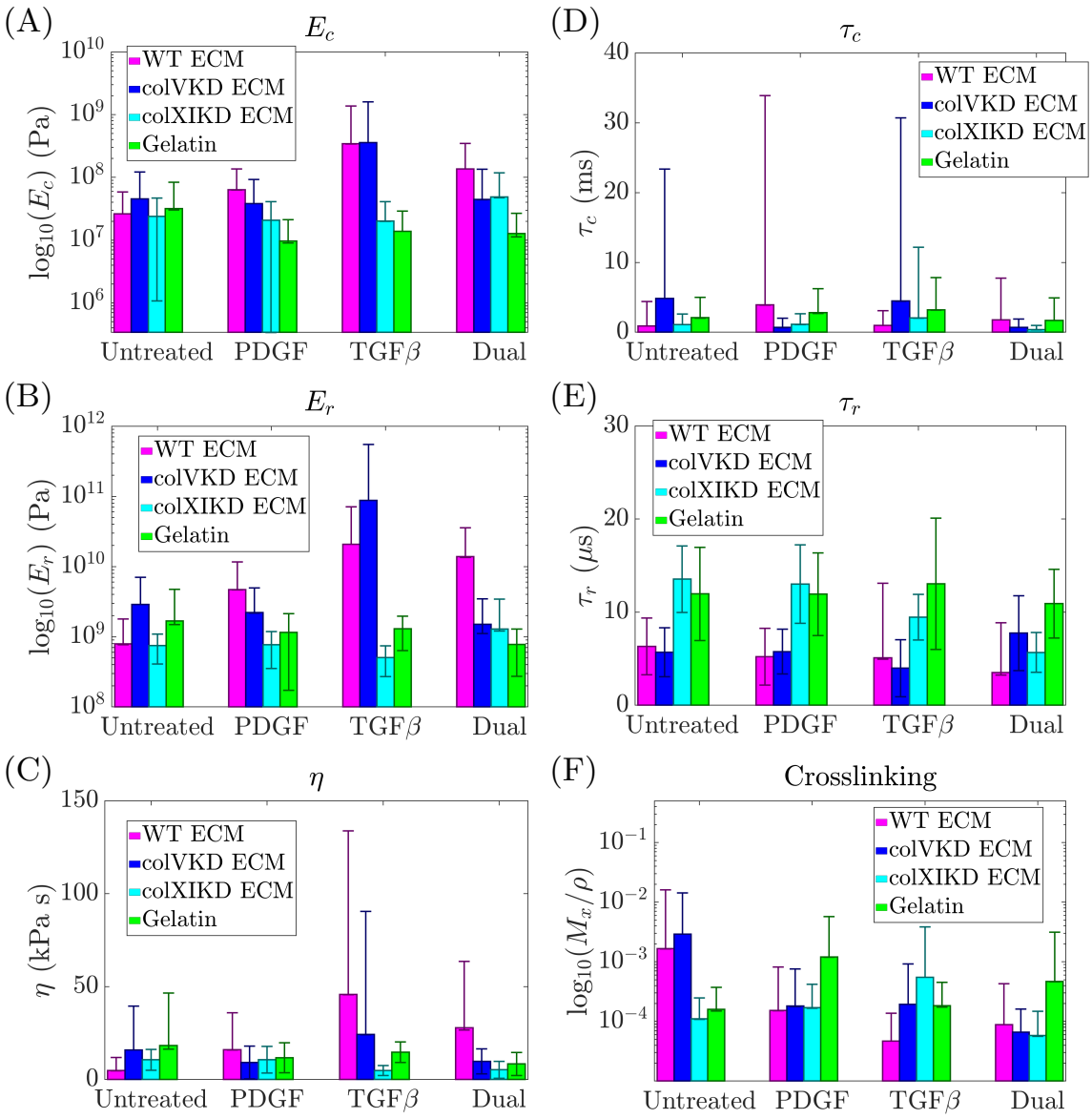


Figure 5.13: Material constants of cell-derived ECMs. Cell-derived ECMs were produced by wild type (WT, magenta) fibroblasts, collagen V knockdown (colVKD, dark blue) mutants, and collagen XI knockdown (colXIKD, light blue) mutants in untreated cultures, PDGF treated cultures, TGFβ treated cultures, or both PDGF and TGFβ (dual) treated cultures. Gelatin (green) served as an acellular control. The mean E_c, E_r, η, τ_c, τ_r, and M_x/ρ are shown in (A)-(F), respectively. The ratio of the molecular weight between crosslinks (M_x) to the density of the ECM (ρ) is related to sample crosslinking. Error bars represent the range of values from all AM-FM AFM images of the sample.

where colXIKD E_r was higher than that of gelatin E_r (p = 0.71, 0.66, 0.25, and 0.05 for untreated, PDGF, TGFβ, and dual, respectively vs. gelatin in the same

treatment). The observation that colVKD mutants only altered ECM elasticity in response to TGFβ while colXIKD mutants only increased ECM elasticity in response to dual treatment, suggests that mutation alters the sensitivity of cells to particular GFs. Gelatin E_c and E_r were not significantly different between GF treatments (p = 0.84, 0.88, 0.72 for PDGF, TGFβ, and dual, respectively vs. untreated), suggesting that the observed changes in cell-derived ECMs were the result of cell activities.

Together, the results in figure 5.13 (A) and (B) suggest that elasticity of ECMs exposed to PDGF, TGFβ, or both GFs increases as a result of cells actively remodeling the matrix. These results agree with literature measurements of fibrotic tissue, which show an increase in macroscopic elasticity [3, 62]. Knockdown of colVKD impairs cell abilities to increase elasticity of the ECM, especially for dual treated and PDGF treated ECMs. Knockdown of colXIKD hinders cell abilities to increase ECM elasticity from that of the acellular control (gelatin), and in response to GFs. Only dual GF treatment caused colXIKD ECMs to exhibit a slight, but much less than WT, increase in elasticity.

Figure 5.13 (C) shows the effect of GF treatment on ECM viscosity (η). Again, WT cells exhibited larger changes in η than mutant ECMs in response to GFs. Untreated WT ECMs exhibited η lower than that of gelatin ($p = 0.05$). GF treatment increased η of WT ECMs. TGFβ treatment resulted in ECMs with the highest viscosity compared to the untreated sample ($p = 0.02$), followed by dual treatment ($p = 0.03$), then PDGF treatment ($p = 0.03$). Only TGFβ treatment significantly increased η of colVKD ECMs ($p = 0.06$). Other GF treatments did not significantly alter η of colVKD ECMs from that of the gelatin control (p = 0.77, 0.62, and 0.54 for untreated, PDGF, and dual, respectively vs. gelatin in the same condition). The value of η remained constant for all colXIKD ECMs (p = 0.99, 0.32, 0.41 for PDGF, TGFβ, and dual, respectively vs. untreated), and was significantly smaller than that of gelatin controls (p = 0.03, 0.08, 0.01, 0.04 for untreated, PDGF, TGFβ, and dual,

respectively vs. gelatin in the same condition). Untreated gelatin samples had higher η than GF treated gelatin ($p < 0.01$ for all three comparisons). This observation suggests that GFs can incorporate into gelatin, and decrease its viscosity. Therefore, cells could potentially modulate ECM η *in vivo* by secreting GFs to incorporate into the matrix. Additionally, this observation supports the notion that increase in η of cell-derived ECMs was due to cell remodeling of the ECM.

Figure 5.13 (D) shows the mean τ_c of each sample. For WT ECMs, τ_c was not significantly different from the gelatin control, except for PDGF treated samples, where τ_c increased ($p = 0.90$, 0.01, 0.98, and 0.88 for untreated, PDGF, TGFβ, and dual, respectively vs. gelatin in the same treatment). These observations suggest that, in spite of alterations to E_c and η with GF treatment besides PDGF, both quantities changed simultaneously, thereby maintaining constant τ_c. Based on the results of figure 5.13 (A) and (C), the increase in τ_c with PDGF treatment is likely due to a slight increase in η relative to E_c of the deposited ECM.

For colVKD ECMs, PDGF and dual treated samples exhibited shorter τ_c than untreated and TGFβ treated ECMs ($p < 0.01$ for all comparisons). For untreated and TGFβ treated samples, τ_c was significantly longer than WT ECMs ($p < 0.01$ for all comparisons). Based on the results of figure 5.13 (A) and (C), the increase in τ_c for untreated and TGFβ treated colVKD ECMs is the result of an increase in η of these samples relative to E_c. For colXIKD ECMs, τ_c remained constant between different GF treatments ($p = 0.98$, 0.90, 0.58 for PDGF, TGFβ, and dual, respectively vs. untreated), and was significantly less than that of gelatin ($p < 0.01$ for all comparisons). For all ECMs, τ_c was significantly different from the gelatin control ($p < 0.01$ for all comparisons). The value of τ_c in gelatin samples was constant regardless of GF treatment ($p = 0.85$, 0.80, and 0.91 for PDGF, TGFβ, and dual, respectively vs. untreated). Together, these observations suggest that observed changes in τ_c of cell-derived ECMs were the result of cell activities, and that cells often, but not always,

altered τ_c of the ECMs they deposited by changing η relative to E_c.

Figure 5.13 (E) shows the mean τ_r of each sample. WT ECMs exhibited constant τ_r regardless of GF treatment ($p = 0.63$, 0.79, and 0.39 for PDGF, TGFβ, and dual, respectively, vs. untreated samples). ECMs produced by colVKD cells exhibited constant τ_r ($p = 0.97$ and 0.43 for PDGF and TGFβ treated samples, respectively, compared to untreated samples), except for dual treated samples, where τ_r increased ($p = 0.01$). The value of τ_r for both WT and colVKD ECMs was significantly less than the gelatin control ($p < 0.01$ for all comparisons). For all colXIKD samples except dual treated samples, τ_r was not significantly different from the gelatin control ($p =$ 0.75, 0.76, 0.23, 0.05 for untreated, PDGF treated, TGFβ treated, and dual treated comparisons with gelatin in the same treatment, respectively). Together, these observations suggest that WT and colVKD cells are able to control the relaxation times of their substrates by making simultaneous changes to E_r and η, while colXIKD cells are less able to do so. Additionally, WT cell modifications to the ECM simultaneously alter E_r and η, so that τ_r remains constant.

Figure 5.13 (F) shows a measure of crosslinking in the sample. As described in section 1.3.7, insight into crosslinking within the ECMs can be gained by applying equation 1.47 to the estimated value of E_c. Since the density ρ of these samples is unknown, applying equation 1.47 can only provide the ratio of the molecular weight of ECM polymers between crosslinks M_x over the density of the ECM, M_x/ρ. Figure 5.13 (F) shows that M_x/ρ changed by several orders of magnitude between samples and treatments. For WT samples, ECMs with more fibers tended to have lower values of M_x/ρ ($p < 0.01$ for all comparisons). This observation suggests (i) that M_x decreased, meaning that the number of crosslinks increased, (ii) that ρ increased, or (iii) both.

It would not be surprising if, as the number of crosslinks between ECM molecules increased, the density of the ECM also increased, since molecules would be held tighter

together by the additional crosslinks. Therefore, it is reasonable to hypothesize that (iii) occurred. This hypothesis is supported by the literature, which suggests that ECM fibers in fibrosis have more crosslinks [265]. Together, these observations suggest that part of the changes in ECM mechanics observed in WT samples could be due to alterations in the crosslinking of the ECMs. Additionally, the value of M_x/ρ varied in gelatin control samples with various GF treatments ($p < 0.01$ for all comparisons). Since PDGF and TGFβ do not crosslink the ECM directly, this observation suggests that GFs change the density of gelatin mats, even in the absence of cells, likely via GF incorporation into the gelatin. Together, these observations suggest that (iii) is true. Crosslinking and changes to ECM density occurred in response to GF treatment in cell-derived WT ECMs.

Crosslinking in colVKD ECMs followed a similar trend to WT ECMs. While M_x/ρ decreased in samples treated with GFs compared to untreated colVKD ECMs ($p < 0.01$ for all comparisons to untreated), M_x/ρ was not significantly different between GF treated samples ($p > 0.4$ for all comparisons). This observation suggests that colVKD cells alter crosslinking and/or ECM density in response to GFs, but are not able to fine tune their alterations as well as WT cells (resulting in a different M_x/ρ for each GF treatment only for WT ECMs). The value of M_x/ρ was constant for all colXIKD samples ($p = 0.80$ and 0.69 for samples treated with PDGF and dual, respectively vs. untreated), except those treated with TGFβ, where M_x/ρ increased ($p < 0.01$). This observation indicates that colXIKD cells are not able to crosslink and/or alter the density of the ECMs they produce as well as WT or colVKD cells. The increase in M_x/ρ for TGFβ treated colXIKD samples suggests that the resulting matrices lost crosslinking and/or were less dense than colXIKD ECMs in other GF treatments.

Figure 5.14 shows the material constants for each biological replicate. In general, the trends are similar to overall means for each sample. However, similar to

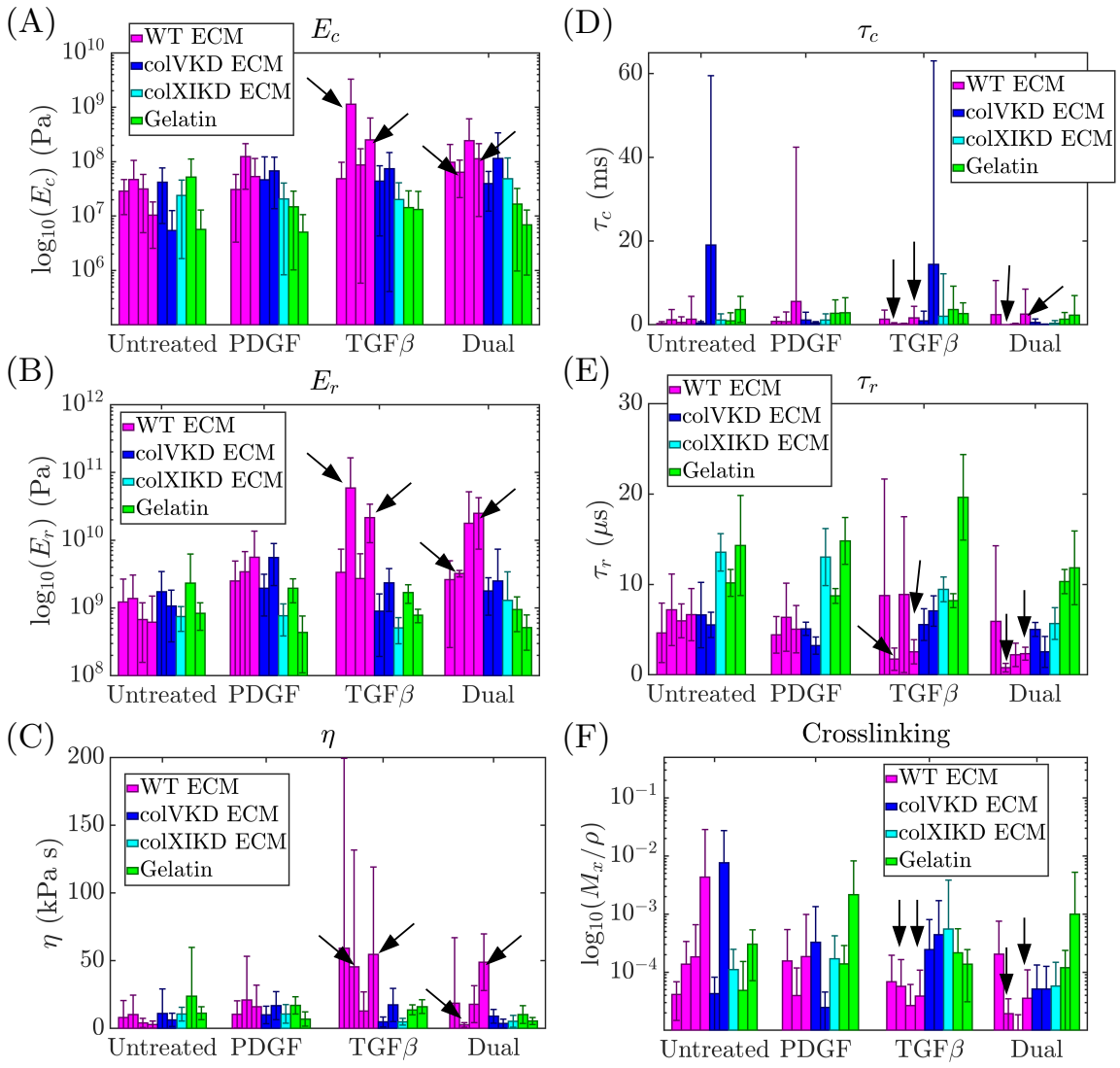


Figure 5.14: Material constants of each biological replicate of cell-derived ECMs. Cell-derived ECMs were produced by wild type (WT, magenta) fibroblasts, collagen V knockdown (colVKD, dark blue) mutants, and collagen XI knockdown (colXIKD, light blue) mutants in untreated cultures, PDGF treated cultures, TGFβ treated cultures, or dual treated cultures. Gelatin (green) served as an acellular control. The mean $\tan\delta$ of each sample is shown in (A). E_c, E_r, η, τ_c, τ_r, and M_x/ρ are shown in (A)-(F), respectively. The ratio of the molecular weight between crosslinks (M_x) to the density of the ECM (ρ) is related to sample crosslinking. Error bars represent standard deviation. Lack of lower error bars in (A), (B), and (F) indicates replicates where the standard deviation was greater then the mean of the sample and hence cannot be plotted on a log scale. Black arrows indicate biological replicates where larger fibers were deposited.

the observations of height, E', and $\tan\delta$ in section 5.3.2, alterations to ECM material constants depended on the biological replicate, indicating that alterations to the mechanical properties of the ECM depend on the cells performing the alterations. Therefore, ECM mechanics are likely spatially heterogeneous, depending on the cells within a given area. Material constants of colVKD ECMs varied more than E' and $\tan\delta$ (section 5.3.2) between biological replicates. This observation indicates that mutant cells still have the ability to alter ECM mechanics, but do so differently depending on the mutation. Additionally, these results suggest that the elasticity, viscosity, and time responses of mutant ECMs *in vivo* vary depending on the cell producing and modifying the matrix. Therefore, like WT samples, the mechanical properties of mutant ECMs are likely spatially heterogeneous, depending on the cells within a given area.

5.4 Conclusions and discussion

AM-FM AFM measurements of the mechanical properties of cell-derived ECMs suggest several important factors to consider about how mechanochemical coupling affects nanoscale ECM mechanics. In most cases, alterations to ECM mechanics occurred as a result of cell behaviors, and not as a result of GFs incorporating into the matrix. An exception to this observation occurred with M_x/ρ, where GF exposure altered the density of gelatin mats, likely due to GF incorporation into the gelatin. This observation suggests that, for ECM properties other than density, GFs exert their influence indirectly by changing cell signaling and activities, rather than by directly altering the physical properties of the ECM.

Observations of ECMs produced by mutant cells suggest that nonfibrillar collagens V and XI play a role in how cells deposit ECM and modify ECM mechanics. Mutant cells have difficulty depositing large fibers, and have restricted abilities, com-

pared to WT cells, to modify the mechanical properties of the resulting ECM. This observation suggests that collagen V and XI, and possibly other nonfibrillar collagens are important in regulating tissue time responses and mechanics. Collagen V and XI seem to play a role in helping cells modify both the elasticity and viscosity of the ECM. Depending on GF exposure, colVKD occasionally affected ECM elasticity or viscosity slightly more than elasticity, thereby altering ECM time responses. WT cells maintained simultaneous changes to ECM elasticity and viscosity in most GF treatments. Therefore, ultimately, colVKD mutants had worse control over ECM time responses, which varied more with GF treatment than ECMs produced by WT cells. Like colVKD mutants, colXIKD mutants have worse control over ECM time responses than WT cells. Additionally colXIKD mutants have difficulty altering ECM mechanics from that of the underlying gelatin, except when the cells are exposed to PDGF and TGFβ at the same time. It is likely that collagen V and XI exert their effects on ECM mechanics by incorporating into the ECM, rather than by altering ECM crosslinking as hypothesized.

While mutation (and GF treatment) altered ECM crosslinking and/or ECM density, no consistent increase or decrease in ECM crosslinking of mutant compared to WT ECMs was observed. This observation suggests that the role of collagen V and collagen XI in modulating ECM mechanics cannot be attributed solely to alterations in ECM crosslinking, as previously hypothesized. Therefore, collagen V and XI likely influence ECM mechanics by incorporating into the ECM, and thereby altering elasticity and viscosity of the ECM. In the future, it would be interesting to test this hypothesis by testing whether the amount of collagen V and collagen XI incorporated into the ECM correlates with changes to ECM E_r, E_c, and η. Such an experiment could be performed as follows. First, AFM could be used to quantify the mechanical properties of the cell-derived ECMs. Once the mechanical properties of the ECM are quantified, the ECM could be digested, and quantitative polymerase chain reaction

or Western blotting could be performed to measure the relative amounts of collagen V and XI incorporated into the matrix.

Regardless of mutation or GF treatment, ECM mechanics varied between biological replicates. This observation suggests that ECM mechanical properties depend on the cells performing ECM deposition and modification. Therefore, these results suggest spatial heterogeneity in ECM mechanics, based on the cells in any given location. This observation is supported by the fact that the multiple spots probed on each sample had varying topology, and that the model test results showed varying outcomes for the same sample, depending on the AM-FM AFM image (section 5.3.3). In the future, it would be interesting to further analyze data between different spots on the sample to study spatial heterogeneity in ECM mechanics in more detail. Regardless, spatial heterogeneity in ECM mechanics likely occurs in both the *in vitro* samples of these experiments, as well as tissues and tumors *in vivo*.

Additionally, while mutation hinders cell abilities to deposit and modify the ECM, mutation does not eliminate variation in the alterations by individual cells (variations between biological replicates). Therefore, knocking down a cell's ability to express collagen V or collagen XI does not necessarily prevent the cell from responding to GFs or altering ECM mechanics. Such alterations simply occur in a different manner from WT cells. This observation could have implications for pancreatic tumor progression. For example, stromal mutations could alter the GF dialog between tumor cells and stromal cells, thereby changing how fibrosis develops within a tumor.

Experiments in this chapter also found that ECM modifications performed by WT fibroblasts in response to GFs resulted in constant ECM time responses. This observation is reminiscent of that in chapter 4, where collagen I time responses were constant, regardless of the ionic strength of the surrounding solution. The ECMs in this chapter consisted mostly of collagen I, as determined by Dr. Alex Gordon-Weeks (data not shown). Therefore, together, these results suggest that the time responses

of collagen I, ECMs, and tissue, could be constant at some spatially heterogeneous value. Since time responses dictate the propagation and attenuation of forces in tissue, and as already hypothesized in chapter 4, alterations to tissue time responses from the baseline constant value, via alterations in pH [188], ion flows (chapter 4), or additional stimuli such as GFs, could serve as a physiological mechanism to alter cell activities. This hypothesis could have important implications for pancreatic tumors, and even solid tumors in general, which also exhibit varying degrees of fibrosis [62], as described in the following section.

5.4.1 Implications for tumor biology

The hypothesis that altered ECM mechanics, and in particular time responses, play a role in tumor progression is supported by *in vivo* experiments performed by Dr. Alex Gordon-Weeks. Growth and progression of pancreatic tumors in colVKD and colXIKD mice is hindered and tumor fibrosis is decreased (not shown). The results in this chapter suggest that the colVKD and colXIKD stroma in these mice have reduced ability to modify the mechanical properties of the ECM in response to tumor GFs. Therefore, the stroma of these mutant mice may be unable to consistently alter the mechanical properties of tumor ECM from that of normal tissue. In this case, "normal" ECM time responses would be maintained, thereby prompting tumor cells to perform normal cell activities, rather than allow tumor progression.

In general, alterations to tissue time responses via a sudden stimulus could serve as a means of tumor initialization. Such a stimulus could be: a mutation that interferes with and potentially increases cellular abilities to remodel the ECM (for example, the opposite of collagen V and collagen XI knockdown), a wound and the voltage generated as the result of a wound [64], a surge of GFs, etc... Regardless of the stimulus, cell activities would change as a result of the altered ECM time responses [15]. The subsequent alterations to ECM remodeling by the newly-changed cells could maintain

the altered tissue time responses, and thereby maintain altered cell activities. Without an additional stimulus to restore the original ECM time responses, cells could potentially maintain altered ECM time responses indefinitely, thereby maintaining new cell behaviors. Such an occurrence may help cells acquire the hallmarks of cancer progression [266] by increasing activities like proliferation and migration. This hypothesis could explain why tumors often form from sites of injury [267], and why additional injuries can sometimes renormalize tumors [2] or result in spontaneous tumor remission [268]. If such injuries alter tissue time responses, such alterations could serve to alter cell behaviors in order to (i) alter cell activities (such as proliferation, trans- or de-differentation, and migration) that contribute to malignant phenotypes and (ii) alter immune cell activity.

Consideration of ECM time responses could also explain why fibrosis sometimes hinders tumor progression [62, 93], and sometimes helps tumor progression [3, 62, 93]. This seemingly contradictory role could potentially be explained by considering the time responses of the fibrotic tissue. For example, fibrosis that restricts tumor progression could potentially exhibit time responses that promote normal cell activities, and thereby renormalize tumor cells to some extent. In cases where fibrosis helps tumor progression, the tumor may have altered the time responses of the fibrotic tissue (potentially via a decrease in pH [188] or via the fluid flows, see chapter 4, within a tumor's necrotic core [269]), and thereby further promote alterations in cell activity that lead to malignant progression. In the future, it would be interesting to measure the time responses of fibrotic tissue from tissues that help and hinder tumor progression, to test this hypothesis.

5.4.2 Future work

The results in this chapter demonstrate the importance of considering tissue elasticity, viscosity, and the ratio of the two (the time responses) together in order to understand

how the mechanical properties of the ECM regulate the behavior of cells within. While the results in this chapter suggest that cell activities are important factors to consider, these experiments did not directly examine cell activities besides ECM remodeling. These experiments also did not propose a mechanism for how ECM mechanics could regulate cell behaviors. One possible mechanism could be that ECM mechanics alter cell mechanics, which in turn alter cell abilities [38, 147–151, 194, 270, 271]. It is already known that changes in the mechanical properties of the ECM and the surrounding fluid alter cell elasticity, viscosity, and time responses [194, 270, 271]. This observation supports the notion that mechanical properties of the ECM regulate cell behaviors by altering the mechanical properties of the cells. This hypothesis can be further tested via experiments designed to link cell activities and mechanics with ECM mechanics, paying special attention to the role of tissue time responses.

The link between cell and ECM mechanical properties can be made by measuring the mechanical properties of cells on ECMs that have not been decellularized. Alternatively, substrates constructed from collagen I [7, 9, 22, 27, 133–136] or from poly(2-hydroxyethyl methacrylate), poly(HEMA) [272], are known to modulate cell shape and behavior, and likely mechanics. These substrates take less time to prepare than cell-derived ECMs (which take roughly 10 days to prepare [264]). Therefore, collagen I or poly(HEMA) are good substitutes for cell-derived ECMs. Regardless of the ECM or substrate used, activities of cells on the substrate can be measured by any number of experiments that include, but are not limited to: invasion assays, immunofluorescence for proteins of interest, viability measurements, SDS-PAGE and Western blotting, and time lapse studies (to observe cell proliferation, migration, death, and morphology through time). Correlating such activity measurements with quantification of cell and ECM mechanical properties could help clarify the role of ECM mechanics, in particular time responses, on modulating cell activities. Further discussion of such experiments is reserved for chapter 6.

Additionally, it would be interesting to perform the experiments in this chapter on tumor spheroids [273, 274] and tumors to see if the mechanical properties of the cell-derived ECMs are similar to those within an actual tumor. Preliminary attempts at AFM of spheroids and tumors were performed in collaboration with Dr. Alex Gordon-Weeks and Dr. Angela Diana. Dr. Angela Diana, a member of Dr. Alex Gordon-Weeks's lab, prepared all spheroids and tumors for the experiments. Preliminary AFM experiments on tumor spheroids in live cell imaging solution using the long, thin tip of RC800PSA cantilevers and BioLeverMini cantilevers suggest that AFM quantification of spheroid mechanics is possible (data not shown), but requires greater optimization of the cantilever/sample pairing. Preliminary AFM experiments using the long, thin tip of RC800PSA cantilevers and BioLeverMini cantilevers on tumors grown from injection of tumor cells into mice found that the resulting tumors were too fluid to detect with the AFM tip (data not shown). This conclusion was reached because during tumor AFM experiments, the tip would enter the tumor (visible to the naked eye), and the deflection would fluctuate, but the trigger point and/or setpoint was never reached. Therefore, in the future, a different cantilever or a different tumor model should be used. For example, tumors grown naturally inside an animal host, rather than injected into the host, may be solid enough to probe with an AFM tip.

Chapter 6

Viscoelasticity of Cell Culture Substrates: Potential Modulation of Cell Behaviors by Substrate Time Responses

The mechanical properties of a cell play an important role in modulating the cell's behavior [38, 147–150]. Furthermore, the mechanical properties of cells are modulated by the environment in which the cell is located [194, 270, 271]. In addition to cell mechanics, the mechanical properties of a cell's environment, in particular those of the substrate on which the cell is located, play a crucial role in modulating cell activities [1, 3, 5–8]. Biological systems are viscoelastic, meaning they exhibit characteristic time delays, called time responses, in response to an applied force [162, 166]. Time responses (τ) dictate the propagation and attenuation of forces in cells and substrates, and represent a combined metric of viscosity (η) and elasticity E, since τ is the ratio of the two [162, 165].

Elasticity, viscosity, and time responses of a substrate on which a cell is located

all influence cell behaviors. For example, substrate elasticity alters proliferation and survival [10–14], differentiation [9, 11, 12, 16–26], migration [27–35], morphology [12, 36–39], cytoskeletal properties and adhesion [23, 40–46], plasma membrane structure [30, 47, 48], cell signaling and gene expression [14, 24, 30, 34, 35, 38, 49–56], and other cell activities [8, 26, 34, 35, 57–59]. Substrate viscosity (η), as well as that of the surrounding fluid (hydration shells or the bulk fluid), is as important as E in dictating cell behaviors [15, 128, 170, 184–194]. Substrate τs also influence cell behaviors. Shorter substrate τ promotes ECM deposition and remodeling, as well as osteogenic differentiation of cells within the substrate [15]. Substrates with longer τ exhibit the opposite effects [184]. As already hypothesized in chapter 4 and 5, substrate τs may be crucial factors regulating cell mechanics and activities. It is possible that substrate mechanical properties, in particular τs, exert their influence on cell behaviors by altering the mechanical properties of cells on the substrate.

The hypothesis that substrate mechanics, and in particular time responses, regulate cell activities by modulating cell mechanics can be tested by measuring and correlating the mechanical properties of cells, mechanical properties of substrates, and cell behaviors. A large variety of cell culture substrates could be used to perform such experiments. Two examples of such substrates are made of poly(2-hydroxyethyl methacrylate), poly(HEMA) [272, 275], or collagen I [133, 229]. Both poly(HEMA) [275–280] and collagen I [170, 188–193, 281–284] substrates are viscoelastic.

Poly(HEMA) substrates strongly influence cell behaviors [272], and are used in biomedical applications such as cell culture, contact lenses, fillings, histology, immobilization of cells and drugs, and implants [275]. The thickness of poly(HEMA) films modulates cell spreading and activities [272, 275]. Higher concentrations of poly(HEMA) within a substrate hinder cell attachment, spreading, and DNA synthesis [272, 275]. Concentrated poly(HEMA) substrates have been shown to decrease DNA synthesis in bovine aortic endothelial cells [272], alter cytoskeleton (actin) dy-

namics in neutrophils [285], alter leukocyte locomotion, force malignant melanoma cells to assume a round morphology and form polykaryons (multiple nuclei within a single cell), and decrease adrenal tumor cell synthesis of steroids [275]. Additionally, the viscoelastic properties of neutrophils are altered on poly(HEMA), compared to glass substrates [285], supporting the notion that effects exerted on cells by poly(HEMA) could be related to alterations to cell mechanical properties.

Collagen I is also a widely used cell culture substrate [133, 229]. The mechanical properties of collagen I substrates regulate cell proliferation [13] and survival [229], alter ECM deposition and remodeling [286], regulate stem cell differentiation [22], and regulate cell migration [27]. One commonly used collagen I substrate is known as pureCol [133]. PureCol is a ready-made solution of purified collagen I isolated from bovine skin and suspended in cell culture medium [287]. PureCol substrates affect cell morphology, proliferation, and viability [133]. Additionally, the elasticity of pureCol substrates is known to influence cell migration [134]. An additional benefit from the use of pureCol and collagen I substrates is that the mechanical properties of the substrates are tuneable via the use of crosslinking agents such a glutaraldehyde (GA) [264, 288–291]. Therefore, collagen substrates are convenient for studying how varying the mechanical properties of a substrate alter cell behaviors and mechanics.

The purpose of the experiments in this chapter is to investigate the notion that the mechanical properties of substrates, in particular time responses, regulate cell behaviors by altering the mechanical properties of the cells. Experiments in this chapter use atomic force microscopy (AFM) to measure the mechanical properties of six different substrates: three different pureCol substrates with varying degrees of GA crosslinking, as well as substrates made from three different concentrations of poly(HEMA). The expected behavior of cells on these substrates is then hypothesized.

Typically, at the bare minimum, both creep ($\tau_c = \eta/E_c$, section 1.3.3.2) and relaxation ($\tau_r = \eta/E_r$, section 1.3.3.1) time responses are present within biological

materials [162, 169]. More commonly, biological systems exhibit multiple τ, associated with various movements of molecules within the system [162, 169]. The response, including the dominant τ, of a biological system to a stimulus is frequency dependent because the frequency of the applied stimulus alters deformations of molecules within the system [169, 227]. Therefore, it is informative to measure the mechanical properties of a system in response to applied stimuli with a range of frequencies [169]. The experiments in this chapter accomplish this task by combining two forms of atomic force microscopy (AFM) to probe the viscoelastic properties of cell culture substrates at frequencies ranging from 0.1 Hz - 10,000 Hz.

6.1 Materials and methods

In order to study the relationship between substrate mechanics, in particular time responses, and cell mechanics and activities, different cell culture substrates based on poly(HEMA) and pureCol were synthesized. The mechanical properties of the six different substrates were then measured at the nanoscale via atomic force microscopy (AFM). Three different poly(HEMA) and pureCol substrates were studied.

Synthesis of poly(HEMA) substrates was carried out per the standard protocol [272]. Briefly, 6 g of poly(HEMA) powder (Sigma-Aldrich P3932) were dissolved in 50 mL of 95% ethanol to create a stock poly(HEMA) solution with 120 mg poly(HEMA) per mL ethanol. This solution was left stirring overnight, in order to ensure that the poly(HEMA) was fully dissolved. The next morning, in order to remove any undissolved poly(HEMA), the stock solution was centrifuged for 30 minutes at 2,500 rpm, then transferred to a new container. The stock solution was then diluted serially in 95% ethanol, resulting in three different poly(HEMA) solutions with: 120 mg poly(HEMA) per mL ethanol, 12 mg poly(HEMA) per mL ethanol, or 1.2 mg poly(HEMA) per mL ethanol. To prepare poly(HEMA) substrates, glass cover-

slips were sterilized with ethanol and placed in a petri dish. The desired solution of poly(HEMA) was then pipetted onto the coverslip, at 95.2 μL poly(HEMA) solution per cm^2 of coverslip surface area. This resulted in substrates with 11.4 mg poly(HEMA) per cm^2 of coverslip surface area, 1.14 mg poly(HEMA) per cm^2, and 0.114 mg poly(HEMA) per cm^2.

Once poly(HEMA) solutions were deposited onto coverslips, the sample was then left to dry at room temperature for 48 hours to ensure that all the ethanol had evaporated. After drying for 48 hours, coverslips with the dry poly(HEMA) substrates were secured to a magnetic disk (which secures the sample to the AFM during an experiment) using double-sided foam (RS Components 554-844), and moved to an Oxford Instruments Asylum Research Cypher ES AFM. In order to simulate physiological conditions, 200 - 400 μL of live cell imaging solution (1x PBS with HEPES, where 1x denotes the fact that the PBS reflects physiological ion concentrations, Sigma-Aldrich A14291DJ) were then pipetted onto the sample. After live cell imaging solution was added, samples were left in the AFM for 30 minutes before performing any experiments, in order to allow the poly(HEMA) substrates to fully swell [272].

Synthesis of pureCol substrates was carried out per the protocol specified by the manufacturer [287]. Briefly, pureCol^{TM} EZ Gel solution (Sigma-Aldrich 5074) was stored at 4^o C, to prevent gelation. To form pureCol substrates, 200 μL of pureCol were added to a custom built sample chamber 0.8 cm x 0.6 cm x 0.3 cm (length, width, height) made of double-sided foam (RS Components 554-844). Custom built chambers were created by cutting 0.8 cm x 0.6 cm rectangles out of double-sided foam with a scalpel, stacking three such strips on top of one uncut strip, and securing the resulting chamber to a magnetic disk (which secures the sample to the AFM during an experiment). Figure 6.1 (A) shows this custom chamber. Figure 6.1 (B) shows the chamber once 200 μL pureCol have been added. Custom chambers were used because purecol tended to detach from coverslips (not shown), and petri dishes could not be

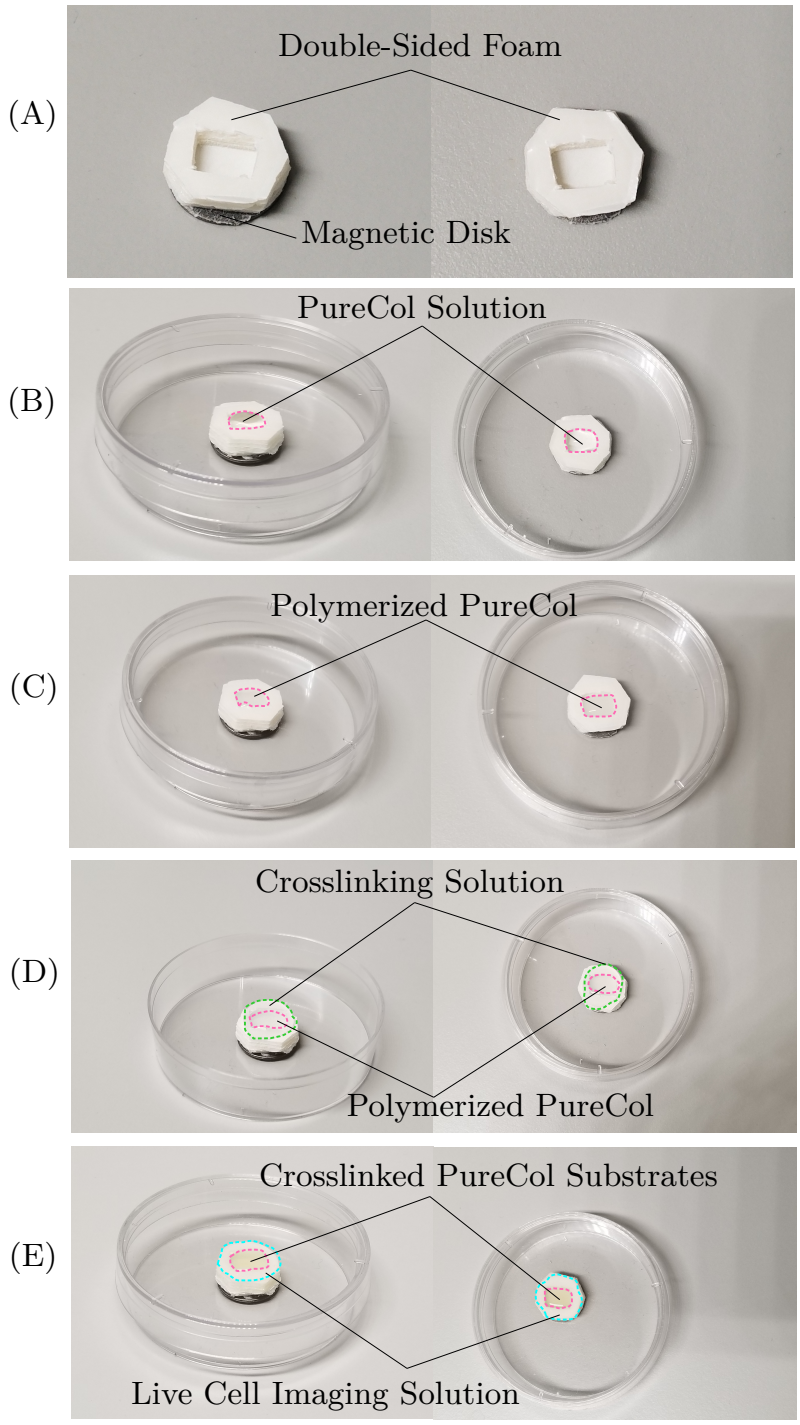


Figure 6.1: Custom chamber for preparation of pureCol substrates. The left column shows a side view of the custom chamber used to create pureCol substrates. The right column shows a top view of the same chamber. Empty chambers, made of double-sided foam secured to a magnetic disk are shown in (A). Chamber dimensions are 0.8 cm x 0.6 cm x 0.3 cm (length, width, height). The same chamber after the addition of pureCol, after pureCol polymerization, and after the addition of 1% glutaraldehyde (crosslinking solution) are shown in (B)-(D), respectively. The crosslinked sample, ready for AFM experimentation in live cell imaging solution, is shown in (E).

used for pureCol substrates because dishes were too large to fit in the Cypher AFM.

After pureCol was added to the custom chamber, the chamber was placed at 37^o C for 90 minutes to allow the collagen to polymerize. The resulting substrate is shown in Figure 6.1 (C). While the collagen polymerized, a 50% glutaraldehyde (GA) solution in water (Sigma-Aldrich 340855) was diluted in Dulbecco's phosphate buffered saline (DPBS) to a final concentration of 1% GA in DPBS. Once polymerization was complete, 400 μL of the 1% GA in DPBS were deposited on top of the pureCol. Samples in this 1% GA solution are shown in figure 6.1 (D). Samples were then left to crosslink in GA at room temperature for: 30 minutes, 2 hours, or 24 hours. Crosslinking duration was varied in this manner in order to alter the number of crosslinks between the three substrates [289, 291]. GA crosslinking durations were based on those used in the literature [264, 289, 290]. This particular crosslinking procedure was adopted for reasons discussed in section 6.2.3.1. After GA crosslinking was complete, samples were washed three times via the following procedure. First, any liquid was pipetted off the sample, next 400 μL of DPBS were pipetted onto the samples, and left to sit for five minutes. This procedure was repeated three times. After the final wash, the DPBS was removed, and replaced with 400 μL of live cell imaging solution (Sigma-Aldrich A14291DJ). The completed sample is shown in figure 6.1 (E). The sample was then transferred to an Oxford Instruments Asylum Research Cypher ES AFM.

For each substrate, amplitude modulation-frequency modulation atomic force microscopy (AM-FM AFM, section 2.1.3.4) was first performed on the sample. Next, photothermal actuation AFM nano-dynamic mechanical analysis (PANDA, section 2.1.3.3) was performed at specific points from the final AM-FM AFM image. PureCol and poly(HEMA) were measured with AC240TSA cantilevers ($k_1 \sim 1.6$ nN/nm, $k_2 \sim 58.8$ nN/nm, $f_1 \sim 21$ kHz in liquid, $f_2 \sim 150$ kHz in liquid, $R = 7 \pm 3$ nm) driven via photothermal actuation (section 2.1.3.1) at full blueDrive$^{\text{TM}}$ power. PureCol substrates were also measured with the short thin tip of an RC800PSA cantilever ($k_{c,1} \sim$

0.2 N/m, $k_{c,2} \sim 18$ N/m, $f_{c,1} \sim 25$ kHz in liquid, $f_{c,2} \sim 170$ kHz in liquid, $R \sim 15$ nm $\pm$ 5 nm) driven by photothermal excitation (section 2.1.3.1) at 0.3x blueDrive$^{\text{TM}}$ power. Cantilevers were calibrated via the Oxford Instruments Asylum Research GetReal$^{\text{TM}}$ calibration method (section 2.1.1) to avoid blunting the tip. All experiments were performed using Oxford Instruments Asylum Research software version 16.9.220 in Igor Pro software version 6.38B01.

PANDA measurements excited each sample over a frequency range of 0.1 - 5,000 Hz. This frequency range was split, and two or three PANDA measurements were performed, in order to avoid crashing the AFM software. For poly(HEMA) measurements, frequencies ranged from 0.1 - 10 Hz during a PANDA dwell of three minutes, from 0.5 to 100 Hz during a PANDA dwell of 60 seconds, and from 1 - 10,000 Hz during a PANDA dwell of 40 seconds. For pureCol measurements, frequencies ranged from 0.1 - 10 Hz during a PANDA dwell of three minutes, and from 1 - 5,000 Hz during a PANDA dwell of 40 seconds. PANDA is an off resonance technique (see section 2.1.3.3.1). Therefore, PANDA was not performed at frequencies higher than 5,000 Hz for RC800PSA measurements and 10,000 Hz for AC240TSA measurements in order to avoid introducing error caused by cantilever resonance effects.

After each experiment, height images of AM-FM AFM data were flattened using Oxford Instruments Asylum Research software version 16.9.220 in Igor Pro software version 6.38B01, in order to remove any variations in sample topology that weren't due to substrate features. This flattening was done by hand, in order to avoid introducing flattening artifacts. The processed files were then analyzed by a custom script written in MATLAB R2019b 9.7.0.1261785. This custom script calculated the loss tangent ($\tan\delta$, section 1.3.3.3) and storage modulus (E', section 1.3.3.3) of the substrates by applying equations 2.21 and 2.24 to AM-FM AFM data. Next, the script calculated the viscoelastic material constants E_c, E_r, η, $\tau_r = \eta/E_r$, and $\tau_c = \eta/E_c$ of the substrates, by applying the analysis described in chapter 3, section 3.2. The custom

script calculated the mean and standard deviation of height, E', and $\tan\delta$ by fitting a Gaussian to the distribution of values within a particular image or within the sample as a whole, as described in section 2.1.3.4.2. This method of calculating the mean and standard deviation was used in order to minimize the effects of bimodal or multimodal distributions of the data, shown in section 6.2.1. The mean and standard deviation of the remaining quantities were calculated in the usual manner, without fitting a Gaussian. Comparison p values were calculated from pairwise t tests between the relevant samples.

Another custom script written in MATLAB R2019b 9.7.0.1261785 was used to analyze PANDA data. This script loaded sample and reference measurements, then applied equation 2.14 - 2.16 in order to calculate the storage and loss stiffness (k' and k'') and $\tan\delta$. Next, the Hertz contact model (section 2.1.2) was applied to calculate E' and the loss modulus (E'') from k' and k'' via equations 2.17 and 2.18. The contact point, where the tip first touches the sample, was manually identified for application of the Hertz contact model. The Hertz model was used in order to directly compare PANDA and AM-FM AFM measurements.

6.2 Results

AM-FM AFM and PANDA were performed on poly(HEMA) and pureCol substrates to measure the effect of poly(HEMA) concentration and pureCol crosslinking on E', E'', and $\tan\delta$ of the substrates over a range of frequencies. It was necessary to perform two control experiments for PANDA measurements. Details of these controls are described in appendix D. The first of these controls, described in section D.1, ruled out the possibility of hydrodynamic drag [292] affecting the results by comparing PANDA data analyzed with reference measurements taken at different heights from the sample. The second control experiment, described in section D.2, demonstrated

that PANDA measurements were performed in the sample's linear viscoelastic regime by comparing PANDA measurements collected on the sample using different trigger points (see section 2.1.3.2).

6.2.1 Substrate AM-FM AFM distributions and statistics

As shown in figure 6.2, individual AM-FM AFM images of the various substrates had varying distributions of E' and $\tan\delta$. Typically, these distributions appeared unimodal, but were best described with a two term Gaussian model (equation 2.28). Since the same material (poly(HEMA) or collagen) was being probed in all areas of the AM-FM AFM images, different peaks in the two term Gaussian fits likely correspond to various structures, orientations, or clumps of a substrate's constituent polymers within the particular area measured in the AM-FM AFM image.

As shown in figure 6.2, bimodal distributions of the AM-FM AFM data prevented accurate calculation of sample means and standard deviations when the standard formulas were used. To overcome this issue, as described in section 2.1.3.4.2, the mean and standard deviation of substrate AM-FM AFM data was calculated by fitting Gaussians to the data distributions, rather than via the standard formulas. In this case, the mean and standard deviation represent the most prominent peak of the distribution, corresponding to the most prevalent polymer structure (for example, polymer orientation, tangling, or other topologies) in the substrate. As shown in figure 6.2, this Gaussian fit method of calculating sample statistics matches the values from the standard formulas if the data distribution is unimodal. Therefore, as described in section 2.1.3.4.2, the mean and standard deviation of all AM-FM AFM data presented in this chapter were calculated by fitting Gaussians to the data distributions. For individual image statistics, the distribution used for the fit comprised of pixel values from a particular AM-FM AFM image. For overall statistics, the distribution comprised of pixel values from all AM-FM AFM images.

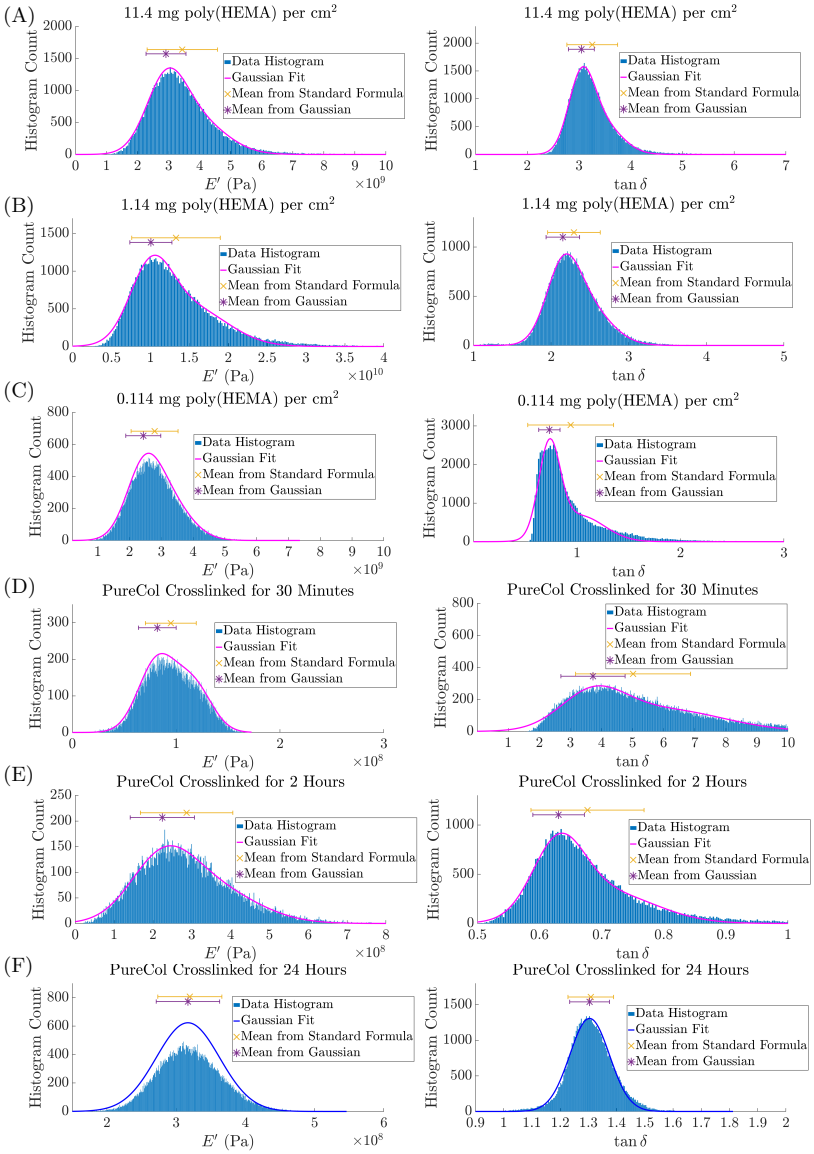


Figure 6.2: Representative distributions from AM-FM AFM of cell culture substrates. All distributions were obtained from the values of individual pixels of a single AM-FM AFM image. Storage modulus, E', and loss tangent, $\tan\delta$, distributions are shown in the left and right column, respectively, for substrates of: 11.2 mg poly(HEMA) per cm^2 of sample surface area (A), 1.12 mg poly(HEMA) per cm^2 (B), 0.112 mg poly(HEMA) per cm^2 (C), pureCol crosslinked with glutaraldehyde (GA) for 30 minutes (D), pureCol crosslinked for 2 hours (E), and pureCol crosslinked for 24 hours (F). A Gaussian fit to the distribution is shown as a magenta line if a two term Gaussian was used or as a blue line if a single term Gaussian was used. Selection of the single or two term Gaussian is described in section 2.1.3.4.2. The mean (points) and standard deviation (error bars) calculated via the standard formulas and from the Gaussian fit constants (as described in section 2.1.3.4.2) are shown as an orange x or a purple asterisks, respectively. While some fits, shown in (A)-(D) and (F), overestimate the histogram peak height, the mean and standard deviation extracted from these fits still match those calculated from the standard formulas.

6.2.2 Viscoelasticity of poly(HEMA) substrates

6.2.2.1 AM-FM AFM measurements of poly(HEMA) substrates

Representative AM-FM AFM images of poly(HEMA) substrates are shown in figure 6.3. The image in figure 6.3 (C) shows that the lowest concentration of poly(HEMA), at 0.114 mg poly(HEMA) per cm^2 of the substrate's surface, formed clumps rather than a uniform coating on the coverslip. These clumps were easy to displace with the AFM tip, and were prone to sticking to the tip. This behavior occasionally interfered with quantification of E' and $\tan\delta$, indicated by magenta arrows in figure 6.3.

The mean height, E', and $\tan\delta$ of poly(HEMA) substrates are shown in figure 6.4. As shown in figure 6.4 (A), the height of the 11.4 and 1.14 mg poly(HEMA) per cm^2 substrates was the same ($p = 0.99$). This observation agrees with the fact that large poly(HEMA) clumps were not observed on these substrates. The mean and standard deviation in film height of the 0.114 mg poly(HEMA) per cm^2 substrates is larger than the other substrates due to the variation in poly(HEMA) clump sizes.

As shown in figure 6.4 (B), the measured E' was higher for the 1.14 mg poly(HEMA) per cm^2 substrate than the other two ($p = 0.02$ vs. the 11.4 mg cm^{-2} sample and $p = 0.05$ vs. the 0.114 mg cm^{-2} sample). Since poly(HEMA) substrates were not crosslinked or modified, this increase in E' is likely the result of thin film effects [293], where the glass from the coverslip underlying the poly(HEMA) was partially probed by the AFM tip through the poly(HEMA). This observation is not surprising, since the thickness of the poly(HEMA) film should decrease when the concentration decreases. For thin films, the contact model of the tip/sample interaction requires a thin film correction, and application of the Hertz contact model in AM-FM AFM would lead to incorrectly high E' [293]. Regardless of the contact model, the observation that 1.14 mg per cm^2 poly(HEMA) films are thin suggests that cells on these substrates are able to probe through the poly(HEMA) to the underlying glass. The thin

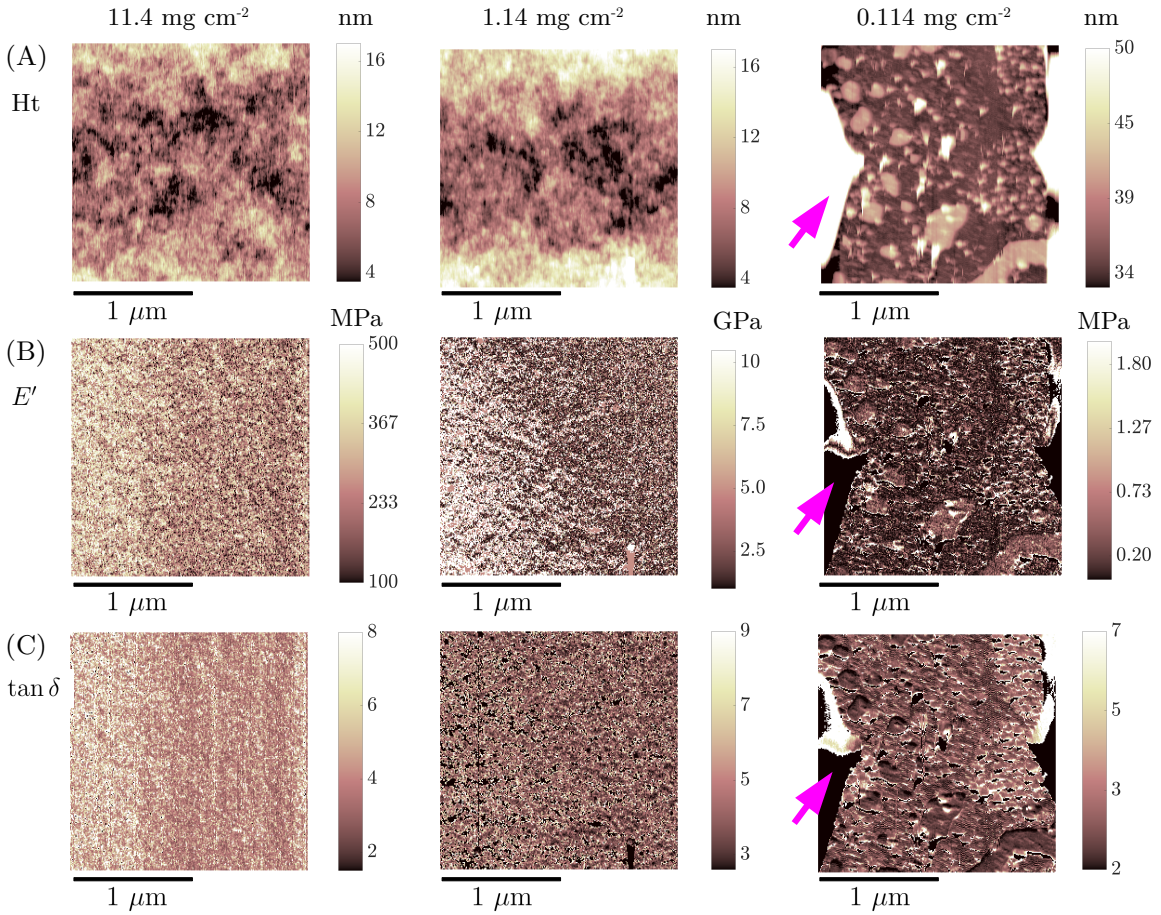


Figure 6.3: Representative AM-FM AFM images of poly(HEMA) substrates. Sample height (Ht) is shown in the top row (A), storage modulus, E', in the middle row (B), and loss tangent, $\tan\delta$, in the bottom row (C). Each column represents a different poly(HEMA) concentration. Substrates with 11.4 mg of poly(HEMA) per cm^2 of sample surface area, 1.14 mg poly(HEMA) per cm^2, and 0.114 mg poly(HEMA) per cm^2 are shown. Magenta arrows indicate regions where poly(HEMA) clumps in the 0.114 mg per cm^2 sample interfered with quantification of E' and $\tan\delta$.

film effect was not as pronounced, but still present, for the 0.114 mg poly(HEMA) per cm^2 substrate. The thin film effect was reduced for the 0.114 mg poly(HEMA) per cm^2 substrate because poly(HEMA) clumps in this sample were higher than the film in the 1.14 mg poly(HEMA) per cm^2 sample.

As shown in figure 6.4 (C), $\tan\delta$ was not significantly different between the different poly(HEMA) substrates ($p > 0.2$ for all comparisons). This observation, combined with the fact that alterations to E' of poly(HEMA) substrates is due to thin

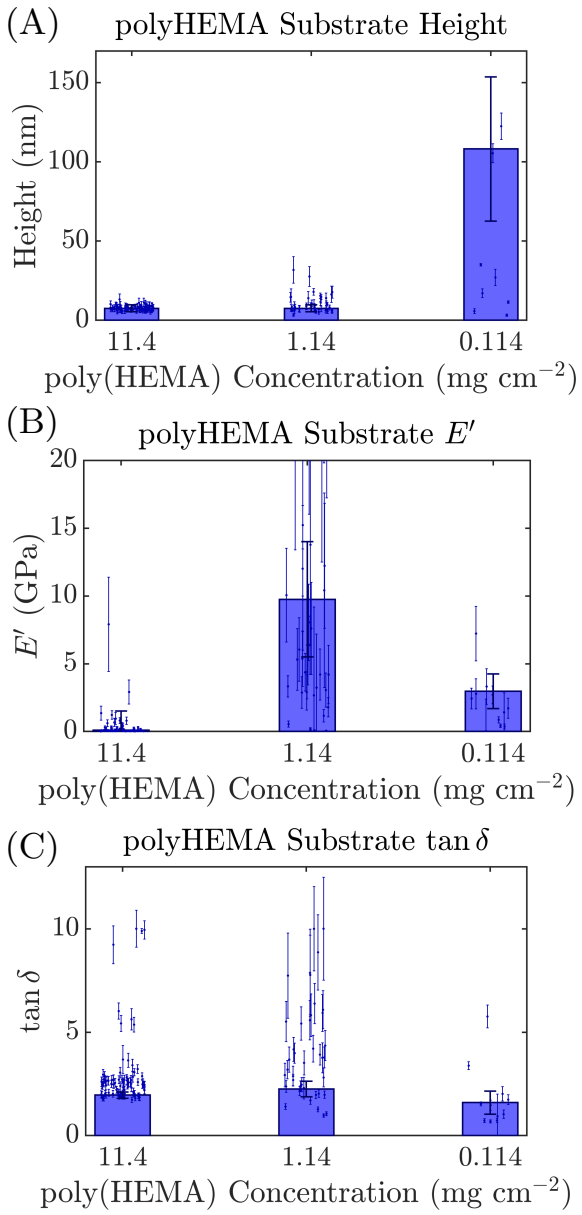


Figure 6.4: Effect of poly(HEMA) concentration on substrate height, E', and $\tan\delta$. The effect of poly(HEMA) concentration on substrate height (A), storage modulus, E' (B), and loss tangent, $\tan\delta$ (C), are shown. Bars represent overall mean values, calculated from all measured pixels. Smaller dots with error bars represent the mean values of individual AM-FM AFM images, calculated from all measured pixels within the image. Error bars represent the standard deviation.

film effects rather than differences in poly(HEMA) mechanical properties, suggests that poly(HEMA) substrates modulate cell activities by how much cells can probe the underlying substrate through the poly(HEMA) film.

Next, the AM-FM AFM model test (section 3.2.1, equation 3.11) was applied to AM-FM AFM measurements of poly(HEMA) films in order to determine if the viscoelasticity of poly(HEMA) substrates could be modeled with the general Maxwell model (GMM, section 1.3.6), standard linear solid (SLS, section 1.3.4), Kelvin-Voigt model (KV, section 1.3.5.1), or Maxwell model (MW, section 1.3.5.2). Figure 6.5 shows example model tests for the three poly(HEMA) substrates. As poly(HEMA) concentration decreased, model tests outcomes were more varied between AM-FM AFM images. For example, a second material is visible in the model tests on substrates with 1.14 mg poly(HEMA) per cm^2 (green circle in figure 6.5 (B)). This second material is likely the underlying glass, due to thin film effects. Additionally, for substrates with 0.114 mg poly(HEMA) per cm^2, the model test outcome varied depending on the position of AM-FM AFM measurements on the sample. This variation is likely due to variation in the size of poly(HEMA) clumps within the sample and how clump size alters thin film effects.

As in chapter 5 (section 5.3.3), large variation in the data meant that the root mean square error (RMSE) was a better metric than the R^2 value to describe how well the model test fit the data. RMSE closer to zero represents a better fit. The mean $\pm$ standard deviation in the RMSE values of the model test fits to each sample were 0.0376 $\pm$ 0.0111 for substrates with 11.4 mg poly(HEMA) per cm^2, 0.0499 $\pm$ 0.0577 for substrates with 1.14 mg poly(HEMA) per cm^2, and 0.1752 $\pm$ 0.1395 for substrates with 0.114 mg poly(HEMA) per cm^2. These RMSE values are reasonably low. Therefore, the data can be approximated by a line well. The model test therefore suggests poly(HEMA) substrates are linear viscoelastic materials. The RMSE values, as well as the standard deviation in RMSE increase as poly(HEMA) concentration decreases. These changes are likely the result of alterations in the tip's ability to probe the underlying glass through the poly(HEMA) and the resulting increased variation in model test outcomes.

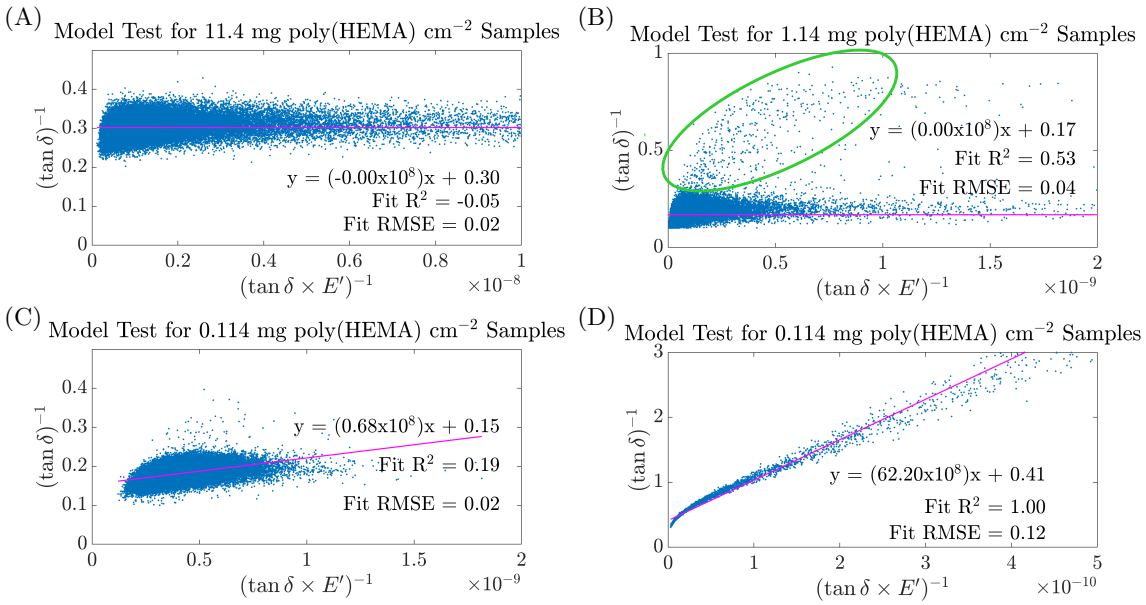


Figure 6.5: Example model tests for poly(HEMA) substrates. Each plot corresponds to a single AM-FM AFM image. Blue dots represent values from individual pixels of the image. The model test line (equation 3.11) is shown in magenta. The fit equation, R^2 value, and root mean square error (RMSE) are also shown. Model tests for substrates with 11.4 mg poly(HEMA) per cm^2 of sample surface area and 1.14 mg per cm^2 are shown in (A) and (B), respectively. The green circle in (B) indicates a second material in the sample. Model tests for two different AM-FM AFM images of 0.114 mg per cm^2 are shown in (C) and (D), to illustrate the variation in model test outcomes for this substrate.

The slope of model tests of substrates with 11.4 and 1.14 mg poly(HEMA) per cm^2 was approximately zero. The y-intercept of the model tests for these samples was greater than zero. Therefore, these observations suggest that poly(HEMA) in these two substrates behaves as a MW material (details in section 3.2.1). Some model tests of substrates with 0.114 mg poly(HEMA) per cm^2 (figure 6.5 (C)) behaved more like MW materials. However, the slope of these model tests was slightly increased, suggesting that the sample could also potentially be modeled as a GMM or SLS. Additionally, other model tests on substrates with 0.114 mg poly(HEMA) per cm^2 had a slope and y-intercept greater than zero, and a hyperbolic shape (figure 6.5 (D)). Therefore, for reasons described in section 3.2.1 and 3.3.2.3, these regions of the substrates behaved as GMMs. It is likely that the appearance of the SLS or GMM

in substrates with 0.114 mg poly(HEMA) per cm^2 is due to thin film effects from the glass underneath the poly(HEMA). Therefore, poly(HEMA) is a MW material, but the combined poly(HEMA)/glass substrate transitions from a MW material to a GMM as the ploy(HEMA) concentration decreases. Additionally, for substrates with low poly(HEMA) concentrations, the poly(HEMA)/glass substrate exhibits spatially heterogeneous materials (some MW and some GMMs), as a result of poly(HEMA) clumping in the sample.

Together, AM-FM AFM measurements of poly(HEMA) substrates suggest that poly(HEMA) is a MW material, and that the mechanical properties of poly(HEMA) remain constant regardless of poly(HEMA) concentration within the substrate. However, the convoluted properties of the poly(HEMA) and underlying glass vary with poly(HEMA) concentration. The ability of the tip, and likely a cell, to feel effects from the glass underlying the poly(HEMA) increases as poly(HEMA) concentration decreases. Additionally, the topology of poly(HEMA) substrates becomes more heterogeneous due to poly(HEMA) clumping as poly(HEMA) concentration decreases. This heterogeneous topology results in varied outcomes of the model test. Parts of the sample behave as MW materials, while others behave as GMMs. Therefore, poly(HEMA)/glass substrates have spatial heterogeneity in their linear viscoelastic behavior for low poly(HEMA) concentrations. Since the effects of the underlying glass played an important role in poly(HEMA) substrate mechanics, cells on poly(HEMA) likely respond to the properties of the combined poly(HEMA)/glass substrate, rather than the poly(HEMA) alone. Further AM-FM AFM reconstruction of poly(HEMA) material constants (section 3.2.3) is not required for these samples, since PANDA, described next, was performed instead.

6.2.2.2 PANDA measurements of poly(HEMA) substrates

It was difficult to obtain consistent PANDA measurements of substrates with 1.14 and 0.114 mg poly(HEMA) per cm^2 of sample surface area (not shown). For the 1.14 mg per cm^2 substrate, this effect could have been due to heterogeneity in the sample and to thin film effects. For the 0.114 mg per cm^2 sample, PANDA measurements were difficult to obtain because poly(HEMA) clumps tended to stick to the tip. For these reasons, PANDA measurements were only obtained for substrates with 11.4 mg poly(HEMA) per cm^2. Representative PANDA measurements of E', E'', and $\tan\delta$ of the 11.4 mg poly(HEMA) per cm^2 substrate are shown in figure 6.6.

The measured $\tan\delta$ agrees with macroscale literature measurements of unmodified poly(HEMA) [276] as well as composite poly(HEMA) acrylamide substrates [277]. E' and E'', calculated by applying the Hertz contact model to measured PANDA k' and k'', are higher than the literature by two or three orders of magnitude [276, 277]. This observation could, in part, be due to the use of the Hertz model when a different contact model may be more appropriate to represent the tip/sample interaction. However, it is unlikely that use of a different contact model would reduce E' and E'' by three orders of magnitude. Therefore, investigation into other contact models is left for future work. Instead, the difference between PANDA measurements and literature measurements likely arises from the fact that PANDA was performed at the nanoscale, while literature measurements [276, 277] were performed at the macroscale [294]. Nanoscale moduli can sometimes be several orders of magnitude higher than macroscale moduli, as a result of the natural scaling behavior of polymers [294].

As shown in figure 6.6, PANDA measurements of $\tan\delta$, E', and E'' did not vary with position on the sample. This observation agrees with AM-FM AFM observations (section 6.2.2.1) that the 11.4 mg poly(HEMA) per cm^2 sample was the thickest, and most homogeneous poly(HEMA) substrate. With this fact in mind, it is not surprising that the viscoelastic properties of these poly(HEMA) films were also uniform with

different PANDA measurements.

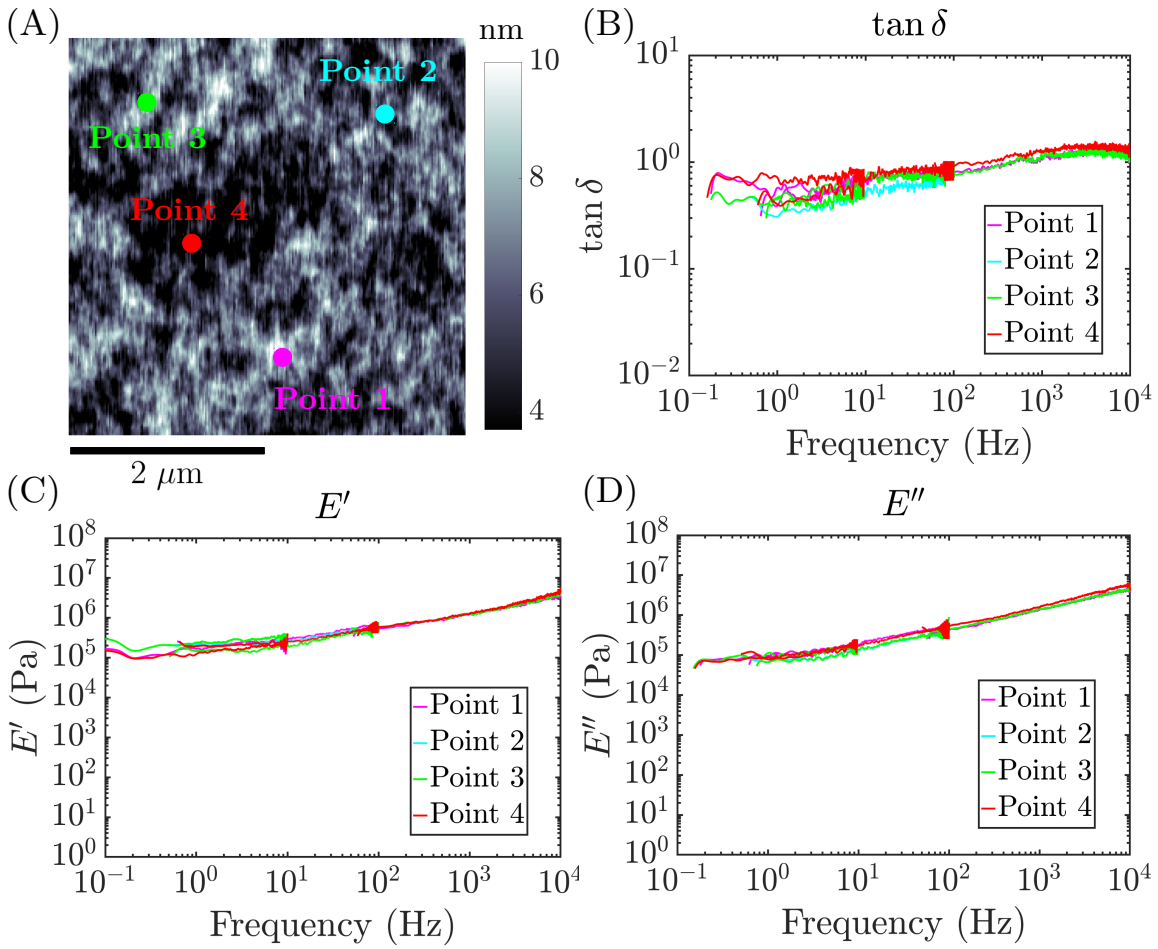


Figure 6.6: PANDA measurements at different points on poly(HEMA) substrates. PANDA was performed on substrates with 11.4 mg poly(HEMA) per cm^2. A topology image of the substrate, as well as the location of each PANDA measurement is shown in (A). The measured loss tangent ($\tan\delta$) is shown in (B). Storage and loss moduli, E' and E'', calculated from PANDA measurements by applying the Hertz contact model are shown in (C) and (D), respectively. These measurements are representative of measurements from two biological replicates of the substrate.

6.2.3 Viscoelasticity of pureCol substrates

Next, AM-FM AFM and PANDA measurements of pureCol substrates with different amounts of crosslinking were performed. Before it was possible to measure pureCol substrates, it was necessary to optimize the preparation of the substrates.

As described in the following section, this optimization was necessary because many pureCol substrates possessed large hydration shells and/or polymer brushes that interfered with AM-FM AFM and PANDA measurements.

6.2.3.1 Optimizing the preparation of pureCol substrates

Attempts at AFM measurements of pureCol substrates that were not crosslinked were performed using AC240TSA cantilevers, RC800PSA cantilevers (all four tips), and bioLeverMini cantilevers. Regardless of the cantilever used, pureCol substrates that had not been crosslinked were too fluid to detect with the AFM tip. This conclusion was reached because, during AFM experiments, the tip would enter the pureCol substrate (visible on the optical microscope in the AFM), and the deflection would fluctuate, but the trigger point and/or setpoint was never reached. Changing the trigger point, and/or setpoint, and manually engaging the sample did not resolve the issue. This observation is reminiscent of preliminary attempts at performing AFM on mouse tumors (see chapter 5, section 5.4.2). Regardless, it was not possible to perform AFM experiments on pureCol substrates that were not crosslinked. It was therefore necessary to crosslink pureCol substrates.

Glutaraldehyde (GA) was used to crosslink the substrates [264, 289, 290]. Crosslink density within a pureCol substrate can be altered by changing the duration to which the substrate is exposed to GA, or by changing the GA concentration [289, 291]. Initial attempts to crosslink pureCol substrates were performed by varying the concentration of GA in the crosslinking solution. GA concentrations of 0.01%, 2%, and 4% were attempted. Substrates crosslinked with 0.01% GA behaved in a similar manner to pureCol that was not crosslinked (not shown). It was not possible to perform AFM on pureCol substrates crosslinked with GA concentrations higher than 1% because a layer of material several microns thick existed on the surface of these substrates.

First, AM-FM AFM was attempted on substrates crosslinked with 2% and 4% GA. This attempt resulted in images of a surface layer similar to those of the hydration shells in section 4.2.4 (not shown). It was not possible to quantify the mechanical properties of this layer with AM-FM AFM because a repulsive tip/sample interaction was never obtained. Additionally, it was not possible to break through the layer to the underlying pureCol with AM-FM AFM. Since AM-FM AFM indentations are typically only a few nanometers deep [220], this observation suggests that the layer was more than tens of nanometers thick.

In spite of the difficulties in performing AM-FM AFM, it was possible to indent (see section 2.1.3.2) through the layer to the underlying pureCol. Example indentations are shown in figure 6.7, demonstrating that the layer was several microns thick. Even though it was possible to indent the underlying pureCol through the layer, the layer interfered with PANDA dwells (not shown). It was therefore difficult to obtain meaningful PANDA results through such thick surface layers. These layer observations were reproducible, and occurred in two to three replicates of each GA concentration. The layers were also fairly uniform over the sample (not shown).

It was possible to distinguish, via the optical microscope built into the AFM, whether the tip had landed on the sample or on the edge of the custom chamber in which the sample polymerized (not shown). Therefore, the observed thick layers were part of the pureCol substrates, not the result of an experimental mistake such as the tip landing on the edge of the sample chamber instead of the pureCol.

Since the interaction of the tip with the surface resembled that of collagen's hydration shells (section 4.2.4), it is possible that the surface layers belonged to a thick hydration shell. If this is the case, this observation further supports the notion that hydration shells play a more significant role in modulating tissue and substrate properties than previously thought. Alternatively, the surfaces may be polymer brushes [295] protruding from the pureCol substrate. Such brushes can form as the result

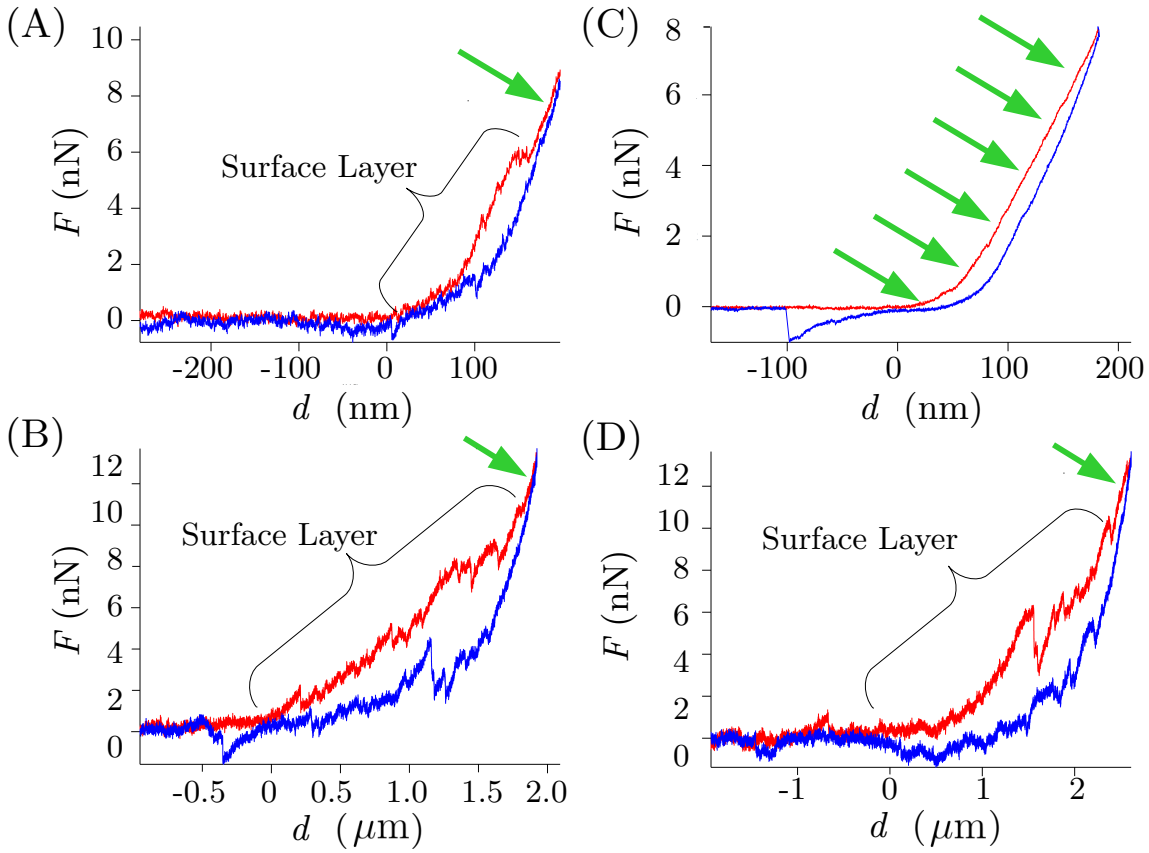


Figure 6.7: Example indentation curves of pureCol substrates. During indentations, an AFM tip is pressed into a sample (red curve), causing the sample to experience some force F and some indentation d. The tip is then retracted from the sample (blue curve). More details on indentations can be found in section 2.1.3.2. A typical F vs. d curve taken with an AC240TSA cantilever on pureCol substrates without thick surface layers is shown in (A). Green arrows indicate the region of the force curve where pureCol is indented. The bump in the approach curve, indicated with a black bracket, indicates that the tip passed through an additional material that was not pureCol. This material is possibly a hydration shell or polymer brush, and was roughly 150 nm thick. An example AC240TSA force curve of a pureCol substrate with a thicker surface layer is shown in (B), where the layer is several microns thick. Similar results were obtained with RC800PSA cantilevers. A typical F vs. d curve taken with an RC800PSA cantilever on pureCol substrates without thick surface layers is shown in (C). This curve was collected on the same substrate as (A). No surface layer is present in this curve. An example F vs. d curve, taken with an RC800PSA, of substrates with thick surface layers is shown in (D). Again, this layer is several microns thick.

of loose polymer ends protruding normal to the surface of the substrate, and can range from tens to hundreds of nanometers [296, 297] to several microns in thick-

ness [295, 298]. Additionally, loose ends of collagen fibrils in tendons (tendons are mostly comprised of collagen) can behave as polymer brushes [299]. In the future, it would be possible to distinguish whether the micron-thick surface layers belong to hydration shells, polymer brushes, or both by comparing the results in this section to measurements taken using cantilevers with longer tips. The cantilevers with longer tips would not be as affected by a polymer brush, but would still be affected by a hydration shell.

The difficulty in performing AM-FM AFM and PANDA through micron-thick surface layers was overcome by altering the crosslinking procedure to create substrates without these layers. Instead of changing the GA concentration, samples were exposed to 1% GA for different amounts of time. PureCol samples exposed to GA for 4 hours also exhibited thick surface layers (not shown). Samples crosslinked for 30 minutes, 2 hours, and 24 hours did not have the thick surface layers. This finding lead to the protocol for pureCol substrate preparation, described in section 6.1 and demonstrates that crosslinking alters hydration shell and/or polymer brush structures in pureCol substrates. In the future, it would be interesting to image and categorize the thick surface layers of pureCol substrates in more detail.

It is interesting to note that AC240TSA cantilevers were more sensitive to the pureCol surface layers than RC800PSA cantilevers on the same substrate (figure 6.7 (A) and (C)). It is likely that AC240TSA cantilevers are more sensitive to the surface layers of pureCol substrates than RC800PSA cantilevers because AC240TSA cantilevers are stiffer. The higher stiffness of AC240TSA cantilevers could mean that the cantilever is not as able to dissipate energy from tip/sample interactions as well as RC800PSA cantilevers. In this case, the AC240TSA would be more sensitive to vibrations and bumps caused by interactions with the surface layer of the substrate than the RC800PSA. This mechanism is analogous to tire pressure in cars. Higher tire pressure (analogous to cantilever stiffness) hinders energy dissipation by the tires.

As a result, the car experiences more bumps and vibration from the road. Lower tire pressure allows the tires to dissipate energy from such bumps and vibrations, resulting in a smoother ride. Regardless of the mechanism, the observation that AC240TSA cantilevers are more sensitive to surface layer effects than RC800PSA cantilevers suggests that similar factors could be at work in biological systems. Cells with different mechanical properties could have altered sensitivity to the hydration shells and/or polymer brushes within tissues.

6.2.3.2 AM-FM AFM measurements of pureCol substrates

AM-FM AFM experiments on pureCol substrates were performed in two phases. First, experiments were performed on a single spot of a pureCol substrate using an RC800PSA cantilever. After measurements using the RC800PSA were complete, the cantilever was changed to an AC240TSA. Thereby, a single pureCol substrate was probed by both cantilevers in roughly the same location on the sample. Representative AM-FM AFM images of pureCol substrates are shown in figure 6.8 and 6.9, for measurements obtained with an RC800PSA and AC240TSA, respectively.

PureCol substrate topology looks different when different cantilevers are used. This difference is likely the result of cantilever interactions with pureCol's hydration shell. It is already known that hydration shells between an AFM tip and sample affect the tip's ability to image a sample [140, 141]. As suggested by the indentation curves in section 6.2.3.1, AC240TSA cantilevers are more sensitive to the hydration shell, or other surface features, of pureCol substrates. Therefore, the different appearance of pureCol substrates in AM-FM AFM performed with the different cantilevers likely arises from different cantilever sensitivities to tip/pureCol interactions.

Figure 6.10 shows the mean feature height, E', and $\tan\delta$ of pureCol substrates. As GA concentration increased, the height of substrate features did so as well ($p < 0.04$ for all comparisons). It is already known that GA crosslinking increases the diame-

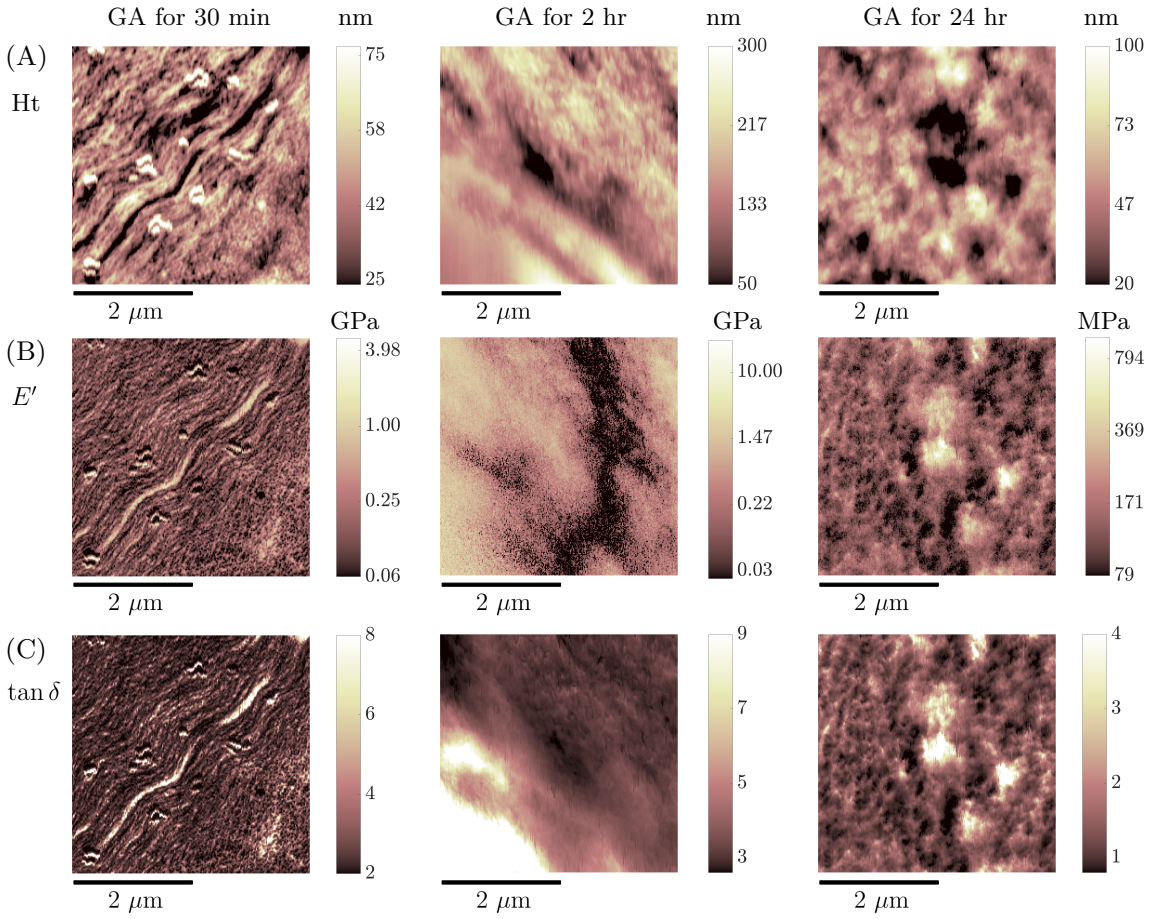


Figure 6.8: Representative AM-FM AFM images of pureCol substrates measured by RC800PSA cantilevers. Sample height (Ht) is shown in the top row (A), storage modulus, E', in the middle row (B), and loss tangent, $\tan\delta$, in the bottom row (C). Each column represents a pureCol substrate with a different amount of time spent crosslinking in glutaraldehyde (GA). Substrates with 30 minutes of GA crosslinking, 2 hours of GA crosslinking, and 24 hours of GA crosslinking are shown.

ter of collagen fibers [288]. The increase in feature height with increasing crosslink duration is likely due to rearrangement of the pureCol substrates by crosslinking. As described in section 6.2.3.1, pureCol is fluid when no crosslinking is performed. Crosslinks formed by GA likely reorient collagen polymers within the substrate as crosslinking occurs. With longer exposure to GA, more crosslinks form [289]. Therefore, more reorientation and bundling of collagen fibrils in the substrate likely occurs, resulting in the observed increase in feature height with crosslinking duration.

Figure 6.10 (B) shows that E' of pureCol substrates varied with crosslinking dura-

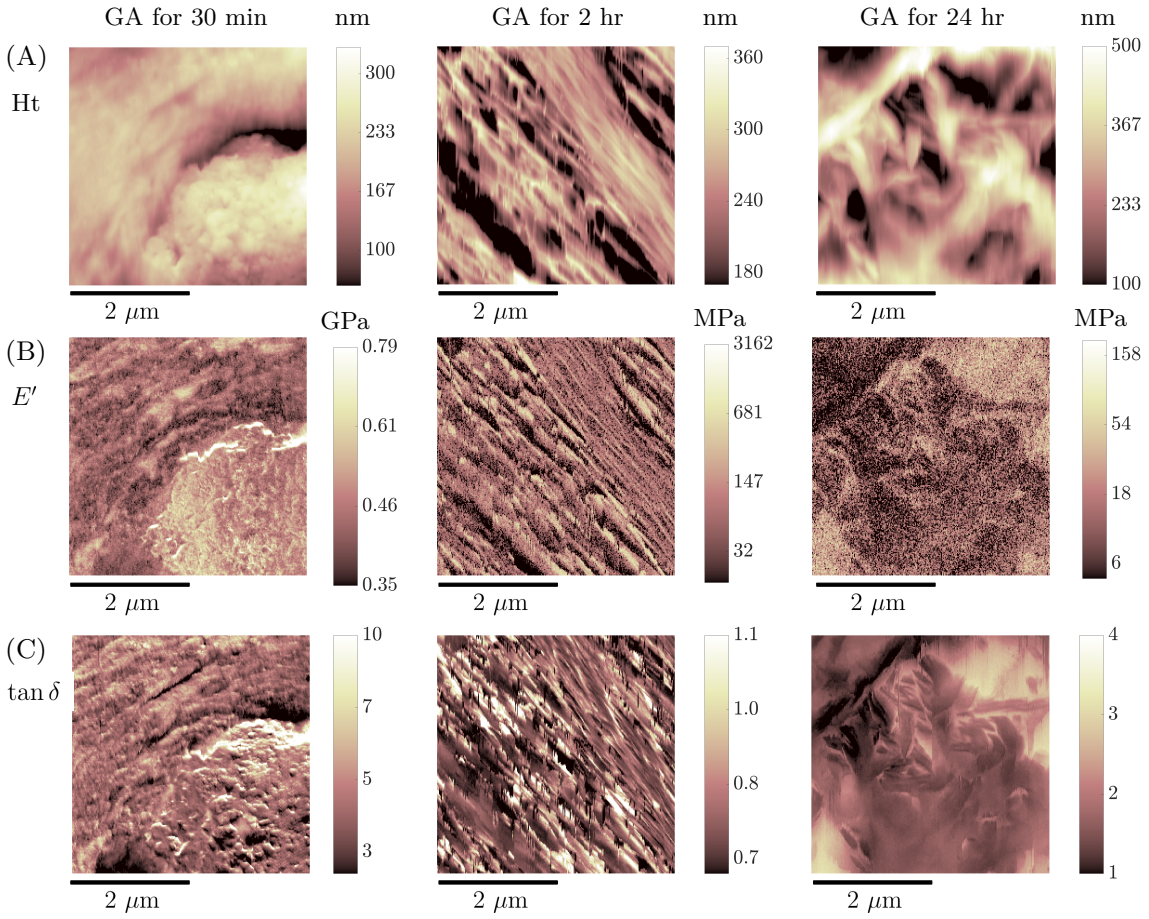


Figure 6.9: Representative AM-FM AFM images of pureCol substrates measured by AC240TSA cantilevers. Sample height (Ht) is shown in the top row (A), storage modulus, E', in the middle row (B), and loss tangent, $\tan\delta$, in the bottom row (C). Each column represents a pureCol substrate with a different amount of time spent crosslinking in glutaraldehyde (GA). Substrates with 30 minutes of GA crosslinking, 2 hours of GA crosslinking, and 24 hours of GA crosslinking are shown.

tion. Substrate E' increased from substrates exposed to GA for 2 hours to substrates exposed to GA for 24 hours ($p < 0.01$ for both cantilevers), likely as a result of the increased crosslink density from the 2 to 24 hour exposure to GA. E' of substrates crosslinked for 30 minutes varied between AM-FM AFM images, as indicated by magenta arrows in figure 6.10 (B). The large variation in E' of the 30 minute GA substrates suggests that the mechanical properties of the substrate were heterogeneous. It is likely that the short (30 minute) crosslinking time of these substrates did not completely saturate the PureCol with crosslinks. It is also likely that crosslinking

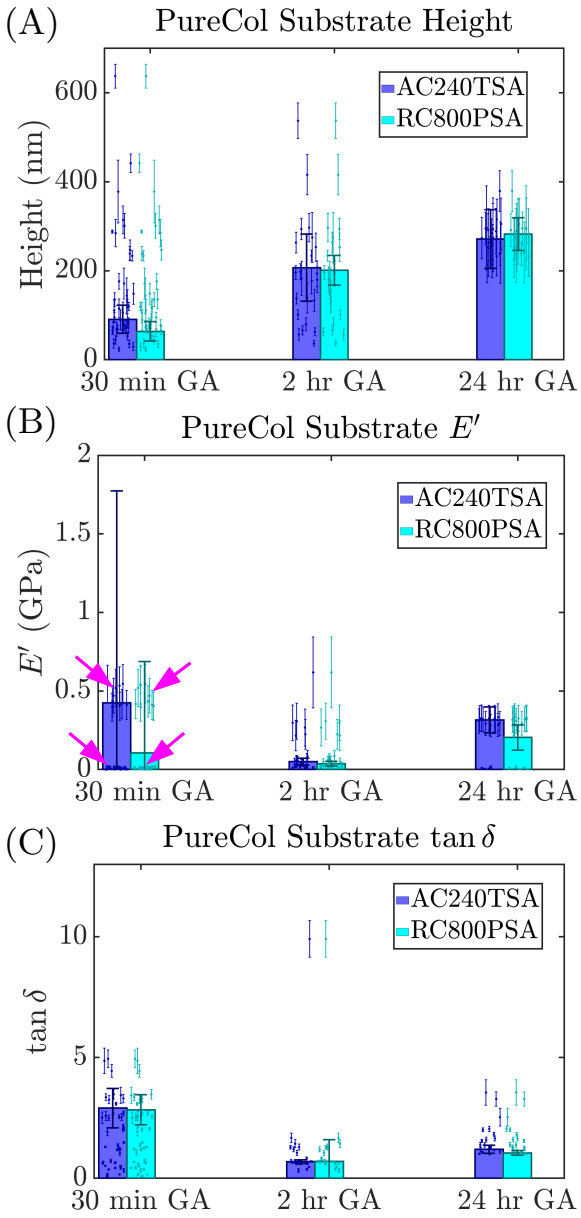


Figure 6.10: Effect of crosslinking on pureCol substrate height, E', and $\tan\delta$. Substrates were crosslinked in glutaraldehyde (GA) for 30 minutes, 2 hours, or 24 hours. The effect of crosslinking duration on pureCol substrate height (A), storage modulus, E' (B), and loss tangent, $\tan\delta$ (C), are shown. Bars represent overall mean values, calculated from all measured pixels. Smaller dots with error bars represent the mean values of individual AM-FM AFM images, calculated from all measured pixels within the image. Error bars represent the standard deviation. Some images of pureCol substrates crosslinked for 30 minutes had smaller E' than others. Magenta arrows indicate these two groups.

was heterogeneous throughout the sample, depending on the orientation of collagen fibrils within the pureCol. Therefore, the different values of E' likely correspond to regions where GA crosslinking was different, depending on collagen fibril orientation.

The value of $\tan\delta$ was not significantly different between samples crosslinked for 2 and 24 hours ($p = 0.64$ for RC800PSA cantilevers and $p = 0.10$ for AC240TSA cantilevers). Substrate $\tan\delta$ was higher for samples crosslinked for 30 minutes ($p \leq 0.01$ for both comparisons with both cantilevers). This observation suggests that the increased crosslink density in the 2 and 24 hour GA substrates resulted in lower $\tan\delta$.

Next, in order to determine if the viscoelasticity of pureCol substrates could be modeled with the MW, KV, SLS, or GMM model, the model test line (equation 3.11, section 3.2.1) was fit to each AM-FM AFM image. Representative model tests are shown in figure 6.11. Some model tests for pureCol substrates crosslinked for 30 minutes had small slopes, and therefore behaved as MW materials (figure 6.11 (A) and (E)). Others (figure 6.11 (B) and (F)) had a slope and y-intercept greater than zero, and therefore potentially obeyed the SLS or GMM. Model tests on substrates crosslinked for 2 or 24 hours had slopes and y intercepts greater than zero, and therefore likely obey the SLS or GMM. The hyperbolic shape of the model test plots supports the notion that pureCol substrates are GMMs for the reasons described in section 3.3.2.3.

As in chapter 5 (section 5.3.3) and for poly(HEMA) substrates (section 6.2.2.1), large variation in the data meant that the root mean square error (RMSE) was a better metric than the R^2 value to describe how well the model test fit the data. RMSE closer to zero represents a better fit. The mean $\pm$ standard deviation in RMSE for measurements performed with an RC800PSA were: 0.22 ± 1.21 for pureCol crosslinked for 30 minutes, 0.05 ± 0.03 for pureCol crosslinked for 2 hours, and 0.03 ± 0.03 for pureCol crosslinked for 24 hours. The mean $\pm$ standard deviation in RMSE for measurements performed with an AC240TSA were: 0.31 ± 1.20 for pureCol

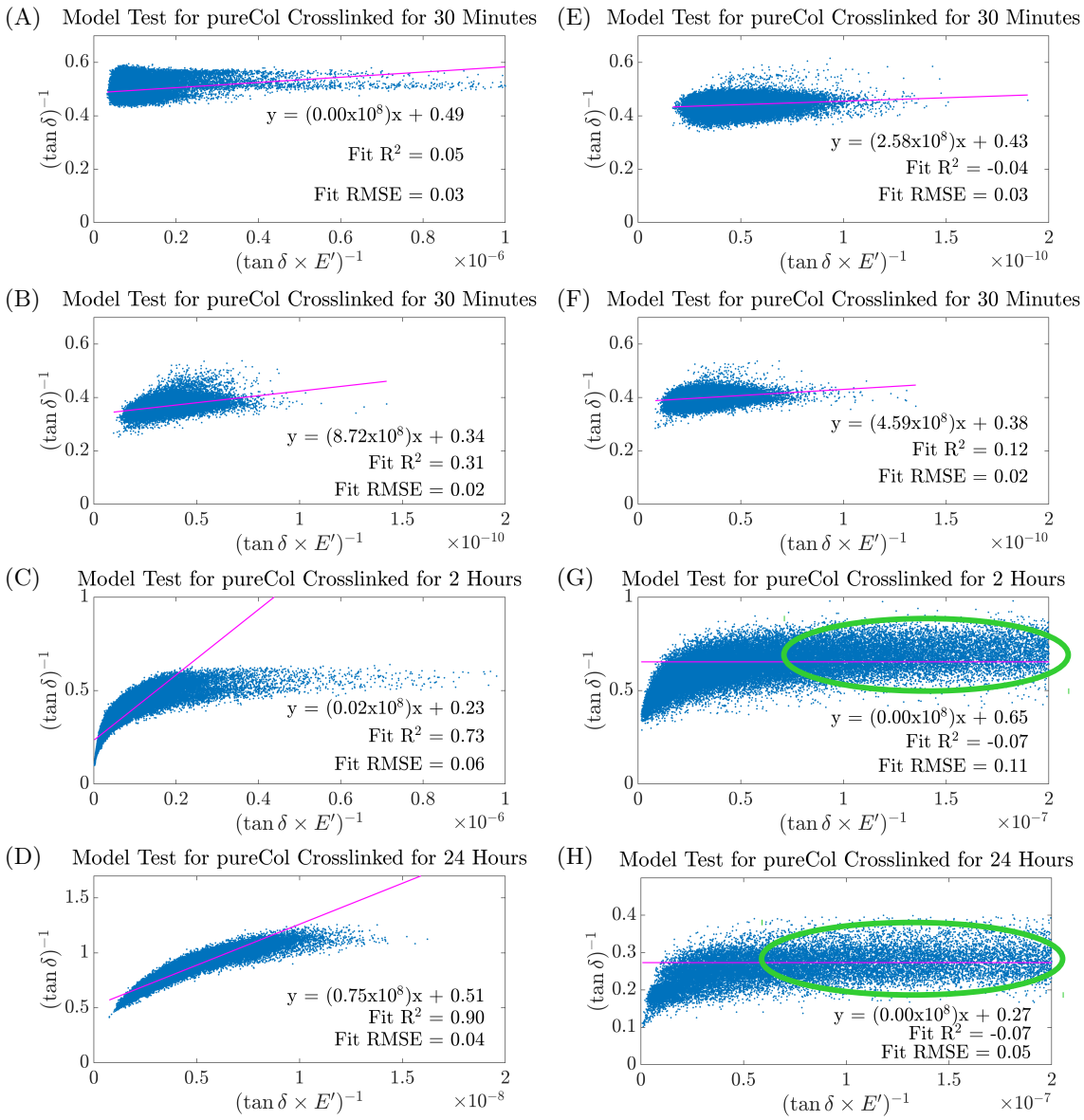


Figure 6.11: Example model tests for pureCol substrates. Each plot corresponds to a single AM-FM AFM image. Blue dots represent values from individual pixels of the image. The model test line (equation 3.11) is shown in magenta. The fit equation, R^2 value, and root mean square error (RMSE) are also shown. Model tests for AM-FM AFM data collected with an RC800PSA cantilever are shown in (A)-(D). Similarly, model tests for data collected with an AC240TSA cantilever are shown in (E)-(H). Green circles indicate a Maxwell material (section 1.3.5.2) in the AC240TSA model tests that is not present in the RC800PSA model tests. Representative model tests for pureCol substrates crosslinked for 30 minutes are shown in (A), (B), (E), and (F). Comparisons of (A) with (B) or (E) with (F) show differences in the model test outcome for these substrates. Representative model tests for pureCol substrates crosslinked for 2 hours are shown in (C) and (G). Representative model tests for pureCol substrates crosslinked for 24 hours are shown in (D) and (H).

crosslinked for 30 minutes, 0.17 ± 0.16 for pureCol crosslinked for 2 hours, 0.05 ± 0.02 for pureCol crosslinked for 24 hours. Regardless of the cantilever used, these RMSE values are reasonably low. Therefore, the data can be approximated by a line well. The model test therefore suggests that the samples are linear viscoelastic materials.

PureCol substrates crosslinked for 30 minutes had the largest variation in RMSE, for both AC240TSA and RC800PSA cantilevers. This observation is likely related to the fact that regions of the sample obeyed different viscoelastic models, and therefore that two types of materials were present in the 30 minute GA substrate. As shown in figure 6.11 (A) and (E), some regions of the sample had model tests with low slopes and thereby behaved as MW materials. Other regions of the sample (figure 6.11 (B) and (F)) had a higher slope, suggesting these regions obey the SLS or GMM. Model test details for MW and GMM materials can be found in section 3.2.1.

As already hypothesized, it is likely that the short (30 minute) crosslinking time of these substrates did not completely saturate the pureCol with crosslinks. It is also likely that crosslinking was heterogeneous throughout the sample, depending on the orientation of collagen fibrils within the pureCol. The MW material may correspond to parts of the sample with less crosslinking while the GMM corresponds to parts of the sample with more crosslinking. This hypothesis is supported by the fact that samples with longer crosslinking duration, and likely more crosslinks [289], did not exhibit the MW material. Additionally, as described in section 6.2.3.1, pureCol substrates without any crosslinking were too fluid to measure in liquid with the AFM. Therefore, pureCol with fewer crosslinks also likely exhibits more fluid behavior. Of the basic models of linear viscoelasticity, the MW model is best to describe samples that are more fluid [165]. It is therefore likely that less crosslinking in regions of the sample would allow these regions to retain more fluid characteristics such as those of a MW material.

The RMSE values were higher for data collected with the AC240TSA cantilever

compared to the RC800PSA. This observation is likely due to the fact that AC240TSA model tests contained a second material that was not apparent in RC800PSA model tests (green circles in figure 6.11). This second material behaved as a MW material. However, the second MW material is likely not the same as the MW material hypothesized to correspond to regions of low crosslinking on the substrate. Unlike the first MW material related to crosslinking, the second material only appears in samples with longer crosslinking duration and is much more prominent in AC240TSA model tests than RC800PSA model tests. Additionally, the second MW material is reminiscent of hydration shell effects observed on collagen fibrils in chapter 4 (section 4.9), where the shell behaved as an additional MW material in the model test. The hypothesis that the MW material corresponds to a layer, a hydration shell and/or polymer brush, on the surface of the pureCol substrate is supported by the observation that AC240TSA cantilevers are more sensitive to pureCol surface layers than RC800PSA cantilevers (section 6.2.3.1), and that the MW material only appears in AC240TSA model tests. Together, these observations suggest that the MW material is pureCol's surface hydration shell and/or polymer brush.

In summary, AM-FM AFM measurements in this section suggest that crosslinked pureCol substrates are GMMs, that crosslinking is heterogeneous within samples, and that pureCol surface layers (hydration shells and/or polymer brushes) behave as MW materials. AM-FM AFM reconstruction of material constants (section 3.2.3) is not required for these samples, since PANDA, described next, was performed instead.

6.2.3.3 PANDA measurements of pureCol substrates

PANDA measurements of pureCol substrates were performed using both RC800PSA and AC240TSA cantilevers. Both cantilevers obtained similar results, shown in appendix D.3. Only measurements obtained using RC800PSA cantilevers are presented in this section, but are representative of measurements obtained with AC240TSA

cantilevers. PANDA measurements were performed in at least two positions on the surface of each pureCol substrate. In general, measured $\tan\delta$ agree with literature values for pureCol and other collagen substrates [281–284]. The Hertz contact model (section 2.1.2.1) was used to calculate E' and E'' of pureCol substrates. E' and E'' of pureCol substrates are several orders of magnitude higher than the literature values [281–284]. This observation could, in part, be due to the use of the Hertz model when a different contact model may be more appropriate to represent the tip/sample interaction. However, it is unlikely that use of a different contact model would change E' and E'' by several orders of magnitude. Therefore, investigation into other contact models is left for future work. The difference between PANDA measurements and literature measurements likely arises from the fact that PANDA was performed at the nanoscale, while literature measurements [281–284] were performed at the macroscale [294]. Nanoscale moduli can sometimes be several orders of magnitude higher than macroscale moduli, as a result of the natural scaling behavior of polymers [294].

Representative PANDA measurements of pureCol substrates crosslinked with GA for 30 minutes are shown in figure 6.12. Two points on the sample were measured. The first measurement was performed on a spot with aligned fibrils. The second was performed on a spot without fibrils. It is unclear if the the second point consisted of collagen that polymerized into globs, or was a region of aligned fibrils that ran into the substrate, rather than along the surface. Regardless, of which is the case, the following discussion still applies.

E' was the same for both points. For frequencies less than 100 Hz, E'' was lower in the spot with fibrils. Therefore, $\tan\delta$ at frequencies less than 100 Hz was also lower for the spot containing fibrils. The fact that E' was the same in both points of the sample is likely related to sample crosslinking. It is likely that GA crosslinking restricted the movement of collagen polymers when the substrate was deformed [291], regardless of the position measured. Values of E'' and $\tan\delta$ were lower for fibrils at frequencies less

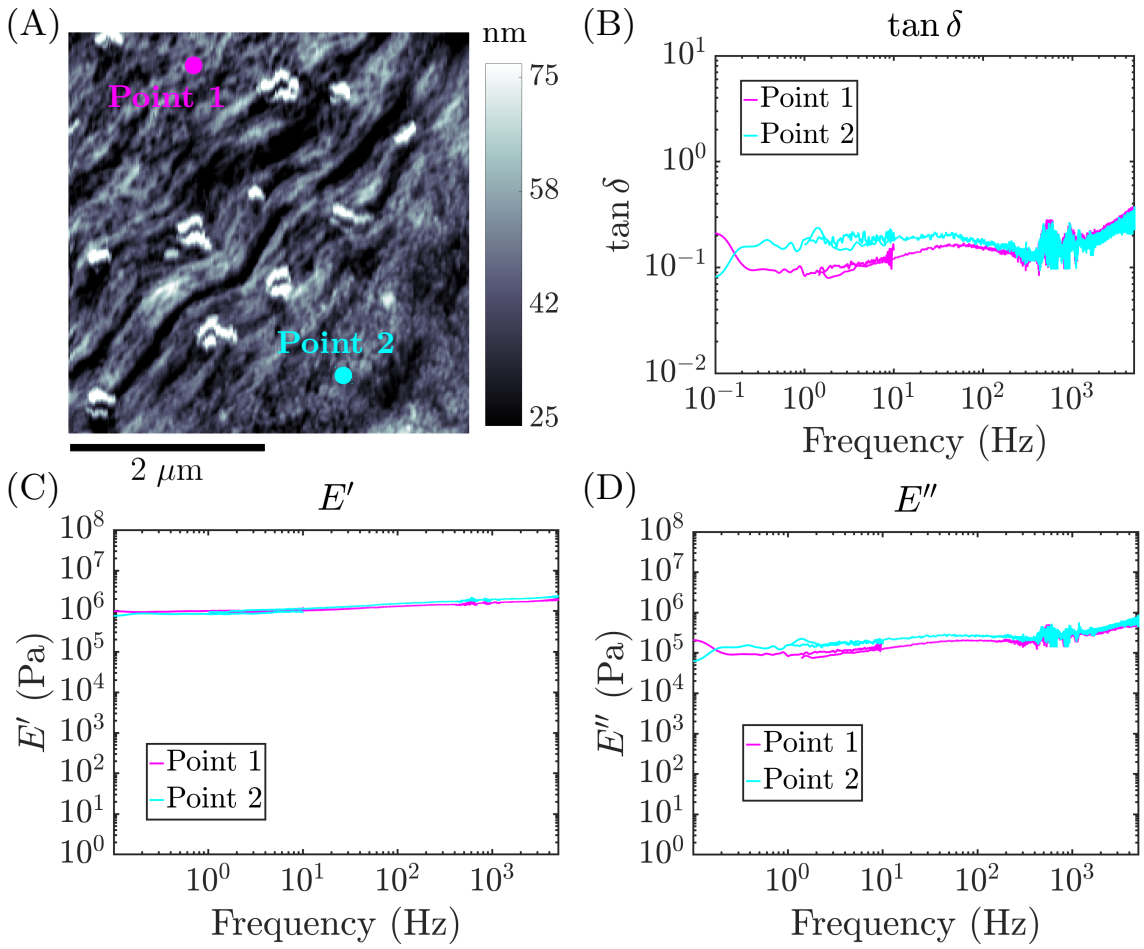


Figure 6.12: PANDA measurements at different points on pureCol substrates crosslinked with glutaraldehyde for 30 minutes. A topology image of the substrate, and the location of each PANDA measurement is shown in (A). Measured loss tangents ($\tan\delta$) are shown in (B). E' and E'' calculated from PANDA measurements by applying the Hertz contact model are shown in (C) and (D), respectively. These measurements are representative of two biological replicates of the substrate.

than 100 Hz, suggesting that fibrils, and regions of the substrate which contain fibrils, do not dissipate as much energy as regions without fibrils. The mechanism behind these observations is likely related to the orientation and confinement, hydration, and potentially the electrical properties of collagen polymers in each point.

Different collagen typologies alter the hydration shell of the molecule, as observed in section 4.2.4. This rearrangement likely alters electrostatic interactions between collagen and the shell. Additionally, changes in collagen topology likely alter inter-

actions between polymers with the substrate. Similarly, the electrical properties of collagen can be affected by the topology of collagen structures, and play an important role in determining the properties of structures arising from collagen [88, 154, 155]. Collagen fibrils posses two axes of electric polarization, one in a longitudinal direction (along the length) of the fiber, and one in an axial direction (perpendicular to the length of the molecule) along the fiber [155]. When collagen fibrils and fibers align, electric polarization of the resulting structures is maintained [88]. Additionally, randomly oriented collagen deposition sometimes cancels out some of the electric polarization of collagen structures [154]. These observations suggest that structures arising from aligned collagen fibrils maintain electric polarization of the fibrils, while structures of randomly oriented collagen may or may not do the same [88, 154, 155]. Therefore, it is reasonable to hypothesize that the electrical properties of pureCol substrates, and any resulting hydration shells or other features that depend on electrostatic interactions, are spatially heterogeneous depending on the orientation of collagen molecules in any given region of the sample. Together, these mechanisms suggest that alterations to energy dissipation in different regions of the substrate could be related to alterations in the electric polarization, hydration, and intermolecular interactions within these regions as a result of altered collagen topology.

Representative PANDA measurements of pureCol substrates crosslinked with GA for 2 hours are shown in figure 6.13. Three points were probed on the sample. The first measurement was performed on a small fiber, with many fibrils distributed over the fiber's surface. The second measurement was performed on a larger fiber, without the small fibrils over the surface. The third measurement was performed on an even larger fiber on the sample. The measured E' and E'' did not vary with position on the sample for frequencies less than 1,000 Hz. At 1,000 Hz, E' and E'' of first point increased slightly compared to the others. Similarly, $\tan\delta$ of the first point also increased compared to the other points at frequencies above 1,000 Hz.

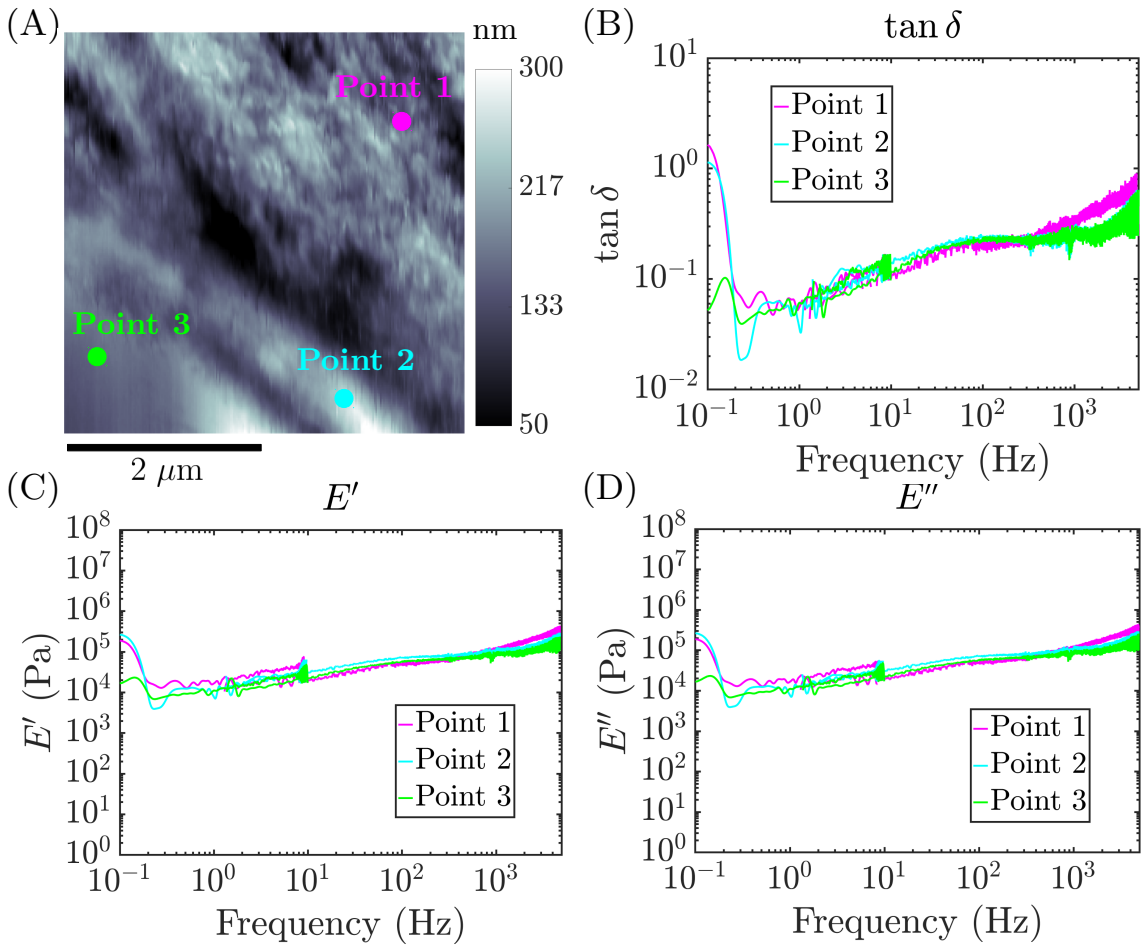


Figure 6.13: PANDA measurements at different points on pureCol substrates crosslinked with glutaraldehyde for 2 hours. A topology image of the substrate, and the location of each PANDA measurement is shown in (A). Measured loss tangents ($\tan\delta$) are shown in (B). E' and E'' calculated from PANDA measurements by applying the Hertz contact model are shown in (C) and (D), respectively. These measurements are representative of two biological replicates of the substrate.

This observation suggests that fibers where collagen fibrils do not completely incorporate themselves into the fiber (point one in figure 6.13) exhibit altered energy storage and dissipation at high frequencies, compared to fibers where the constituent fibrils are fully incorporated. This observation could potentially be due to increased freedom of movement for fibrils that are only partially incorporated into fibers. Regardless, some spatial heterogeneity is present in the mechanical properties at particular frequencies of pureCol substrates crosslinked for 2 hours. However, less hetero-

geneity is present than in samples crosslinked for 30 minutes (figure 6.12).

Representative PANDA measurements of pureCol substrates crosslinked with GA for 24 hours are shown in figure 6.14. Two points were probed on the sample. The first measurement was performed on a region of clumped collagen on the substrate. The second measurement was performed on a point between collagen clumps. The measured E', E'', and $\tan\delta$ did not vary between the two points. The lack of variation in the mechanical properties of pureCol substrates crosslinked for 24 hours is likely

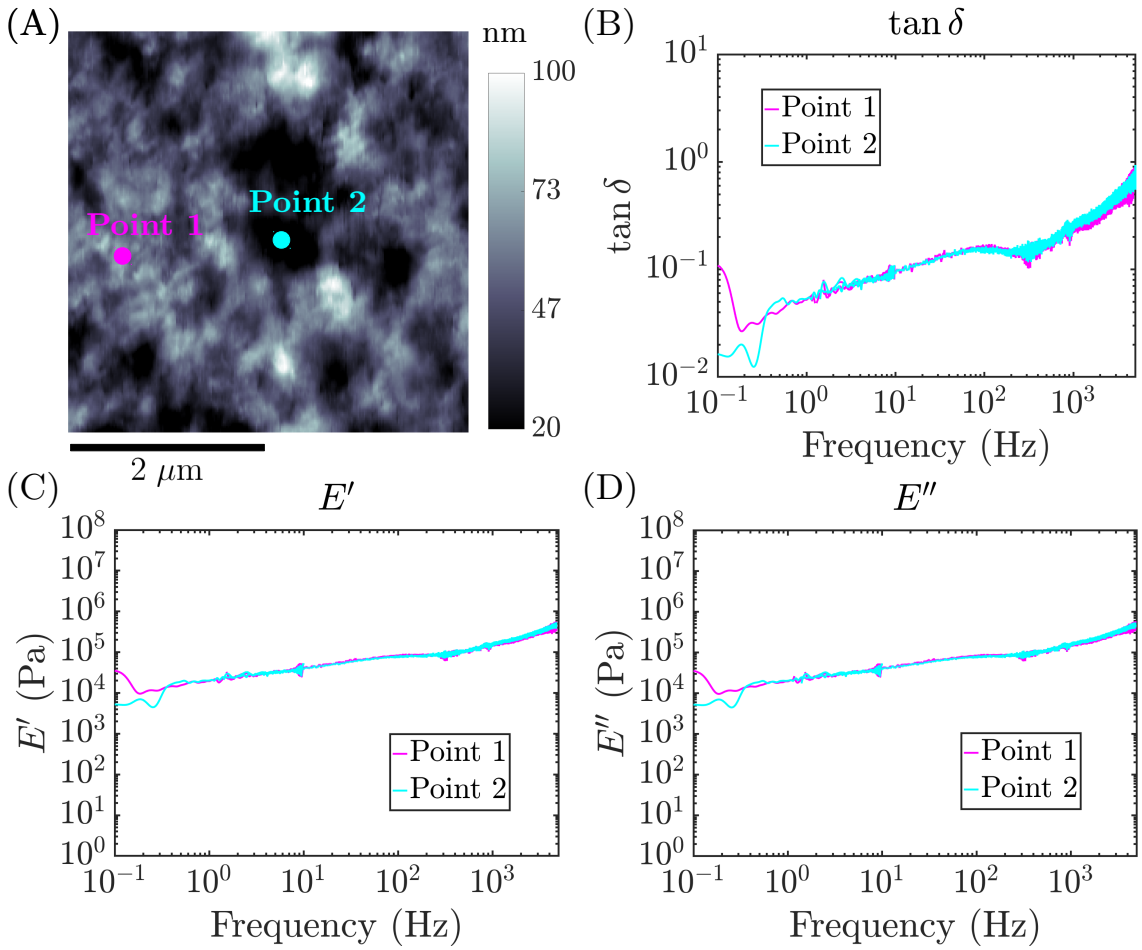


Figure 6.14: PANDA measurements at different points on pureCol substrates crosslinked with glutaraldehyde for 24 hours. A topology image of the substrate, and the location of each PANDA measurement is shown in (A). Measured loss tangents ($\tan\delta$) are shown in (B). E' and E'' calculated from PANDA measurements by applying the Hertz contact model are shown in (C) and (D), respectively. These measurements are representative of two biological replicates of the substrate.

related to the crosslinking in the sample. It is reasonable to hypothesize that the number of crosslinks in these substrates is saturated, since the GA had ample time to interact with and crosslink collagen in the substrate [289]. Therefore, with so many crosslinks, crosslinking likely limited the movement of collagen polymers within the substrate [291], and thereby restricted spatial heterogeneity in their energy storage and dissipation.

In summary, PANDA measurements of the different pureCol substrates demonstrated that substrates crosslinked for 30 minutes exhibit greater spatial heterogeneity in their energy dissipation than the other substrates. This spatial heterogeneity is likely the result of different collagen typology in the substrate and possibly heterogeneous crosslinking in the sample, which likely alter collagen/hydration shell interactions and collagen/collagen interactions within the substrate. Additionally, the heterogeneity in the mechanical properties of substrates with 30 minute GA crosslinking could potentially arise from differences in the electrical properties of the substrate. In the future, this hypothesis can be tested via techniques such as Kelvin probe force microscopy [300–302]. PureCol substrates crosslinked for 2 hours exhibited spatial heterogeneity in their mechanical properties, but less than substrates crosslinked for 30 minutes. The mechanical properties of substrates crosslinked for 24 hours were spatially uniform, likely due to the high degree of crosslinking in these samples. Further comparison of the different pureCol substrates, as well as comparison of pureCol and poly(HEMA) substrates, is saved for section 6.2.4.

6.2.4 Substrate comparisons

Next, the different substrates were compared by averaging PANDA and AM-FM AFM measurements of each substrate. AM-FM AFM E'' was calculated by substituting GMM material constants of each substrate (calculated from AM-FM AFM data via the procedure in section 3.2.3) into equation 1.30. Figure 6.15 shows the behavior of

E', E'', and $\tan\delta$ over the measured frequencies for the various substrates.

The measured E' and E'' were similar for all substrates (figure 6.15 (A) and (B)). AM-FM AFM measurements of E' and calculations of E'' align with PANDA values. E' and E'' of all substrates increased with increasing frequency. This increase started around 10^3 or 10^4 Hz for pureCol substrates and 10 Hz for poly(HEMA) substrates. The observed increase in moduli is likely due to the glass transition (or a similar transition) of the substrates [169, 175]. Details on the glass transition can be found in section 1.3.7. In spite of the fact that the glass transition of poly(HEMA) substrates began around 10 Hz, AM-FM AFM measurements of E' and E'' are similar for poly(HEMA) and pureCol substrates. This observation suggests that the glass transition may be broader for poly(HEMA) than for pureCol.

AM-FM AFM model tests of poly(HEMA) substrates (figure 6.5) suggested that poly(HEMA) behaves as a MW material, but can behave as a GMM as the result of effects from the glass underlying the poly(HEMA). For MW materials, $E' \sim 0$ at low frequencies, then begins to increase as frequency increases (equation 1.41). While the observed increase in poly(HEMA) E' occurs at relatively low frequencies and thereby exhibits MW-like changes, poly(HEMA) E' at low frequencies is comparable to pureCol crosslinked for 30 minutes. This observation suggests that the model test PANDA indentations may have been deep enough to measure some poly(HEMA)/glass effects, resulting in GMM behavior. This observation supports the hypothesis that cells on poly(HEMA) substrates could feel the glass underneath the poly(HEMA) in a similar manner, rather than solely interacting with the poly(HEMA). Thin film corrections [293] to PANDA measurements were not performed, since the aim is to understand viscoelastic properties that a cell may feel on the substrate, even if those properties arise from a convolution of the substrate and underlying glass.

AM-FM AFM model tests of pureCol substrates (figure 6.11) suggest that these substrates behave as GMMs. This observation is supported by PANDA measure-

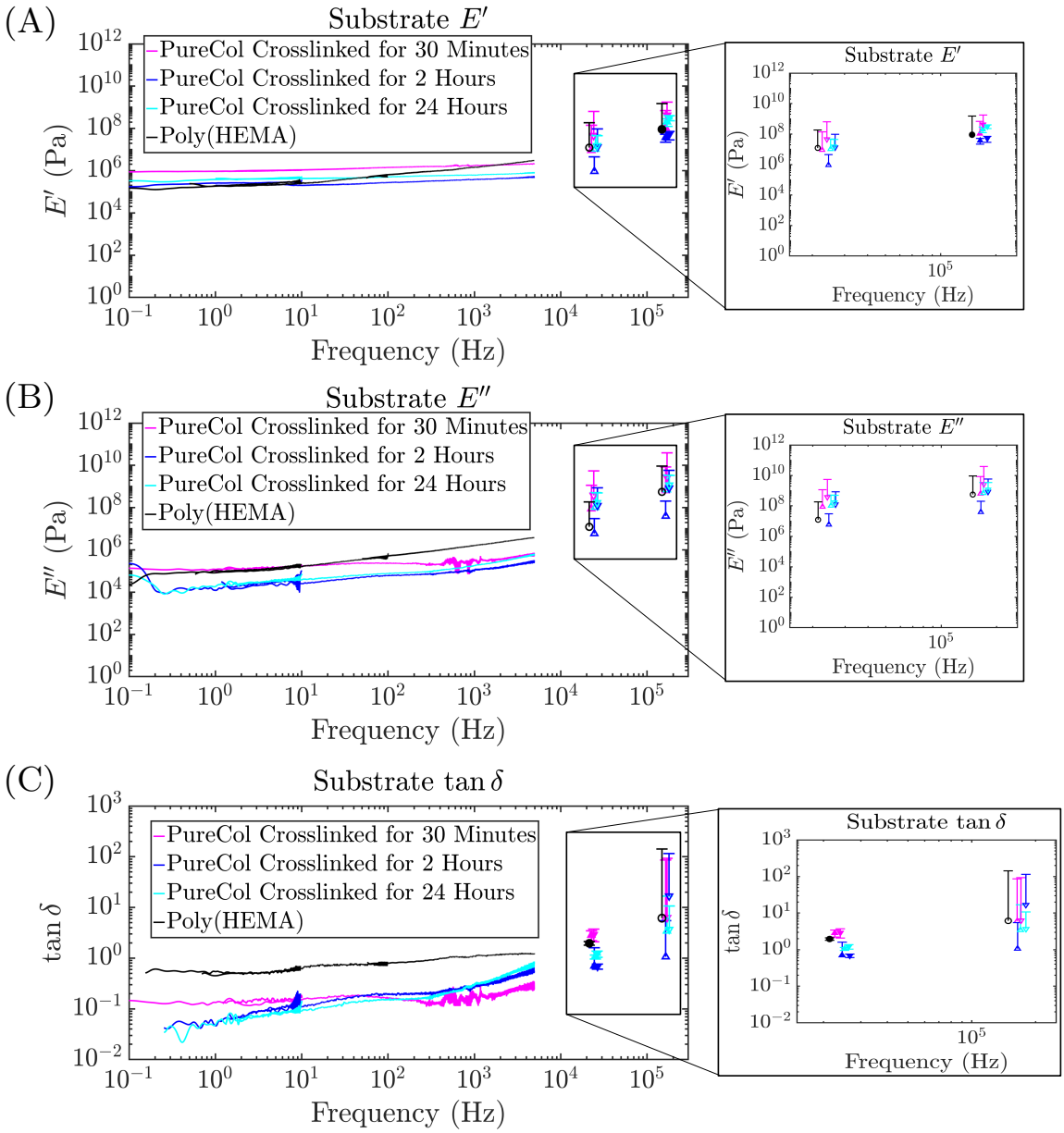


Figure 6.15: Comparison of substrate viscoelasticity. Measurements of pureCol substrates crosslinked in GA for 30 minutes (magenta), 2 hours (blue), and 24 hours (cyan), in addition to a poly(HEMA) substrate at a concentration of 11.4 mg poly(HEMA) per cm^2 of substrate surface area (black) are shown. PANDA measurements (lines), as well as AM-FM AFM measurements (points) are shown for each substrate. For AM-FM AFM measurements, triangles pointing down represent measurements of pureCol substrates taken with an AC240TSA, triangles pointing up represent pureCol measurements taken with an RC800PSA, and circles represent AM-FM AFM measurements of poly(HEMA) substrates with 11.4 mg poly(HEMA) per cm^2 of sample surface area. Error bars represent the standard deviation. Filled markers represent AM-FM AFM measurements. Open markers represent AM-FM AFM reconstructions, calculated from material constants (section 3.2.3).

ments, which show (i) a non-zero E' and E'' at low frequencies and (ii) a gradual change in E' and E'' with frequency. As described in section 1.3.6 and 1.3.7, this behavior is characteristic of materials that obey the GMM [169]. Therefore, PANDA measurements and AM-FM AFM model tests are in agreement about the viscoelastic behavior of these substrates.

Of the pureCol substrates, pureCol crosslinked for 30 minutes exhibited the highest E' and E'' in both AM-FM AFM (figure 6.10 (B)) and PANDA (figure 6.15). This observation seems unexpected, since GA crosslinking increases storage and loss moduli at the macroscale [288, 303]. However, GA crosslinking modulates viscoelasticity of collagen substrates by restricting the movement of fibrils within the substrate, rather than by directly altering the mechanical properties of the fibrils [291]. Therefore, differences in E' and E'' between pureCol substrates should be thought of in terms of how easily collagen polymers can deform within each substrate.

With less crosslinking, it is likely that polymer movement is only partially restricted, and collagen chains have more freedom to deform, interact with one another, and interact with hydration layers. In other words, there are more ways to store and dissipate energy in response to deformation in substrates with less crosslinking. E'' could increase in the 30 minute GA substrates as a result of increased ability of chains in the substrate to slide and transfer kinetic energy to their surroundings, compared to the 2 hour and 24 hour GA samples. Increased E' could potentially arise from charge interactions within the substrate or between the substrate and shell (similar to the mechanism described in figure 4.15). The reduction in E' and E'' of the 2 hour and 24 hour GA substrates compared to the 30 minute GA substrate likely arises from the fact that movement of collagen fibrils in response to deformation is restricted more in these substrates, thereby limiting interactions that store and dissipate energy.

E' of poly(HEMA) substrates was comparable to pureCol substrates crosslinked for 2 or 24 hours. E'' was comparable to pureCol substrates crosslinked for 30 minutes.

Therefore, poly(HEMA) exhibited a higher ratio of E''/E' than pureCol samples. As shown in figure 6.15 (C), $\tan\delta$ of poly(HEMA) substrates was roughly one order of magnitude higher than that of pureCol substrates. The loss tangent of pureCol substrates was similar for all substrates. However, alterations in $\tan\delta$ with frequency varied between the substrates. In samples crosslinked for 30 minutes, $\tan\delta$ was constant for frequencies less than 10^3 Hz, then began to increase. For substrates crosslinked 2 and 24 hours, $\tan\delta$ steadily increased with increasing frequency. The increase in $\tan\delta$ is due to the glass transition [169, 175] of the substrates (already discussed). The observed alterations to the glass transition of pureCol substrates likely arise from crosslinks altering the distribution of time responses within the substrate.

In order to further investigate time responses of each substrate, the relaxation time that contributed most to the material's behavior at any given frequency was calculated as follows. As described in section 1.3.6 and 3.2.1.1, the GMM can be thought of as N different SLSs connected in parallel. The nth arm of the GMM has a relaxation time τ_n. Each of the N SLSs in the GMM has resonance frequency $f_n = 1/\tau_n$ [227]. Therefore the nth SLS in a GMM contributes most to E', E'', and $\tan\delta$ when the arm is excited by a stimulus with frequency $f = 1/\tau_n$ [227]. This observation means that GMM data at a particular frequency can be modeled by the SLS representing the dominant/resonating arms of the GMM at the particular excitation frequency [169]. For PANDA data, it is therefore possible to calculate $\tau_r(f)$ of the sample by recalling that, for the SLS, $E' = E_c + \tau_r\omega E''$ (equation 1.29). Therefore, τ_r can be calculated from PANDA data as follows.

$$\tau_r(f) = \frac{E'(f) - E_c}{2\pi f E''(f)} \tag{6.1}$$

The value of E_c can be taken as the value of E' for PANDA measurements at low frequencies (equation 1.44). Relaxation times calculated in this manner are shown

in figure 6.16 and compared to AM-FM AFM calculations of τ_r (calculated via the method described in section 3.2.2.1).

The value of τ_r at high frequencies is similar for all substrates. At low frequencies, τ_r is roughly one order of magnitude shorter for poly(HEMA) and pureCol substrates crosslinked for 30 minutes, than for pureCol substrates crosslinked for 2 or 24 hours. The differences between E' of these two groups are smaller than the differences in E'' (figure 6.15 (A) and (B)). Therefore, together these observations suggest that longer τ_r at low frequencies are the result of greater changes in energy dissipation relative to energy storage between the two groups. Further discussion about the implications of these different τ_r at low frequencies is saved for section 6.3.

It is also interesting to note that τ_r of pureCol substrates crosslinked in GA for 2 hours matches that of pureCol substrates crosslinked for 24 hours at frequencies

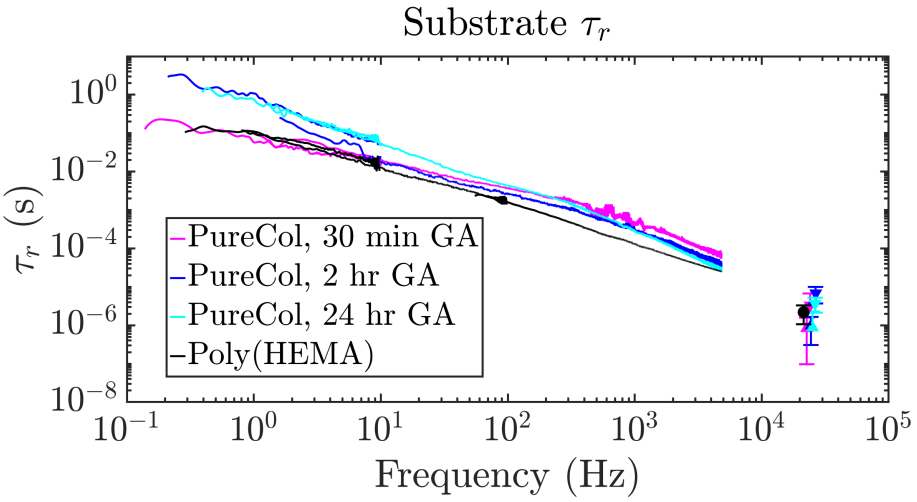


Figure 6.16: Substrate time responses. Calculated relaxation times (τ_r) of pureCol substrates crosslinked in glutaraldehyde (GA) for 30 minutes (magenta), 2 hours (blue), and 24 hours (cyan) are shown in addition to a poly(HEMA) substrate at a concentration of 11.4 mg poly(HEMA) per cm^2 of substrate surface area (black). Lines represent PANDA calculations (via equation 6.1), while markers represent AM-FM AFM calculations (calculated as described in 3.2.2.1). For AM-FM AFM calculations, error bars represent the standard deviation, triangles pointing down represent mean values from pureCol substrates measured with an AC240TSA, triangles pointing up represent mean values from pureCol measurements with an RC800PSA, and circles represent mean values from poly(HEMA).

less than 1 Hz. Between 1 and 100 Hz, τ_r of pureCol substrates crosslinked for 2 hours transitions to values similar to those of pureCol crosslinked for 30 minutes. At frequencies around 300 Hz, all three pureCol substrates exhibit similar τ_r. This observation suggests that substrates with 2 hour GA crosslinking have an intermediate distribution of τ_r between the other pureCol substrates, likely since the crosslinking in this sample is also the intermediate of the pureCol substrates.

6.3 Conclusions, discussion, and future work

In summary, the AFM measurements of cell culture substrates in this chapter determined several important features of these substrates. Investigation of poly(HEMA) substrates demonstrated that poly(HEMA) substrates are not uniform films, and that the activities of cells on poly(HEMA) are likely due to how much of the underlying glass the cells can sense through the poly(HEMA). Therefore, to obtain a full picture of what cells sense on poly(HEMA) substrates, it is likely necessary to consider the convoluted poly(HEMA)/underlying material properties. To test this hypothesis in the future, poly(HEMA) films can be prepared on substrates to which cells do not attach (for example, agar). If cell attachment to the poly(HEMA), and any resulting cell activities are altered compared to poly(HEMA) on glass, this observation would support the notion that cells sense a convolution of the material underlying poly(HEMA) as well as the poly(HEMA) itself.

AFM of pureCol substrates suggested that the substrates possess a surface layer, ranging from nanometers to micrometers in thickness. This layer is likely a hydration shell and/or polymer brush on the substrate surface. The layers were solid enough to probe with the AFM tip, and potentially exhibited linear viscoelastic behavior by behaving as a MW material in AM-FM AFM model tests performed with AC240TSA cantilevers (section 6.2.3.2). If the layer is a hydration shell, these results are remi-

niscent of those in chapter 4.2.4, where collagen hydration shells were solid enough to probe with the AFM tip, suggesting that hydration shells could function as a non-fluid component of pureCol substrates.

Restriction of chain movement is the mechanism by which GA alters the mechanical properties of collagen substrates [291]. Both AM-FM AFM and PANDA observations suggested that crosslinking was spatially heterogeneous in pureCol substrates with shorter GA exposure. Substrates with exposure to GA for 2 or 24 hours exhibited less spatial heterogeneity in their mechanical properties. This decrease in heterogeneity likely arose from the increasing number of crosslinks within the samples, and the resulting restriction of collagen chain conformations in the substrate by the crosslinks. Additionally, both AM-FM AFM and PANDA measurements demonstrated that E', E'', and $\tan\delta$ changed with different amounts of GA crosslinking. These changes likely arose from altered interaction between collagen molecules, potential alterations in the charge distribution of the substrate, and alterations to interactions between collagen and the surrounding solution and hydration shell.

Experiments in this chapter also showed that different substrates exhibited different relaxation times at low frequencies. Cells probe their substrate at low frequencies [143]. Therefore, the mechanical properties of substrates at low frequency deformations are particularly relevant to what cells sense on the substrate [143]. At low frequencies, pureCol substrates crosslinked with GA for 2 or 24 hours exhibited longer relaxation times, by roughly one order of magnitude, than poly(HEMA) substrates and pureCol substrates crosslinked for 30 minutes. While both energy storage and dissipation were different between the "slow" and "fast" substrates, alterations to the relaxation times were the result of greater differences in energy dissipation than differences in energy storage between the "slow" and "fast" substrates.

The different substrate time responses at low frequencies have interesting implications for cell behaviors on the substrates. It is already known that shorter τ_r promotes

ECM deposition and remodeling, as well as differentiation of cells within the substrate [15], and that longer τ_r demonstrates the opposite effects [184]. Additionally, cells proliferate more [304, 305], perform less ECM remodeling and contraction [304, 305], and differentiate less [304] on substrates crosslinked with GA. Cells also exhibit increased seeding efficiency (more cells attach to the substrate when they are seeded onto the substrate), and infiltrate the substrate faster (show increased invasion and migration) with more GA crosslinking [305]. These literature observations of cells on substrates crosslinked with GA and the findings in this chapter agree. The findings in this chapter show that substrates with more GA crosslinking exhibit longer time responses, and cells on these substrates exhibit the same behaviors as cells on substrates with longer time responses [15, 184, 304, 305]. Therefore, it is reasonable to hypothesize that, in general, shorter time responses promote ECM remodeling and differentiation, and hinder cell attachment, proliferation, and migration (invasion and infiltration). The reverse seems to be true for longer time responses.

Additionally, the results of this chapter show that poly(HEMA) substrates exhibit shorter time responses at low frequencies. The inability of cells to attach to poly(HEMA) [272] supports the hypothesis that shorter substrate relaxation times result in decreased cell attachment. Additionally, the reduced DNA synthesis [272], reduced cell activation [285], reduced cell migration, and reduced cell signaling [275] by cells on poly(HEMA) all coincide with the hypothesized effects of shortened response times. Additionally, it is interesting to note that poly(HEMA) promoted the formation of multiple nuclei within malignant melanoma cells [275]. In tissues, cells with multiple nuclei (polykaryons) normally form as the result of immune, muscle, or placental cell differentiation processes [306, 307]. Therefore, the formation of polykaryons on poly(HEMA) could suggest that these cells underwent some type of altered differentiation. If this is the case, this observation agrees with shorter time responses promoting cell differentiation.

It is interesting to note that poly(HEMA) and pureCol crosslinked for 30 minutes had similar time responses at low frequencies. In spite of the same time responses, cells attach and spread on pureCol [304, 305], but not to poly(HEMA) [272]. This observation suggests that other properties of the substrate also play an important role in cell behavior. For example, the hydrophilic nature of poly(HEMA) plays an important role in preventing cell attachment [275]. Additionally, it is already known that poly(HEMA) alters the mechanical properties of cells, likely by altering cytoskeleton dynamics [285]. Together, these observations suggest that chemical properties (and likely other properties such as electrical, and possibly magnetic properties) of a substrate could potentially alter the effects of substrate time responses by altering cell mechanics, and thereby the sensitivity of the cells to substrate mechanics.

The different physical properties of a substrate likely combine to regulate cell mechanics, and thereby cell activities. Therefore, an important next step in investigating the effect of time responses on cells is to determine how substrate properties affect the mechanical properties of cells on the substrate. Now that the mechanical properties of substrates in this chapter have been categorized, the next step in investigating the relationship between cells and these substrates is to add cells to the system. Once substrates are synthesized, the cells can be seeded directly onto the substrate. The mechanical properties of the system with cells can then be measured by PANDA combined with techniques such as AM-FM AFM or other cell measurement methods [271, 308], and a variety of experiments can be performed to link cell mechanics, substrate mechanics, and cell activities.

First, the mechanical properties of the substrate can be measured at different times after cell seeding. These measurements would indicate how much substrate remodeling cells perform. Second, the mechanical properties of cells on the substrates can be measured at different times after cell seeding. These measurements would indicate how substrate mechanics alter cell mechanics. Third, proliferation, viability,

DNA synthesis, and migration assays can be performed on the cells. It would be ideal if this third batch of experiments could also make use of time lapse imaging, to allow observation of cell behaviors and morphology in real time. This third set of experiments would indicate how cell activities are altered by cell and substrate mechanics. It would be ideal to perform all three experiments together (measure substrate mechanics, cell mechanics, and cell activities) at each time point after cell seeding, so that all measured properties correspond to the same cell/substrate system. Performing all three experiments together would correlate cell behaviors with the measured cell and substrate mechanics.

Chapter 7

Conclusions and Future Work

Interactions between cells and the extracellular matrix (ECM) are crucial for maintaining healthy tissues and organisms [1, 2, 62]. The viscoelastic properties of both cells and the ECM are important in this interaction. Specifically, ECM elasticity, viscosity, and time responses (the ratio of viscosity to elasticity) play a crucial role in dictating cell behaviors over multiple length scales [15, 170, 185–194]. These quantities relate to the storage and dissipation of energy by the system [166, 168]. Additionally, the viscoelastic properties of biological systems are coupled to the electrical, magnetic, and chemical properties of the system [78, 79, 83, 87–92]. Exploiting the coupling of physical properties in biological systems shows promise in treating disease by renormalizing diseased tissues [2, 62, 87, 106, 108, 111–118]. The aim of this thesis was to improve understanding of the physical properties of tissues, and hypothesize how these properties may be exploited to improve renormalization therapies. To this aim, multifrequency atomic force microscopy (AFM) was used to measure the effect of various types of stimuli on ECM viscoelasticity in physiological conditions at the nanoscale, relevant to cells [15, 59, 120–124]. The main experimental technique of this thesis was amplitude modulation-frequency modulation (AM-FM) AFM (section 2.1.3.4). Additionally, a novel dynamic AFM technique known as photothermal ac-

tuation AFM nano-DMA (PANDA, section 2.1.3.3), was employed to measure the mechanical properties of cell culture substrates over a large range of frequencies.

First, a new analysis method was developed for AM-FM AFM data (chapter 3) to test whether samples behaved as linear viscoelastic materials, and if so, which model of linear viscoelasticity best described the sample (section 3.2). This model test determined that all the samples measured in this thesis exhibited linear viscoelasticity (sections 4.2.2.2, 4.2.3.2, 4.2.4, 5.3.3, 6.2.2.1, and 6.2.3.2). Most samples in this thesis, including some collagen hydration shells, obeyed the general Maxwell model (GMM, section 1.3.6). Additionally, the model test proved useful in observing multiple materials and spatial heterogeneity in mechanics within a sample (sections 4.2.3.2, 5.3.3, 6.2.2.1, and 6.2.3.2). Of particular interest was an additional Maxwell (MW, section 1.3.5.2) material to the sample GMM, which appeared in many model tests and likely belonged to sample hydration shells (sections 4.2.3.2, 4.2.4, 5.3.3, and 6.2.3.2). Therefore, model test results not only determined the viscoelastic behavior of samples in this thesis, but also suggested that hydration shells can directly alter the mechanics of the ECM and substrates by behaving as a linear viscoelastic material. The new analysis method served as a useful tool to gain insight into sample properties from AM-FM AFM data. In the future, it would be interesting to expand the capabilities of the model test to identify different materials within the model test and retrace their location to the original AM-FM AFM image.

The first set of experiments in this thesis (chapter 4) examined mechanoelectric coupling in the ECM by studying how electrostatics and flowing ions altered the viscoelastic properties of collagen I, the most prevalent component of the ECM. For collagen fibrils, energy storage and dissipation simultaneously increased with increasing ionic strength of the surrounding solution (section 4.2.2 and 4.2.3). The mechanism behind this increase is likely related to dynamics between collagen molecules and ions (section 4.2.5). Since energy storage and dissipation were altered simultaneously, the

time responses of the fibrils remained constant. Only by flowing ions over collagen fibrils did fibril time responses change (section 4.3). This observation suggests that there is a feedback which maintains constant collagen time responses, unless an additional stimulus is applied. Additionally, it was possible to image collagen's hydration shell during these experiments and quantify the mechanical properties of the shell, or a convolution of the shell and underlying collagen (section 4.2.4). These results suggest that the hydration shell around collagen is stable, could potentially behave as a linear viscoelastic material, and could contribute to collagen mechanics.

The second set of experiments in this thesis (chapter 5) examined the effects of mechanochemical coupling (cell activity and chemical signaling) on ECM viscoelasticity by measuring the mechanics of ECMs produced by cells in response to growth factors (GFs) and mutation. AM-FM AFM measurements of the mechanical properties of these cell-derived ECMs suggested several important factors to consider about how mechanochemical coupling affects nanoscale ECM mechanics. For ECM properties other than density, GFs exerted their influence on tissue mechanics indirectly by changing cell signaling and activities, rather than by directly altering the physical properties of the ECM. Mutation altered cellular abilities to modify ECM mechanics and produce large ECM fibers.

As described in section 5.3.2 - 5.3.4, when wild type (WT) cells were exposed to GFs, their remodeling activities simultaneously altered both elasticity and viscosity of the ECM. In general, ECMs with larger fibers tended to exhibit higher elasticity, higher viscosity, and higher crosslinking and ECM density. However, since viscosity and elasticity changed in a similar manner, the time responses of the ECM remained constant regardless of GF treatment. Only PDGF was able to shorten time responses of WT ECMs. Observations of ECMs produced by mutant cells suggested that non-fibrillar collagens V and XI play a role in how cells deposit ECM and modify ECM mechanics, likely by directly incorporating into the ECM. Mutant cells did not de-

posit large fibers, and had restricted abilities, compared to WT cells, to modify the mechanical properties of the resulting ECM. The reduced ability of mutant cells to modify the ECM resulted in diminished ability of mutant cells to maintain constant ECM time responses, compared to WT cells.

The last set of experiments in this thesis, chapter 6, measured the viscoelastic properties of common cell culture substrates known to alter cell behaviors and hypothesized preliminary correlations between substrate viscoelasticity, specifically time responses, and cell behaviors. The measured substrates were poly(HEMA) films made with different concentrations of poly(HEMA), and pureCol (a common cell culture substrate consisting mainly of collagen I) substrates with different amounts of glutaraldehyde crosslinking.

AFM of poly(HEMA) substrates (section 6.2.2) demonstrated that poly(HEMA) films are not uniform, and that the activities of cells on poly(HEMA) are likely due to how much of the underlying glass the cell can sense through the poly(HEMA). AFM of pureCol substrates suggested that the substrates possess a surface hydration shell and/or polymer brush, that ranges from nanometers to micrometers in thickness (section 6.2.3.1). If the surface arises from a hydration shell, these findings are similar to those of chapter 4.2.4 in that hydration shells were solid enough to probe with the AFM tip, potentially exhibited linear viscoelastic behavior (section 6.2.3.2), and thereby act as a non-fluid component of pureCol substrates. Both AM-FM AFM and PANDA observations of pureCol substrates (section 6.2.3) demonstrated that glutaraldehyde crosslinking modulated both energy storage and dissipation of the substrates. These effects were likely due to altered interactions between collagen molecules within the substrate, alterations in the charge distribution of the substrate, and alterations to interactions between collagen and the surrounding solution and hydration shell. Changes to energy storage and dissipation in the tested substrates resulted in different substrate time responses at low frequencies, but similar

time responses at high frequencies (section 6.2.4). As described in section 6.3, correlating the measured substrate time responses to literature studies [15, 184, 304, 305] suggested that shorter substrate time responses promote ECM remodeling and differentiation activities and hinder cell attachment, proliferation, and migration (invasion and infiltration). The reverse seems to be true for longer substrate time responses.

Together, there are two main biological findings in this thesis. The first is that hydration shells are a non-fluid component of the tissue that alters ECM mechanics. The second finding is that constant time responses are maintained by the ECM and substrates in a variety of environmental conditions.

7.1 Hydration shells

The charged nature of biomolecules results in the structuring of water and ions around the surface of the molecule [137–139, 164]. This layer of organized water is the molecule's hydration shell, and can modulate the properties of the encased biomolecule [137, 138, 162]. Hydration shells are solid enough to probe experimentally at cellular length scales (nanoscale and microscale) [139–141], suggesting that shells could also be sensed by cells. Additionally, shells play an important role in dictating the properties and assembly of collagen and the ECM [170, 233, 234].

Collagen's hydration shell was observed in samples throughout this thesis. Shells were observed around collagen fibrils, and were a few nanometers thick (section 4.2.4). Shells were also potentially observed on the surface of collagen (pureCol) substrates. These potential shells were nanometers to several microns thick (section 6.2.3.1). Additionally, all shells in this thesis behaved as MW or GMM materials during AM-FM AFM model tests (section 4.2.4 and 6.2.3.2). Whether the shell behaved as a MW or GMM material likely depended on how far the AFM tip penetrated the shell.

Water and ions in hydration shells become increasingly organized as proximity

to the surface of a biomolecule increases [137, 138]. Therefore, it is reasonable to hypothesize that tip/shell interactions measured in this thesis changed based on shell organization, and how deeply the tip penetrated into the shell. If the tip probed the first few layers of the shell, furthest from the sample, the tip could detect a structure, but the structure was not solid enough to quantify. The majority of tip/hydration shell interactions behaved in this manner. In this case, the tip detected shell features during AM-FM AFM measurements, but could not obtain a repulsive tip/shell interaction to quantify the mechanical properties of shell features (section 4.2.4 and 6.2.3.1). If the imaging parameters were then adjusted so the tip pushed further into the shell, quantification of the mechanical properties became possible (section 4.2.4). In this case, it is likely that, as the tip indented further into the shell, the tip began to probe increasingly organized layers of the shell, and the shell began behaving as a "fluid solid" that could be modeled as a MW material (section 4.14). If the tip continued to push through the shell closer to the biomolecule's surface, the shell was organized enough to behave as a "solid fluid," modeled by the GMM (section 4.14).

Alternatively, the observed MW material and GMM attributed to shells could be a convolution of the hydration shell and underlying substrate. Even if this convolution is the case, the resulting substrate/shell structure can still behave as an additional solid within a sample, and contribute to sample mechanics, as apparent from AM-FM AFM model test results (section 4.2.4 and 6.2.3.2). Regardless of whether these mechanical properties belong to shells alone or shell/collagen convolutions, they still support the notion that fluids in biology contribute directly to the mechanical properties of tissues, rather than indirectly by modulating tissue electrostatics [137, 138, 162, 164], and can potentially be thought of as additional solids in the tissue.

Even when not directly contributing to tissue mechanics, shells likely played a key role in regulating energy storage and dissipation by the samples measured in this thesis. The results in section 4.2.3 and 4.2.4 demonstrated that shell mechanical prop-

erties varied in conditions where collagen mechanical properties remained constant. This observation suggests that hydration shells may be more sensitive to various environmental conditions than the underlying collagen. Therefore, certain stimuli could potentially exert their effect not by changing the mechanics of the biomolecules in the system, but by changing the mechanics of the system's hydration shells. Alterations to shell mechanics could serve as a means of altering tissue mechanics. The pureCol results in chapter 6 support this hypothesis, since changes in substrate mechanical properties as a result of glutaraldehyde crosslinking likely arose from spatial confinement of collagen that altered shell/collagen dynamics (section 6.2.3).

In summary, hydration shell observations in this thesis suggest that hydration shells contribute directly (as linear viscoelastic materials) and indirectly (by modulating molecular charge and electrostatic interactions) to tissue mechanics. These observations raise the possibility that cells could potentially fine tune how they interact with tissues by controlling how far they push through hydration shells to sense the underlying ECM. Additionally, alterations to the mechanical properties of hydration shells could potentially influence changes in cell behaviors without altering the mechanics of the underlying ECM or substrate. It would be interesting to develop better methods to measure hydration shell mechanics in order to study their role in tissue mechanics and potentially exploit the fluid environment of tissues to treat disease. Additionally, theoretical modeling of hydration shell physics could enhance understanding of the role that such shells play in biological systems.

7.2 Biological time responses

The second theme of this thesis is that constant time responses were maintained in a variety of conditions. Literature investigations [166, 189, 190, 227, 285, 309–311] suggest that constant time responses are not only limited to the samples in

this thesis, but are maintained in many biological systems. Constant time responses of collagen fibrils are maintained at the nanoscale, regardless of ion concentration in the surrounding solution (chapter 4). Constant collagen time responses are also maintained at the macroscale regardless of temperature, hydration, and mechanical pre-loading [189, 190]. ECM modifications by fibroblasts maintain constant time responses, even when ECM topology, elasticity, and viscosity are altered (chapter 5). Plant cell walls also maintain constant time responses regardless of wall orientation [166, 227], and throughout growth zones of the plant, despite changes in energy storage, energy dissipation, elasticity, and viscosity in these regions [166]. Similar coupling between energy storage and dissipation (related to elasticity and viscosity) in cells has also been observed [285, 309–311]. Together, these results suggest a multiscale, and potentially universal coupling of energy storage and dissipation in biological systems that maintains constant time responses in a variety of conditions.

While many stimuli do not alter biological time responses, others have the ability to do so. For example, flowing ions over collagen fibrils shortened the creep timescale of the fibrils (section 4.3). Mutation of collagen V or XI hindered cell modifications to the ECM, and time responses of the resulting ECMs varied more than the WT in response to GFs (chapter 5). Additionally, PDGF treatment increased viscosity relative to elasticity of WT cell-derived ECMs, and thereby slightly lengthened the creep timescale of the ECMs (relaxation timescales remained constant, however). Additionally, varying degrees of crosslinking altered time responses of collagen substrates to low frequency stimuli (section 6.2.4). Other possible stimuli that could alter tissue time responses are pH, and divalent ions such as Ca^{2+} or Mg^{2+} [231, 244]. It is interesting to note that these stimuli with the ability to alter tissue time responses all undergo dramatic changes during wound healing [2, 64], embryonic development [2, 64], in diseases such as cancer [4, 266], and even in action potentials [87], and alter cell behaviors in these conditions.

Literature observations [15, 184, 304, 305], in combination with the observations in section 6.2.4 and 6.3, suggest that shorter substrate time responses promote ECM remodeling and differentiation activities and hinder cell attachment, proliferation, and migration. The reverse seems to be true for longer substrate time responses. As hypothesized in section 6.3, these changes in cell activities seem to be the result of alterations to cell mechanics on the substrate. Additionally, since the physical properties of biological systems are coupled [78, 79, 83, 87–92], the chemical, electrical, and possibly magnetic properties of a substrate could potentially alter the effects of substrate time responses on cell behaviors by altering cell mechanics, and thereby the sensitivity of the cells to substrate mechanics. A physiological mechanism of altering cell activities could be to tailor tissue time responses via (coupled) stimuli. For example, electric fields such as those found in wounds, embryonic development, and tumors, dramatically alter cell activities through unclear mechanisms [2, 4, 64, 266]. It is worth investigating whether such fields exert their influence on cell activities by changing tissue time responses and cell mechanics.

It is important to note that, while substrate time responses are important in dictating cell behaviors, elasticity and viscosity alone can also alter cell activities [1, 3, 5–8, 15, 128, 170, 184–194]. This observation is not surprising, since, for the models of viscoelasticity applied in this thesis (section 1.3.4 - 1.3.6), time responses are the ratio of viscosity to elasticity. Therefore, control of tissue time responses may serve as a means for particular stimuli to alter cell activities by creating a larger alteration to tissue elasticity or viscosity than usual. Additionally, the results in this thesis suggest that, while time responses are constant in any given location in response to many stimuli, there is spatial heterogeneity in the value of the time responses, depending on factors such as cell activities (chapter 5) or heterogeneous distribution of crosslinks (chapter 6). This heterogeneity in substrate time responses and mechanics likely has important implications for the normal functioning of tissues.

Bearing these facts in mind, figure 7.1 shows a schematic of the proposed interactions between the time responses of the ECM or substrate, elasticity and viscosity of the ECM, cell behaviors, and the various stimuli studied in this thesis.

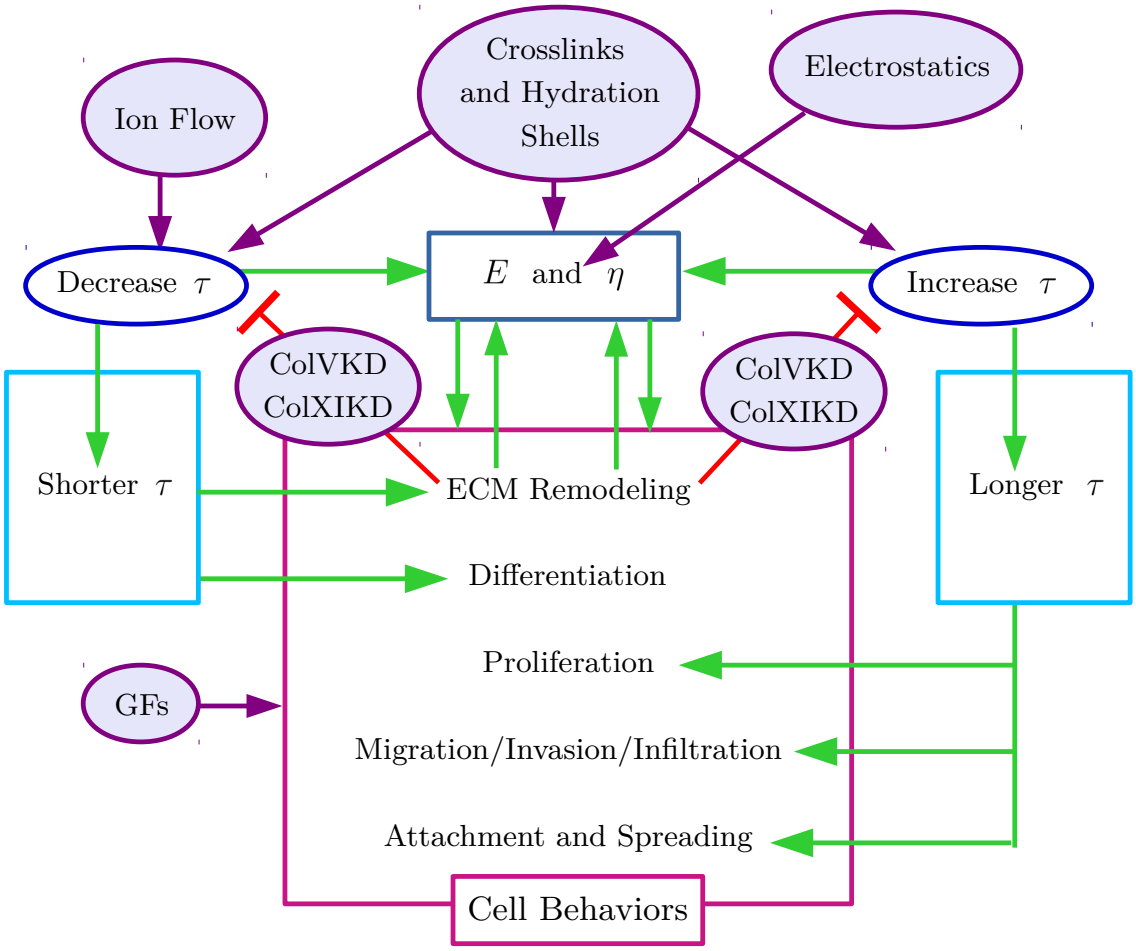


Figure 7.1: Proposed relationship between substrate time responses, substrate mechanics, cell behaviors, and various external stimuli. Interactions which promote cell activities or alter substrate mechanics are indicated by green arrows. Interactions which prevent alterations are indicated by red bars. Mechanical properties (elasticity E, viscosity η, and time responses τ) of the ECM or substrate are shown in shapes with blue outlines. External stimuli studied in this thesis, including growth factors (GFs) and mutation of collagen V (colVKD) or mutation of collagen XI (colXIKD), are shown in purple circles. Stimulus effects are indicated by purple arrows.

7.3 Implications for disease renormalization

It is interesting to note the effects of various stimuli studied in this thesis in their physiological context. For example, PDGF lengthened the creep timescale of WT ECMs 5.3.4. In tumors, PDGF serves as a means of promoting fibrosis, and is correlated with more invasive tumors and reduced patient survival [249, 258–263]. Lengthened ECM time responses (in response to PDGF) could potentially promote proliferation, migration, and invasion, and reduce cell differentiation [15, 184]. All these behaviors are hallmarks of malignant cells [266]. Therefore, lengthening of tumor time responses in response to PDGF could play a role in the effects of PDGF in tumor progression. As an alternative example, ion flow increased elasticity of collagen relative to viscosity, and shortened the creep timescale of collagen fibrils (section 4.3). Ion flows are crucial to the correct healing of wounds and to embryonic development, where cells need to differentiate and perform ECM remodeling activities such as healing a wound or forming a tissue [2, 64]. Therefore, shortened timescales of collagen in response to ion flow could play a role in the effects these flows exert on cells. Interestingly, the stimuli in these two examples are not solely mechanical in origin.

Coupling of physical properties in biological systems can serve as a means of altering tissue mechanics [78, 79, 83, 87–92], and potentially time responses. Additionally, comparison of pureCol and poly(HEMA) substrates that exhibit similar time responses (measured in section 6.2.4) to observations in the literature [272, 275, 285, 304, 305] suggests that the coupled properties of a substrate could potentially alter cell sensitivity to substrate mechanics by making alterations to the mechanical properties of cells.

If coupled stimuli operate by altering tissue time responses and cell mechanics to alter cell behaviors, this mechanism could be exploited for the treatment of disease. Future treatments could potentially alter and tailor the physical properties of tissues by exploiting the coupling of physical properties in the system to control and

renormalize diseased cells. For example, such therapies could potentially be used in the future to treat tumors. Tumors are diseases where malignant cell proliferation, migration, invasion, and de-differentiation (where the tumor cells begin behaving like stem cells) occur at abnormal levels [266]. Since shorter substrate time responses are hypothesized to reduce proliferation and migration, and promote differentiation of cells [15, 184], shortening tumor time responses could potentially reduce malignant phenotypes, and thereby help the tumor heal. Tumor time responses could potentially be shortened in such treatments via the application of coupled stimuli (such as electric fields, ultrasounds, or magnetic fields) to alter tumor mechanics, and thereby override malignant cell activities. Similarly, for regeneration therapies, stimuli could be applied to lengthen tissue time responses in order to promote cell differentiation and tissue remodeling to help regenerate and heal the diseased tissue.

Early attempts at therapies that exploit the coupling of physical properties in biological systems to renormalize cells show promise in treating many different conditions that include: neurodegenerative disorders. [87, 111, 112], wound healing [113, 114], restoring sensation and motor control in paralyzed patients [114, 115], and cancer treatments [116–118]. While promising, these therapies are still in their infancy because there is still much to understand regarding the basic mechanisms underlying the coupled physical properties of a cell and its environment. Perhaps the efficacy of these treatments would increase if they are performed with the aim of performing strategic alterations to tissue time responses and mechanics.

7.3.1 Future work

There are still many basic facts to understand before renormalization therapies can be designed to strategically alter tissue mechanics. First, mathematical modeling of the system, validated against experiments, will likely prove a useful tool to understand the physics behind the coupled interactions between cells and the ECM. Such

modeling could make use of thermodynamics and off-equilibrium thermodynamics such as the Onsager principle [166], polymer physics [162], and other theoretical tools to understand the coupled properties of biological systems. Mathematical modeling beyond the standard models of hydration shells and the electrical double layer [164] could also help link hydration shell effects to tissue mechanics. Additionally, mathematical modeling will be helpful in optimizing renormalization therapies once the physics of the system are better understood.

In order to improve renormalization therapies, better understanding of cell/ECM interactions is necessary. Therefore, better understanding of the relationship between cell mechanics, tissue mechanics and cell activities is needed. An important next step in this investigation is to determine how substrate mechanics, specifically time responses, affect the mechanical properties of cells on the substrate. The first step in this process would be to seed cells on different substrates, then collect cell activity data (for example viability, proliferation, and migration assays), measure the mechanical properties of the cells on the substrate, and measure the mechanical properties of the substrate at several time points after cell seeding. Such experiments would correlate cell behaviors to the measured cell and substrate mechanics. It would also be helpful to measure the mechanical properties, specifically time responses, of cells and cell constructs that are more similar to tissues [273, 274, 312]. For example, it would be interesting to study the mechanical properties of spheroids [273, 274] or organoids [273, 312] on different substrates.

Additionally, it is necessary to directly test whether stimuli used in renormalization therapies alter tissue mechanics and change tissue time responses. It is also necessary to understand how long such changes persist. In this regard, preliminary experiments could apply electric fields, magnetic, fields, and ultrasound to *in vitro* cultures (monolayers, spheroids, or organoids), and measure the resulting changes to the mechanical properties of the substrates and cells in the system at different time

points during and after the stimulus. Additionally, preliminary experiments could also use poly(HEMA) substrates and test whether applying external stimuli (electric fields, magnetic fields or ultrasounds) could alter cell responses to the poly(HEMA) and help them attach to the substrate.

It is also necessary to test whether endogenous stimuli such as voltages and ion flows in wounds and embryos [2, 64] alter the time responses of the tissue *in vivo*. For example, it would be interesting to measure the mechanical properties of developing or regenerating limbs, or of healing wounds to see if tissue time responses (and other mechanical properties) are altered in the affected area of the tissue, and if these altered time responses are behind the dramatic alterations to cell activities. It would also be helpful to measure and compare the time responses of normal and diseased tissue, to test if/how tissue time responses are altered in disease.

Additionally, it is still not clear what type of stimulus is best to apply during a renormalization therapy. For example, it is not clear whether stimuli should be combined (for example an ultrasound and an electric field together), what length scale the stimulus should be applied at for greatest efficacy, or what stimulus frequencies should be used. It is possible that renormalization stimuli may need to be applied together. For example, combining mechanical stimuli (physical therapy) with electrical stimuli is more effective at treating paralysis [114, 115]. Preliminary experiments to investigate how best to apply renormalization stimuli could apply various combinations of stimuli to cells on substrates, or to cell constructs such as spheroids and organoids, in order to determine which types of stimuli and combinations thereof have the greatest impact on the mechanics of the system and cell behaviors.

Techniques such as PANDA could provide insight into nanoscale ECM and cell mechanics, and potentially inform the frequencies with which to apply renormalization stimuli [92]. For example, PANDA results in chapter 6 showed that substrate time responses varied more at low frequencies than high frequencies. It is therefore possible

that manipulating the low frequency time responses of substrates, potentially by applying low frequency stimuli, may prove more useful than manipulating the already similar high frequency time responses. Additionally, PANDA could potentially be employed to detect mechanical resonances in biological systems and diseased tissue. Exploiting such resonances could help enhance drug delivery to the diseased tissue or inform the frequencies at which to apply renormalization therapies [92].

The investigations proposed in this section are only the beginning in understanding and exploiting the physics of biological systems to treat disease. Regardless, renormalization therapies show promise in treating disease [87, 111–118]. Better understanding of the coupling of physical properties in biological systems, and how this coupling regulates cell behaviors is necessary to realize the true potential of renormalization treatments. The results in this thesis, building on the literature, lead to the hypothesis that the efficacy of renormalization therapies can potentially be increased if the therapies are designed to control tissue time responses. In this case, the therapy would control and renormalize cells by exploiting the coupled physical properties of biological systems to apply controlled alterations to tissue time responses, and thereby control cell mechanics and activities. The work presented in this thesis is one in a series of first steps to enhance the understanding of the physical properties of tissues, how mechanoelectric and mechanochemical coupling alter ECM mechanics, and how coupled stimuli could potentially regulate cell behaviors.

Appendix A

Chapter 1 Appendix

A.1 Deriving monomer pKa shifts using the Gibbs free energy

When monomers are charged in their associated or dissociated state, the charge can interact with neighboring charges on other monomers or in solution. This interaction shifts the pKa value of a monomer [162]. An expression for the shift in pKa value due to interacting charges can be derived by comparing the Gibbs free energy of the system, G, when charge interactions are not taken into account, to G when charges are taken into account, as derived in this section [162].

For the following manipulations, it is helpful to define the dissociation constant in terms of number density, $\tilde{k}_{HM}$, rather than in terms of molarities, k_{HM}, as in section 1.2.2. Note that $\tilde{c}$ is the number density of a molecule in number of molecules per unit volume.

$$\tilde{k}_{HM} = \frac{\tilde{c}_H \tilde{c}_M}{\tilde{c}_{HM}} \tag{A.1}$$

$$\tilde{k}_{HM} = N_A k_{HM} \tag{A.2}$$

The Gibbs free energy, G, of the system is related to the number density of the monomers within.

A.1.1 Gibbs free energy of dissociation independent of molecular charge

If the monomer's dissociation is independent of the monomer's charge, meaning that the monomer is free in solution or sufficiently screened from others in the system, the expression for G is the following, where V_o is a reference volume, k_B is Boltzmann's constant, and T is the temperature.

$$G = G_o + k_B T \ln\left(\frac{1}{\tilde{c}V_o}\right) \tag{A.3}$$

The difference in the free energy between the associated and dissociated states of the mth monomer independent of charge is as follows.

$$\Delta G_m = G_M - G_{HM} = \Delta G_o + k_B T \ln\left(\frac{\tilde{c}_H \tilde{c}_M}{\tilde{c}_{HM}} V_o\right) \tag{A.4}$$

At equilibrium, $\Delta G = 0$. Applying this equilibrium condition and the definition of $\tilde{k}_{HM}$ (equation A.1) to equation A.4 results in the following.

$$\tilde{k}^o_{HM} = \frac{1}{V_o} e^{-\frac{\Delta G_o}{k_B T}} \tag{A.5}$$

The pKa value of the monomer when the monomer is free in solution can be obtained by taking the logarithm of the expression for $\tilde{k}^o_{HM}$ (equation A.5). However, if two charged monomers are close to one another, (i.e. confined next to each other in a polymer) the charges will alter the expression for G and equation A.5 will be altered as derived in the following section.

A.1.2 Gibbs free energy of dissociation accounting for molecular charge

The shift in a monomer's pKa value due to electrostatic interactions with other charged monomers is derived in this section. First, it is assumed that the interaction energy, U, of charged monomers obeys Coulomb's law, and that these Coulombic interactions between monomer m with each jth monomer in the system can be summed [162].

$$U_m = \frac{e_o^2 z_m}{4\pi\varepsilon} \sum_{j \neq m} \frac{z_j}{\ell_{j,m}} \tag{A.6}$$

Here, e_o is the elementary charge, ε is the dielectric constant of the surrounding solution, ℓ is the distance between the two interacting monomers, and z_m is the valence of the monomer in its current state (associated or dissociated). The expression for the Gibbs free energy therefore becomes the following.

$$G_m = G_o + k_B T \ln\left(\frac{1}{\tilde{c} V_o}\right) - \frac{e_o^2 z_m}{4\pi\varepsilon} \sum_{j \neq m} \frac{z_j}{\ell_{j,m}} \tag{A.7}$$

The difference in the free energy between the fully associated and dissociated states (fully associated means that no monomer in the system lost its proton, and fully dissociated means all monomers in the system lost their protons) of the system are therefore as follows. Here, z denotes the valence of a dissociated monomer while z^* denotes the valence of an associated monomer.

$$\Delta G_m = \Delta G_o + k_B T \ln\left(\tilde{k}_{HM} V_o\right) + \frac{e_o^2}{4\pi\varepsilon}\left[z_m \left(\sum_{j \neq m} \frac{z_j}{\ell_{j,m}}\right) - z_m^* \left(\sum_{j \neq m} \frac{z_j^*}{\ell_{j,m}}\right)\right] \tag{A.8}$$

Applying the equilibrium condition ($\Delta G = 0$), the definition of $\tilde{k}_{HM}$ from equation A.1 [162], and substituting equation A.5 into equation A.8 results in the following

expression for $\tilde{k}_{HM}$.

$$\tilde{k}_{HM} = \frac{1}{V_o} e^{-\frac{\Delta G_o}{k_B T}} \exp\left\{ \frac{e_o^2}{4\pi\varepsilon k_B T} \left[z_m^* \left(\sum_{j \neq m} \frac{z_j^*}{\ell_{j,m}} \right) - z_m \left(\sum_{j \neq m} \frac{z_j}{\ell_{j,m}} \right) \right] \right\} \tag{A.9}$$

$$= \tilde{k}_{HM}^o \exp\left\{ \frac{e_o^2}{4\pi\varepsilon k_B T} \left[z_m^* \left(\sum_{j \neq m} \frac{z_j^*}{\ell_{j,m}} \right) - z_m \left(\sum_{j \neq m} \frac{z_j}{\ell_{j,m}} \right) \right] \right\} \tag{A.10}$$

$$= \tilde{k}_{HM}^o \beta \tag{A.11}$$

Finally, equation A.2 can be applied to convert $\tilde{k}_{HM}$ to k_{HM} as follows.

$$\begin{aligned} \tilde{k}_{HM} &= \beta \tilde{k}_{HM}^o \\ \frac{\tilde{k}_{HM}}{N_A} &= \beta \frac{\tilde{k}_{HM}^o}{N_A} \\ k_{HM} &= \beta k_{HM}^o \\ \text{pKa} &= \text{pKa}_0 - \log_{10}(\beta) \end{aligned} \tag{A.12}$$

Here, pKa_0 is the original pKa value of the monomer when electrostatic interactions are not taken into account [162]. The expression for the monomer's pKa shift from equation A.12 is the same as equation 1.7.

A.2 Effect of ions on molecular charge

For any charge on the surface of a molecule, a thin layer of counterions (free ions with an opposite charge to that of the surface) will exist around that charge [162, 164]. This layer of counterions is essentially bound to the surface of the monomer via electrostatic correlations [162, 164]. In order to solve for the number density of bound ions to the monomer, it is typically assumed that these ions follow a Boltzmann

distribution and obey the Nernst equation [164].

$$\tilde{c}_i(r) = \tilde{c}_{i,b} e^{-\frac{e_o z_i \psi(r)}{k_B T}} \tag{A.13}$$

Here, $\tilde{c}_i$ is the number density of ion i attached to the monomer via electrostatic correlations at a distance r from the monomer's surface, $\tilde{c}_{i,b}$ is the number density of free ion i in the bulk solution (far from the monomer), ψ is the electric potential of the system, and the other constants are as defined in equation 1.7.

Substituting the Nernst equation into the Poisson equation results in the Poisson-Boltzmann equation [164].

$$\nabla^2 \psi(r) = -\frac{e_o}{\varepsilon} \sum_i z_i \tilde{c}_i(r) - \frac{e_o}{\varepsilon} \sum_i \tilde{c}_{i,b} e^{-\frac{e_o z_i \psi(r)}{k_B T}} \tag{A.14}$$

Taylor-expanding the exponential in equation A.14, and applying the condition that the bulk solution must be electrically neutral gives the simplest approximation for the counterion distribution around the monomer, known as the Debye-Hückel approximation [162, 164].

$$\begin{aligned} e^{-\frac{e_o z_i \psi(r)}{k_B T}} &\approx 1 - \frac{e_o z_i \psi(r)}{k_B T} \\ \nabla^2 \psi(r) - \kappa^2 \psi(r) &= -\frac{e_o}{\varepsilon} \sum_i z_i \tilde{c}_{i,b} \end{aligned} \tag{A.15}$$

The units of $1/\kappa$ are meters, meaning that κ is related to a characteristic length of the solution to the Debye-Hückel approximation [162, 164]. This characteristic length is the Debye length, ℓ_D, the distance over which the effect of a fixed charge persists

through the solution, and is defined as follows [162, 164].

$$\kappa^2 = \frac{2e_o N_A I}{\epsilon k_B T}$$
$$\ell_D = \frac{1}{\kappa} = \sqrt{\frac{\varepsilon k_B T}{2e_o^2 N_A I}}$$

This is the expression in equation 1.10 of section 1.2.2.1.3.

Appendix B

Chapter 3 Appendix

B.1 Dynamic mechanical analysis (DMA)

DMA is one of the standard tools to quantify the macroscopic viscoelastic properties of a sample [92, 167]. DMA apparatuses exist in a variety of geometries in order to apply stimuli in different orientations relative to the surface of a sample [92, 167]. The DMA experiments provided for this thesis used axial geometry, which applies a force normal (perpendicular) to the sample's surface [92, 167]. Additionally, multiple operational modes exist for DMA apparatuses [92, 167]. The DMA experiments in this thesis were performed in tension mode to measure the storage (E') and loss (E'') modulus (section 1.3.3.3) of a sample [92]. In tension mode DMA, a sample is clamped at both ends in the apparatus, a sinusoidal force is applied to one end of the sample, and the resulting sinusoidal force F and sinusoidal axial displacement z of the sample

are recorded [92]. These quantities can then be converted to E' and E'', depending on the geometry of the sample [92]. The following equations apply if the sample is rectangular, which was the case for the SBR sample used in the DMA experiments provided for this thesis [92]. Here, H, W, and L are the undeformed thickness, width, and length of the sample, F_o is the amplitude of F, z_o is the amplitude of z, and ϕ is the phase angle between F and z.

$$E' = \frac{F_o L}{z_o W H} \cos\phi \tag{B.1}$$

$$E'' = \frac{F_o L}{z_o W H} \sin\phi \tag{B.2}$$

B.2 Propagating tip radius uncertainty in AM-FM calculation of sample E'

AM-FM AFM quantifies E' of a sample via equation 2.24.

$$E'_{\text{eff}} = \sqrt{\frac{2}{RA_1}} \frac{\Delta k_2^2}{\Delta k_1} = \frac{Q}{\sqrt{R}}$$

Knowledge of the tip radius R is required in order to apply equation 2.24. In the case that R is calibrated, the user manually enters R into the software after taking AM-FM AFM measurements on a calibration sample. Therefore, R is treated as a

constant. In this case, the error (S) of E' only depends on the error in Q as follows.

$$\begin{aligned}
\sqrt{R}\,(S_{E',\text{calibrated}}) &= S_Q \\
\sqrt{R}\left(\frac{S_{E'}}{|\overline{E'}|}\right)_{\text{calibrated}} &= \left(\frac{S_Q}{|\overline{E'}|}\right) \\
&= S_Q \left|\frac{\sqrt{\overline{R}}}{Q}\right| \\
\left(\frac{S_{E'}}{|\overline{E'}|}\right)^2_{\text{calibrated}} &= \left(\frac{S_Q}{|\overline{Q}|}\right)^2
\end{aligned} \tag{B.3}$$

If the radius R is not calibrated, the mean tip radius, $\overline{R}$, and the standard deviation in the radius, S_R, can be obtained from the tip specifications provided by the manufacturer. The error in R can then be propagated to the error in E' as follows.

$$\begin{aligned}
\left(\frac{S_{E'}}{|\overline{E'}|}\right)_{\text{uncalibrated}} &= \sqrt{\left(\frac{S_Q}{|\overline{Q}|}\right)^2 + \left(\frac{1}{2}\frac{S_R}{|\overline{R}|}\right)^2} \\
\left(\frac{S_{E'}}{|\overline{E'}|}\right)^2_{\text{uncalibrated}} &= \left(\frac{S_Q}{|\overline{Q}|}\right)^2 + \left(\frac{1}{2}\frac{S_R}{|\overline{R}|}\right)^2
\end{aligned} \tag{B.4}$$

The difference in the error of E' with uncalibrated and calibrated R is the difference between equation B.4 and B.3.

$$\begin{aligned}
\left(\frac{S_{E'}}{|\overline{E'}|}\right)^2_{\text{uncalibrated}} - \left(\frac{S_{E'}}{|\overline{E'}|}\right)^2_{\text{calibrated}} &= \left(\frac{1}{2}\frac{S_R}{|\overline{R}|}\right)^2 \\
\left(\frac{S_{E'}}{|\overline{E'}|}\right)_{\text{uncalibrated}} &= \sqrt{\left(\frac{1}{2}\frac{S_R}{|\overline{R}|}\right)^2 + \left(\frac{S_{E'}}{|\overline{E'}|}\right)^2_{\text{calibrated}}}
\end{aligned} \tag{B.5}$$

If R is not calibrated, the standard deviation in the measured E' is larger than what it appears from the raw data. The standard deviation of E' from the raw data can be used to calculate the "calibrated" term of equation B.5. This observation, along with manufacturer values for S_R and $|\overline{R}|$, allow calculation of the error in E' when R is not calibrated via equation B.5. Equation B.5 corresponds to equation 3.5

in section 3.1 of the thesis.

B.3 AC160TSA reconstructions of the SBR's frequency dependent behavior

The value of sterine-butadiene rubber (SBR) E', E'', and $\tan\delta$ over a range of frequencies was reconstructed from AM-FM AFM imaging of the SBR using an AC160TSA cantilever. These reconstrictions are shown in figure B.1.

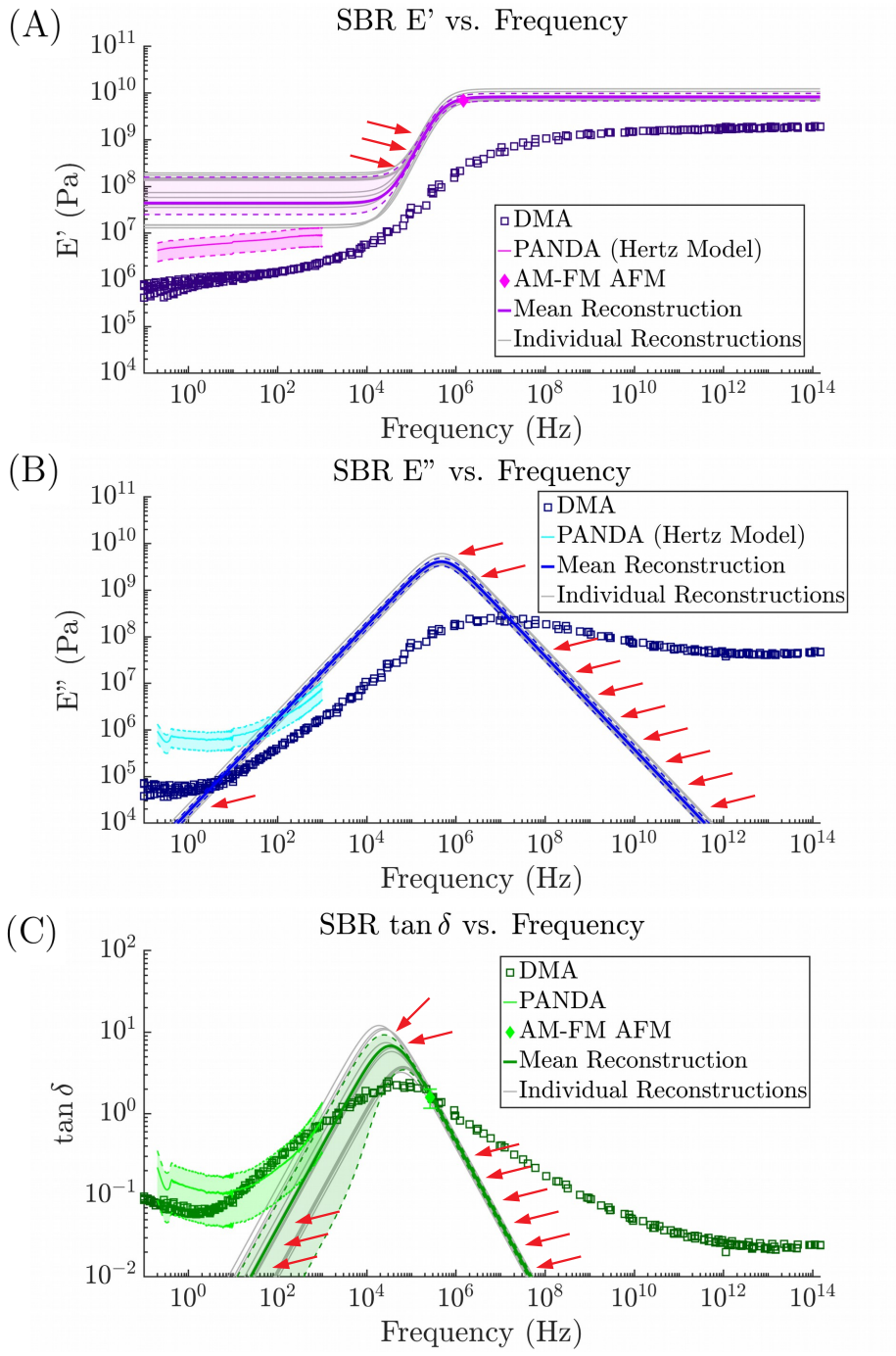


Figure B.1: Frequency dependent behavior of the SBR (AC160TSA). Storage moduli (E'), loss moduli (E''), and loss tangents ($\tan\delta$) over a range of frequencies are shown in (A), (B), and (C), respectively. Mean AM-FM AFM reconstructions are compared to control DMA (squares) and PANDA measurements. AM-FM AFM reconstructions from each of the 13 individual AM-FM AFM images are also shown in gray. Red arrows indicate regions where the reconstruction deviates from the controls by failing to account for all arms in the GMM. PANDA E' and E'' were calculated using the Hertz contact model. PANDA and AM-FM AFM were performed using an AC160TSA cantilever. Error bars and shading represent the standard deviation.

Appendix C

Chapter 4 Appendix

C.1 Distributions and statistics of collagen and hydration shell AM-FM AFM data

As shown in figure C.1 and C.2, individual AM-FM AFM images of sparse (0.02 mg collagen per mL of PBS) and concentrated (0.2 mg collagen per mL of PBS) collagen samples had varying distributions of E' and $\tan\delta$. Typically, these distributions were bimodal and well described by a two term Gaussian model (equation 2.28), suggesting that two materials may be present in the samples. The first material, corresponding to the most prominent peak in the distribution, likely represents collagen. The second, less prominent, peak in the distribution likely corresponds to fibril features such as D-bands or hydration shells, or to possible effects from the underlying mica. Some unimodal distributions were also present, and likely represent collagen fibrils alone.

Figure C.3 shows representative distributions of E' and $\tan\delta$ values from AM-FM AFM images of collagen's hydration shell. Again, the distributions of shell E' and $\tan\delta$ are mostly bimodal. However, some unimodal distributions were present as well. The bimodal distributions may arise from the varied components (organized ions and water, and the resulting local structure) of the hydration shell. Alternatively, the bi-

modal distributions of shell measurements may be the result of the tip simultaneously measuring shell and collagen properties, as described in section 4.2.4.

As shown in figure C.1-C.3, bimodal distributions of the collagen and shell AM-FM AFM data prevented accurate calculation of sample means and standard deviations when the standard formulas were used. To overcome this issue, as described in section 2.1.3.4.2, the mean and standard deviation of AM-FM AFM data were calculated by fitting Gaussians to the data distributions, rather than via the standard formulas. In this case, the mean and standard deviation represent the most prominent peak of the distribution, corresponding to the most prevalent component of the collagen or shell. As shown by figure C.1-C.3, this Gaussian fit method of calculating sample statistics matches the values from the standard formulas if the data distribution is unimodal. Therefore, as described in section 2.1.3.4.2, the mean and standard deviation of all AM-FM AFM data presented in chapter 4 were calculated by fitting Gaussians to the data distributions. For biological replicate statistics, the distribution used for the fit comprised of pixel values from all AM-FM AFM images of a particular biological replicate. For overall statistics, the distribution comprised of pixel values from all AM-FM AFM images of the sample.

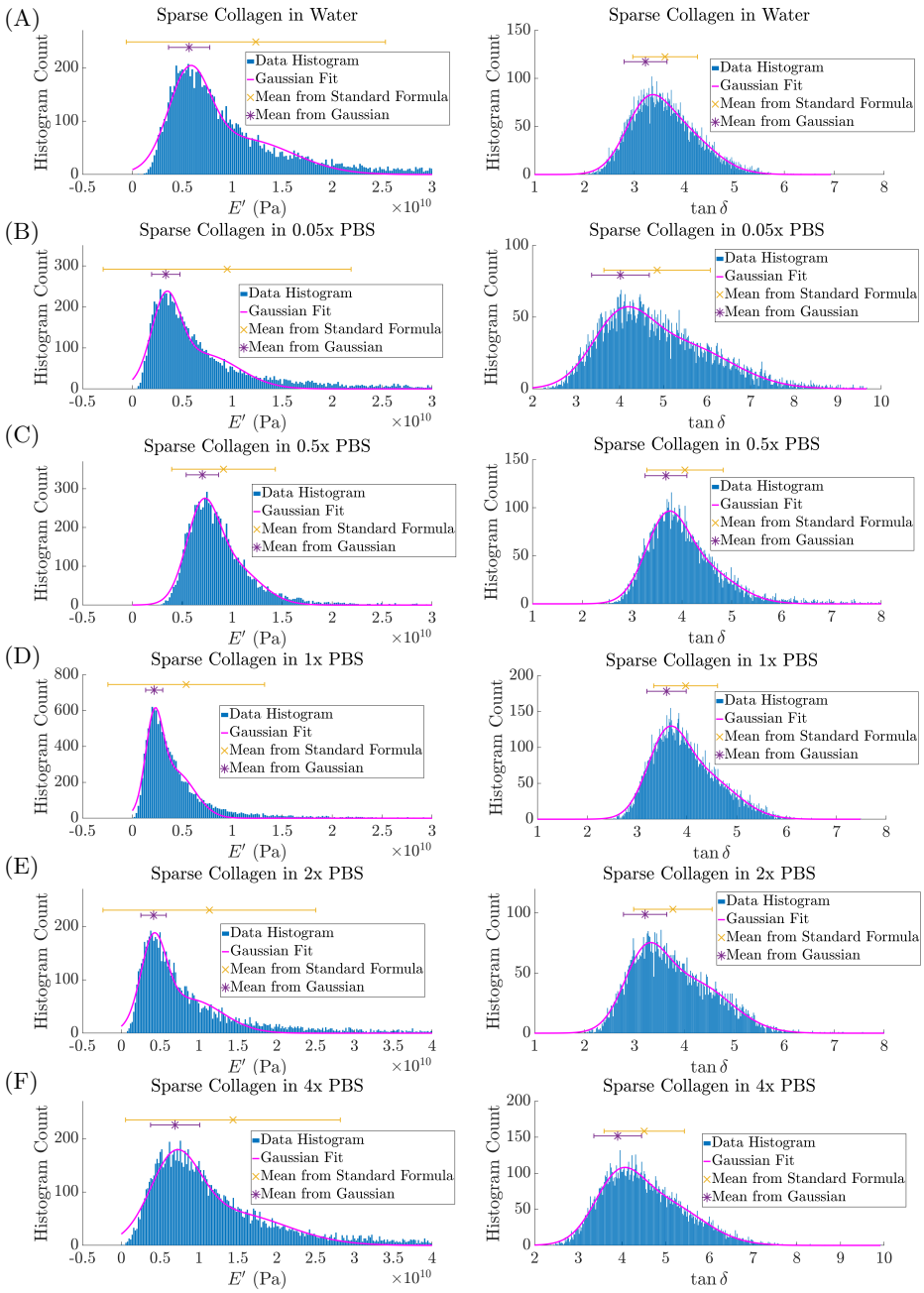


Figure C.1: Representative distributions of AM-FM AFM measurements of sparse collagen samples. All distributions were obtained from the values of individual pixels of a single AM-FM AFM image. Storage modulus, E', and loss tangent, $\tan\delta$, distributions are shown in the left and right column, respectively, for collagen in water (A), 0.05x PBS (B), 0.5x PBS (C), 1x PBS (D), 2x PBS (E), and 4x PBS (F). A two term Gaussian fit to the distribution is shown as a magenta line. The two term Gaussian was selected as described in section 2.1.3.4.2. The mean (points) and standard deviation (error bars) calculated via the standard formulas and calculated from the Gaussian fit constants as described in section 2.1.3.4.2 are shown as an orange x or a purple asterisks, respectively.

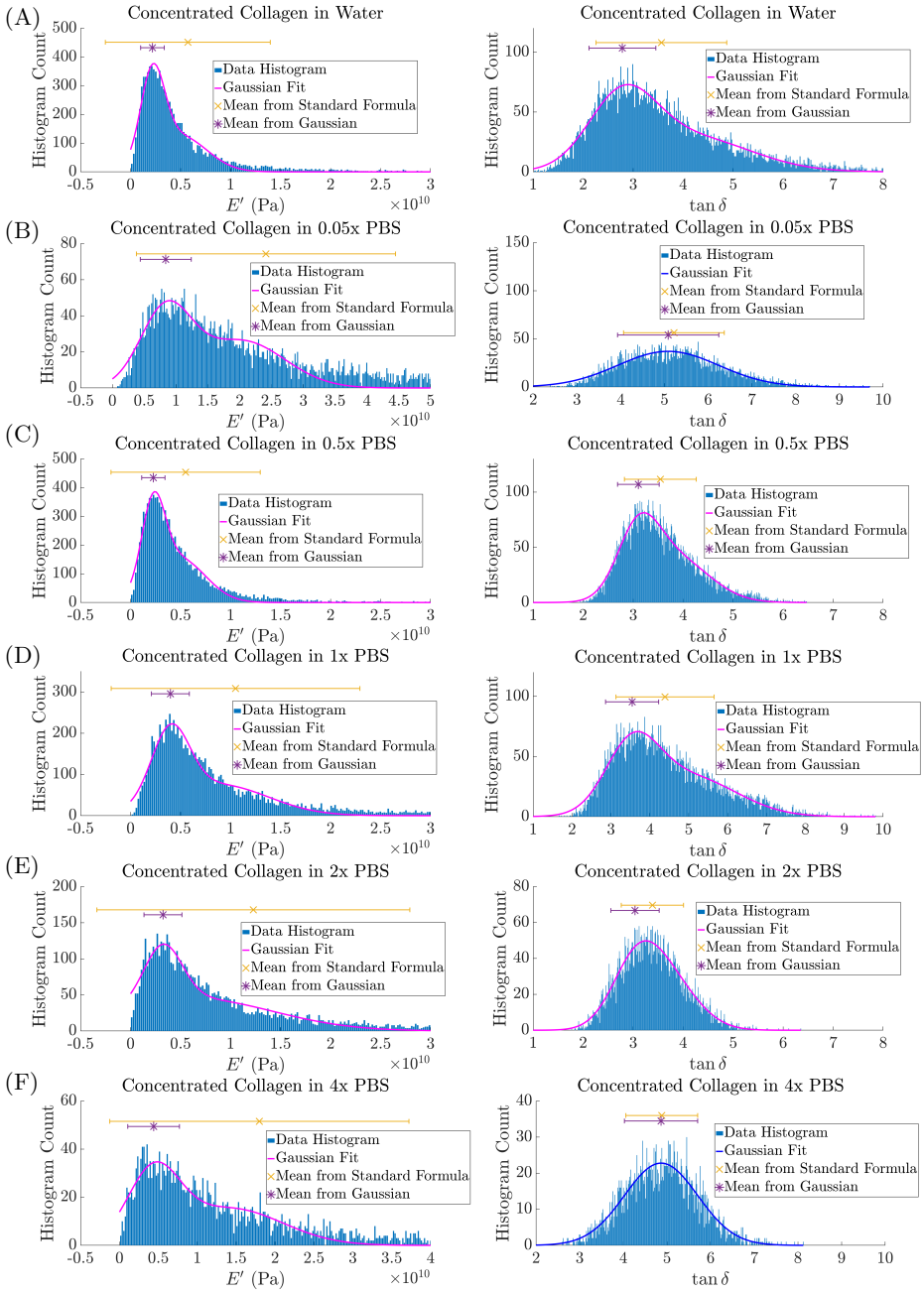


Figure C.2: Representative distributions of AM-FM AFM measurements of concentrated collagen samples. All distributions were obtained from the values of individual pixels of a single AM-FM AFM image. Storage modulus, E', and loss tangent, $\tan\delta$, distributions are shown in the left and right column, respectively, for collagen in water (A), 0.05x PBS (B), 0.5x PBS (C), 1x PBS (D), 2x PBS (E), and 4x PBS (F). A Gaussian fit to the distribution is shown as a magenta line if a two term Gaussian was used or as a dark blue line if a single term Gaussian was used. Selection of the single or two term Gaussian is described in section 2.1.3.4.2. The mean (points) and standard deviation (error bars) calculated via the standard formulas and calculated from the Gaussian fit constants as described in section 2.1.3.4.2 are shown as an orange x or a purple asterisks, respectively.

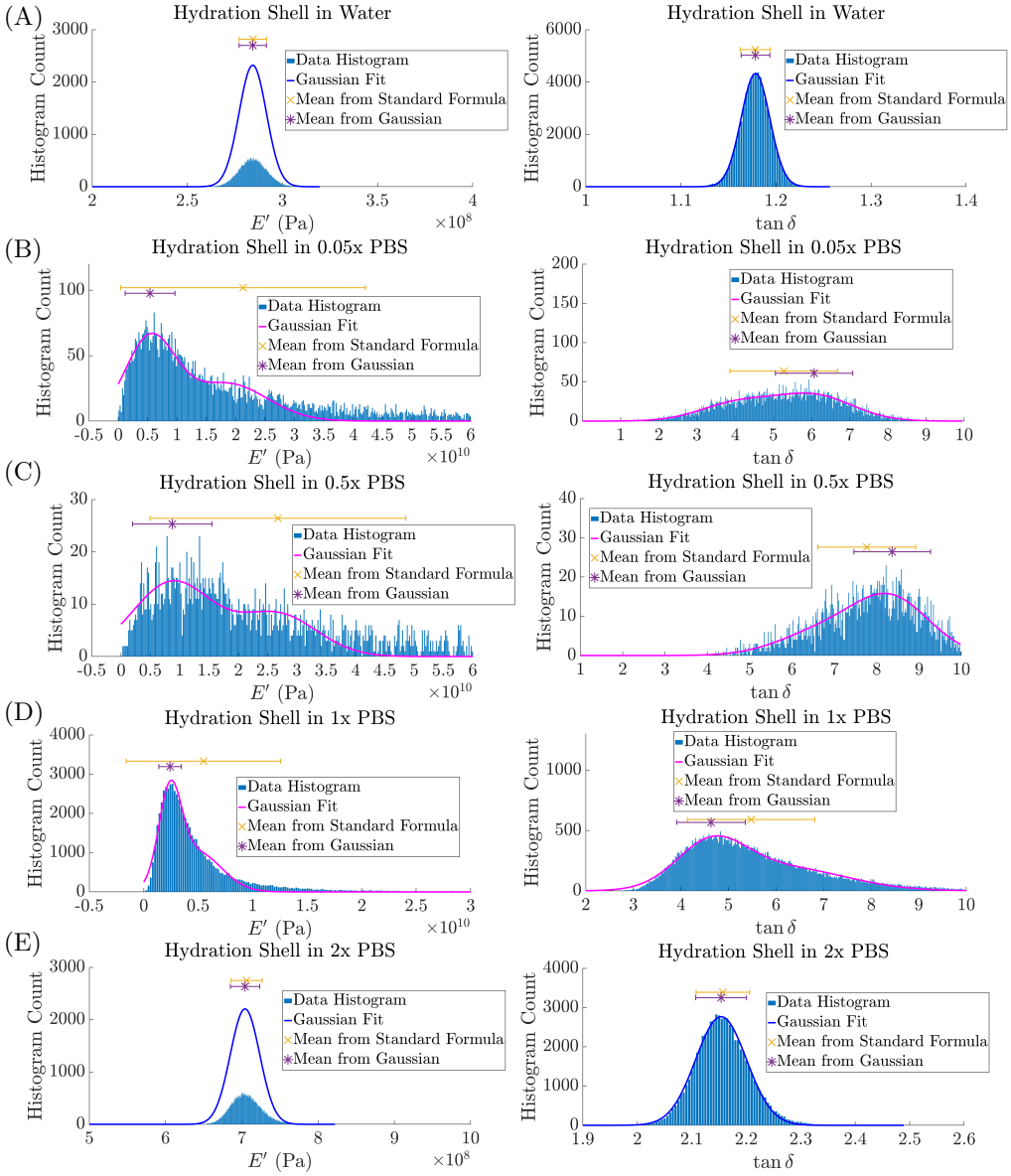


Figure C.3: Representative distributions of AM-FM AFM measurements of collagen hydration shells. All distributions were obtained from the values of individual pixels of a single AM-FM AFM image. Storage modulus, E', and loss tangent, $\tan\delta$, distributions are shown in the left and right column, respectively, for collagen hydration shells in water (A), 0.05x PBS (B), 0.5x PBS (C), 1x PBS (D), and 2x PBS (E). It was not possible to measure hydration shells in 4x PBS. A Gaussian fit to the distribution is shown as a magenta line if a two term Gaussian was used or as a dark blue line if a single term Gaussian was used. Selection of the single or two term Gaussian is described in section 2.1.3.4.2. The mean (points) and standard deviation (error bars) calculated via the standard formulas and calculated from the Gaussian fit constants as described in section 2.1.3.4.2 are shown as an orange x or a purple asterisks, respectively. While some unimodal fits, shown in (A) and (E), overestimate the height of the histogram peak, the mean and standard deviation extracted from these fits still match those calculated via the standard formulas.

Appendix D

Chapter 6 Appendix

D.1 Testing for hydrodynamic drag in PANDA measurements

In liquid, hydrodynamic drag can potentially alter cantilever movement [292], and could thereby interfere with PANDA (section 2.1.3.3) measurements. Hydrodynamic drag is typically accounted for by taking the reference measurement within 4 μm of the sample surface [292]. In order to examine whether hydrodynamic drag needed to be taken into account during PANDA measurements of cell culture substrates (chapter 6), initial PANDA experiments were performed by collecting reference measurements at different distances from the sample. First, a single measurement was performed on the sample, using a trigger point (section 2.1.3.2) of 4 nN, resulting in a sample indentation of approximately 100 nm. Second, the cantilever was moved at least 100 μm from the sample surface. Next, reference measurements were collected at various, decreasing, reference heights, until the tip was so close to the sample that an accurate reference measurement could not be obtained, or the reference measurement inadvertently indented the sample. The effect of reference measurement height on PANDA data for poly(HEMA) and pureCol substrates is shown in figure D.1.

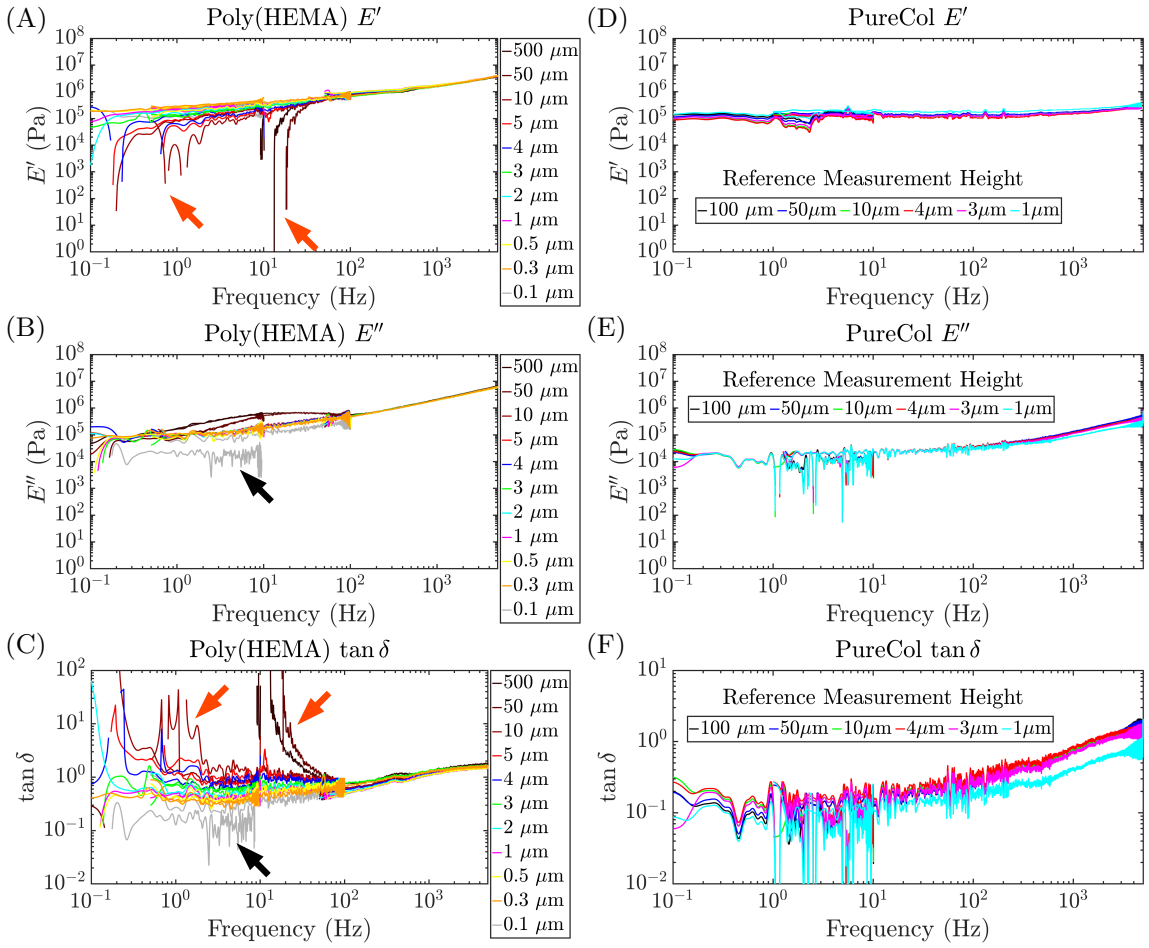


Figure D.1: Testing for hydrodynamic drag effects in PANDA measurements of poly(HEMA) and pureCol substrates. A single PANDA measurement was collected on the sample. Next, reference measurements were collected at different heights from the sample surface. The resulting storage modulus (E'), loss modulus (E''), and loss tangent ($\tan\delta$), calculated from each sample/reference pair are shown in (A)-(C) for poly(HEMA) substrates and (D)-(F) for pureCol substrates. The data in (D)-(F) were taken with an RC800PSA. Orange arrows in (A) and (C) indicate measurements affected by hydrodynamic drag. Black arrows in (B) and (C) indicate measurements where the reference was collected too close to the sample.

For poly(HEMA) substrates, PANDA measurements of low frequency sample behavior only worked if the reference height was less than 5 μm. References collected at heights higher than 5 μm had elevated values of E' and $\tan\delta$ at low frequencies. Both E' and $\tan\delta$ approached an asymptote for references taken 50 μm or higher from the sample surface. These measurements were reproducible with different AC240TSA cantilevers and different biological replicates of the poly(HEMA) sample. Therefore,

these effects are likely the result of hydrodynamic drag.

For measurements of pureCol substrates, the same E', E'', and $\tan\delta$ were obtained regardless of reference height. These results were reproducible in at least two biological replicates, and on all samples. Similar results were obtained with AC240TSA cantilevers. However, the sample began affecting reference measurements at heights of 10 μm or less from the sample surface when AC240TSA cantilevers were used (not shown). The inability of the AC240TSA reference measurements to move as close to the sample surface as the RC800PSA is likely related to the AC240TSA's increased sensitivity to pureCol surface layers (hydration shells or polymer brushes) compared to that of the RC800PSA (section 6.2.3.1).

Together, these results suggest that effects of hydrodynamic drag depend on the particular cantilever/sample pairing. Situations where drag affects the PANDA measurements are clear, such as the case with reference heights greater than 50 μm for poly(HEMA) substrates. As long as a continuous PANDA measurement is obtained, any reference height can be used without hydrodynamic drag interfering with the measurement. For any new sample/cantilever pairing, it would be wise to perform the reference height test in this section, to determine the best reference height for the particular sample/cantilever pairing.

D.2 Testing the effect of the trigger point on PANDA measurements

When a sample behaves as a linear viscoelastic material, the elasticity (E) and viscosity (η) of the material are constants, not functions, as described in section 1.3.1 [165]. This fact plays an important role in PANDA measurements. If the sample exhibits linear viscoelasticity, the measured E, η, and quantities arising from E and η such as the storage (E') and loss (E'') moduli will be constant regardless of how

the sample is indented [165]. If the sample is not a linear viscoelastic material, or the sample's indentation is so deep that PANDA no longer probes the sample's linear viscoelastic regime, the measured E' and E'' will vary with indentation depth [165].

In order to ensure that PANDA experiments were performed in the linear viscoelastic regime of the substrates, sample measurements were collected with several different trigger points. The higher the trigger point, the higher the indentation of

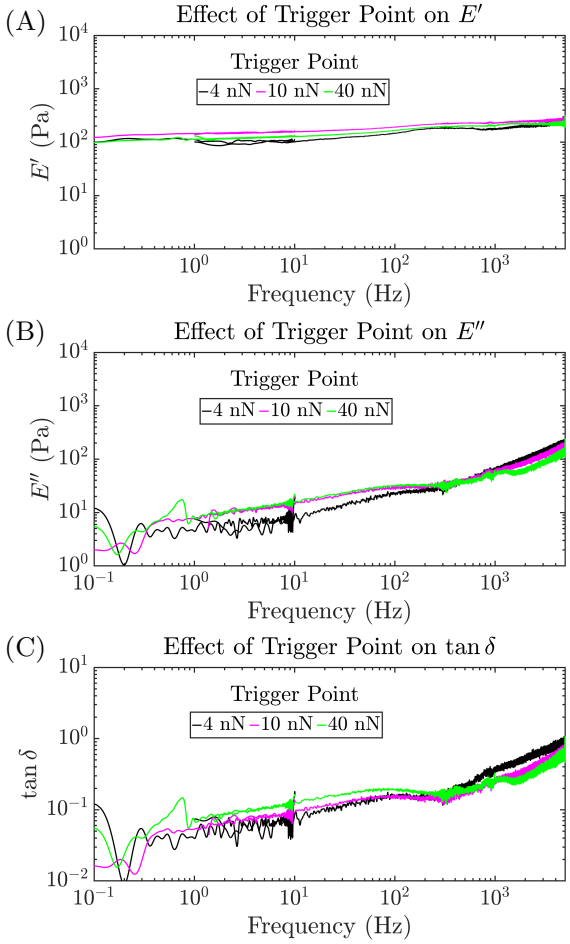


Figure D.2: Representative effects of trigger point on PANDA measurements. Several different PANDA measurements of the sample were collected, each with a different trigger point. All sample measurements were then compared to a single reference measurement. The resulting storage modulus (E'), loss modulus (E''), and loss tangent ($\tan\delta$) calculated from each sample/reference pair are shown in (A)-(C). The data in this figure was obtained with an RC800PSA on pureCol substrates crosslinked in glutaraldehyde for 24 hours. However, (A)-(C) are representative of trigger point tests on all biological replicates of all substrates used in chapter 6.

the sample (see section 2.1.3.2). Each sample measurement was analyzed against a single reference measurement. The resulting values of E' and E'', calculated with the Hertz model (section 2.1.2.1), as well as $\tan\delta$, are shown in figure D.2.

The measurements in figure D.2 were collected using an RC800PSA cantilever on pureCol crosslinked in glutaraldehyde for 24 hours, but are representative of trigger point tests on all substrates. The same result is obtained for E', E'', and $\tan\delta$ regardless of trigger point. These results were reproducible in multiple points on the sample, and in at least two biological replicates (not shown). Therefore, these observations confirm that samples were measured in their linear viscoelastic regime for these experiments.

D.3 Effect of the cantilever on PANDA results

PANDA measurements of pureCol substrates collected with AC240TSA cantilevers were similar to measurements collected with an RC800PSA. Figure D.3, shows a comparison of PANDA measurements collected on the same substrate (a single biological replicate of a pureCol substrate crosslinked for two hours) using an RC800PSA cantilever and an AC240TSA cantilever. This comparison is representative of measurements on all pureCol substrates and all biological replicates. The measured $\tan\delta$ is the same for both cantilevers. E' and E'' are slightly higher when measured by AC240TSA cantilevers. This observation could be due to the AC240TSA's increased sensitivity to substrate surface layer effects compared to the RC800PSA, as described in section 6.2.3.1. However, since $\tan\delta$ was the same for both cantilevers, this observation suggests that the different E' and E'' could also potentially arise from different contact mechanics between the RC800PSA/pureCol and AC240TSA/pureCol interaction [165]. Regardless, the fact that both cantilevers measured the same $\tan\delta$ supports the reproducibility of PANDA measurements and demonstrates that both

cantilevers are able to accurately measure pureCol substrate mechanics.

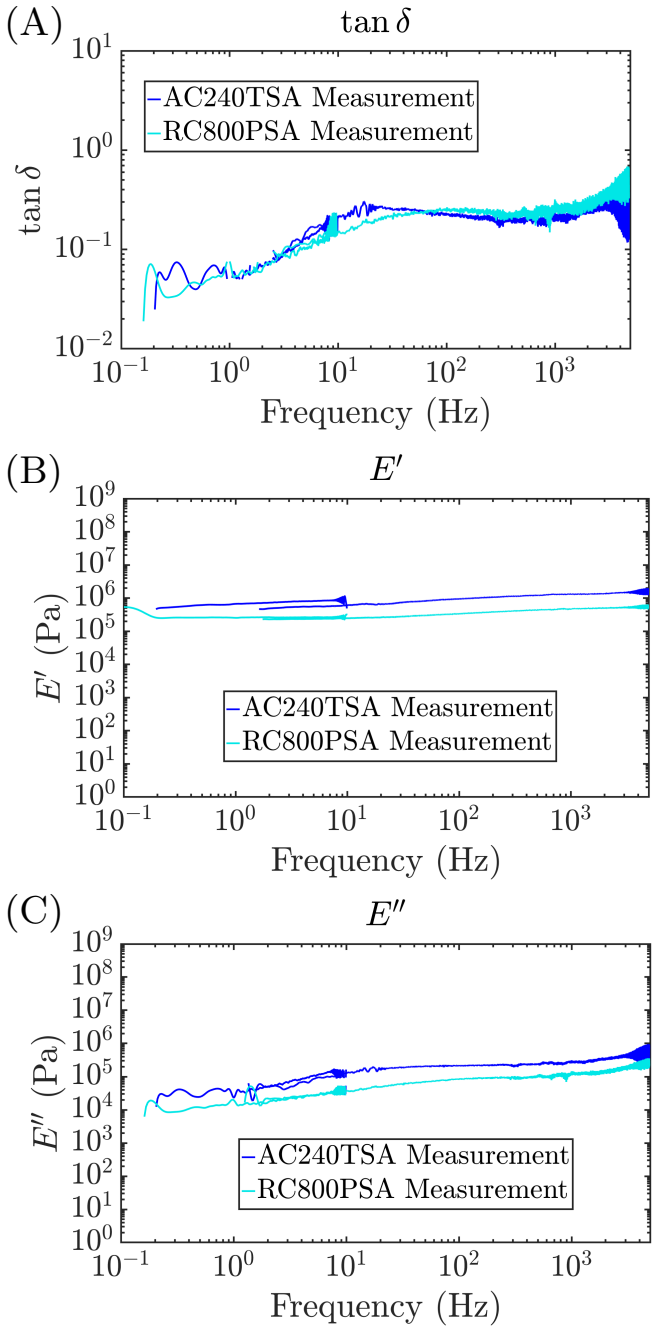


Figure D.3: Effect of cantilever on PANDA measurements of pureCol substrates. Substrate loss tangent ($\tan\delta$), shown in (A), was measured on the sample with an AC240TSA cantilever (dark blue) and an RC800PSA cantilever (cyan). The storage (E', (B)) and loss (E'', (C)) moduli were calculated from PANDA measurements of k' and k'' by applying the Hertz contact model (section 2.1.2.1). The measurements in this figure were collected on pureCol substrates crosslinked for 2 hours, but are representative of all pureCol substrates.

Bibliography

1. Weaver, V. M. Cell and tissue mechanics: the new cell biology frontier. *Molecular Biology of the Cell* **28,** 1815–1818 (July 7, 2017).
2. Levin, M. Morphogenetic fields in embryogenesis, regeneration, and cancer: Non-local control of complex patterning. *Biosystems* **109,** 243–261 (Sept. 2012).
3. Bonnans, C. *et al.* Remodelling the extracellular matrix in development and disease. *Nature Reviews Molecular Cell Biology* **15,** 786–801 (Dec. 2014).
4. Plopper, G. *Principles of cell biology* Second edition. 565 pp. (Jones & Bartlett Learning, Burlington, MA, 2016).
5. Brindley, D. *et al.* Bioprocess Forces and Their Impact on Cell Behavior: Implications for Bone Regeneration Therapy. *Journal of Tissue Engineering,* 620247 (Oct. 6, 2011).
6. Tee, S.-Y. *et al.* The mechanical cell. *Current Biology* **19,** R745–R748 (Sept. 2009).
7. Humphrey, J. D. *et al.* Mechanotransduction and extracellular matrix homeostasis. *Nature Reviews Molecular Cell Biology* **15,** 802–812 (Dec. 2014).
8. Vogel, V. & Sheetz, M. Local force and geometry sensing regulate cell functions. *Nature Reviews Molecular Cell Biology* **7,** 265–275 (Apr. 2006).
9. Engler, A. J. *et al.* Matrix Elasticity Directs Stem Cell Lineage Specification. *Cell* **126,** 677–689 (Aug. 2006).
10. Klein, E. A. *et al.* Cell-Cycle Control by Physiological Matrix Elasticity and In Vivo Tissue Stiffening. *Current Biology* **19,** 1511–1518 (Sept. 2009).
11. Wang, H.-B. *et al.* Substrate flexibility regulates growth and apoptosis of normal but not transformed cells. *American Journal of Physiology-Cell Physiology* **279,** C1345–C1350 (Nov. 2000).
12. Kong, H. J. *et al.* FRET measurements of cell-traction forces and nano-scale clustering of adhesion ligands varied by substrate stiffness. *Proceedings of the National Academy of Sciences* **102,** 4300–4305 (Mar. 22, 2005).
13. Koyama, H. *et al.* Fibrillar collagen inhibits arterial smooth muscle proliferation through regulation of Cdk2 inhibitors. *Cell* **87,** 1069–1078 (Dec. 13, 1996).
14. Huang, S. & Ingber, D. E. The structural and mechanical complexity of cell-growth control. *Nature Cell Biology* **1,** E131–E138 (Sept. 1999).

15. Chaudhuri, O. *et al.* Hydrogels with tunable stress relaxation regulate stem cell fate and activity. *Nature Materials* **15,** 326–334 (Mar. 2016).

16. Fu, J. *et al.* Mechanical regulation of cell function with geometrically modulated elastomeric substrates. *Nature Methods* **7,** 733–736 (Sept. 2010).

17. Kilian, K. A. *et al.* Geometric cues for directing the differentiation of mesenchymal stem cells. *Proceedings of the National Academy of Sciences* **107,** 4872–4877 (Mar. 16, 2010).

18. Karnik, S. K. A critical role for elastin signaling in vascular morphogenesis and disease. *Development* **130,** 411–423 (Jan. 15, 2003).

19. Brooke, B. S. *et al.* New insights into elastin and vascular disease. *Trends in Cardiovascular Medicine* **13,** 176–181 (July 2003).

20. Montell, D. J. Morphogenetic Cell Movements: Diversity from Modular Mechanical Properties. *Science* **322,** 1502–1505 (Dec. 5, 2008).

21. Solon, J. *et al.* Pulsed Forces Timed by a Ratchet-like Mechanism Drive Directed Tissue Movement during Dorsal Closure. *Cell* **137,** 1331–1342 (June 2009).

22. Trappmann, B. *et al.* Extracellular-matrix tethering regulates stem-cell fate. *Nature Materials* **11,** 642–649 (July 2012).

23. Viswanathan, P. *et al.* 3D surface topology guides stem cell adhesion and differentiation. *Biomaterials* **52,** 140–147 (June 2015).

24. Task, K. *et al.* Systems level approach reveals the correlation of endoderm differentiation of mouse embryonic stem cells with specific microstructural cues of fibrin gels. *Journal of The Royal Society Interface* **11,** 20140009–20140009 (Apr. 9, 2014).

25. Discher, D. E. *et al.* Growth Factors, Matrices, and Forces Combine and Control Stem Cells. *Science* **324,** 1673–1677 (June 26, 2009).

26. Lecuit, T. & Lenne, P.-F. Cell surface mechanics and the control of cell shape, tissue patterns and morphogenesis. *Nature Reviews Molecular Cell Biology* **8,** 633–644 (Aug. 2007).

27. Charras, G. & Sahai, E. Physical influences of the extracellular environment on cell migration. *Nature Reviews Molecular Cell Biology* **15,** 813–824 (Dec. 2014).

28. Wei, S. C. *et al.* Matrix stiffness drives epithelial-mesenchymal transition and tumour metastasis through a TWIST1-G3BP2 mechanotransduction pathway. *Nature Cell Biology* **17,** 678–688 (May 2015).

29. Peyton, S. R. & Putnam, A. J. Extracellular matrix rigidity governs smooth muscle cell motility in a biphasic fashion. *Journal of Cellular Physiology* **204,** 198–209 (July 2005).

30. Pelham, R. J. & Wang, Y. l. Cell locomotion and focal adhesions are regulated by substrate flexibility. *Proceedings of the National Academy of Sciences of the United States of America* **94,** 13661–13665 (Dec. 9, 1997).

31. Plotnikov, S. *et al.* Force Fluctuations within Focal Adhesions Mediate ECM-Rigidity Sensing to Guide Directed Cell Migration. *Cell* **151,** 1513–1527 (Dec. 2012).

32. Brammer, K. S. *et al.* Enhanced cellular mobility guided by TiO2 nanotube surfaces. *Nano Letters* **8,** 786–793 (Mar. 2008).

33. Lo, C.-M. *et al.* Cell Movement Is Guided by the Rigidity of the Substrate. *Biophysical Journal* **79,** 144–152 (July 2000).

34. Miteva, D. O. *et al.* Transmural Flow Modulates Cell and Fluid Transport Functions of Lymphatic Endothelium. *Circulation Research* **106,** 920–931 (Mar. 19, 2010).

35. Shields, J. D. *et al.* Autologous Chemotaxis as a Mechanism of Tumor Cell Homing to Lymphatics via Interstitial Flow and Autocrine CCR7 Signaling. *Cancer Cell* **11,** 526–538 (June 2007).

36. Yeung, T. *et al.* Effects of substrate stiffness on cell morphology, cytoskeletal structure, and adhesion. *Cell Motility and the Cytoskeleton* **60,** 24–34 (Jan. 2005).

37. Yoshigi, M. *et al.* Mechanical force mobilizes zyxin from focal adhesions to actin filaments and regulates cytoskeletal reinforcement. *The Journal of Cell Biology* **171,** 209–215 (Oct. 24, 2005).

38. Iyer, K. *et al.* Mechanical Activation of Cells Induces Chromatin Remodeling Preceding MKL Nuclear Transport. *Biophysical Journal* **103,** 1416–1428 (Oct. 2012).

39. Cavalcanti-Adam, E. A. *et al.* Lateral spacing of integrin ligands influences cell spreading and focal adhesion assembly. *European Journal of Cell Biology* **85,** 219–224 (Apr. 2006).

40. Totsukawa, G. *et al.* Distinct roles of ROCK (Rho-kinase) and MLCK in spatial regulation of MLC phosphorylation for assembly of stress fibers and focal adhesions in 3T3 fibroblasts. *The Journal of Cell Biology* **150,** 797–806 (Aug. 21, 2000).

41. Kaunas, R. *et al.* Cooperative effects of Rho and mechanical stretch on stress fiber organization. *Proceedings of the National Academy of Sciences of the United States of America* **102,** 15895–15900 (Nov. 1, 2005).

42. Girard, P. R. & Nerem, R. M. Shear stress modulates endothelial cell morphology and F-actin organization through the regulation of focal adhesion-associated proteins. *Journal of Cellular Physiology* **163,** 179–193 (Apr. 1995).

43. Chrzanowska-Wodnicka, M. & Burridge, K. Rho-stimulated contractility drives the formation of stress fibers and focal adhesions. *The Journal of Cell Biology* **133,** 1403–1415 (June 1996).

44. Riveline, D. *et al.* Focal contacts as mechanosensors: externally applied local mechanical force induces growth of focal contacts by an mDia1-dependent and ROCK-independent mechanism. *The Journal of Cell Biology* **153,** 1175–1186 (June 11, 2001).

45. Choquet, D. *et al.* Extracellular matrix rigidity causes strengthening of integrin-cytoskeleton linkages. *Cell* **88,** 39–48 (Jan. 10, 1997).

46. Colombelli, J. *et al.* Mechanosensing in actin stress fibers revealed by a close correlation between force and protein localization. *Journal of Cell Science* **122,** 1665–1679 (May 15, 2009).

47. Gaus, K. *et al.* Integrin-mediated adhesion regulates membrane order. *The Journal of Cell Biology* **174,** 725–734 (Aug. 28, 2006).

48. Altrock, E. *et al.* The significance of integrin ligand nanopatterning on lipid raft clustering in hematopoietic stem cells. *Biomaterials* **33,** 3107–3118 (Apr. 2012).

49. Bissell, M. J. & Aggeler, J. Dynamic reciprocity: how do extracellular matrix and hormones direct gene expression? *Progress in Clinical and Biological Research* **249,** 251–262 (1987).

50. Chiquet, M. *et al.* From mechanotransduction to extracellular matrix gene expression in fibroblasts. *Biochimica et Biophysica Acta (BBA) - Molecular Cell Research* **1793,** 911–920 (May 2009).

51. Verma, S. K. *et al.* Rac1 and RhoA differentially regulate angiotensinogen gene expression in stretched cardiac fibroblasts. *Cardiovascular Research* **90,** 88–96 (Apr. 1, 2011).

52. Gawlak, G. *et al.* Paxillin mediates stretch-induced Rho signaling and endothelial permeability *via* assembly of paxillin-p42/44MAPK-GEF-H1 complex. *The FASEB Journal* **28,** 3249–3260 (July 2014).

53. Sako, Y. Barriers for lateral diffusion of transferrin receptor in the plasma membrane as characterized by receptor dragging by laser tweezers: fence versus tether. *The Journal of Cell Biology* **129,** 1559–1574 (June 1, 1995).

54. Kusumi, A. *et al.* Paradigm shift of the plasma membrane concept from the two-dimensional continuum fluid to the partitioned fluid: high-speed single-molecule tracking of membrane molecules. *Annual Review of Biophysics and Biomolecular Structure* **34,** 351–378 (2005).

55. O'Callaghan, C. J. & Williams, B. Mechanical strain-induced extracellular matrix production by human vascular smooth muscle cells: role of TGF-beta(1). *Hypertension (Dallas, Tex.: 1979)* **36,** 319–324 (Sept. 2000).

56. Tamada, M. *et al.* Activation of a Signaling Cascade by Cytoskeleton Stretch. *Developmental Cell* **7,** 709–718 (Nov. 2004).

57. Winer, J. P. *et al.* Non-Linear Elasticity of Extracellular Matrices Enables Contractile Cells to Communicate Local Position and Orientation. *PLoS ONE* **4** (ed Kreplak, L.) e6382 (July 24, 2009).

58. Sawhney, R. K. & Howard, J. Slow local movements of collagen fibers by fibroblasts drive the rapid global self-organization of collagen gels. *The Journal of Cell Biology* **157,** 1083–1092 (June 10, 2002).

59. Balaban, N. Q. *et al.* Force and focal adhesion assembly: a close relationship studied using elastic micropatterned substrates. *Nature Cell Biology* **3,** 466–472 (May 2001).

60. Mintz, B. & Illmensee, K. Normal genetically mosaic mice produced from malignant teratocarcinoma cells. *Proceedings of the National Academy of Sciences of the United States of America* **72,** 3585–3589 (Sept. 1975).

61. Rose, S. M. & Wallingford, H. M. Transformation of renal tumors of frogs to normal tissues in regenerating limbs of salamanders. *Science (New York, N.Y.)* **107,** 457 (May 7, 1948).

62. Bissell, M. J. & Hines, W. C. Why don't we get more cancer? A proposed role of the microenvironment in restraining cancer progression. *Nature Medicine* **17,** 320–329 (Mar. 2011).

63. Weaver, V. *et al.* Reversion of the Malignant Phenotype of Human Breast Cells in Three-Dimensional Culture and In Vivo by Integrin Blocking Antibodies. *Journal of Cell Biology* **137,** 231–245 (Apr. 7, 1997).

64. Pullar, C. E. *The Physiology of Bioelectricity in Development, Tissue Regeneration and Cancer.* OCLC: 714568640 (CRC Press, Hoboken, 2011).

65. Lim, J.-H. *et al.* Alternating Current Electric Fields of Varying Frequencies: Effects on Proliferation and Differentiation of Porcine Neural Progenitor Cells. *Cellular Reprogramming* **15,** 405–412 (Oct. 2013).

66. McCullen, S. D. *et al.* Application of Low-Frequency Alternating Current Electric Fields Via Interdigitated Electrodes: Effects on Cellular Viability, Cytoplasmic Calcium, and Osteogenic Differentiation of Human Adipose-Derived Stem Cells. *Tissue Engineering Part C: Methods* **16,** 1377–1386 (Dec. 2010).

67. Huang, H. *et al.* Remote control of ion channels and neurons through magnetic-field heating of nanoparticles. *Nature Nanotechnology* **5,** 602–606 (Aug. 2010).

68. Bai, H. DC Electric Fields Induce Distinct Preangiogenic Responses in Microvascular and Macrovascular Cells. *Arteriosclerosis, Thrombosis, and Vascular Biology* **24,** 1234–1239 (July 1, 2004).

69. Nakajima, A. *et al.* Effect of Pulsatile Electric Field on Cultured Muscle Cells in Vitro. **10,** 1–6 (2012).

70. Li, X. & Kolega, J. Effects of Direct Current Electric Fields on Cell Migration and Actin Filament Distribution in Bovine Vascular Endothelial Cells. *Journal of Vascular Research* **39,** 391–404 (2002).

71. Tang, Q. *et al.* Effects of ELF electric field on proliferation of mouse osteoblastic cells. *Bioelectrochemistry and Bioenergetics* **47,** 349–353 (Dec. 1998).

72. Borys, P. On the biophysics of cathodal galvanotaxis in rat prostate cancer cells: Poisson-Nernst-Planck equation approach. *European Biophysics Journal* **41,** 527–534 (June 2012).

73. Hronik-Tupaj, M. *et al.* Osteoblastic differentiation and stress response of human mesenchymal stem cells exposed to alternating current electric fields. *BioMedical Engineering OnLine* **10,** 9 (2011).

74. Chang, H.-F. *et al.* Pulsed DC Electric FieldInduced Differentiation of Cortical Neural Precursor Cells. *PLOS ONE* **11** (ed Hu, W.) e0158133 (June 28, 2016).

75. Schimmelpfeng, J. & Dertinger, H. The action of 50 Hz magnetic and electric fields upon cell proliferation and cyclic AMP content of cultured mammalian cells. *Bioelectrochemistry and Bioenergetics* **30,** 143–150 (Mar. 1993).

76. Kobelt, L. J. *et al.* Short Duration Electrical Stimulation to Enhance Neurite Outgrowth and Maturation of Adult Neural Stem Progenitor Cells. *Annals of Biomedical Engineering* **42,** 2164–2176 (Oct. 2014).

77. Santini, M. T. *et al.* A 50 Hz sinusoidal magnetic field does not damage MG-63 three-dimensional tumor spheroids but induces changes in their invasive properties. *Bioelectromagnetics* **27,** 132–141 (Feb. 2006).

78. Kondrachuk, A. *The mechanisms of the effects of magnetic fields on cells* in *34th COSPAR Scientific Assembly* **34** (Jan. 2002), 78.

79. Zablotskii, V. *et al.* How a High-Gradient Magnetic Field Could Affect Cell Life. *Scientific Reports* **6,** 37407 (Dec. 2016).

80. Ikeya, N. & Woodward, J. R. Cellular autofluorescence is magnetic field sensitive. *Proceedings of the National Academy of Sciences* **118,** e2018043118 (Jan. 19, 2021).

81. Miyakoshi, J. Effects of static magnetic fields at the cellular level. *Progress in Biophysics and Molecular Biology* **87,** 213–223 (Feb. 2005).

82. Norimura, T. *et al.* Effects of Strong Magnetic Fields on Cell Growth and Radiation Response of Human T-lymphocytes in Culture. *Journal of UOEH* **15,** 103–112 (1993).

83. Azeloglu, E. U. & Iyengar, R. Signaling Networks: Information Flow, Computation, and Decision Making. *Cold Spring Harbor Perspectives in Biology* **7,** a005934 (Apr. 2015).

84. Messerli, M. A. & Graham, D. M. Extracellular Electrical Fields Direct Wound Healing and Regeneration. *The Biological Bulletin* **221,** 79–92 (Aug. 2011).

85. Lowry, C. The electric embryo: how electric fields mold the embryos growth pattern and shape. *21st Century,* 56–70 (1999).

86. Jaffe, L. F. & Nuccitelli, R. Electrical Controls of Development. *Annual Review of Biophysics and Bioengineering* **6,** 445–476 (June 1977).

87. Jerusalem, A. *et al.* Electrophysiological-mechanical coupling in the neuronal membrane and its role in ultrasound neuromodulation and general anaesthesia. *Acta Biomaterialia* **97,** 116–140 (Oct. 2019).

88. Athenstaedt, H. Pyroelectric and Piezoelectric Properties of Vertebrates. *Annals of the New York Academy of Sciences* **238,** 68–94 (Oct. 1974).

89. Micheletti, C. Comparing proteins by their internal dynamics: Exploring structurefunction relationships beyond static structural alignments. *Physics of Life Reviews* **10,** 1–26 (Mar. 2013).

90. Brini, E. *et al.* Protein storytelling through physics. *Science* **370,** eaaz3041 (Nov. 27, 2020).

91. Frauenfelder, H. *et al. The physics of proteins: an introduction to biological physics and molecular biophysics* OCLC: ocn646392217. 448 pp. (Springer, New York, 2010).

92. Piacenti, A. *Atomic Force Microscope-Based Methods for the Nano-Mechanical Characterisation of Hydrogels and other Viscoelastic Polymeric Materials for Biomedical Applications* PhD thesis (Oxford University, 2021). 241 pp.

93. Pandol, S. *et al.* Desmoplasia of Pancreatic Ductal Adenocarcinoma. *Clinical Gastroenterology and Hepatology* **7,** S44–S47 (Nov. 2009).

94. Blumberg, D. Parasitoid Encapsulation as a Defense Mechanism in the Coccoidea (Homoptera) and Its Importance in Biological Control. *Biological Control* **8,** 225–236 (Mar. 1997).

95. Barr, L. C. The encapsulation of tumours. *Clinical & Experimental Metastasis* **7,** 277–282 (May 1989).

96. Lemaitre, B. & Hoffmann, J. The Host Defense of *Drosophila melanogaster*. *Annual Review of Immunology* **25,** 697–743 (Apr. 2007).

97. Ibrahim-Hashim, A. *et al.* Artificial selection for host resistance to tumour growth and subsequent cancer cell adaptations: an evolutionary arms race. *British Journal of Cancer* **124,** 455–465 (Jan. 19, 2021).

98. Jackson, T. L. & Byrne, H. M. A mechanical model of tumor encapsulation and transcapsular spread. *Mathematical Biosciences* **180,** 307–328 (Nov. 2002).

99. Kleppner, S. R. *et al.* Transplanted human neurons derived from a teratocarcinoma cell line (NTera-2) mature, integrate, and survive for over 1 year in the nude mouse brain. *The Journal of Comparative Neurology* **357,** 618–632 (July 10, 1995).

100. Pierce, G. in *Current Topics in Developmental Biology* 223–246 (Elsevier, 1967).

101. Dolberg, D. S. & Bissell, M. J. Inability of Rous sarcoma virus to cause sarcomas in the avian embryo. *Nature* **309,** 552–556 (June 1984).

102. Stevens, L. C. in *Advances in Morphogenesis* 1–31 (Elsevier, 1967).

103. Stoker, A. W. *et al.* The embryonic environment strongly attenuates v-src oncogenesis in mesenchymal and epithelial tissues, but not in endothelia. *Journal of Cell Biology* **111,** 217–228 (July 1, 1990).

104. Pierce, G. *et al.* Ultrastructural Analysis of the Early Development of Teratocarcinomas2. *JNCI: Journal of the National Cancer Institute* (Oct. 1967).

105. Howlett, A. R. *et al.* A Novel Function for the nm23-H1 Gene: Overexpression in Human Breast Carcinoma Cells Leads to the Formation of Basement Membrane and Growth Arrest. *JNCI Journal of the National Cancer Institute* **86,** 1838–1844 (Dec. 21, 1994).

106. Rizki, A. *et al.* A Human Breast Cell Model of Preinvasive to Invasive Transition. *Cancer Research* **68,** 1378–1387 (Mar. 1, 2008).

107. Hendrix, M. J. C. *et al.* Reprogramming metastatic tumour cells with embryonic microenvironments. *Nature Reviews Cancer* **7,** 246–255 (Apr. 2007).

108. Weaver, V. M. *et al.* The development of a functionally relevant cell culture model of progressive human breast cancer. *Seminars in Cancer Biology* **6,** 175–184 (June 1995).

109. Needham, J. New Advances in the Chemistry and Biology of Organized Growth: (Section of Pathology). *Proceedings of the Royal Society of Medicine* **29,** 1577–1626 (Oct. 1936).

110. Waddington, C. H. Cancer and the Theory of Organisers. *Nature* **135,** 606–608 (Apr. 1935).

111. Luan, S. *et al.* Neuromodulation: present and emerging methods. *Frontiers in Neuroengineering* **7** (July 15, 2014).

112. Elder, G. J. & Taylor, J.-P. Transcranial magnetic stimulation and transcranial direct current stimulation: treatments for cognitive and neuropsychiatric symptoms in the neurodegenerative dementias? *Alzheimer's Research & Therapy* **6,** 74 (Dec. 2014).

113. Kloth, L. C. Electrical Stimulation Technologies for Wound Healing. *Advances in Wound Care* **3,** 81–90 (Feb. 2014).

114. Ievins, A. & Moritz, C. T. Therapeutic Stimulation for Restoration of Function After Spinal Cord Injury. *Physiology* **32,** 391–398 (Sept. 2017).

115. Moritz, C. A giant step for spinal cord injury research. *Nature Neuroscience* **21,** 1647–1648 (Dec. 2018).

116. Mehta, M. *et al.* Critical review of the addition of tumor treating fields (TTFields) to the existing standard of care for newly diagnosed glioblastoma patients. *Critical Reviews in Oncology/Hematology* **111,** 60–65 (Mar. 2017).

117. Carrieri, F. A. *et al.* Tumor Treating Fields: At the Crossroads Between Physics and Biology for Cancer Treatment. *Frontiers in Oncology* **10,** 575992 (Oct. 30, 2020).

118. Li, Z. *et al.* Recent Advances in Nanomaterials-Based Chemo-Photothermal Combination Therapy for Improving Cancer Treatment. *Frontiers in Bioengineering and Biotechnology* **7,** 293 (Oct. 22, 2019).

119. Hannezo, E. & Heisenberg, C.-P. Mechanochemical Feedback Loops in Development and Disease. *Cell* **178,** 12–25 (June 2019).

120. Tan, J. L. *et al.* Cells lying on a bed of microneedles: An approach to isolate mechanical force. *Proceedings of the National Academy of Sciences* **100,** 1484–1489 (Feb. 18, 2003).

121. Amschler, K. *et al.* Nanoscale Integrin Ligand Patterns Determine Melanoma Cell Behavior. *ACS Nano* **8,** 9113–9125 (Sept. 23, 2014).

122. Arnold, M. *et al.* Activation of Integrin Function by Nanopatterned Adhesive Interfaces. *ChemPhysChem* **5,** 383–388 (Mar. 19, 2004).

123. Oria, R. *et al.* Force loading explains spatial sensing of ligands by cells. *Nature* (Dec. 6, 2017).

124. Alenghat, F. J. & Ingber, D. E. Mechanotransduction: All Signals Point to Cytoskeleton, Matrix, and Integrins. *Science Signaling* **2002,** pe6–pe6 (Feb. 12, 2002).

125. Trichet, L. *et al.* Evidence of a large-scale mechanosensing mechanism for cellular adaptation to substrate stiffness. *Proceedings of the National Academy of Sciences* **109,** 6933–6938 (May 1, 2012).

126. Gordon, V. D. & Wang, L. Bacterial mechanosensing: the force will be with you, always. *Journal of Cell Science* **132,** jcs227694 (Apr. 1, 2019).

127. Bhat, S. *et al.* in *Viscoelasticity - From Theory to Biological Applications* (ed De Vicente, J.) (InTech, Nov. 7, 2012).

128. Adam, J. A. *et al.* Growth of microorganisms in an interfacially driven space bioreactor analog. *npj Microgravity* **6,** 11 (Dec. 2020).

129. Kular, J. K. *et al.* The extracellular matrix: Structure, composition, age-related differences, tools for analysis and applications for tissue engineering. *Journal of Tissue Engineering* **5,** 204173141455711 (Feb. 21, 2014).

130. Verzr, F. in *International Review of Connective Tissue Research* 243–300 (Elsevier, 1964).

131. Gautieri, A. *et al.* Hierarchical Structure and Nanomechanics of Collagen Microfibrils from the Atomistic Scale Up. *Nano Letters* **11,** 757–766 (Feb. 9, 2011).

132. Williams, B. R. *et al.* Collagen fibril formation. Optimal in vitro conditions and preliminary kinetic results. *The Journal of Biological Chemistry* **253,** 6578–6585 (Sept. 25, 1978).

133. Serban, M. A. *et al.* Effects of extracellular matrix analogues on primary human fibroblast behavior. *Acta Biomaterialia* **4,** 67–75 (Jan. 2008).

134. Zaman, M. H. *et al.* Migration of tumor cells in 3D matrices is governed by matrix stiffness along with cell-matrix adhesion and proteolysis. *Proceedings of the National Academy of Sciences of the United States of America* **103,** 10889–10894 (July 18, 2006).

135. Stamov, D. R. & Pompe, T. Structure and function of ECM-inspired composite collagen type I scaffolds. *Soft Matter* **8,** 10200 (2012).

136. Li, Q. *et al.* Stretch-Induced Collagen Synthesis in Cultured Smooth Muscle Cells from Rabbit Aortic Media and a Possible Involvement of Angiotensin II and Transforming Growth Factor-β. *Journal of Vascular Research* **35,** 93–103 (1998).

137. Ball, P. Water is an active matrix of life for cell and molecular biology. *Proceedings of the National Academy of Sciences* **114,** 13327–13335 (Dec. 19, 2017).

138. Laage, D. *et al.* Water Dynamics in the Hydration Shells of Biomolecules. *Chemical Reviews* **117,** 10694–10725 (Aug. 23, 2017).

139. Fukuma, T. Water distribution at solid/liquid interfaces visualized by frequency modulation atomic force microscopy. *Science and Technology of Advanced Materials* **11,** 033003 (Feb. 2010).

140. Votchovsky, K. *et al.* Direct mapping of the solidliquid adhesion energy with subnanometre resolution. *Nature Nanotechnology* **5,** 401–405 (June 2010).

141. Contera, S. A. *et al.* Controlled ionic condensation at the surface of a native extremophilemembrane. *Nanoscale* **2,** 222–229 (2010).

142. Yap, A. S. *et al.* Mechanosensing and Mechanotransduction at CellCell Junctions. *Cold Spring Harbor Perspectives in Biology* **10,** a028761 (Aug. 2018).

143. Labernadie, A. *et al.* Protrusion force microscopy reveals oscillatory force generation and mechanosensing activity of human macrophage podosomes. *Nature Communications* **5,** 5343 (Dec. 2014).

144. Delvoye, P. *et al.* Measurement of mechanical forces generated by skin fibroblasts embedded in a three-dimensional collagen gel. *The Journal of Investigative Dermatology* **97,** 898–902 (Nov. 1991).

145. Ohashi, K. *et al.* Roles of the cytoskeleton, cell adhesion and rho signalling in mechanosensing and mechanotransduction. *Journal of Biochemistry,* mvw082 (Jan. 12, 2017).

146. Block, M. R. *et al.* Podosome-type adhesions and focal adhesions, so alike yet so different. *European Journal of Cell Biology* **87,** 491–506 (Sept. 2008).

147. Kirby, T. J. & Lammerding, J. Emerging views of the nucleus as a cellular mechanosensor. *Nature Cell Biology* **20,** 373–381 (Apr. 2018).

148. Mao, X. *et al.* Nuclear Mechanics and Stem Cell Differentiation. *Stem Cell Reviews and Reports* **11,** 804–812 (Dec. 2015).

149. Wang, N. *et al.* Mechanotransduction at a distance: mechanically coupling the extracellular matrix with the nucleus. *Nature Reviews Molecular Cell Biology* **10,** 75–82 (Jan. 2009).

150. Lovett, D. B. *Nuclear shape control in fibroblasts* PhD thesis (University of Florida, 2013). 93 pp.

151. Mammoto, A. *et al.* Mechanosensitive mechanisms in transcriptional regulation. *Journal of Cell Science* **125,** 3061–3073 (July 1, 2012).

152. Kim, S.-H. *et al.* Extracellular matrix and cell signalling: the dynamic cooperation of integrin, proteoglycan and growth factor receptor. *Journal of Endocrinology* **209,** 139–151 (May 2011).

153. Hastings, J. F. *et al.* The extracellular matrix as a key regulator of intracellular signalling networks: ECM regulation of intracellular signalling networks. *British Journal of Pharmacology* **176,** 82–92 (Jan. 2019).

154. Athenstaedt, H. Permanent electric polarization and pyroelectric behaviour of the vertebrate skeleton: III. The axial skeleton of man. *Zeitschrift fr Zellforschung und Mikroskopische Anatomie* **93,** 484–504 (1968).

155. Athenstaedt, H. Permanent electric polarization of the meninges of man. *Zeitschrift fr Zellforschung und Mikroskopische Anatomie* **98,** 300–322 (1969).

156. Athenstaedt, H. Pyroelectricity in human skin related to physiological skin properties. *Ferroelectrics* **39,** 1243 –1243 (1981).

157. Guldiken, R. & Onen, O. in *MEMS for Biomedical Applications* 120–149 (Elsevier, 2012).

158. Schauble, M. K. & Habal, M. B. Electropotentials of tumor tissue. *Journal of Surgical Research* **9,** 517–520 (Sept. 1969).

159. Nuccitelli, R. *et al.* Imaging the electric field associated with mouse and human skin wounds. *Wound Repair and Regeneration* **16,** 432–441 (May 2008).

160. Birgersson, U. *et al.* A methodology for extracting the electrical properties of human skin. *Physiological Measurement* **34,** 723–736 (June 1, 2013).

161. Chiang, M. *et al.* Electrical fields in the vicinity of epithelial wounds in the isolated bovine eye. *Experimental Eye Research* **54,** 999–1003 (June 1992).

162. Doi, M. *Soft matter physics* First edition. OCLC: ocn857650756. 257 pp. (Oxford University Press, Oxford ; New York, 2013).

163. Moore, D. S. Amino acid and peptide net charges: A simple calculational procedure. *Biochemical Education* **13,** 10–11 (Jan. 1985).

164. Israelachvili, J. N. *Intermolecular and surface forces* Third edition. OCLC: 249272556. 676 pp. (Elsevier, Academic Press, Amsterdam, 2011).

165. Popov, V. L. *et al. Handbook of Contact Mechanics: Exact Solutions of Axisymmetric Contact Problems* (Springer Berlin Heidelberg, Berlin, Heidelberg, 2019).

166. Seifert, J. *In vivo dynamic AFM mapping of viscoelastic properties of the primary plant cell wall* PhD thesis (University of Oxford, 2018). 244 pp.

167. Lakes, R. S. Viscoelastic measurement techniques. *Review of Scientific Instruments* **75,** 797–810 (Apr. 2004).

168. Schwarz, U. S. & Safran, S. A. Physics of adherent cells. *Reviews of Modern Physics* **85,** 1327–1381 (Aug. 27, 2013).

169. Ferry, J. D. *Viscoelastic properties of polymers* 3d ed. 641 pp. (Wiley, New York, 1980).

170. Xu, B. *et al.* Understanding the viscoelastic behavior of collagen matrices through relaxation time distribution spectrum. *Biomatter* **3,** e24651 (July 19, 2013).

171. Dhume, R. Y. & Barocas, V. H. Emergent structure-dependent relaxation spectra in viscoelastic fiber networks in extension. *Acta Biomaterialia* **87,** 245–255 (Mar. 2019).

172. Honerkamp, J. & Weese, J. Determination of the relaxation spectrum by a regularization method. *Macromolecules* **22,** 4372–4377 (Nov. 1989).

173. Orbey, N. & Dealy, J. M. Determination of the relaxation spectrum from oscillatory shear data. *Journal of Rheology* **35,** 1035–1049 (Aug. 1991).

174. Hansen, S. L. *et al.* Mechanical Properties of Plant Cell Walls Probed by Relaxation Spectra. *Plant Physiology* **155,** 246–258 (Jan. 2011).

175. Roylance, D. *Engineering Viscoelasticity.* Massachusetts Institute of Technology. https://web.mit.edu/course/3/3.11/www/modules/visco.pdf. 2001.

176. Sperling, L. H. *Introduction to physical polymer science* 4th ed. 845 pp. (Wiley, Hoboken, N.J, 2006).

177. Nielsen, L. E. & Landel, R. F. *Mechanical properties of polymers and composites* 2nd ed., rev. and expanded. *Mechanical engineering* **90.** 557 pp. (M. Dekker, New York, 1994).

178. Bueche, F. J. *Physical properties of polymers* 354 pp. (Interscience Publishers, New York, 1962).

179. Flory, P. J. *Principles of polymer chemistry* 19. print. OCLC: 254754780. 672 pp. (Cornell Univ. Press, Ithaca, NY, 2006).

180. Rodriguez, F. *Principles of polymer systems* 3rd ed. 640 pp. (Hemisphere Pub. Corp, New York, 1989).

181. Rodriguez, F. *Principles of polymer systems* 2nd. 575 pp. (Hemisphere Publishing Corporation, Washington, D.C., 1982).

182. Tobolsky, A. V. *Properties and structure of polymers* 331 pp. (Wiley, New York, 1960).

183. Treloar, L. R. G. *The physics of rubber elasticity* 3rd. 254 pp. (Clarendon Press, Oxford, 1949).

184. Charrier, E. E. *et al.* Control of cell morphology and differentiation by substrates with independently tunable elasticity and viscous dissipation. *Nature Communications* **9,** 449 (Dec. 2018).

185. Bennett, M. *et al.* Molecular clutch drives cell response to surface viscosity. *Proceedings of the National Academy of Sciences* **115,** 1192–1197 (Feb. 6, 2018).

186. Vining, K. H. & Mooney, D. J. Mechanical forces direct stem cell behaviour in development and regeneration. *Nature Reviews. Molecular Cell Biology* **18,** 728–742 (Dec. 2017).

187. Umut Ozcan, M. *et al.* Characterization of frequency-dependent material properties of human liver and its pathologies using an impact hammer. *Medical Image Analysis* **15,** 45–52 (Feb. 2011).

188. Amis, E. J. *et al.* Effect of pH on collagen flexibility determined from dilute solution viscoelastic measurements. *International Journal of Biological Macromolecules* **7,** 130–134 (June 1985).

189. Meghezi, S. *et al.* Effects of a Pseudophysiological Environment on the Elastic and Viscoelastic Properties of Collagen Gels. *International Journal of Biomaterials* **2012,** 1–9 (2012).

190. Nam, S. *et al.* Strain-enhanced stress relaxation impacts nonlinear elasticity in collagen gels. *Proceedings of the National Academy of Sciences* **113,** 5492–5497 (May 17, 2016).

191. Sasaki, N. in *Viscoelasticity - From Theory to Biological Applications* (ed De Vicente, J.) (InTech, Nov. 7, 2012).

192. Shen, Z. *et al.* Viscoelastic Properties of Isolated Collagen Fibrils. *Biophysical Journal* **100,** 3008–3015 (June 2011).

193. Sopakayang, R. *et al.* Elastic and viscoelastic properties of a type I collagen fiber. *Journal of Theoretical Biology* **293,** 197–205 (Jan. 2012).

194. Gonzalez-Molina, J. *et al.* Extracellular fluid viscosity enhances liver cancer cell mechanosensing and migration. *Biomaterials* **177,** 113–124 (Sept. 2018).

195. Liu, W. & Wu, C. Rheological Study of Soft Matters: A Review of Microrheology and Microrheometers. *Macromolecular Chemistry and Physics* **219,** 1700307 (Feb. 2018).

196. Butt, H.-J. *et al.* Force measurements with the atomic force microscope: Technique, interpretation and applications. *Surface Science Reports* **59,** 1–152 (Oct. 2005).

197. Efremov, Y. M. *et al.* Measuring viscoelasticity of soft biological samples using atomic force microscopy. *Soft Matter* **16,** 64–81 (2020).

198. Haugstad, G. *Atomic force microscopy: understanding basic modes and advanced applications* 464 pp. (John Wiley & Sons, Hoboken, N.J, 2012).

199. Garca, R. Dynamic atomic force microscopy methods. *Surface Science Reports* **47,** 197–301 (Sept. 2002).

200. Castro Garca, R. *Amplitude modulation atomic force microscopy* OCLC: 1180151008 (2011).

201. *Get Real - Automated Probe Calibration* Oxford Instruments Asylum Research Forums. https://support.asylumresearch.com/articles/video-tutorials-aa/19721-getreal-automated-probe-calibration. 2014.

202. *Applications Guide Version 16 Revision* Oxford Instruments Asylum Research Manual. 2018.

203. Hutter, J. L. & Bechhoefer, J. Calibration of atomic-force microscope tips. *Review of Scientific Instruments* **64,** 1868–1873 (July 1993).

204. Higgins, M. J. *et al.* Noninvasive determination of optical lever sensitivity in atomic force microscopy. *Review of Scientific Instruments* **77,** 013701 (Jan. 2006).

205. Sader, J. E. *et al.* Calibration of rectangular atomic force microscope cantilevers. *Review of Scientific Instruments* **70,** 3967–3969 (Oct. 1999).

206. Sader, J. E. *et al.* Spring constant calibration of atomic force microscope cantilevers of arbitrary shape. *Review of Scientific Instruments* **83,** 103705 (Oct. 2012).

207. Walters, D. A. *et al.* Short cantilevers for atomic force microscopy. *Review of Scientific Instruments* **67,** 3583–3590 (Oct. 1996).

208. Hertz, H. Ueber die Berhrung fester elastischer Krper. *Journal fr die reine und angewandte Mathematik (Crelles Journal)* **1882,** 156–171 (Jan. 1, 1882).

209. Sun, Y. *et al.* Using the Adhesive Interaction between Atomic Force Microscopy Tips and Polymer Surfaces to Measure the Elastic Modulus of Compliant Samples. *Langmuir* **20,** 5837–5845 (July 2004).

210. Benaglia, S. *et al.* Fast and high-resolution mapping of elastic properties of biomolecules and polymers with bimodal AFM. *Nature Protocols* **13,** 2890–2907 (Dec. 2018).

211. Rabe, U *et al.* Influence of the cantilever holder on the vibrations of AFM cantilevers. *Nanotechnology* **18,** 044008 (Jan. 31, 2007).

212. Schffer, T. E. *et al.* Studies of vibrating atomic force microscope cantilevers in liquid. *Journal of Applied Physics* **80,** 3622–3627 (Oct. 1996).

213. Kiracofe, D. *et al.* High efficiency laser photothermal excitation of microcantilever vibrations in air and liquids. *Review of Scientific Instruments* **82,** 013702 (Jan. 2011).

214. Marti, O. *et al.* Mechanical and thermal effects of laser irradiation on force microscope cantilevers. *Ultramicroscopy* **42-44,** 345–350 (July 1992).

215. Nishida, S. *et al.* Photothermal excitation of a single-crystalline silicon cantilever for higher vibration modes in liquid. *Journal of Vacuum Science & Technology B: Microelectronics and Nanometer Structures* **27,** 964 (2009).

216. Ramos, D. *et al.* Photothermal excitation of microcantilevers in liquids. *Journal of Applied Physics* **99,** 124904 (June 15, 2006).

217. Ratcliff, G. C. *et al.* Photothermal modulation for oscillating mode atomic force microscopy in solution. *Applied Physics Letters* **72,** 1911–1913 (Apr. 13, 1998).

218. Umeda, N. Scanning attractive force microscope using photothermal vibration. *Journal of Vacuum Science & Technology B: Microelectronics and Nanometer Structures* **9,** 1318 (Mar. 1991).

219. Labuda, A. *et al.* Tapping Mode AFM Imaging in Liquids with blueDrive Photothermal Excitation. *Microscopy Today* **26,** 12–17 (Nov. 2018).

220. Kocun, M. *et al.* Fast, High Resolution, and Wide Modulus Range Nanomechanical Mapping with Bimodal Tapping Mode. *ACS Nano* **11,** 10097–10105 (Oct. 24, 2017).

221. Labuda, A. *et al.* Generalized Hertz model for bimodal nanomechanical mapping. *Beilstein Journal of Nanotechnology* **7,** 970–982 (July 5, 2016).

222. Solares, S. D. & Chawla, G. Frequency response of higher cantilever eigenmodes in bimodal and trimodal tapping mode atomic force microscopy. *Measurement Science and Technology* **21,** 125502 (Dec. 1, 2010).

223. Proksch, R. & Yablon, D. G. Loss tangent imaging: Theory and simulations of repulsive-mode tapping atomic force microscopy. *Applied Physics Letters* **100,** 073106 (Feb. 13, 2012).

224. Proksch, R. *et al.* Practical loss tangent imaging with amplitude-modulated atomic force microscopy. *Journal of Applied Physics* **119,** 134901 (Apr. 7, 2016).

225. Herruzo, E. T. & Garcia, R. Theoretical study of the frequency shift in bimodal FM-AFM by fractional calculus. *Beilstein Journal of Nanotechnology* **3,** 198–206 (Mar. 7, 2012).

226. Al-Rekabi, Z. & Contera, S. Multifrequency AFM reveals lipid membrane mechanical properties and the effect of cholesterol in modulating viscoelasticity. *Proceedings of the National Academy of Sciences* **115,** 2658–2663 (Mar. 13, 2018).

227. Seifert, J. *et al.* Mapping cellular nanoscale viscoelasticity and relaxation times relevant to growth of living Arabidopsis thaliana plants using multifrequency AFM. *Acta Biomaterialia* **121,** 371–382 (Feb. 2021).

228. Harandi, M. H. *et al.* Morphological and mechanical properties of styrene butadiene rubber/nano copper nanocomposites. *Results in Physics* **7,** 338–344 (2017).

229. Yang, J. & Nandi, S. in *International Review of Cytology* 249–286 (Elsevier, 1983).

230. Fessler, J. H. Self-assembly of collagen. *Journal of Supramolecular Structure* **2,** 99–102 (1974).

231. Bianchi, E. *et al.* The role of pH, temperature, salt type, and salt concentration on the stability of the crystalline, helical, and randomly coiled forms of collagen. *The Journal of Biological Chemistry* **242,** 1361–1369 (Apr. 10, 1967).

232. Freudenberg, U. *et al.* Electrostatic Interactions Modulate the Conformation of Collagen I. *Biophysical Journal* **92,** 2108–2119 (Mar. 2007).

233. Bella, J. *et al.* Hydration structure of a collagen peptide. *Structure* **3,** 893–906 (Sept. 1995).

234. Cameron, I *et al.* Verification of simple hydration/dehydration methods to characterize multiple water compartments on Tendon Type 1 Collagen. *Cell Biology International* **31,** 531–539 (June 2007).

235. Li, Y. *et al.* Viscosity of Collagen Solutions: Influence of Concentration, Temperature, Adsorption, and Role of Intermolecular Interactions. *Journal of Macromolecular Science, Part B* **53,** 893–901 (May 4, 2014).

236. Weinstock, A. *et al.* The ion-binding characteristics of reconstituted collagen. *The Biochemical Journal* **102,** 983–988 (Mar. 1967).

237. Rosenblatt, J. *et al.* Injectable collagen as a pH-sensitive hydrogel. *Biomaterials* **15,** 985–995 (Oct. 1994).

238. Dutov, P. *et al.* Measurement of Elastic Modulus of Collagen Type I Single Fiber. *PLOS ONE* **11** (ed Dague, E.) e0145711 (Jan. 22, 2016).

239. Wenger, M. P. *et al.* Mechanical Properties of Collagen Fibrils. *Biophysical Journal* **93,** 1255–1263 (Aug. 2007).

240. Yang, L. *et al.* Mechanical Properties of Native and Cross-linked Type I Collagen Fibrils. *Biophysical Journal* **94,** 2204–2211 (Mar. 2008).

241. Achilli, M. & Mantovani, D. Tailoring Mechanical Properties of Collagen-Based Scaffolds for Vascular Tissue Engineering: The Effects of pH, Temperature and Ionic Strength on Gelation. *Polymers* **2,** 664–680 (Dec. 6, 2010).

242. Phosphate-buffered saline (PBS): *Cold Spring Harbor Protocols.* 10.1101/pdb.rec8247. http://www.cshprotocols.org/lookup/doi/10.1101/pdb.rec8247 (2006).

243. Al-Ghobashy, M. A. Electrophoretic behavior of charge regulated zwitter ionic buffers in covalently and dynamically coated fused silica capillaries. *Bulletin of Faculty of Pharmacy, Cairo University* **52,** 71–78 (June 2014).

244. Urry, D. W. Neutral sites for calcium ion binding to elastin and collagen: a charge neutralization theory for calcification and its relationship to atherosclerosis. *Proceedings of the National Academy of Sciences of the United States of America* **68,** 810–814 (Apr. 1971).

245. Carney, R. P. *et al.* Electrical Method to Quantify Nanoparticle Interaction with Lipid Bilayers. *ACS Nano* **7,** 932–942 (Feb. 26, 2013).

246. Vunder, V. *Modeling and characterization of back-relaxation of ionic electroactive polymer actuators* PhD thesis (University of Tartu, 2016).

247. Guan, M. J. & Liao, W. H. On the Equivalent Circuit Models of Piezoelectric Ceramics. *Ferroelectrics* **386,** 77–87 (Aug. 12, 2009).

248. Park, C. H. On the Circuit Model of Piezoceramics. *Journal of Intelligent Material Systems and Structures* **12,** 515–522 (July 2001).

249. Nandy, D. & Mukhopadhyay, D. Growth Factor Mediated Signaling in Pancreatic Pathogenesis. *Cancers* **3,** 841–871 (Feb. 24, 2011).

250. Mak, K. M. *et al.* Type V Collagen in Health, Disease, and Fibrosis. *The Anatomical Record* **299,** 613–629 (May 2016).

251. Sun, M. *et al.* Targeted Deletion of Collagen V in Tendons and Ligaments Results in a Classic Ehlers-Danlos Syndrome Joint Phenotype. *The American Journal of Pathology* **185,** 1436–1447 (May 2015).

252. Seet, L.-F. *et al.* Upregulation of distinct collagen transcripts in post-surgery scar tissue: a study of conjunctival fibrosis. *Disease Models & Mechanisms* **10,** 751–760 (June 1, 2017).

253. Garca-Pravia, C. *et al.* Overexpression of COL11A1 by Cancer-Associated Fibroblasts: Clinical Relevance of a Stromal Marker in Pancreatic Cancer. *PLoS ONE* **8** (ed Real, F.) e78327 (Oct. 23, 2013).

254. Ganesh, S. K. *et al.* Clinical and biochemical profiles suggest fibromuscular dysplasia is a systemic disease with altered TGF-β expression and connective tissue features. *The FASEB Journal* **28,** 3313–3324 (Aug. 2014).

255. Shen, W. *et al.* TGF-β in pancreatic cancer initiation and progression: two sides of the same coin. *Cell & Bioscience* **7,** 39 (Dec. 2017).

256. Truty, M. J. & Urrutia, R. Basics of TGF-β and Pancreatic Cancer. *Pancreatology* **7,** 423–435 (Oct. 2007).

257. Meng, X.-m. *et al.* TGF-β: the master regulator of fibrosis. *Nature Reviews Nephrology* **12,** 325–338 (June 2016).

258. Klinkhammer, B. M. *et al.* PDGF in organ fibrosis. *Molecular Aspects of Medicine* **62,** 44–62 (Aug. 2018).

259. Chaudhary, N. I. *et al.* Inhibition of PDGF, VEGF and FGF signalling attenuates fibrosis. *European Respiratory Journal* **29,** 976–985 (May 1, 2007).

260. Trojanowska, M. Role of PDGF in fibrotic diseases and systemic sclerosis. *Rheumatology* **47,** v2–v4 (Supplement 5 Oct. 1, 2008).

261. Hwang, R. F. *et al.* Inhibition of platelet-derived growth factor receptor phosphorylation by STI571 (Gleevec) reduces growth and metastasis of human pancreatic carcinoma in an orthotopic nude mouse model. *Clinical Cancer Research: An Official Journal of the American Association for Cancer Research* **9,** 6534–6544 (Dec. 15, 2003).

262. Yuzawa, S. *et al.* PDGFR expression in tumor stroma of pancreatic adenocarcinoma as a reliable prognostic marker. *Medical Oncology* **29,** 2824–2830 (Dec. 2012).

263. McCarty, M. F. *et al.* Overexpression of PDGF-BB decreases colorectal and pancreatic cancer growth by increasing tumor pericyte content. *Journal of Clinical Investigation* **117,** 2114–2122 (Aug. 1, 2007).

264. FrancoBarraza, J. *et al.* Preparation of Extracellular Matrices Produced by Cultured and Primary Fibroblasts. *Current Protocols in Cell Biology* **71** (June 2016).

265. Piersma, B. & Bank, R. Collagen cross-linking mediated by lysyl hydroxylase 2: an enzymatic battlefield to combat fibrosis. *Essays in Biochemistry* **63** (ed Adams, J.) 377–387 (Sept. 13, 2019).

266. Hanahan, D. & Weinberg, R. Hallmarks of Cancer: The Next Generation. *Cell* **144,** 646–674 (Mar. 2011).

267. Rigby, J. E. *et al.* Can physical trauma cause breast cancer? *European Journal of Cancer Prevention* **11,** 307–311 (June 2002).

268. Jessy, T. Immunity over inability: The spontaneous regression of cancer. *Journal of Natural Science, Biology and Medicine* **2,** 43 (2011).

269. Follain, G. *et al.* Fluids and their mechanics in tumour transit: shaping metastasis. *Nature Reviews Cancer* **20,** 107–124 (Feb. 2020).

270. Tee, S.-Y. *et al.* Cell Shape and Substrate Rigidity Both Regulate Cell Stiffness. *Biophysical Journal* **100,** L25–L27 (Mar. 2011).

271. Roca-Cusachs, P. *et al.* Quantifying forces in cell biology. *Nature Cell Biology* **19,** 742–751 (June 19, 2017).

272. Folkman, J. & Moscona, A. Role of cell shape in growth control. *Nature* **273,** 345–349 (June 1978).

273. Zanoni, M. *et al.* Modeling neoplastic disease with spheroids and organoids. *Journal of Hematology & Oncology* **13,** 97 (Dec. 2020).

274. Mueller-Klieser, W. Multicellular spheroids: A review on cellular aggregates in cancer research. *Journal of Cancer Research and Clinical Oncology* **113,** 101–122 (Apr. 1987).

275. Montheard, J.-P. *et al.* 2-Hydroxyethyl Methacrylate (HEMA): Chemical Properties and Applications in Biomedical Fields. *Journal of Macromolecular Science, Part C: Polymer Reviews* **32,** 1–34 (Feb. 1992).

276. Karpushkin, E. *et al.* Rheological properties of homogeneous and heterogeneous poly(2-hydroxyethyl methacrylate) hydrogels. *Polymer International* **61,** 328–336 (Feb. 2012).

277. Bat, N. *et al.* Rheology and adhesive properties versus structure of poly(acrylamide-co-hydroxyethyl methacrylate) hydrogels. *International Journal of Adhesion and Adhesives* **96,** 102449 (Jan. 2020).

278. Janek, J. Mechanical Behavior of Hydroxyalkyl Methacrylate Polymers and Copolymers. *Journal of Macromolecular Science, Part C: Polymer Reviews* **9,** 3–47 (Jan. 1973).

279. Lewis, C. L. & Anthamatten, M. Synthesis, swelling behavior, and viscoelastic properties of functional poly(hydroxyethyl methacrylate) with ureidopyrimidinone side-groups. *Soft Matter* **9,** 4058 (2013).

280. Stevenson, W. T. K. & Sefton, M. V. The equilibrium water content of some thermoplastic hydroxyalkyl methacrylate polymers. *Journal of Applied Polymer Science* **36,** 1541–1553 (Sept. 20, 1988).

281. Salom Machado, A. A. *et al.* Thermal and Rheological Behavior of Collagen. Chitosan blends. *Journal of Thermal Analysis and Calorimetry* **67,** 491–498 (2002).

282. Knapp, D. M. *et al.* Rheology of reconstituted type I collagen gel in confined compression. *Journal of Rheology* **41,** 971–993 (Sept. 1997).

283. Brazdaru, L. *et al.* Structural and rheological properties of collagen hydrogels containing tannic acid and chlorhexidine digluconate intended for topical applications. *Comptes Rendus Chimie* **18,** 160–169 (Feb. 2015).

284. Zuidema, J. M. *et al.* A protocol for rheological characterization of hydrogels for tissue engineering strategies: A Protocol for Rheological Characterization of Hydrogels. *Journal of Biomedical Materials Research Part B: Applied Biomaterials* **102,** 1063–1073 (July 2014).

285. Roca-Cusachs, P. *et al.* Rheology of Passive and Adhesion-Activated Neutrophils Probed by Atomic Force Microscopy. *Biophysical Journal* **91,** 3508–3518 (Nov. 2006).

286. Engelmayr, G. C. *et al.* Guidance of engineered tissue collagen orientation by large-scale scaffold microstructures. *Journal of Biomechanics* **39,** 1819–1831 (Jan. 2006).

287. *PureCol EZ Gel solution* Sigma-Aldrich Preparation Note. https://www.sigmaaldrich.com/catalog/product/sigma/5074?lang=en&region=GB. 2020.

288. Tian, Z. *et al.* Physicochemical properties of collagen solutions cross-linked by glutaraldehyde. *Connective Tissue Research* **55,** 239–247 (June 2014).

289. Ruijgrok, J. M. *et al.* Optimizing glutaraldehyde crosslinking of collagen: effects of time, temperature and concentration as measured by shrinkage temperature. *Journal of Materials Science: Materials in Medicine* **5,** 80–87 (Feb. 1994).

290. Olde Damink, L. H. H. *et al.* Glutaraldehyde as a crosslinking agent for collagen-based biomaterials. *Journal of Materials Science: Materials in Medicine* **6,** 460–472 (Aug. 1995).

291. Chandran, P. L. *et al.* Structural Mechanism for Alteration of Collagen Gel Mechanics by Glutaraldehyde Crosslinking. *Connective Tissue Research* **53,** 285–297 (Aug. 2012).

292. Alcaraz, J. *et al.* Correction of Microrheological Measurements of Soft Samples with Atomic Force Microscopy for the Hydrodynamic Drag on the Cantilever. *Langmuir* **18,** 716–721 (Feb. 2002).

293. Gavara, N. & Chadwick, R. S. Determination of the elastic moduli of thin samples and adherent cells using conical atomic force microscope tips. *Nature Nanotechnology* **7,** 733–736 (Nov. 2012).

294. Akhtar, R. *et al.* Characterizing the elastic properties of tissues. *Materials Today* **14,** 96–105 (Mar. 2011).

295. Chen, W.-L. *et al. 50th Anniversary Perspective* : Polymer Brushes: Novel Surfaces for Future Materials. *Macromolecules* **50,** 4089–4113 (June 13, 2017).

296. Dokukin, M. E. *et al.* AFM Study of Polymer Brush Grafted to Deformable Surfaces: Quantitative Properties of the Brush and Substrate Mechanics. *Macromolecules* **50,** 275–282 (Jan. 10, 2017).

297. Jalili, K. *et al.* In situ probing of switchable nanomechanical properties of responsive high-density polymer brushes on poly(dimethylsiloxane): An AFM nanoindentation approach. *Journal of the Mechanical Behavior of Biomedical Materials* **93,** 118–129 (May 2019).

298. Üzüm, C. *et al.* Growth behaviour and mechanical properties of PLL/HA multilayer films studied by AFM. *Beilstein Journal of Nanotechnology* **3,** 778–788 (Nov. 21, 2012).

299. Gutsmann, T. *et al.* Sacrificial Bonds in Polymer Brushes from Rat Tail Tendon Functioning as Nanoscale Velcro. *Biophysical Journal* **89,** 536–542 (July 2005).

300. Rezende, C. A. *et al.* Detection of charge distributions in insulator surfaces. *Journal of Physics: Condensed Matter* **21,** 263002 (July 1, 2009).

301. Nonnenmacher, M. *et al.* Kelvin probe force microscopy. *Applied Physics Letters* **58,** 2921–2923 (June 24, 1991).

302. Braga, M. *et al.* Scanning Electric Potential Microscopy Imaging of Polymer Latex Films: Detection of Supramolecular Domains with Nonuniform Electrical Characteristics. *The Journal of Physical Chemistry B* **105,** 3005–3011 (Apr. 2001).

303. Sauer, F. *et al.* Collagen networks determine viscoelastic properties of connective tissues yet do not hinder diffusion of the aqueous solvent. *Soft Matter* **15,** 3055–3064 (2019).

304. Chen, D.-C. *et al.* Osteoblastic response to collagen scaffolds varied in freezing temperature and glutaraldehyde crosslinking. *Journal of Biomedical Materials Research Part A* **80A,** 399–409 (Feb. 2007).

305. Haugh, M. G. *et al.* Crosslinking and Mechanical Properties Significantly Influence Cell Attachment, Proliferation, and Migration Within Collagen Glycosaminoglycan Scaffolds. *Tissue Engineering Part A* **17,** 1201–1208 (May 2011).

306. Brooks, P. J. *et al.* An Overview of the Derivation and Function of Multinucleated Giant Cells and Their Role in Pathologic Processes. *The American Journal of Pathology* **189,** 1145–1158 (June 2019).

307. Chambers, T. J. Multinucleate giant cells. *The Journal of Pathology* **126,** 125–148 (Nov. 1978).

308. Raman, A. *et al.* Mapping nanomechanical properties of live cells using multi-harmonic atomic force microscopy. *Nature Nanotechnology* **6,** 809–814 (Dec. 2011).

309. Alcaraz, J. *et al.* Microrheology of Human Lung Epithelial Cells Measured by Atomic Force Microscopy. *Biophysical Journal* **84,** 2071–2079 (Mar. 2003).

310. Fabry, B. *et al.* Scaling the Microrheology of Living Cells. *Physical Review Letters* **87,** 148102 (Sept. 13, 2001).

311. Trepat, X. *et al.* Thrombin and histamine induce stiffening of alveolar epithelial cells. *Journal of Applied Physiology* **98,** 1567–1574 (Apr. 2005).

312. Kim, J. *et al.* Human organoids: model systems for human biology and medicine. *Nature Reviews Molecular Cell Biology* **21,** 571–584 (Oct. 2020).